Investigation of instability and turbulence effects on gas explosions: experiments and modelling

Helene Hisken

UNIVERSITY OF BERGEN

Investigation of instability and turbulence effects on gas explosions: experiments and modelling

Helene Hisken

Thesis for the Degree of Philosophiae Doctor (PhD)
at the University of Bergen

2018

Date of defence: 09.03.2018

Year: 2018

Title: Investigation of instability and turbulence effects on gas explosions: experiments and modelling

Name: Helene Hisken

Print: Skipnes Kommunikasjon / University of Bergen

Acknowledgements

Abstract

Safe design of industrial facilities requires models that can predict the consequences of accidental gas explosions in complex geometries with sufficient accuracy. Computational fluid dynamics (CFD) models are widely used for consequence assessment in the process industries. The primary mechanism for flame acceleration during gas explosions in congested geometries is the positive feedback between turbulence generated in the reactant mixture, especially in shear and boundary layers from explosion-driven flow past obstacles and walls, and enhanced combustion rates. Additionally, a range of instability phenomena can significantly increase flame acceleration in gas explosions.

This doctoral project addresses the following research question: *"how can the sub-grid representation of flame acceleration mechanisms due to instability effects and flow past obstructed regions be improved in a CFD tool used for consequence assessment of gas explosions?"*. The thesis presents and validates new sub-grid models developed for the CFD tool FLACS, focusing on the following flame acceleration mechanisms: (i) the influence of the hydrodynamic and thermal–diffusive instabilities (intrinsic instabilities) on flame acceleration in the initial phase of a gas explosion, (ii) the influence of thermal–diffusive effects on the rate of turbulent combustion for different fuels and mixture concentrations, (iii) the role of the Bénard–von Kármán (BVK) instability downstream of bluff-body obstacles in explosion-induced flow, (iv) how the Rayleigh–Taylor (RT) instability developing on a flame front that is accelerated over an obstacle or a vent opening may enhance the combustion rate, and (v) how flexible obstructions with very small components (in the form of vegetation) induce flame acceleration in gas explosions. There was a lack of available experimental work describing the relative importance of several of the aforementioned effects. Therefore, three experimental campaigns were designed and conducted as part of the doctoral study. Experimental findings thus constitute a significant part of the original scientific contribution of the present work; these can be used to develop sub-grid models for any consequence model system. Three additional campaigns, performed by other research groups, were simulated in order to validate the new sub-grid models.

The first experimental campaign presented in the thesis concerned explosion experiments performed in a large-scale, empty, vented enclosure comprising two chambers separated by a doorway. Simulations indicate that model performance might improve by introducing the effect of the RT instability. Furthermore, the results suggest that the model should account for thermal–diffusive instability effects both in the initial phase of a gas explosion and in the regime of turbulent combustion.

The onset and growth rate of intrinsic instabilities in gas explosions are closely linked to the value of the Markstein number of the fuel-air mixture. The second experimental campaign presented in the thesis was performed as part of the doctoral study to explore the effect of varying the fuel concentration on overpressures and flame speeds in a series of propane-air explosions. The variations in the fuel concentration effec-

tively change the Markstein number of the mixture. The dissertation compares experimental results with predictions from a version of FLACS that includes a Markstein number-dependent combustion model, developed as part of the doctoral project. For negative Markstein numbers, the new model version performs significantly better than the original model. This work addresses mechanisms (i) and (ii).

The thesis elaborates on instability effects relevant for scenarios where explosion-induced flow interacts with partial confinement and obstacles, focusing on BVK and RT instabilities in particular, i.e. mechanisms (iii) and (iv). A third experimental campaign was performed as part of the present study to investigate the relative contribution of vortex shedding, caused by the BVK instability, to the overpressure generation in gas explosions with a single obstacle inserted. Vortex shedding was observed in the baseline laboratory-scale experiments, and then suppressed by two passive flow control methods. The most effective configuration reduced the maximum overpressures by approximately 32 %. The results can be used to model the flame surface area increase downstream of obstacles in any consequence model system. However, further experimental work, building on the findings of the present doctoral study, is required to formulate a sub-grid model for mechanism (iii).

A sub-grid model for flame wrinkling due to the RT instability (mechanism (iv)), based on the linearised growth rate of instabilities on an accelerated flame front, was implemented in FLACS. The thesis presents updated model results for two series of vented explosion experiments, obtained with a version of FLACS that includes both the Markstein number-dependent burning velocity model and the RT instability effect. The first test case involved a series of fuel-lean hydrogen-air explosions. The second test case revisited the campaign performed in the twin-compartment enclosure that was presented in the very beginning of the thesis. A third test case was included to investigate whether the sub-grid models that were initially developed and validated for explosions with a high degree of confinement and idealised obstacle configurations could produce improved results also for explosions in complex geometries with a low degree of confinement. Therefore, a series of large-scale natural gas-air explosions performed in a full-scale offshore module was simulated. All three test cases were performed by other research groups. The sub-grid models developed as part of the present doctoral study significantly improve the representation of several of these experiments.

The fourth experimental campaign was motivated by a need for an improved approach to sub-grid modelling of the effect of vegetation on gas explosions in CFD tools, i.e. mechanism (v). Recent accidents have shown that this is highly relevant for risk assessment for onshore process facilities. The presence of foliage on spruce branches notably enhanced maximum overpressures in the experiments, suggesting that obstructions of very small dimensions may contribute significantly to the flame acceleration. Highly flexible, fractal-like obstructions require additional modelling considerations. Based on the experimental results, the effects of foliage and flexibility were included in FLACS simulations by constructing congestion blocks, representing the effective drag area that is expected to produce flame acceleration. This modelling approach successfully reproduces the experimental trends.

In conclusion, the results of the experimental campaigns presented in this thesis have improved the understanding of several important physical effects related to flame acceleration in industrial-scale explosions. Furthermore, the thesis demonstrates how this knowledge may be used to model gas explosions more accurately.

List of papers

1. Pedersen, H.H.*, Tomlin, G., Middha, P., Phylaktou, H.N. & Andrews, G.E. (2013). Modelling large-scale vented gas explosions in a twin compartment enclosure. *Journal of Loss Prevention in the Process Industries*, **26**: 1604–1615.

2. Hisken, H.*, Enstad, G.A., Middha, P. & van Wingerden, K. (2015). Investigation of concentration effects on the flame acceleration in vented channels. *Journal of Loss Prevention in the Process Industries*, **36**: 447–459.

3. Hisken, H.*, Enstad, G.A. & Narasimhamurthy, V.D. (2016). Vortex shedding in gas explosions and its mitigation: an experimental study. *Journal of Loss Prevention in the Process Industries*, **43**: 242–254.

4. Pedersen, H.H.*, Enstad, G.A., Skjold, T. & Brewerton, R.W. (2013). The effect of vegetation with various degrees of foliage on gas explosions in a 1.5 m channel. *Proceedings Seventh International Seminar on Fire and Explosion Hazards (ISFEH), Providence, 5-10 May 2013*, Research Publishing, Singapore: 646–655. ISBN: 978-981-07-5936-0.

*The candidate changed her name from Helene Hisken Pedersen to Helene Hisken in 2015.

List of papers not included in the present dissertation

1. Pedersen, H.H.*, Middha, P., van Wingerden, K., Skjold, T. & Arntzen, B.J. (2011). Modelling of flame acceleration due to intrinsic instabilities in industrial scale explosions. *Twenty-third International Colloquium on the Dynamics of Explosions and Reactive Systems (ICDERS), Irvine, 24-29 July 2011*.

2. Pedersen, H.H.* & Middha, P. (2012). Modelling of vented gas explosions in the CFD tool FLACS. *Chemical Engineering Transactions*, **26**: 357-362. ISBN 978-88-95608-17-4. ISSN 1974–9791.

3. Skjold, T., Christensen, S.O., Bernard, L., Pedersen, H.H.* & Narasimhamurthy, V.D. (2012). Urban canyon blast load calculations. *Twenty-second International Symposium on Military Aspects of Blast and Shock (MABS), Bourges, 4-9 November 2012*.

4. Skjold, T., Pedersen, H.H.*, Bernard, L., Middha, P., Narasimhamurthy, V.D., Landvik, T., Lea, T. & Pesch, L. (2013). A matter of life and death: validating,

qualifying and documenting models for simulating flow-related accident scenarios in the process industry. *Chemical Engineering Transactions*, **31**: 187–192. ISBN: 978-88-95608-22-8. ISSN: 1974-9791.

5. Pedersen, H.H.*, Davis, S., Middha, P., Arntzen, B.J. & Skjold, T. (2013). Sensitivity analysis and parameter optimization for the improved modelling of gas explosions. *Twenty-fifth International Colloquium on the Dynamics of Explosions and Reactive Systems (ICDERS), Taipei, 28 July - 2 August 2013*.

6. Skjold, T., Pedersen, H.H.*, Narasimhamurthy, V.D., Lakshmipathy, S., Pesch, L., Atanga, G.F., Folusiak, M., Bernard, L., Siccama, D. & Storvik, I.E. (2014). Pragmatic modelling of industrial explosions in complex geometries: review of the state-of-the-art and prospects for the future. *Zel'dovich Memorial: Accomplishments in the combustion science in the last decade, Volume 1*: 70–74. Edited by A.A. Borisov & S.M. Frolov. ISBN 978-5-94588-156-3. Torus Press, Moscow.

7. Skjold, T. & Hisken, H.* (2015). Numerical investigation of constant volume propane-air explosions in a 3.6-metre flame acceleration tube. *Twenty-fifth International Colloquium on the Dynamics of Explosions and Reactive Systems (ICDERS), Leeds, 2-7 August 2015*.

8. Narasimhamurthy, V.D., Hisken, H.*, Atanga, G. & Skjold, T. (2015). Porosity/distributed resistance modelling for industrial CFD applications. *Eighth National Conference on Computational Mechanics, MekIT'15, 18-19 May 2015, Trondheim, Norway*. B. Skallerud & H.I. Andersson (Eds), International Center for Numerical Methods in Engineering (CIMNE): 321–331. ISBN: 9788494424496.

9. Skjold, T., Siccama, D., Hisken, H.*, Brambilla, A., Middha, P., Groth, K.M. & LaFleur, A.C. (2017). 3D risk management for hydrogen installations. *International Journal of Hydrogen Energy*, **42**(11): 7721–7730.

10. Braatz, A.-L., Hisken, H.* & Rückmann, J.-J. (2016). Surrogate-based optimisation of model parameters for the improved modelling of industrial-scale gas explosions. *Proceeding Fifth International Conference on Engineering Optimization, Iguassu Falls, Brazil, 19-23 June 2016*.

11. Hisken, H.*, Atanga, G., Skjold, T., Lakshmipathy, S. & Middha, P. (2016). Validating, documenting and qualifying models used for consequence assessment of hydrogen explosion scenarios. *Proceedings Eleventh International Symposium on Hazards, Prevention and Mitigation of Industrial Explosions, Dalian, 24-29 July 2016*: 1069–1086. ISBN 978-7-89437-165-2.

12. Braatz, A.-L. & Hisken, H.* (2017). Response surfaces for advanced consequence models: Two approaches. *Journal of Loss Prevention in the Process Industries*, 49: 683-699.

13. Skjold, T., Hisken, H.*, Lakshmipathy, S., Atanga, G., Carcassi, M., Schiavetti, M., Stewart, J.R., Newton, A., Hoyes, J.R., Tolias, I.C., Venetsanos, A.G.,

Hansen, O.R., Geng, J., Huser, A., Helland, S., Jambut, R., Ren, K., Kotchourko, A., Jordan, T., Daubech, J., Lecocq, G., Hanssen, A.G., Kumar, C., Krumenacker, L., Jallais, S., Miller, D. & Bauwens, C.R. (2017). Blind-prediction: estimating the consequences of vented hydrogen deflagrations for homogeneous mixtures in 20-foot ISO containers. *Proceedings Seventh International Conference on Hydrogen Safety (ICHS 2017), Paper # 225, Hamburg, 11-13 September 2017*: 639-652. ISBN 978-88-902391.

14. Skjold, T., Hisken, H.*, Lakshmipathy, S., Atanga, G., van Wingerden, M., Olsen, K.L., Holme, M.N., Turøy, N.M., Mykleby, M. & van Wingerden, K. (2017). Influence of congestion on vented hydrogen deflagrations in 20-foot ISO containers: homogeneous fuel-air mixtures. *Twenty-Sixth International Colloquium on the Dynamics of Explosions and Reactive Systems (26 ICDERS), Boston, 30 July – 4 August 2017*.

15. Skjold, T., Hisken, H.*, Lakshmipathy, S., Atanga, G., van Wingerden, M., Olsen, K.L., Holme, M.N., Turøy, N.M., Mykleby, M. & van Wingerden, K. (2017). Vented hydrogen deflagrations in containers: effect of congestion for homogeneous mixtures. *Proceedings Seventh International Conference on Hydrogen Safety (ICHS 2017), Paper # 223, Hamburg, 11-13 September 2017*: 591-603. ISBN 978-88-902391.

16. Atanga, G., Lakshmipathy, S., Skjold, T., Hisken, H.* & Hanssen, A.G. (2017). Structural response for vented hydrogen deflagrations: coupling CFD and FE tools. *Proceedings Seventh International Conference on Hydrogen Safety (ICHS 2017), Paper # 224, Hamburg, 11-13 September 2017*: 378-387. ISBN 978-88-902391.

17. Lakshmipathy, S., Skjold, T., Hisken, H.* & Atanga, G. (2017). Consequence models for vented hydrogen deflagrations: CFD vs. engineering models. *Proceedings Seventh International Conference on Hydrogen Safety (ICHS 2017), Paper # 222, Hamburg, 11-13 September 2017*: 615-626. ISBN 978-88-902391.

Scientific environment

The doctoral project was funded by the Research Council of Norway (RCN) through the Industrial PhD scheme, grant number 209745, and Gexcon AS. The work was organised as a four year project, with three years of funding from RCN and Gexcon for the doctoral study, and the remaining time reserved for other company assignments. The candidate has been associated with the Research Group for Petroleum and Process Technology, Department of Physics and Technology at the University of Bergen throughout the project period, under the principal supervision of associate professor Bjørn J. Arntzen.

The candidate has been employed as a Research Engineer in the Research and Development (R&D) department at Gexcon since August 2010. Co-supervisors at Gexcon have been Dr. Kees van Wingerden, Dr. Prankul Middha and Dr. Vagesh D. Narasimhamurthy. Dr. Bjørn J. Arntzen also holds a part-time position in the R&D department at Gexcon.

Gexcon R&D develops and maintains the computational fluid dynamics (CFD) solver Flacs, capable of simulating gas dispersion, fires and explosions in large-scale realistic geometries. Flacs belongs to the family of CFD solvers that apply the porosity/distributed resistance (PDR) concept to represent complex geometry in simulations of flow-related accident scenarios. Flacs is an integrated part of the commercial software product FLACS.

A significant part of the doctoral study has involved documenting, updating and improving the source code for premixed combustion in Flacs. Furthermore, the candidate has contributed to the development of an integrated framework for validating the model, in close cooperation with members of the Gexcon R&D team. The candidate has also been involved in customer support throughout the project period.

Through the work as Research Engineer, the candidate has contributed to the joint industry projects (JIPs) "FLACS 2011 and beyond" (2009-2013) and "Modelling Escalating Accident Scenarios and the Use of Risk-reducing technology for Explosion safety (MEASURE)" (2013-2016). The two JIPs have progressed in parallel with the doctoral project, and results from the doctoral project have been used extensively in both projects. However, due to confidentiality issues, experimental results originating from JIP MEASURE have not been used in the doctoral project. The work as Research Engineer has also entailed the supervision of MSc candidate Laurence Bernard in 2012, and support of MSc candidate Knut-Arne Vik in 2013-2014.

The candidate conducted the modelling work for three experimental campaigns performed as part of the JIP "Buncefield Phase 2" together with Robert W. Brewerton from Natabelle Technology Ltd. This JIP was initiated in the aftermath of the devastating vapour cloud explosion that occurred on the Buncefield oil storage depot in Hemel Hempstead, UK, on 11 December 2005. The objective of the experimental campaigns

was to study the effect of vegetation on flame acceleration in large-scale gas explosions.

The candidate has contributed to the project "Improving Hydrogen Safety for Energy Applications through pre-normative research on vented deflagrations (HySEA)" (2015-2018). The HySEA project receives funding from the Fuel Cells and Hydrogen 2 Joint Undertaking under grant agreement no 671461. This Joint Undertaking receives support from the European Union's Horizon 2020 research and innovation programme and United Kingdom, Italy, Belgium and Norway. Furthermore, the candidate has contributed to the innovation project "3D Risk Management for Hydrogen Installations (Hy3DRM)" (2015-2017), funded by RCN under the ENERGIX programme. Results from the doctoral project have been used extensively in both projects.

The candidate has worked with Dr. Scott G. Davis from the Gexcon US office on optimisation techniques developed for detailed chemical kinetics models, and applied them to parameter optimisation in FLACS. The candidate developed this methodology further in cooperation with fellow PhD candidate Anna-Lena Braatz, also employed as a Research Engineer in the R&D department at Gexcon and associated with the Department of Informatics at the University of Bergen. This work is not included in the present thesis.

The candidate has worked with fellow PhD student Gary B. Tomlin from DNV GL and Leeds University, and his supervisors Dr. Roth Phylaktou and Professor Gordon E. Andrews from Leeds University, on the analysis and modelling of a set of previously un-published data from the research of British Gas in the 1980s. The candidate assisted with an experimental campaign to extend this work, led by Gary B. Tomlin at the DNV GL test site at Spadeadam, England, for one week in June 2012.

Finally, the candidate has planned and conducted three small-scale experimental campaigns in the laboratory facilities at the Gexcon office at Fantoft, as well as one medium-scale campaign at Gexcon's test site at the island of Sotra, with assistance from the Gexcon Laboratories department.

Nomenclature

Roman letters

a_d	Amplitude of disturbance
A	Area
A_f	Flame surface area
A_w	Effective area contributing to the wall resistance
B_ε	Buoyancy effect on production of ε
c	Progress variable
$c_{p,k}$	Specific heat capacity defined at constant pressure for species k
c_{ph}	Complex phase speed
c_q	Critical progress variable
c_s	Speed of sound
C_D	Drag coefficient
$C_{c_q}, C_{\beta D}, C_{\beta w}$	Model constants in the β flame model
C_κ	The von Karman constant
$C_\mu, C_{1\varepsilon}, C_{2\varepsilon}, C_{3\varepsilon}$	Model constants in the 'standard' $k - \varepsilon$ model
$\mathcal{C}_i$	Characteristic parameter for sub-grid obstructions in the ith direction
D	Fractal dimension
D_{cyl}	Diameter
D_{fj}	Forward rate of reaction of jth reaction
D_{rj}	Reverse rate of reaction of jth reaction
D_β	Diffusion coefficient for Y_F in the β flame model
$\mathcal{D}_k$	Mass diffusivity for species k
$\mathcal{D}_{th}$	Thermal diffusivity
$\mathcal{D}_\Phi$	Diffusion coefficient for the general flow variable Φ
e	Internal energy
E^+	Dimensionless boundary of the viscous sub-layer

f	Frequency
$f_{k,i}$	Body force on species k in the ith direction
$F_{o,i}$	Resistance due to sub-grid obstructions in the ith direction
$F_{w,i}$	Resistance due to walls in the ith direction
$\mathbf{g}$	Gravity acceleration vector
h	Static enthalpy
$h_{f,k}^0$	Standard enthalpy of formation for species k
h_t	Total enthalpy
k	Turbulence kinetic energy
k_w	Wave number
L	Characteristic length scale
ℓ	Turbulence length scale
ℓ_{lim}	Geometric extent of a confining geometry
ℓ_G	Gibson length scale
ℓ_I	Integral length scale of turbulence
ℓ_λ	Taylor microscale of turbulence
$\mathcal{L}$	Markstein length
$\mathcal{L}_b$	Markstein length relative to burnt mixture
$\mathcal{L}_u$	Markstein length relative to unburnt mixture
$\dot{m}$	Mass flow rate
M_k	Molecular weight of species k
$\mathbf{n}_f$	Normal vector for flame surface
o_i	Obstacle dependent parameter for turbulence production due to sub-grid obstacles in the ith direction
O	Order
p	Pressure
p_{ext}	Peak pressure due to external explosion
p_{obs}	Peak pressure due to maximum flame surface area being obtained in an enclosure
p_{vib}	Peak pressure due to flame-acoustic interactions
P	Pitch
P_k	Production of turbulence kinetic energy
P_ε	Production of dissipation rate of turbulence kinetic energy
q_i	Energy flux in the ith direction
$\dot{Q}$	Heat rate source term in energy equation
r	Radius
r_f	Flame radius
r_f^{cr}	Critical flame radius for onset of instability
R_Φ	Resistance term for the general flow variable Φ
$\mathcal{R}$	Ideal gas constant, $8.314 \, \text{J mol}^{-1} \, \text{K}^{-1}$

s	Generic burning velocity
S	Flame speed
S_l	Laminar flame speed
S_{ql}	Quasi-laminar flame speed
S_Φ	Source term for the general flow variable Φ
t_η	Kolmogorov timescale
T	Temperature
T_a	Activation temperature
T_b	Temperature in burnt mixture
T_u	Temperature in unburnt mixture
$\mathbf{u}$	Velocity vector
u_i	Velocity component in the ith direction
u_l	Laminar burning velocity
u_n	Stretched laminar burning velocity
u_{nr}	Stretched laminar burning velocity representing the rate of generation of combustion products associated with the flame front
u_{ql}	Quasi-laminar burning velocity
u_t	Turbulent burning velocity
u'	Turbulence velocity fluctuation
u'_k	Effective turbulence velocity fluctuation
U	Characteristic velocity
$\mathcal{U}$	Characteristic turbulence velocity
$v_{k,i}$	Diffusion speed for species k in the ith direction
V	Volume
$\dot{w}_k$	Consumption or creation rate of species k
$\dot{w}_F$	Consumption rate of fuel
W	Reaction rate coefficient
x_o	Observed (experimental) value of a generic variable
x_p	Predicted value of a generic variable
X_k	Mole fraction of species k
y^+	Dimensionless wall distance
Y_k	Mass fraction of species k
Y_F	Fuel mass fraction
Y_O	Oxidiser mass fraction

Greek letters

α	Scaling factor of u_t
β	Exponent of K in u_t
β_i	Surface area porosity in the ith direction
β_v	Volume porosity
γ_p	Constant for the pressure correction of the laminar burning velocity
Γ_Φ	Effective turbulence diffusion coefficient for the general flow variable Φ
δ_{ij}	Kronecker delta
δ_l	Laminar flame thickness
Δ	Control volume length in the direction of flame propagation
ε	Dissipation rate of turbulence kinetic energy
ζ	Fractal excess
η	Kolmogorov microscale of turbulence
θ_{ij}	Normal stress tensor
κ	Stretch rate
κ_b	Stretch rate relative to burnt mixture
κ_u	Stretch rate relative to unburnt mixture
λ	Wavelength
Λ	Eigenvalue of the 1D steady transport equation for the progress variable
μ	Dynamic viscosity
μ_{eff}	Effective dynamic viscosity
μ_B	Bulk dynamic viscosity
μ_T	Turbulent dynamic viscosity
ν	Kinematic viscosity
ξ	Mixture fraction
Ξ	Flame wrinkling factor
Ξ_{LD}	Flame wrinkling factor due to the Landau–Darrieus instability
Ξ_{RT}	Flame wrinkling factor due to the Rayleigh–Taylor instability
Ξ_S	Flame wrinkling factor due to sub-grid obstacles
Ξ_T	Flame wrinkling factor due to turbulence
ρ	Density
ρ_b	Density of burnt mixture
ρ_u	Density of unburnt mixture
σ	Expansion ratio
σ_Φ	Prandtl/Schmidt number for variable Φ
τ_{ij}	Viscous stress tensor
$\tau_{w,i}$	Shear stresses due to walls in the ith direction
υ	Reaction coefficient

ϕ	Equivalence ratio
Φ	General flow variable
χ	Backflow parameter
Ψ	Streamfunction
ω	Angular frequency
Ω	Growth rate parameter
Ω_{ij}	Tangential stress tensor

Dimensionless numbers

K	Karlovitz stretch factor
Ka	Karlovitz number
Le	Lewis number
Ma	Markstein number
Ma_c	Markstein number related to curvature
Ma_s	Markstein number related to strain rate
Ma_{cr}	Markstein number related to curvature, associated with u_{nr}
Ma_{sr}	Markstein number related to strain rate, associated with u_{nr}
Pe	Peclet number
Pr	Prandtl number
Re	Reynolds number
Re_T	Turbulence Reynolds number
Sc	Schmidt number
St	Strouhal number

Abbreviations

BG	British Gas
BVK	Bénard–von Kármán
CFD	Computational fluid dynamics
CFL	Courant–Friedichs–Lewy
CMI	Chr. Michelsen Institute
CMR	Christian Michelsen Research
CV	Control volume
DNS	Direct numerical simulation
FAC2	Fraction of predictions that are within a factor two of the observed values
JIP	Joint industry project
KH	Kelvin–Helmholtz
LD	Landau–Darrieus
LDA	Laser-Doppler anemometry
LES	Large eddy simulation
MG	Geometric mean bias
PDE	Partial differential equation
PDR	Porosity/distributed resistance
QRA	Quantitative risk assessment
RANS	Reynolds-averaged Navier–Stokes equations
RCN	The Research Council of Norway
RM	Richtmyer–Meshkov
RT	Rayleigh–Taylor
SPM	Statistical performance measure
VG	Geometric mean variance

Contents

List of Figures

Chapter 1

Introduction

1.1 Accidental gas explosions in industry and society

The hazard posed by accidental gas explosions in industry is evident from the devastating consequences of accidents such as Flixborough (1 June 1974, 28 fatalities), Piper Alpha (6 July 1988, 167 fatalities), Buncefield (11 December 2005), Deepwater Horizon (20 April 2010, 11 fatalities) and Fukushima Daiichi (11 March 2011). According to Marsh (2016), gas explosions are represented in 11 of the 20 largest accidental losses in the hydrocarbon industry in the period 1974-2015, representing approximately 9.28 billion US $ when inflated to December 2015 values. Severe incidents continue to happen: five gas explosion accidents that occurred in the period 2012-2015 were part of the '100 largest losses' list published biennially by Marsh (2016). Gas explosions also pose a hazard to residential buildings where gaseous fuels are used for heating and cooking (Tomlin, 2015).

Risk management entails systematic application of management policies and procedures to analyse, evaluate and control risk. Figure 1.1 illustrates that *risk assessment* and *risk analysis* are components of the overall process of risk management (Aven and Vinnem, 2007; Vinnem, 2014). *Consequence analysis* of flow-related accident scenarios, such as explosions and fires, is an inherent part of the risk analysis in industry. The present study focuses on topics that are relevant for predicting the consequences of gas explosions.

1.1.1 Physical phenomena

Bjerketvedt et al. (1993) define a gas explosion as *"...a process where combustion of a premixed gas cloud, i.e. fuel-air or fuel/oxidiser is causing rapid increase of pressure..."*. Gas explosions are inherently complex, as they involve physical phenomena on a wide range of spatial and temporal scales (Oran, 2014).

Skjold et al. (2014b) describe the likely phases of an accidental gas explosion event: loss of containment of gaseous and/or liquid fuel, evaporation (liquids), dispersion and mixing to form a flammable fuel-air cloud, ignition, quasi-laminar and/or turbulent premixed combustion, pressure build-up, and subsequent propagation of blast waves into the surroundings. All these processes depend, often in a non-linear fashion, on the initial conditions and the geometric configuration of the scenario. In turn, the magnitude of the pressure loads depends strongly on the rate of combustion, which is deter-
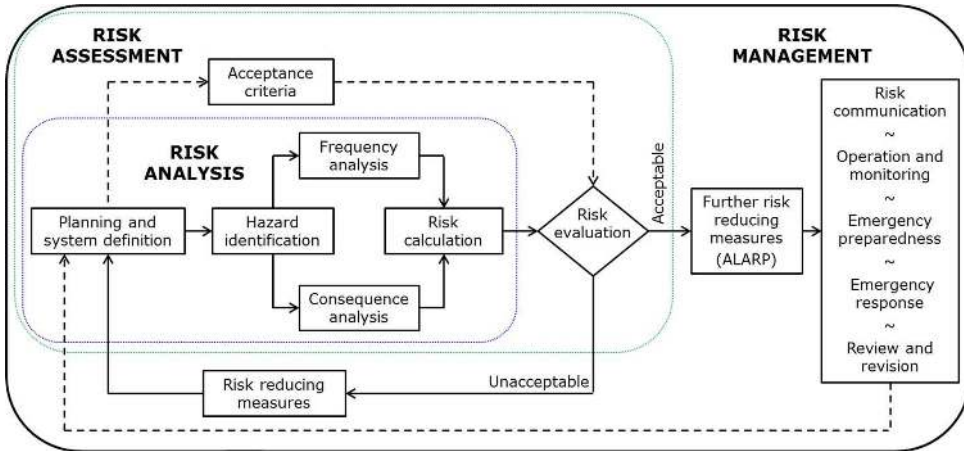
Figure 1.1: Schematic representation of risk management, risk assessment and risk analysis (Skjold, 2014).

mined by factors such as degree of congestion, degree of confinement, the reactivity of the fuel-air mixture, and properties of the reactive flow. The primary mechanism for flame acceleration in congested geometries is the positive feedback between expansion of combustion products, turbulence generated in the unreacted mixture, especially in shear and boundary layers from flow past obstacles and walls, and enhanced combustion rates (Hjertager, 1984; Kuhl, 1981; Moen et al., 1980, 1982; Schelkin, 1940). Hence, considering the spatial scale and geometry layout is very important for determining the consequences of gas explosions.

In addition to the explosion-induced formation of turbulent shear layers from obstructions and confining walls, various instability phenomena can significantly affect the flame acceleration in gas explosions. Ciccarelli and Dorofeev (2008) and Oran (2015) summarise the instability mechanisms that are commonly assumed important for industrial-scale gas explosions. In the initial, quasi-laminar phase of an explosion, or for scenarios with a low degree of congestion, the Landau–Darrieus instability govern the flame acceleration. The Landau–Darrieus instability is caused by the expansion of gas through the flame front (Darrieus, 1938; Landau, 1944), and results in the appearance of a cellular structure on the surface of the propagating flame. Laminar premixed flames are in general also subject to thermal–diffusive effects, affecting both the onset and appearance of flame cellularity (Barenblatt et al., 1962; Sivashinsky, 1977; Williams, 1985). These mechanisms are termed *intrinsic instabilities*.

Obstructions and/or confinement may trigger stronger mechanisms. Instabilities that are assumed to be *geometry-induced* include the Rayleigh–Taylor instability (occurring when a lighter fluid is accelerated into a heavier fluid), the Richtmyer–Meshkov instability (occurring when two fluids of different densities are accelerated, e.g. when a shock wave interacts with a flame front) and the Kelvin–Helmholtz instability (caused by velocity shear). In addition, the Bénard–von Kármán wake instability is expected to enhance flame acceleration downstream of bluff-body obstructions. Finally, in particular for closed or vented enclosures, acoustic instabilities may produce significant overpressures (van Wingerden and Zeeuwen, 1983a). These geometry-induced insta-

bilities contribute to the generation of vorticity in gas explosions, which effectively results in overall enhanced turbulence levels, flame acceleration, and enhanced over-pressures (Oran, 2015).

1.1.2 Engineering models for consequence analysis

Safe design of industrial facilities requires models that are efficient to use, and can predict the consequences of gas explosions in complex geometries with sufficient accuracy (Vinnem, 2014). The main categories of engineering models used for assessing the consequences of gas explosions are 1) venting guidelines 2) complex empirical models 3) phenomenological models and 4) computational fluid dynamics (CFD) models (van Wingerden, 2013). Models of type 1), 2) and 3) are built on empirical correlations and simplified physical considerations, and are quick and relatively easy to use. However, the domain of validity of these models is limited. CFD models simulate physical processes by solving partial differential equations describing the conservation of mass, momentum, energy and chemical species. The solution varies in time and three-dimensional space, and the effect of complex geometry can be taken into account as part of the numerical solution. Models of type 4) are therefore in principle the most general.

Although the governing equations for turbulent fluid flow with chemical reactions are well established, analytical solutions are primarily of theoretical interest. The level of detail of discrete solutions obtained from CFD models is restricted by the available computing power and the acceptable simulation time. For example, solutions by direct numerical simulation (DNS) can currently only be realised for small systems and low Reynolds number flows. Models based on large eddy simulations (LES) have gained increasing popularity in recent years – both in academic and industrial settings. However, within the context of simulating industrial accident scenarios as part of quantitative risk analyses (QRAs), most commercial CFD tools still rely on turbulence models based on the Reynolds-averaged Navier-Stokes (RANS) equations, such as the k-ε model (Launder and Spalding, 1974).

For industrial-scale explosions, the practically applicable computational cell sizes will in general be larger than the scales where the geometry, flow and flame front interact. Therefore, CFD models normally use phenomenological and/or empirical sub-grid models to account for processes that are not resolved on the grid. Sub-grid models based on empirical correlations provide closure for the governing equations (Hjertager, 1982), but include model parameters that have to be determined theoretically or experimentally. The validity of these model components determines the applicability range of the model system (Tam and Lee, 1998). Extensive validation against experiments and clear guidelines for how to use the CFD model are therefore necessary.

1.2 The CFD tool FLACS

Chr. Michelsen Institute (CMI) initiated the development of a CFD model for simulating gas explosions in offshore geometries in 1980. The joint industry project (JIP) 'Gas explosion research project' (1980-1986) resulted in the release of FLame ACceleration Simulator (FLACS) in 1986 (Hjertager, 1986). The development continued at

Christian Michelsen Research (CMR) from 1992 to 2000. Currently, Gexcon develops FLACS. The CFD tool is widely used for consequence assessment in the process industries; versions of the tool have been used to perform all simulations for the present doctoral study.

1.2.1   Previous research

Considerable efforts were undertaken in the years from 1990 to 2000 to improve the general predictive capabilities of FLACS for premixed combustion modelling (Arntzen, 1998). This was done in connection with a series of JIPs: 'Modelling and Experimental Research into Gas Explosions' (MERGE) (Mercx, 1994; Popat et al., 1996), 'Extended Modelling and Experimental Research into Gas Explosions' (EMERGE) (Mercx, 1996) and 'Blast and Fire Engineering for Topside Structures' (BFETS) Phase 2 (Foisselon et al., 1998; Selby and Burgan, 1998), Phase 3A (Al-Hassan and Johnson, 1998; Evans et al., 1999; Foisselon et al., 1998) and Phase 3B (Johnson and Cleaver, 2002). Furthermore, a series of Gas Safety Programmes (GSPs) were conducted both before and in parallel with these projects (in the period from 1980 to 2000). As part of the JIPs, a considerable amount of model validation data was produced (Johnson, 2013; van Wingerden, 2013). These experiments, primarily performed with natural gas, comprise the main sources of validation data for industrial explosion codes.

After the first release to the sponsors in 1986, the CFD tool FLACS has been updated and released regularly. Since 2000, applications for simulating dust explosions (Skjold, 2014), pressurised liquefied gas releases into the atmosphere (Ichard, 2012), and jet- and pool fires (Gexcon, 2016; Muthusamy and Lilleberg, 2012) have been included. However, the model system for premixed combustion has not changed significantly since a selection of the developments described by Arntzen (1998) were included.

The main goal of the JIP 'Modelling Escalating Accident Scenarios and the Use of Risk-reducing technology for Explosion safety' (MEASURE) (2013-2016) was to implement fundamental improvements to the turbulence and combustion models in FLACS, and thereby improve the performance of the model system for unconfined congested geometries, including so-called safety gap scenarios (cf. Section 1.3). Several of the results produced as part of the present doctoral study have been used in this JIP.

1.2.2   Overview of the model system

This section provides a brief overview of the modelling approaches that are applied in FLACS for simulating gas explosions.

The numerical model solves the Favre-averaged conservation equations for mass, momentum, enthalpy, mixture fraction, mass fraction of fuel, turbulence kinetic energy and the rate of dissipation of turbulence kinetic energy on a structured Cartesian grid. The system of equations is closed by invoking the ideal gas equation of state and the standard k-ε model for turbulence (Launder and Spalding, 1974). Boundary layers are not resolved in FLACS, instead wall-functions are used to compute turbulence production and drag forces for objects that are on-grid, i.e. larger than the size of the computational cell.

Geometry is represented on the computational grid using the porosity/distributed resistance (PDR) concept, first introduced by Patankar and Spalding (1974) for modelling of flow in heat exchangers. The concept was later extended by Sha et al. (1982) to include complex turbulence modelling, and Hjertager (1986) adopted the PDR approach for simulating gas explosions in complex geometries. A volume porosity β_v, denoting the ratio of open volume to the total volume of each computational cell, is computed prior to the simulation and defined at the respective grid cell centre. Similarly, the area porosity β_j represents the ratio of the projected open area between two neighbouring cell centres to the total area of the respective control volume face. A general Favre-averaged variable $\widetilde{\Phi}$ is thus integrated over the porous part of the control volume, and the flux terms in the conservation equation for $\widetilde{\Phi}$ are weighted with the area porosity β_j. On difference form, the conservation equation for the general variable $\widetilde{\Phi}$ can be expressed as

$$\frac{\partial}{\partial t}(\beta_v \overline{\rho} \widetilde{\Phi}) + \frac{\partial}{\partial x_j}(\beta_j \overline{\rho} \widetilde{\Phi} \widetilde{u}_j) - \frac{\partial}{\partial x_j}\left(\beta_j \Gamma_\Phi \frac{\partial \widetilde{\Phi}}{\partial x_j}\right) = \beta_v (S_\Phi - R_\Phi) \ , \qquad (1.1)$$

where Γ_Φ is the effective turbulent diffusion coefficient, S_Φ is the source term for $\widetilde{\Phi}$, and R_Φ represents additional resistance, additional mixing, and/or additional heat transfer caused by solid obstructions in the flow. The k-ε model is extended with a source term for the turbulence generation due to sub-grid obstructions. To model premixed combustion, FLACS applies the flamelet concept with one-step reaction kinetics. Empirical burning velocity expressions, depending on the local mixture reactivity, pressure, temperature and flow conditions, are used to model the chemical reaction rate. The burning velocity is adjusted to account for flame folding around sub-grid obstructions. The flame zone, defined by the gradient of the fuel mass-fraction, is numerically thickened to cover approximately 3-5 control volumes (Arntzen, 1998).

Efficient geometry handling, accounting for structures that cannot be resolved on the computational grid, is a prerequisite for successful representation of industrial-scale explosions. Simulations with CFD models based on the PDR formulation therefore presently represent the industry standard for assessing explosion loads in the offshore industry (Vinnem, 2014).

1.3   Modelling challenges

The range of applications for which CFD models are used to simulate gas explosions has expanded significantly over the last two decades. The topics chosen for in-depth analysis in the present thesis are motivated by modelling challenges that have emerged because of this development, as described in the following.

1.3.1   Gas explosions at onshore facilities

A recent trend in the hydrocarbon industry is to apply CFD tools for risk assessment in onshore processing facilities. Compared to offshore installations, it is much more likely that the blast from a gas explosion in an onshore facility will affect third party

stakeholders. Hence, it is crucial that the CFD model is able to capture the dominating mechanisms that govern flame propagation for a variety of fuel-air mixtures, in all relevant regimes of premixed combustion.

Gas explosion incidents at onshore facilities often involve fuels such as gasoline vapours, propane or ethylene. The physicochemical properties of these fuels differ significantly from those of natural gas, leading to dissimilar trends with variations in the fuel concentration. To ensure accurate representation of the flame propagation in gas clouds from realistic releases, validated sub-grid models for a wide range of mixture compositions are required.

Meanwhile, simulation results presented by Skjold et al. (2014a, 2013b) indicate that FLACS under-predicts the consequences of explosions in fuel-rich propane-air mixtures. Fuel-rich mixtures involving propane or higher hydrocarbons are more prone to develop flame instabilities than fuel-lean and stoichiometric mixtures with the same fuels. Furthermore, recent publications (Bradley et al., 2005, 2013, 2011a) suggest that the physicochemical properties that govern the onset and appearance of intrinsic instabilities, expressed in terms of the mixture's Markstein number, also affect the rate of turbulent combustion. In effect, fuel-rich propane-air explosions may be significantly more severe than what would be expected from considering only the unstretched laminar burning velocity of the mixture (Skjold et al., 2014a). The majority of large-scale gas explosion experiments involving hydrocarbons found in the literature have been performed using near-stoichiometric fuel-air mixtures, as these mixtures often are assumed to lead to the most severe consequences. Thus, further experimental work is needed to support the development of improved sub-grid models for non-stoichiometric mixtures.

After the explosion at Buncefield in 2005 there is growing awareness of the potential for realising high overpressures and flame speeds in large congested fuel-air clouds (Johnson et al., 2015; Tam and Johnson, 2016). The spatial scale of onshore facilities can be orders of magnitude larger than typical offshore installations. Therefore, in the event of an accidental gas explosion, flame propagation can occur over several hundred meters. Significant flame acceleration has been observed in large-scale experiments involving relatively low degrees of congestion in elongated rigs, see e.g. (Cronin and Wickens, 1986, 1988; Davis et al., 2016).

Modelling work presented in (Skjold et al., 2013b) showed that FLACS under-predicted flame acceleration and overpressures for several of the experiments in the project Blast and Fire Engineering for Topside Structures (BFETS), Phase 3A (sponsored by the Health and Safety Executive). The campaign included 45 explosion experiments with natural gas in offshore modules of dimensions 28 m × 12 m × 8 m (Al-Hassan and Johnson, 1998; Evans et al., 1999). The under-prediction was particularly pronounced for the end-ignition cases (Foisselon et al., 1998), with a low degree of confinement. In the FLACS simulations of these scenarios, sub-grid models for turbulence production, turbulent premixed combustion and localised flame folding around sub-grid obstructions generate the flame acceleration. To improve model performance, it is relevant to investigate and include the effect of additional flame acceleration mechanisms that can be significant in obstructed regions, such as the Bénard–von Kármán and Rayleigh–Taylor instabilities.

Meanwhile, it is not straightforward to study the isolated effects of the various physical phenomena occurring in obstacle wakes. Differentiating the increase in flame sur-

face area due to flame folding around objects from that generated by various instabilities, or in turbulent shear layers, poses a challenge. To support the development of improved sub-grid models, there is a need for experimental work that systematically investigates the contributions to flame acceleration from relevant mechanisms.

Physical mechanisms for the dispersion and explosion of large vapour clouds were thoroughly addressed in the aftermath of the Buncefield explosion, cf. (SCI, 2009, 2014). In this incident, the presence of trees and bushes at the site was assumed to have caused flame acceleration and significant overpressures. Vegetation has some properties that differ from those of fixed structures: vegetation is to some degree flexible, its fractal nature can result in a significant amount of very small-scale obstructions (often increasingly flexible with decreasing size) and the presence of foliage can potentially increase the effective turbulence-generating drag area of the region significantly. The combined effect of these factors, and how to represent such congestion with a CFD model based on the PDR concept, is not straightforward to anticipate. Such situations require specialised sub-grid modelling approaches.

1.3.2   Hydrogen safety

Explosions and fires represent a significant hazard for hydrogen installations, such as electrolysers, fuel cell backup systems and refuelling stations, and special measures must be applied to reduce the risk to an acceptable level. For example, the accidental release and ignition of hydrogen from high-pressure systems located in containers – such as those found at hydrogen refuelling stations – may lead to violent explosions (Sommersel et al., 2017). Installing pressure relief panels can provide effective mitigation against the consequences of gas explosions in these enclosures.

Consequence modelling for hydrogen applications is often handled with guidelines from standards based on simplified analytical models and empirical correlations. However, it is challenging to find an analytical model that can give reliable results for a wide range of geometry configurations. The use of a CFD model may therefore be required for complicated cases, e.g. in the presence of multiple vents, obstacles, stratified hydrogen layers, etc. (Vyazmina and Jallais, 2016). Furthermore, CFD models provide three-dimensional results that can be used for e.g. design input and gas detector optimisation (Skjold et al., 2017b). Hence, there is a need for CFD tools that are validated for simulating hydrogen-air explosions.

For fuel-lean hydrogen-air mixtures, thermal–diffusive effects significantly enhance the flame surface area wrinkling due to the Darrieus–Landau instability. As noted in Section 1.3.1, these effects influence burning rates in both the quasi-laminar and turbulent regimes of premixed combustion. FLACS therefore includes corrections applied directly to the laminar burning velocity of hydrogen (Middha, 2010). However, recent validation work suggests that this sub-model may be a source of inaccuracy when simulating fuel-lean hydrogen-air deflagrations (Hisken et al., 2016). An updated sub-grid model for premixed combustion of hydrogen-air mixtures in FLACS is therefore needed.

1.3.3   Vented explosions

In industrial and process enclosures, installing pressure relief panels can provide effective mitigation against the consequences of accidental gas explosions. Accurate consequence modelling of vented explosions is important e.g. for several hydrogen safety applications, cf. Section 1.3.2. Representing the flame acceleration mechanisms of vented explosions is also crucial for simulating gas explosions in dwellings (Tomlin, 2015).

Several researchers have conducted experimental work and/or discussed consequence predictions of vented explosions, see e.g. (Bauwens et al., 2009a, 2010; Butlin and Tonkin, 1974; Cooper et al., 1986; Harrison and Eyre, 1987; Keenan et al., 2013; Solberg et al., 1981; Tomlin et al., 2015; van Wingerden, 1989; van Wingerden and Zeeuwen, 1983a,b; Vyazmina and Jallais, 2016). These publications highlight the subtle, complex interactions between the flame front, turbulence production, and the range of instability phenomena that affect the development of a vented explosion. In particular, the different physical phenomena in such explosions can result in multiple, distinct overpressure peaks, where the magnitude of each peak may vary greatly with changes in ignition position, vent size, the presence and yielding pressure of pressure relief panels, the congestion level in the enclosure, and the concentration of the fuel-air mixture. Turbulence production and various flame instability effects dominate in different stages of the explosion history.

Performing model validation for vented explosions is therefore highly useful for investigating how the model represents a wide range of physical phenomena. In particular, the Rayleigh–Taylor instability is considered an important source of flame surface area in vented explosions, see e.g (Bauwens et al., 2009a,b; Cooper et al., 1986; Solberg et al., 1981; Tsuruda and Hirano, 1987). Many of the same mechanisms will obviously be active in e.g. large-scale gas explosions at offshore or onshore process facilities, cf. Section 1.3.1. The present doctoral study uses results from vented explosions to investigate different flame acceleration mechanisms experimentally, as well as for developing and validating sub-grid modelling approaches for the CFD tool FLACS.

1.4   Scope of the present thesis

This dissertation addresses the following research question: *"how can the sub-grid representation of flame acceleration mechanisms due to instability effects and flow past obstructed regions be improved in a CFD tool used for consequence assessment of gas explosions?"*. To address the research question, the thesis discusses results from several experimental campaigns together with the corresponding modelling work. Four scientific publications present a significant part of the findings of the doctoral study; these are further expanded on in the dissertation. The experimental campaigns analysed in each of the publications were designed to investigate key flame acceleration mechanisms in different flame propagation regimes relevant for industrial-scale gas explosions. All simulations for the present doctoral study have been performed with the CFD tool FLACS. Results from the experiments are used to discuss, develop and validate improved sub-grid models for premixed combustion in the CFD tool.

Specific flame acceleration mechanisms have been subject to in-depth analysis. The

following topics are addressed in the publications and/or are expanded on in subsequent chapters: (i) the influence of the hydrodynamic and thermal–diffusive instabilities (intrinsic instabilities) on flame acceleration in the initial phase of a gas explosion, (ii) the influence of thermal–diffusive effects on the rate of turbulent combustion for different fuels and mixture concentrations, (iii) the role of the Bénard–von Kármán (BVK) instability downstream of bluff-body obstacles in explosion-induced flow, (iv) how the Rayleigh–Taylor (RT) instability developing on a flame front accelerating over an obstacle or a vent opening may enhance the combustion rate, and (v) how flexible obstructions with very small components (in the form of vegetation) induce flame acceleration in gas explosions.

All these mechanisms are key for representing explosions in various industrial applications, are associated with flame instabilities, and/or are important for representing turbulent flame propagation through obstructed regions. Furthermore, recent validation work performed for the CFD tool FLACS suggests that these phenomena may not be sufficiently represented by the model, and that formulating sub-grid models to account for their effect would require further research. As there was a lack of available experimental work describing the relative importance of several of the aforementioned effects, three experimental campaigns were designed and conducted as part of the doctoral study. Experimental findings thus constitute a significant part of the original scientific contribution of the present work; these can be used to develop sub-grid models for any consequence model system.

1.5   Thesis outline

This section outlines the structure of the thesis.

Sections 1.1-1.3 in the present chapter provide the background and motivation for the doctoral study. Chapter 2 summarises the relevant governing equations and thermodynamic relations in FLACS, while Chapter 3 presents the general modelling framework for premixed combustion used by the CFD tool. Hence, chapters 2 and 3 provide the technical framework for the modelling work of the present thesis.

Chapters 4, 5 and 6 elaborate on the theoretical background for the experiments and modelling work in the publications. These chapters discuss key results from each paper, including additional model developments and simulation results to support the findings. Chapters 4, 5 and 6 thus expand on and consolidate the individual pieces of work.

In particular, Chapter 4 focuses on intrinsic flame instabilities, which occur in gas explosions independently of the presence of geometry. Intrinsic instabilities induce a cellular structure on the initially smooth surface of a freely propagating laminar flame front, increasing the flame surface area and causing flame acceleration. The flame front can be stabilised or further destabilised by thermal-diffusive effects, depending on the physicochemical properties of the fuel-oxidiser mixture, the initial pressure, etc. Chapter 4 uses linear stability theory to explain and describe the development of disturbances leading to intrinsic instabilities. The theory can be used to formulate sub-grid models accounting for flame acceleration in the cellular regime, relevant for representing the initial phase of gas explosions, as well as flame propagation in extended regions with little congestion. Furthermore, Chapter 4 explores how the physicochemical properties

of a premixed fuel-air mixture that influence the growth rate of intrinsic instabilities also affect the rate of turbulent combustion. Chapter 4 therefore mainly expands on the aforementioned topics (i) and (ii) (cf. Section 1.4), and refers in particular to Paper 1 and Paper 2 of the present thesis.

Paper 1 presents experimental and model results from an extensive campaign involving a series of explosion experiments performed in a large–scale empty, vented enclosure. The experimental configuration was, to the authors' knowledge, unique; the enclosure was divided in two chambers separated by a narrow doorway (called a 'twin-compartment' configuration). Figure 1.2 shows the layout of the experimental rig. The CFD tool FLACS has mainly been developed for predicting the effects of explosions in highly congested areas, where flow and flame front interactions with complex sub-grid obstructions constitute the main flame acceleration mechanism. It is therefore a valuable exercise to analyse the performance of the model in enclosures with a low degree of congestion, where other phenomena may govern the flame propagation and overpressure generation. Based on the analysis, Paper 1 suggests that model performance may be improved by (1) introducing updated sub-grid models for the initial phase of flame propagation, where intrinsic instabilities govern the flame acceleration, and (2) by including the effect of instabilities developing on an accelerating flame front due to the Rayleigh–Taylor instability. Furthermore, the results in Paper 1 suggest that (3) changing how the combustion rate responds to the turbulence generated by flow through vent openings may improve the representation of the explosion mechanisms. Chapter 4 expands on issues (1) and (3), while issue (2) is addressed in Chapter 5.
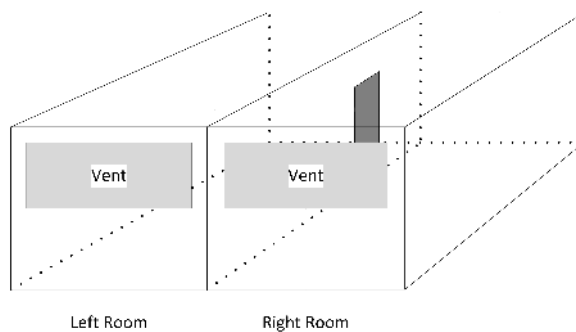
Figure 1.2: Sketch of the twin-compartment enclosure used for the experiments in Paper 1.

Chapter 4 and Paper 2 discuss how the models accounting for flame acceleration in both the initial (quiescent) phase of a gas explosion and in the turbulent regime of combustion can be improved. To support this investigation, Paper 2 presents results from an extensive experimental campaign that was designed, performed and analysed as part of the doctoral study. In this campaign, the effect of varying the fuel concentration in a propane-air mixture, thus effectively changing the physicochemical properties of the mixture in terms of the Markstein number, was explored for different flow regimes. Two different rigs, one small-scale and one medium-scale, with various obstruction configurations, were used for the experiments. Figure 1.3 and Figure 1.4 show the experimental setups used for the small-scale and medium-scale experiments, respectively. Paper 2 compares the experimental results with model predictions from a development

version of FLACS, where sub-grid models for premixed combustion developed as part of the present doctoral study have been implemented. Chapter 4 significantly expands on the theoretical background for this work.
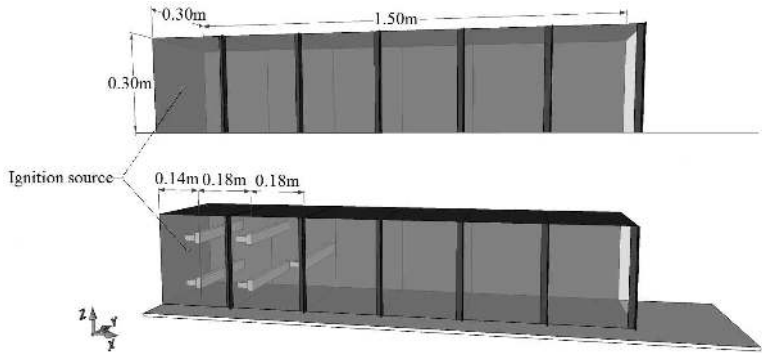
Figure 1.3: Layout of small-scale experiments performed for Paper 2.
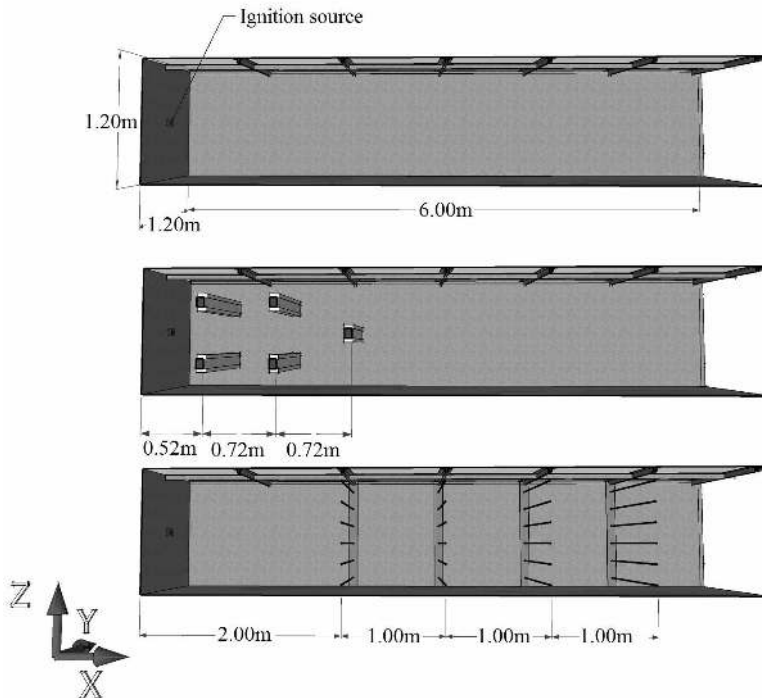
Figure 1.4: Layout of medium-scale experiments performed for Paper 2.

The general instability theory presented in Chapter 4 is also highly relevant for analysing the findings of Paper 3 and Paper 4. These results are discussed in Chapter 5, which focuses on extrinsic effects, i.e. flame acceleration mechanisms triggered by the presence of partial confinement, vent openings and obstacles. Chapter 5 addresses

topics (iii) – (iv) from Section 1.4 in particular. For completeness, Chapter 5 also briefly discusses Kelvin–Helmholtz and acoustic instability effects.

Although geometry-induced instabilities constitute powerful flame acceleration mechanisms in gas explosions, previous studies of their explicit representation in the CFD tool FLACS have been limited. For example, the Bénard–von Kármán instability causes vortex shedding in bluff-body wakes for Reynolds numbers exceeding a certain value. It is clear that these energetic, coherent structures will increase the flame surface area and thus contribute to the flame acceleration downstream of obstacles (Arntzen, 1998; Kong, 1996; Kong and Sand, 1996). However, data relevant for transient, explosion driven flow past different types of bluff-bodies appear to be extremely scarce. Therefore, for Paper 3, an experimental campaign was performed to investigate the contribution of vortex shedding to the overpressure generation in gas explosions with a single obstacle inserted. The baseline experimental configuration is shown in Figure 1.5. In addition to highlighting the importance of modelling this effect in the consequence analysis, the results trigger the question of whether suppression of vortex shedding could be used as a potential explosion mitigation method in process facilities. This is discussed further in Chapter 5.
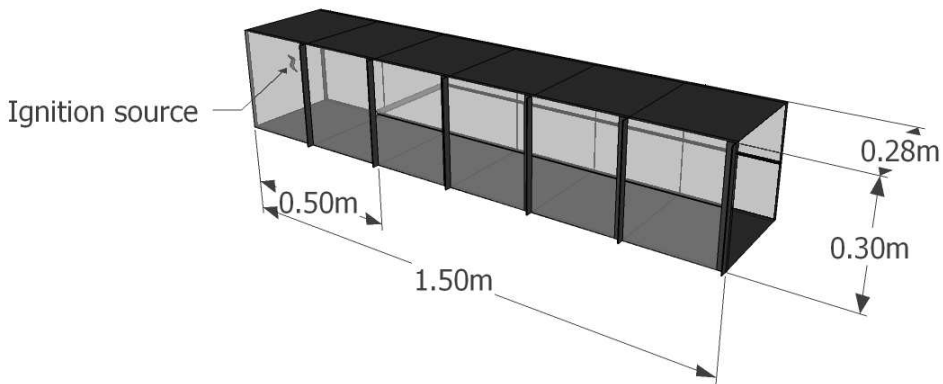
Figure 1.5: Baseline layout of the experiments performed for Paper 3.

Paper 1 suggests that model performance may be improved by including the effect of the Rayleigh–Taylor instability in FLACS. To study this mechanism, Chapter 5 uses the linear stability analysis describing the growth rate of intrinsic instabilities from Chapter 4, and includes the effect of acceleration in the analysis. Furthermore, Chapter 5 develops a sub-grid model for the Rayleigh–Taylor instability for FLACS, based on the linear stability analysis and the approaches proposed by Bauwens et al. (2009b, 2011, 2012).

The experimental campaign performed for Paper 4 of the present thesis involved inserting branches from different types of trees into an small-scale, open-ended channel during a series of explosion experiments. The campaign applied the same small-scale rig that was used for the experiments in Paper 2 and Paper 3 (cf. figures 1.3 and 1.5). Figure 1.6 shows spruce branches, with and without needles, inserted in the experimental rig. The investigation in Paper 4 was motivated by a need for representing the effect of vegetation on the flame acceleration in gas explosion simulations, identified in the af-

(a) Spruce branch with needles.   (b) Spruce branches without needles.

Figure 1.6: Spruce branches inserted in the experimental rig for Paper 4.

termath of the severe incident that occurred at the fuel storage depot Buncefield, UK, in 2005 (BMIIB, 2008). Here, the presence of vegetation is assumed to have caused flame acceleration and significant overpressures. A two-stage research project was initiated to investigate the explosion mechanism that led to the overpressure damage observed at Buncefield (SCI, 2009, 2014). The project involved both medium-and large scale experimental campaigns, involving gas explosions in extensive regions with vegetation, in addition to corresponding modelling work. Consequently, the experimental study described in Paper 4 was conducted to support the development of a general sub-grid modelling approach to account for vegetation in industrial-scale gas explosions. Chapter 5 elaborates on the findings of Paper 4.

In order to investigate the performance of key sub-grid models developed as part of the present doctoral study, Chapter 6 presents updated simulation results for two experimental campaigns conducted in vented enclosures, as well as one campaign performed in a full-scale offshore module. The experiments from Paper 1 are revisited. These campaigns were performed by other research groups, i.e. not as part of the present doctoral study. Finally, Chapter 7 summarises the main results from the doctoral study, while Chapter 8 includes suggestions for further work.

Appendix A provides an overview of the numerical methods that are used to solve the equations in Chapter 2, Appendix B includes additional details about the experiments, Appendix C describes the wall functions that are used in FLACS, while the last chapter contains the four scientific publications associated with the dissertation.

Chapter 2

Governing equations

This chapter describes the governing equations and thermodynamic relations used for modelling premixed combustion in the CFD tool FLACS (Gexcon, 2016). The chapter provides a reference for the subsequent chapters, where modelling approaches to account for various flame acceleration mechanisms in gas explosions are discussed and developed. Sections 2.1 – 2.9 present key assumptions that are applied by the model, and aim to connect the modelling approaches in FLACS with the general literature on reactive flow. Finally, Section 2.10 summarises the averaged partial differential equations (PDEs) that are discretised and solved in the CFD model. The discretisation and solution processes are described in Appendix A.

2.1 Definitions and thermodynamic relations for reacting flow

A generalised global reaction equation representing the combustion reaction between a fuel F and an oxidiser O to produce a mixture of combustion products, can be expressed as

$$\upsilon_F F + \upsilon_O O \rightarrow Products \ , \tag{2.1}$$

where υ_F and υ_O are the reaction coefficients of the fuel and oxidiser, respectively. In a *stoichiometric* mixture, υ_F and υ_O assume values that theoretically lead to a complete consumption of both fuel and oxidiser.

Chemically reacting flow will in general involve multiple components that must be accounted for individually. The mole fraction X_k of the kth species is the ratio of the number of moles of species k in a volume V to the total number of moles of all species in V. The mixture's average molecular weight is defined as

$$\overline{M} = \sum_{k=1}^{N} X_k M_k \ , \tag{2.2}$$

where M_k is the molecular weight of species $k = 1, ..., N$, and N is the total number of species. The mass fraction Y_k of the kth species in V can be related to the mole fractions and the molecular weights as

$$Y_k = \frac{X_k M_k}{\overline{M}} \ . \tag{2.3}$$

The equivalence ratio ϕ is commonly used to characterise mixtures of a flammable gas and oxidiser, and can be defined as

$$\phi = \left(\frac{Y_F}{Y_O}\right) \bigg/ \left(\frac{Y_F}{Y_O}\right)_{\text{stoich}} , \qquad (2.4)$$

where Y_F and Y_O are the mass fractions of fuel and oxidiser, respectively, and $(Y_F/Y_O)_{\text{stoich}}$ is the mass fraction ratio of the corresponding stoichiometric mixture. It follows that fuel-rich mixtures ($\phi > 1$), will have an excess of fuel, while fuel-lean mixtures ($\phi < 1$) will have an excess of oxidiser in the combustion reaction.

An equation of state is needed to relate the density ρ to the pressure p and the absolute temperature T. In FLACS, the *ideal gas law* is used for modelling premixed combustion,

$$p\overline{M} = \rho \mathcal{R} T , \qquad (2.5)$$

where $\mathcal{R}$ is the ideal gas constant $\left(\mathcal{R} = 8.314 \text{ J mol}^{-1} \text{ K}^{-1}\right)$. The ideal gas law neglects the space occupied by the molecules in the gas, assuming that the average distance between molecules is much larger than their size. Furthermore, any interaction between gas particles is neglected. In the following, the ideal gas law is assumed applicable for the ranges of pressures and temperatures that normally are encountered in industrial-scale gas explosions (Kuo and Acharya, 2012).

The *static enthalpy h*, related to the internal energy e by $e = h - p/\rho$, is used in the energy conservation equation in FLACS (cf. Section 2.5). The static specific enthalpy can be expressed as

$$h = \sum_{k=1}^{N} Y_k h_k = \sum_{k=1}^{N} Y_k \int_{T_0}^{T} c_{p,k}(T^*) \, \mathrm{d}T^* + \sum_{k=1}^{N} h_{f,k}^0 Y_k , \qquad (2.6)$$

where $c_{p,k}$ is the specific heat capacity for species k defined at constant pressure and $h_{f,k}^0$ is the standard enthalpy of formation, i.e. the enthalpy required to form 1 kg of species k at the reference temperature $T_0 = 298$ K and $p = 1$ bar. The first and second term on the right hand side of Equation (2.6) are the *sensible* and *chemical enthalpy* of the mixture, respectively (Lieuwen, 2012; Poinsot and Veynante, 2011). The *total enthalpy* h_t also includes kinetic energy, and is defined as

$$h_t = h + \frac{|\mathbf{u}|^2}{2} , \qquad (2.7)$$

where $\mathbf{u}$ is the velocity vector.

In FLACS, the initial enthalpy h is computed from Equation (2.6) using tabulated values of the standard enthalpy of formation $h_{f,k}^0$, and assuming a linear dependence of $c_{p,k}$ on T. The temperature in the combustion products can be computed from Equation (2.6) by assuming that the enthalpy h does not change from reactants to products (Warnatz et al., 2006). The combustion products in FLACS will include several species, depending on the fuel type. According to the analysis by Arntzen (1998), the mass fraction of each species is estimated using a set of equilibrium constants for the relevant chemical reactions, depending on the equivalence ratio ϕ of the mixture. Arntzen (1998) presents further details on the computation of the *expansion ratio* $\sigma = \rho_u/\rho_b$ of the fuel-oxidiser mixture, where ρ_u and ρ_b are the densities of the unburnt reactants and combustion products, respectively.

2.2 The porosity/distributed resistance (PDR) concept

Figure 2.1 shows the computational grid arrangement in FLACS in the $x_1 x_2$-plane, illustrating the staggered grid for velocity components (u_1 and u_2 are the velocity components in the x_1- and x_2-directions, respectively) and the cell-centred position for scalar variables (e.g. density ρ, pressure p and temperature T). The three-dimensional grid cells are denoted *control volumes (CVs)*. The computational grid is revisited in Section A.1.
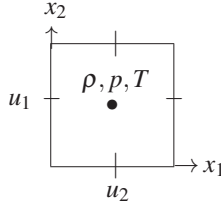
Figure 2.1: Staggered Cartesian grid arrangement in FLACS, horizontal view.

Using the porosity/distributed resistance (PDR) formulation (Hjertager, 1986), each of the terms in the governing equations is integrated over the part of the control volume that is unblocked, i.e. containing fluid. A *volume porosity* β_v, denoting the ratio of open volume to the total volume of each grid cell, is defined at the cell-centred point in Figure 2.1. The *surface area porosity* β_{ij} is a second-order tensor, representing the porosity in the ith direction for fluid flow in the jth direction. For flow around objects immersed in fluid, where the objects are all aligned with the main coordinates, the area porosity tensor β_{ij} can be assumed diagonal (Bakke, 1986). The non-zero diagonal components β_{jj} are defined as the ratio of the projected open area between two neighbouring cell centres to the total area of the respective control volume face in the jth direction. In the following, β_{jj} is simply written β_j, and is excluded from the Einstein summation convention in the partial differential equations. The flux terms in the governing equations are weighted against the area porosities β_j.

Using Gauss' divergence theorem to write the fluxes in terms of a volume integral instead of a surface integral, the integrated conservation equation for the general variable Φ can be written as

$$\int_{V_{CV}} \frac{\partial}{\partial t} \left(\beta_v \rho \Phi \right) dV + \int_{V_{CV}} \left[\frac{\partial}{\partial x_j} \left(\beta_j \rho \Phi u_j \right) - \frac{\partial}{\partial x_j} \left(\beta_j \rho \mathcal{D}_\Phi \frac{\partial \Phi}{\partial x_j} \right) \right] dV =$$
$$\int_{V_{CV}} \beta_v \left(S_\Phi - R_\Phi \right) dV , \qquad (2.8)$$

where u_j is the jth velocity component, $\mathcal{D}_\Phi$ is a diffusion coefficient, S_Φ is the source term for Φ, and R_Φ represents additional resistance, additional mixing, and/or additional heat transfer caused by solid obstructions in the flow. The porosities β_j and β_v are computed with a pre-processor prior to solving the partial differential equations. The lumped effects of geometry on all spatial scales are taken into account partly through β_j and β_v, and partly by R_Φ.

In the CFD model, the equations are *averaged* before they are discretised and solved, and the density-weighted diffusion coefficient $\rho \mathcal{D}_\Phi$ in Equation (2.8) is replaced by an *effective turbulence diffusion coefficient* Γ_Φ. The averaging procedure is defined in Section 2.8. The specific conservation equations are discussed below, on differential (rather than integral) form.

2.3   Conservation of mass

The continuity equation describes the overall conservation of mass, relating the fluid density to the velocity by

$$\frac{\partial}{\partial t}(\beta_v \rho) + \frac{\partial}{\partial x_j}(\beta_j \rho u_j) = \frac{\dot{m}}{V} \, , \tag{2.9}$$

where the source term on the right hand side accounts for mass that is added to or taken out of the simulation domain.

2.4   Conservation of momentum

The momentum equations express Newton's second law of motion for continuous fluids (Lieuwen, 2012). The conservation of momentum is described by

$$\frac{\partial}{\partial t}(\beta_v \rho u_i) + \frac{\partial}{\partial x_j}(\beta_j \rho u_i u_j) = -\frac{\partial}{\partial x_j}(\beta_v p \delta_{ij}) + \frac{\partial}{\partial x_j}(\beta_j \Omega_{ij}) + \frac{\partial}{\partial x_j}(\beta_v \theta_{ij}) + F_{o,i}$$
$$+ \beta_v (\rho - \rho_0) g_i \, , \tag{2.10}$$

where g_i is the ith component of the gravity vector. The fluid is assumed to be isotropic, and the *viscous stress tensor* $\tau_{ij} = \Omega_{ij} + \theta_{ij}$ is assumed to be proportional to the velocity gradients (*Newtonian fluid*):

$$\Omega_{ij} = \mu \left(\frac{\partial u_i}{\partial x_j} + \frac{\partial u_j}{\partial x_i} \right) \, , \tag{2.11}$$

$$\theta_{ij} = \left(\mu_B - \frac{2}{3}\mu \right) \frac{\partial u_k}{\partial x_k} \delta_{ij} \, , \tag{2.12}$$

where μ is the *dynamic molecular viscosity* and δ_{ij} is the Kronecker delta. Equation (2.11) represents the deformation by shear stresses (tangential stresses) that change the shape of a material volume without changing the volume. Equation (2.12) represents normal stresses that will change the volume of a material volume without changing the shape (Anderson, 1995). The bulk viscosity μ_B accounts for viscous dissipation due to normal stresses, occurring when a fluid expands (Warnatz et al., 2006). In the following, μ_B is assumed to be negligible (the Stokes hypothesis). The source term $F_{o,i}$ represents the resistance (drag force per volume) due to sub-grid obstructions

$$F_{o,i} = -\frac{1}{2}\rho C_D \frac{A}{V} u_i |u_i| \, , \tag{2.13}$$

where C_D is a drag coefficient, A is an effective drag area based on the area blockage $(1 - \beta_i)$, and V is the volume of the control volume (Hoerner, 1965). The last term of Equation (2.10) accounts for the effect of buoyancy. Additional terms that appear in the momentum equation after averaging and accounting for turbulence effects are treated in Section 2.8.

2.5 Conservation of energy

The general conservation equation for the static enthalpy h can be written as

$$\frac{\partial}{\partial t}(\beta_v \rho h) + \frac{\partial}{\partial x_j}(\beta_j \rho h u_j) = \beta_v \frac{Dp}{Dt} - \frac{\partial}{\partial x_j}(\beta_j q_j) + \beta_j \tau_{ij}\frac{\partial u_i}{\partial x_j} + \frac{\dot{Q}}{V} + \beta_v \rho \sum_{k=1}^{N} Y_k f_{k,j} v_{k,j} \, ,$$

(2.14)

where Dp/Dt accounts for pressure work, q_j is the energy flux, $\tau_{ij}\partial u_i/\partial x_j$ represents the heat produced by viscous friction, $\dot{Q}/V$ is a heat rate source term (e.g. accounting for heat transferred by radiation) and $\rho \sum_{k=1}^{N} Y_k f_{k,j} v_{k,j}$ accounts for the power produced by body forces $f_{k,j}$ in the jth direction on species k (Poinsot and Veynante, 2011). Here, $v_{k,j}$ is a diffusion speed for species k in the jth direction. The latter term of Equation (2.14) can be set to zero if gravity is the only external body force – this term is therefore omitted. Furthermore, the effect of viscous friction in Equation (2.14), represented by $\beta_j \tau_{ij}\partial u_i/\partial x_j$, is assumed to be negligible. By assuming that q_j can be expressed in terms of the enthalpy gradient and a thermal diffusivity $\mathcal{D}_{th}$, the enthalpy equation can be written as

$$\frac{\partial}{\partial t}(\beta_v \rho h) + \frac{\partial}{\partial x_j}(\beta_j \rho h u_j) = \frac{\partial}{\partial x_j}\left(\beta_j \rho \mathcal{D}_{th}\frac{\partial h}{\partial x_j}\right) + \beta_v \frac{Dp}{Dt} + \frac{\dot{Q}}{V} \, .$$

(2.15)

2.6 Conservation of species mass

If a fluid consists of several species in the same phase, the conservation of the mass fraction Y_k of species $k = 1, ..., N$, can be written as

$$\frac{\partial}{\partial t}(\beta_v \rho Y_k) + \frac{\partial}{\partial x_j}(\beta_j \rho Y_k u_j) = \frac{\partial}{\partial x_j}(-\beta_j \rho Y_k v_{k,j}) + \beta_v \dot{w}_k \, ,$$

(2.16)

where $\dot{w}_k$ is the consumption or creation rate of species k and $v_{k,j}$ is a diffusion speed for species k in the jth direction. The mass diffusion term $-\rho Y_k v_{k,j}$ can be modelled by Fick's law

$$-\rho Y_k v_{k,j} = \rho \mathcal{D}_k \frac{\partial Y_k}{\partial x_j} \, ,$$

(2.17)

where $\mathcal{D}_k$ is the mass diffusivity for the kth species, assuming that the Soret effect, pressure diffusion and body force effects can be neglected (Hirschfelder et al., 1964; Poinsot and Veynante, 2011). Hence, Equation (2.16) states that the time rate of change of the mass of species k inside a fixed volume equals the convective and diffusive flux in or out of the volume, in addition to the generation or consumption of the species by chemical reactions.

The source term $\dot{w}_k$ represents the consumption or creation rate of species k, and would strictly require the construction and validation of complex chemical schemes, involving a large number of species and reactions (Poinsot and Veynante, 2011). It is presently not considered feasible to undertake this rigorous procedure for modelling industrial-scale gas explosions for use in QRA studies. Chapter 3 describes the simplified approach that the CFD tool FLACS applies to model this term.

In the FLACS PDE solver for premixed combustion, $N = 3$, where N is the total number of species. In other words, the premixed reactants, the combustion products and the surrounding atmosphere (which may theoretically contain a flammable, premixed component) are accounted for separately. The fuel mass fraction Y_F in the premixed cloud is defined as a single species according to

$$\frac{\partial}{\partial t}(\beta_v \rho Y_F) + \frac{\partial}{\partial x_j}(\beta_j \rho Y_F u_j) = \frac{\partial}{\partial x_j}\left(\beta_j \rho \mathcal{D}_{Y_F}\frac{\partial Y_F}{\partial x_j}\right) + \beta_v \dot{w}_F \ . \tag{2.18}$$

The mass fraction of oxidiser Y_O can be derived from Y_F, and the initially defined fuel type, oxidiser composition and stoichiometry of the premixed gas cloud. Accounting for $N = 3$ species requires $(N - 1) = 2$ equations. The additional equation that is required is a conservation equation for the mixture fraction.

2.7   Conservation of mixture fraction

The mixture fraction ξ takes a value between 0 and 1, and defines the degree of mixing between two well-defined states. For gas explosion simulations performed with FLACS, the mixture fraction denotes the degree of mixing between two pre-defined gas compositions – representing the premixed fuel-oxidiser component and the surrounding atmosphere, respectively. The conservation equation for the mixture fraction does not involve any source terms, and can be written as

$$\frac{\partial}{\partial t}(\beta_v \rho \xi) + \frac{\partial}{\partial x_j}(\beta_j \rho \xi u_j) = \frac{\partial}{\partial x_j}\left(\beta_j \rho \mathcal{D}_\xi \frac{\partial \xi}{\partial x_j}\right) \ , \tag{2.19}$$

where $\mathcal{D}_\xi$ is the diffusion coefficient for ξ.

2.8   Modelling the effect of turbulence

The Reynolds number $Re = UL/\nu$, where U is a characteristic velocity, L is a characteristic length scale, and ν is the kinematic viscosity, measures the relative importance of inertial forces compared to viscous forces in the flow. At a certain critical Reynolds number, inertial forces create shear instabilities in the flow that cannot be dampened by viscous forces, and the flow becomes *turbulent*. Below the critical Reynolds number, the fluid moves in stable, side-by-side layers. This is the *laminar* flow regime. Turbulent flows are irregular and chaotic, characterised by vortices over a range of spatial scales, from those comparable to the geometric extent of the configuration, down to scales where viscous forces dominate.

The largest eddies are dominated by inertial effects, drawing energy from the mean flow. The turbulence eddies that are slightly smaller are stretched by the larger structures. In this manner, kinetic energy is transferred from larger to smaller scales. This *energy cascade* continues until the vortices are on the *Kolmogorov microscale* η, where viscous stresses dominate and the kinetic energy dissipates to thermal energy. Overall, turbulent flows are characterised by higher energy dissipation and increased mixing rates, compared to laminar flow (Versteeg and Malalasekera, 2007).

The vortices result in fluctuations in the flow variables. Therefore, turbulence can be described in terms of the mean values of the flow variables, together with the statistical characteristics of the fluctuations. In order to model the effect of turbulence fluctuations, Reynolds (1895) suggested to split all instantaneous variables Φ into their mean value $\overline{\Phi}$ and a separate term representing the fluctuation, Φ', e.g. $u_i = \overline{u_i} + u_i'$. The mean value $\overline{\Phi}$ can for example be defined as averaged in time

$$\overline{\Phi} = \frac{1}{\Delta t} \int_{t - \frac{1}{2}\Delta t}^{t + \frac{1}{2}\Delta t} \Phi(t)\, dt\ ,$$

where Δt is larger than the time scale of the fluctuation, and smaller than the time scale of variations in the mean field. Alternatively, $\overline{\Phi}$ can be defined as the expected value from a probability density function $f(\Phi)$

$$\overline{\Phi} = \int_{-\infty}^{\infty} c f(c)\, dc\ . \tag{2.20}$$

For modelling varying density flows it is customary to use *Favre averaging* (Favre, 1965),

$$\Phi_i = \widetilde{\Phi_i} + \Phi_i''\ , \tag{2.21}$$

where

$$\widetilde{\Phi_i} = \frac{\overline{\rho \Phi_i}}{\overline{\rho}}\ . \tag{2.22}$$

This approach is used in FLACS, since combustion problems in general involve significant changes of density in the flow.

Averaging the governing equations introduces additional unknowns on the form $\overline{\rho \Phi'' u_i''}$, requiring additional equations for the system to be closed. This is generally referred to as the *turbulence closure problem*. For example, the averaged momentum equations may be written as

$$\frac{\partial}{\partial t} \left(\beta_v \overline{\rho} \widetilde{u_i} \right) + \frac{\partial}{\partial x_j} \left(\beta_j \overline{\rho} \widetilde{u_i} \widetilde{u_j} \right) = -\frac{\partial}{\partial x_j} \left(\beta_v \overline{p} \delta_{ij} \right) + \beta_v \left(\overline{\rho} - \overline{\rho_0} \right) g_i$$
$$+ \frac{\partial}{\partial x_j} \left(\beta_j \left[\overline{\tau_{ij}} - \overline{\rho u_i'' u_j''} \right] \right)\ . \tag{2.23}$$

The term $-\overline{\rho u_i'' u_j''}$ in Equation (2.23) has the same dimensions as the viscous stress tensor $\overline{\tau_{ij}}$ in the momentum equation. The additional terms are therefore often called *Reynolds stresses*. They can be modelled in a manner analogous to τ_{ij}, which is assumed to be proportional to the velocity gradients (ref. Equations (2.11) and (2.12)).

Similarly, $-\overline{\rho u_i'' u_j''}$ can be related to the flow strain by introducing a *turbulent dynamic viscosity*, or *eddy viscosity*, μ_T (Boussinesq, 1877) according to

$$-\overline{\rho u_i'' u_j''} = \mu_T \left(\frac{\partial \widetilde{u}_i}{\partial x_j} + \frac{\partial \widetilde{u}_j}{\partial x_i} \right) - \frac{2}{3} \left(\overline{\rho} \widetilde{k} + \mu_T \frac{\partial \widetilde{u}_l}{\partial x_l} \right) \delta_{ij} , \qquad (2.24)$$

where $\widetilde{k}$ is the Favre-averaged *turbulence kinetic energy* (to be defined in the following). In Equation (2.24), μ_T has the dimension of viscosity. In analogy to the model for molecular viscosity, the turbulent dynamic viscosity μ_T can be modelled as the product of a turbulence velocity scale $\mathcal{U}$ and a length scale characteristic of the larger, more energetic eddies ℓ, i.e. $\mu_T \sim \rho \, \ell \, \mathcal{U}$. Consequently, μ_T will be a property of the flow and not the fluid itself (Ertesvåg, 2000).

FLACS uses the 'standard' $k - \varepsilon$ model (Launder and Spalding, 1974) to model turbulence, solving conservation equations for the turbulence kinetic energy $k = 1/2 \, \widetilde{u_i'' u_i''}$, and its rate of dissipation $\varepsilon = C_\mu k^{3/2}/\ell$. Here, u_i'' is the ith component of the turbulence velocity fluctuation, ℓ is a turbulence length scale, and C_μ is a model constant, determined empirically. In the $k - \varepsilon$ model, ε can be viewed as an expression for the energy transfer from larger to smaller eddies. The expression for the dissipation rate ε can be derived from dimensional analysis, or by using physical arguments, looking at the energy loss from the drag force working on a "turbulence ball" on the order of ℓ and a velocity on the order of u'' relative to the mean flow (Prandtl, 1945). Using $k^{1/2} \sim u_i''$, the turbulence viscosity μ_T is related to k and ε as

$$\mu_T = \rho \, \ell \, \mathcal{U} = \rho \left(C_\mu \frac{k}{\varepsilon} k^{1/2} \right) k^{1/2} = \rho C_\mu \frac{k^2}{\varepsilon} . \qquad (2.25)$$

Scalar turbulence transport (e.g. in the equations for $\widetilde{h}$, $\widetilde{\xi}$, $\widetilde{Y_F}$, etc.) are modelled in a similar way as for the momentum equation, by introducing a turbulence diffusivity in addition to the molecular diffusivity. The turbulence diffusivity can be set proportional to the eddy viscosity μ_T with a set of *turbulence Prandtl/Schmidt numbers*, σ_Φ, cf. Table 2.1. The eddy viscosity is written together with the molecular viscosity in the governing equations by introducing an *effective dynamic viscosity* $\mu_{\text{eff}} = \mu + \mu_T$. Averaging the sink term due to chemical reactions, $\dot{w}_F$, in the conservation equation for the fuel mass fraction, $\widetilde{Y_F}$, (cf. Equation (2.18)), however, is not straightforward. This term requires additional modelling. Chapter 3 presents the approach used in FLACS; its description is therefore omitted here.

2.9 Turbulence kinetic energy k and its rate of dissipation ε

Conservation equations are defined and solved in FLACS for the Favre-averaged turbulence kinetic energy $\widetilde{k}$ and its dissipation rate $\widetilde{\varepsilon}$ according to the 'standard' $k - \varepsilon$ model (Launder and Spalding, 1974)

$$\frac{\partial}{\partial t} \left(\beta_v \overline{\rho} \widetilde{k} \right) + \frac{\partial}{\partial x_j} \left(\beta_j \overline{\rho} \widetilde{k} \widetilde{u}_j \right) = \frac{\partial}{\partial x_j} \left(\beta_j \frac{\mu_{\text{eff}}}{\sigma_k} \frac{\partial \widetilde{k}}{\partial x_j} \right) + \beta_v P_k - \beta_v \overline{\rho} \widetilde{\varepsilon} \quad \text{and} \qquad (2.26)$$

$$\frac{\partial}{\partial t}\left(\beta_v \overline{\rho}\widetilde{\varepsilon}\right) + \frac{\partial}{\partial x_j}\left(\beta_j \overline{\rho}\widetilde{\varepsilon}\widetilde{u}_j\right) = \frac{\partial}{\partial x_j}\left(\beta_j \frac{\mu_{\text{eff}}}{\sigma_\varepsilon}\frac{\partial \widetilde{\varepsilon}}{\partial x_j}\right) + \beta_v P_\varepsilon - C_{2\varepsilon}\beta_v \overline{\rho}\frac{\widetilde{\varepsilon}^2}{\widetilde{k}}\,, \qquad (2.27)$$

where σ_k and σ_ε are turbulence Prandtl/Schmidt numbers defined in Table 2.1 and P_k and P_ε represent the production of turbulence kinetic energy and production of dissipation rate of turbulence kinetic energy, respectively. Table 2.2 summarises the values for the model constants in the 'standard' $k - \varepsilon$ model (Launder and Spalding, 1974). The modelled P_k is given by

$$P_k = G_s + G_w + G_b + G_o \,, \qquad (2.28)$$

where G_s, G_w, G_b and G_o are terms contributing to turbulence generation due to fluid-shear, wall-shear, buoyancy and sub-grid obstructions, respectively.

An exact equation for the turbulence kinetic energy k can be obtained from Equation (2.10). The model term for turbulence generation due to fluid-shear appearing in Equation (2.28), G_s , has been derived from the production term in the exact equation for k:

$$\overline{\rho}\left(P_k\right)_{\text{exact}} = -\overline{\rho u_i'' u_j''}\frac{\partial \widetilde{u}_i}{\partial x_j} \,. \qquad (2.29)$$

Replacing the Reynolds stresses with the Boussinesq expression from Equation (2.24) leads to

$$G_s = \mu_T \left(\frac{\partial \widetilde{u}_i}{\partial x_j} + \frac{\partial \widetilde{u}_j}{\partial x_i}\right)\frac{\partial \widetilde{u}_i}{\partial x_j} - \frac{2}{3}\left(\overline{\rho}\widetilde{k} + \mu_T \frac{\partial \widetilde{u}_k}{\partial x_k}\right)\frac{\partial \widetilde{u}_i}{\partial x_i} \,. \qquad (2.30)$$

The production term accounting for wall-shear G_w is given by wall functions, detailed in Appendix C. The turbulence production due to buoyancy is modelled as

$$G_b = -\frac{1}{\overline{\rho}}\frac{\mu_{\text{eff}}}{\sigma_b}g_i \frac{\partial \overline{\rho}}{\partial x_i} \,, \qquad (2.31)$$

where σ_b is given the value 0.9.

The term G_o in Equation (2.28) accounts for turbulence generation due to sub-grid objects, as these are otherwise not "seen" by the turbulence model. Modelling sub-grid turbulence generation is crucial for representing industrial-scale explosions on a relatively coarse grid (Arntzen, 1998). Following Sha and Launder (1979), G_o can be expressed as

$$G_o = C_o \beta_v \overline{\rho}\,|\widetilde{\mathbf{u}}|\,\widetilde{u}_j^2 o_j \,, \qquad (2.32)$$

where C_o is a model constant specific to FLACS and o_j is a parameter that depends on the position, shape and size of the sub-grid object in the control volume (Narasimhamurthy et al., 2015). With reference to Equation (2.13), a physical interpretation of G_o relates it to the energy loss due to sub-grid drag in the momentum equation (Popat et al., 1996). In Equation (2.27), the production of ε is modelled as

$$P_\varepsilon = C_{1\varepsilon}\frac{\widetilde{\varepsilon}}{\widetilde{k}}P_k\left(1 + C_{3\varepsilon}B_\varepsilon\right), \qquad (2.33)$$

where B_ε is a term accounting for the effect of buoyancy, and $C_{1\varepsilon}$ and $C_{3\varepsilon}$ are listed in Table 2.2.

Table 2.1: Turbulence Prandtl/Schmidt numbers.

σ_k	σ_ε	σ_h	σ_{Y_F}	σ_ξ	σ_b
1.0	1.3	0.7	0.7	0.7	0.9

Table 2.2: Model constants in the 'standard' $k - \varepsilon$ model.

C_μ	$C_{1\varepsilon}$	$C_{2\varepsilon}$	$C_{3\varepsilon}$
0.09	1.44	1.92	0.8

2.10   The Favre-averaged governing equations in FLACS

This section summarises the equations from sections 2.3 – 2.9, *after the Favre-averaging and including the effect of turbulent mixing.* Tables 2.1 and 2.2 summarise the values of the model constants in the 'standard' $k - \varepsilon$ model and the turbulence Prandtl/Schmidt numbers used in the equations, respectively. In the following, β_v is the volume porosity and β_j denotes the area porosity in the jth direction (cf. Section 2.2).

The continuity equation describes the conservation of mass:

$$\frac{\partial}{\partial t}\left(\beta_v\overline{\rho}\right) + \frac{\partial}{\partial x_j}\left(\beta_j\overline{\rho}\widetilde{u}_j\right) = \frac{\dot{m}}{V} \ . \tag{2.34}$$

The conservation of momentum is expressed by

$$\frac{\partial}{\partial t}\left(\beta_v\overline{\rho}\widetilde{u}_i\right) + \frac{\partial}{\partial x_j}\left(\beta_j\overline{\rho}\widetilde{u}_i\widetilde{u}_j\right) = -\frac{\partial}{\partial x_j}\left(\beta_v\overline{p}\delta_{ij}\right) + \frac{\partial}{\partial x_j}\left(\beta_j\overline{\Omega}_{ij}\right) + \frac{\partial}{\partial x_j}\left(\beta_v\overline{\theta}_{ij}\right) + F_{o,i}$$
$$+ F_{w,i} + \beta_v\left(\overline{\rho} - \overline{\rho_0}\right)g_i \ , \tag{2.35}$$

where

$$\overline{\Omega}_{ij} = \mu_{\text{eff}}\left(\frac{\partial\widetilde{u}_i}{\partial x_j} + \frac{\partial\widetilde{u}_j}{\partial x_i}\right) \tag{2.36}$$

$$\overline{\theta}_{ij} = -\frac{2}{3}\left(\overline{\rho}\widetilde{k} + \mu_{\text{eff}}\frac{\partial\widetilde{u}_k}{\partial x_k}\right)\delta_{ij} \ , \tag{2.37}$$

and

$$\mu_{\text{eff}} = \mu + \overline{\rho}C_\mu\frac{\widetilde{k}^2}{\widetilde{\varepsilon}}. \tag{2.38}$$

The source term $F_{o,i}$ represents the resistance (drag force per volume) due to sub-grid obstructions:

$$F_{o,i} = -\frac{1}{2}\overline{\rho}C_D\frac{A}{V}\widetilde{u}_i\left|\widetilde{u}_i\right| \ . \tag{2.39}$$

The term $F_{w,i}$ represents the resistance (drag force per volume) due to walls, cf. Appendix C. The last term in Equation (2.35), $\beta_v\left(\overline{\rho} - \overline{\rho_0}\right)g_i$, accounts for the effect of buoyancy.

The energy equation represents the conservation of static enthalpy h as

$$\frac{\partial}{\partial t}\left(\beta_v\overline{\rho}\widetilde{h}\right) + \frac{\partial}{\partial x_j}\left(\beta_j\overline{\rho}\widetilde{h}\widetilde{u}_j\right) = \frac{\partial}{\partial x_j}\left(\beta_j\frac{\mu_{\text{eff}}}{\sigma_h}\frac{\partial\widetilde{h}}{\partial x_j}\right) + \beta_v\frac{D\overline{p}}{Dt} + \frac{\dot{Q}}{V}\,, \qquad (2.40)$$

where $D\overline{p}/Dt$ accounts for pressure work and $\dot{Q}/V$ is the heat source term (e.g. from radiation).

The degree of mixing between an initially defined gas cloud and the surrounding atmosphere is tracked with the mixture fraction $\widetilde{\xi}$,

$$\frac{\partial}{\partial t}\left(\beta_v\overline{\rho}\widetilde{\xi}\right) + \frac{\partial}{\partial x_j}\left(\beta_j\overline{\rho}\widetilde{\xi}\widetilde{u}_j\right) = \frac{\partial}{\partial x_j}\left(\beta_j\frac{\mu_{\text{eff}}}{\sigma_\xi}\frac{\partial\widetilde{\xi}}{\partial x_j}\right)\,. \qquad (2.41)$$

Convection, diffusion and consumption of premixed reactants are represented by the conservation equation for the mass fraction of fuel $\widetilde{Y}_F$,

$$\frac{\partial}{\partial t}\left(\beta_v\overline{\rho}\widetilde{Y}_F\right) + \frac{\partial}{\partial x_j}\left(\beta_j\overline{\rho}\widetilde{Y}_F\widetilde{u}_j\right) = \frac{\partial}{\partial x_j}\left(\beta_j\frac{\mu_{\text{eff}}}{\sigma_F}\frac{\partial\widetilde{Y}_F}{\partial x_j}\right) + \beta_v\widetilde{w}_F\,, \qquad (2.42)$$

where $\widetilde{w}_F$ is the Favre-averaged fuel reaction rate. The modelling of $\widetilde{w}_F$ and $\mu_{\text{eff}}/\sigma_F$ in the flame zone is described and discussed in Chapter 3.

Turbulence is modelled by the 'standard' $k-\varepsilon$ model (Launder and Spalding, 1974), solving individual transport equations for the turbulence kinetic energy $\widetilde{k}$ and its dissipation rate $\widetilde{\varepsilon}$, cf. equations (2.26) and (2.27). Appendix C describes the wall functions.

Chapter 3

Framework for premixed combustion modelling

In order to address the research question *"how can the sub-grid representation of flame acceleration mechanisms due to instability effects and flow past obstructed regions be improved in a CFD tool used for consequence assessment of gas explosions?"*, it is essential to establish the assumptions behind the modelling approach for premixed combustion. This chapter gives an overview of the framework that the CFD tool FLACS (Gexcon, 2016) applies for simulating industrial-scale gas explosions. The discussions related to model developments and results in the subsequent chapters build on the theory presented here.

3.1 Premixed combustion modelling

One of the main challenges in the modelling of turbulent premixed combustion is to represent the Favre-averaged sink term accounting for consumption of fuel due to chemical reaction, $\widetilde{w}_F$, in the conservation equation for the Favre-averaged fuel mass fraction $\widetilde{Y}_F$ (Lipatnikov and Chomiak, 2002):

$$\frac{\partial}{\partial t}\left(\beta_v\overline{\rho}\widetilde{Y}_F\right) + \frac{\partial}{\partial x_j}\left(\beta_j\overline{\rho}\widetilde{Y}_F\widetilde{u}_j\right) = \frac{\partial}{\partial x_j}\left(\beta_j\frac{\mu_{\text{eff}}}{\sigma_F}\frac{\partial\widetilde{Y}_F}{\partial x_j}\right) + \beta_v\widetilde{w}_F \ . \tag{3.1}$$

The derivation of Equation (3.1) from the general principles of species mass conservation, cf. Equation (2.16), is presented in Section 2.6. The rate $\dot{w}_k$ in Equation (2.16) is the sum of rates $\dot{w}_{k,j}, j = 1, ..., N$, for a system of N reactions, and involves an exponential function of the temperature through the empirical Arrhenius rate law for the forward or reverse reaction rate for the jth reaction according to

$$D_{fj} = A_{fj}T^{b_j}\exp\left(-\frac{T_{aj}}{T}\right) \quad \text{and} \quad D_{rj} = A_{rj}T^{b_j}\exp\left(-\frac{T_{aj}}{T}\right) \ . \tag{3.2}$$

In Equation (3.2), D_{fj} is the forward reaction rate, D_{rj} is the reverse reaction rate, A_{fj}, A_{rj} and b_j are reaction constants, and T_{aj} is the activation temperature for reaction j.

Due to the highly non-linear nature of $\dot{w}_F$, it is not straightforward to estimate this term using mean values. Instead, closure is normally obtained by physical analysis (Poinsot and Veynante, 2011). To formulate a model for $\widetilde{w}_F$, it is relevant to study the temporal and spatial scales of the chemical reactions relative to those of the turbulence.

3.1.1   Mixture reactivity

According to Bray (1990), the *laminar burning velocity u_l* can be defined as *"...the speed at which a planar, unstretched, steadily propagating laminar flame moves, in a direction directly perpendicular to itself, into a stationary combustible mixture..."*. The laminar burning velocity can be determined by either experimental or numerical study, the latter by using complex chemistry models with extensive reaction mechanisms. FLACS does not perform complex chemistry computations as part of the simulation, but uses a library of laminar burning velocities from the literature to represent u_l.

The measured laminar burning velocity for a specific mixture must be corrected for stretch effects to obtain u_l. Early measurements of laminar burning velocities showed a significant degree of scatter, up to ± 0.1 m/s for methane in air at atmospheric pressure (Ranzi et al., 2012). After the role of flame stretch was recognized (Wu and Law, 1985), and non-linear effects were understood (Kelley and Law, 2009; Wang et al., 2009), correction methods lead to more consistent data. Although the scatter in the laminar burning velocities determined by different procedures and research groups has been significantly reduced over the last decades, some uncertainty remains. Ranzi et al. (2012) present recent values for the laminar burning velocity for a range of mixtures. For example, methane and propane premixed with air to an equivalence ratio of 1.1, burning at atmospheric pressure and an ambient temperature of 298 K, show a scatter of approximately ± 0.02 m/s for methane and ± 0.01 m/s for propane. These estimates are based on data from (Bosschaart and de Goey, 2004; Gu et al., 2000; Halter et al., 2010; Hassan et al., 1998; Jomaas et al., 2005; Park et al., 2011; Rozenchan et al., 2002; Vagelopoulos and Egolfopoulos, 1998).

Laminar flame propagation is controlled by the molecular transport of energy and species. Hence, u_l can be regarded as a fundamental property of a fuel-oxidiser mixture, representing the mixture's overall reactivity, diffusivity and exothermicity. A laminar flame consists of a *preheat zone*, where reactants are heated, and a *reaction zone*, where the main chemical reactions take place. The preheat zone is often assumed to be approximately 10 times thicker than the reaction zone (Peters, 2013). The *laminar flame thickness* δ_l can be approximated by ν/u_l, where ν is the kinematic viscosity. The laminar burning velocity u_l and the laminar flame thickness δ_l are commonly used to represent the characteristic temporal and spatial scales of the chemical reactions.

3.1.2   Regimes of premixed combustion

The combustion model in the CFD tool FLACS applies the *flamelet concept* to represent premixed combustion in gas explosions. This approach provides the basis for the development of sub-grid models in the present thesis.

The flamelet concept assumes that turbulent premixed combustion can be represented by an array of laminar flame structures with a finite thickness δ_l embedded in a turbulent flow field. The assumption is only strictly valid for the turbulence regimes where δ_l is smaller than or equal to the eddies on the Kolmogorov microscale η, as the turbulence structures are unable to interact with the internal flame structure. This limit is termed the *Klimov–Williams criterion*.

Figure 3.1 illustrates the regimes of turbulent premixed combustion in the Borghi diagram (Borghi, 1984), following the presentation by Peters (2013). The dashed line
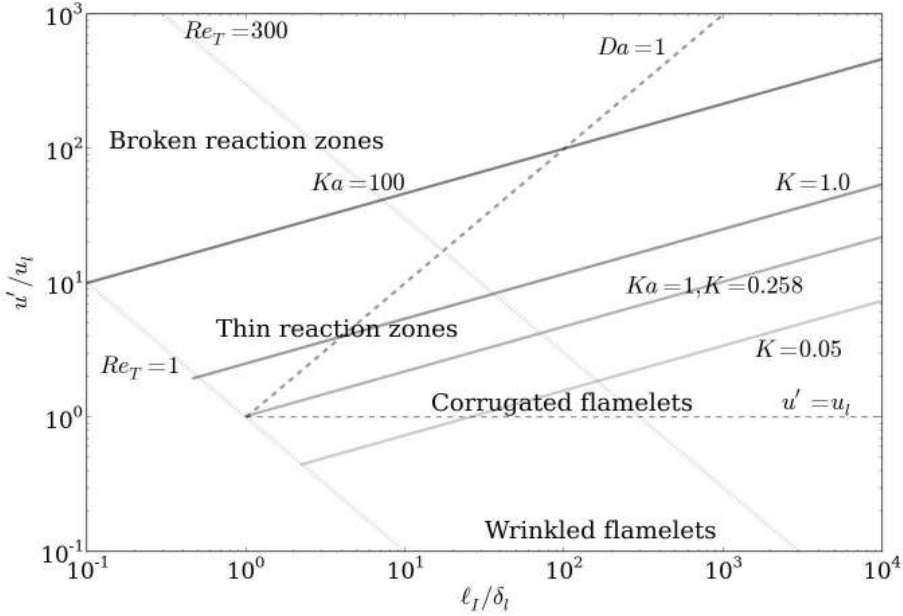
Figure 3.1: Regimes of premixed combustion.

marked "$Re_T = 1$" represents a turbulence Reynolds number $Re_T = u'\ell_I/\nu$ of 1, where u' is the turbulence velocity fluctuation and ℓ_I is the integral length scale. This line marks the boundary between turbulent and laminar flow. Based on empirical observations, the integral length scale of turbulence can be approximated by (Bradley et al., 2011c)

$$\ell_I \approx 0.51 \, \frac{k^{3/2}}{\varepsilon}. \tag{3.3}$$

A turbulence length scale ℓ can be derived from the k-ε model (cf. sections 2.8 and 2.9 according to

$$\ell = 0.09 \, \frac{k^{3/2}}{\varepsilon}. \tag{3.4}$$

The stretch rate that the turbulence induces on the flame surface, i.e. the change in flame surface area A_f per surface area element per time, $1/A_f \left(dA_f/dt \right)$, significantly affects the local burning rate, and must therefore be accounted for. The Eulerian root mean square strain rate u'/ℓ_λ, where ℓ_λ is the Taylor microscale, can be used to approximate the stretch rate on a flame surface element in isotropic turbulence (Batchelor, 1952). Furthermore, the relationship between u'/ℓ_λ and the mass specific rate of energy dissipation for isotropic homogeneous turbulence, ε, can be expressed as $\sqrt{\varepsilon/\nu} = \sqrt{15}u'/\ell_\lambda$. The integral length scale ℓ_I can be related to the Taylor microscale ℓ_λ by an empirical parameter $A = 16$ (Bradley et al., 2011c), according to

$$\frac{\ell_\lambda^2}{\ell_I} = \frac{A\nu}{u'} \, . \tag{3.5}$$

The *Karlovitz stretch factor K* used for turbulent premixed combustion expresses the stretch rate on an randomly orientated surface in isotropic turbulence normalised by the chemical timescale according to

$$K = \frac{u'}{\ell_\lambda} \frac{\delta_l}{u_l}. \tag{3.6}$$

The *Karlovitz number Ka* represents the ratio between the chemical timescale and the timescale of the Kolmogorov microscale eddies according to

$$Ka = \left(\frac{\varepsilon}{\nu}\right)^{\frac{1}{2}} \frac{\delta_l}{u_l}. \tag{3.7}$$

Ka and *K* can be reformulated in terms of the variables of the Borghi diagram, u'/u_l and ℓ_I/δ_l, as

$$Ka = \sqrt{0.51} \left(\frac{3}{2}\right)^{\frac{3}{4}} \left(\frac{u'}{u_l}\right)^{\frac{3}{2}} \left(\frac{\ell_I}{\delta_l}\right)^{-\frac{1}{2}}, \tag{3.8}$$

$$K = \frac{1}{\sqrt{16}} \left(\frac{u'}{u_l}\right)^{\frac{3}{2}} \left(\frac{\ell_I}{\delta_l}\right)^{-\frac{1}{2}}. \tag{3.9}$$

It is clear that the lines of constant *Ka* and constant *K* will be parallel in the Borghi diagram. Figure 3.1 shows lines of selected constant *Ka* and *K*.

The Klimov–Williams criterion is satisfied in the *wrinkled flamelets* and the *corrugated flamelets* regime ($Ka \leq 1$ or $K \leq 0.258$ in Figure 3.1). The Kolmogorov scale eddies are able to penetrate neither the preheat zone nor the reaction zone. In the wrinkled flamelets regime, the turbulence velocity fluctuation u' is smaller than or equal to the laminar burning velocity u_l, so laminar burning and flame instabilities dominate over the corrugating effect of turbulence. While the Kolmogorov eddies are still unable to perturb the flame structure in the corrugated flamelets regime, the turbulence intensity is higher, and the eddies with a turn-over velocity larger than the laminar burning velocity will corrugate the flame front significantly. The eddies on the Gibson scale $\ell_G = u_l^3/\varepsilon$ have a turnover velocity of the laminar burning velocity, and are therefore the smallest eddies that can interact with and wrinkle the laminar flamelets (Peters, 1988).

In the *thin reaction zones* regime, the Kolmogorov eddies penetrate the flame preheat zone, while the reaction zone remains thin. The line $Ka = 100$ in Figure 3.1 marks the upper boundary of the thin reaction zones regime if the reaction zone is assumed to be $1/10$ of the total flame thickness.

Several researchers have proposed that the Klimov–Williams criterion for applying the flamelet approach may be overly strict (Bradley, 1992). Poinsot et al. (1991) presented direct numerical simulations suggesting that flamelet modelling gives reasonable results approximately up to the boundary between the thin reaction zones regime and the *broken reaction zones* regime (see Figure 3.1). In the broken reaction zones regime, the Kolmogorov eddies penetrate and distort the reaction zone itself, and quenching of the flame due to high turbulence levels will start to occur. Williams (1976) pointed out that for fixed turbulence intensities and flame speeds, large length scales – such

as those encountered in industrial-scale gas explosions – lead to a better fit with the flamelet approach.

In summary, the flamelet assumption may be considered representative for a wide range of turbulence levels if the possibility of flamelet quenching is accounted for. The CFD tool FLACS uses the concept to model gas explosion scenarios where premixed combustion frequently transitions from the laminar regime, through the wrinkled and corrugated flamelet regimes, to the regime assuming thin reaction zones and, eventually, quenching of flamelets due to high stretch rates.

3.1.3 The progress variable

In the flamelet regimes, it can be assumed that a single *progress variable* can represent the change of all scalars of the flow across the reaction- and preheat zone. The progress variable c varies from 0 in the reactants to 1 in the burnt products, and can be defined e.g. in terms of the temperature, according to

$$T = T_u + c\,(T_b - T_u)\ ,$$

where the subscript u denotes the unburnt mixture, and b the burnt products. Alternatively, any appropriate scalar can be tracked (**Warnatz et al., 2006**). Solving for the fuel mass fraction $\widetilde{Y}_F$ in Equation (3.1) is in principle equivalent to tracking the progress variable, as

$$\widetilde{c} = 1 - \frac{\widetilde{Y}_F}{Y_{F0}}\ , \tag{3.10}$$

where Y_{F0} is the fuel mass fraction that was initially available in the specific control volume.

3.2 Premixed combustion modelling in FLACS

The modelling approach for premixed combustion in FLACS involves both the diffusion coefficient $\mu_{\text{eff}}/\sigma_F$ and the source term $\widetilde{w}_F$ in Equation (3.1). The numerical representation of the flame zone is separated from the modelling of the burning velocity.

3.2.1 Numerical representation of the flame zone

The *flame model*, denoted the β *model* by **Arntzen** (1998), defines the criteria for combustion and the spatial distribution of reaction rate across the numerical flame zone. The model defines the diffusion coefficient and the reaction rate in Equation (3.1) from an input burning velocity s. In the following, the flame model equations are rewritten in terms of the progress variable $\widetilde{c}$ rather than the fuel mass fraction $\widetilde{Y}_F$, since the analysis by **Arntzen** (1998) was performed for the progress variable. For implementation in FLACS, the equations are written to be consistent with the diffusion and reaction rate in Equation (3.1).

The reaction rate for the progress variable $\widetilde{w}_c = -\widetilde{w}_F/Y_{F0}$ is expressed as a function of $\widetilde{c}$ according to

$$\widetilde{w}_c = \overline{\rho} W \min\left(\widetilde{c}, 9(1-\widetilde{c})\right) , \qquad (3.11)$$

where the reaction rate coefficient W is given as

$$W = C_{\beta w} \frac{s}{\Delta} . \qquad (3.12)$$

Here, $C_{\beta w}$ is a model constant, s is the burning velocity, and Δ is the control volume length in the direction of flame propagation.

The reaction rate $\widetilde{w}_c$ is set to zero if the progress variable $\widetilde{c}$ is less than a critical value c_q. In FLACS, the critical progress variable c_q depends on the expansion ratio of the mixture according to

$$(\sigma - 1) c_q = C_{c_q}, \qquad (3.13)$$

where $\sigma = \rho_u/\rho_b$ and C_{c_q} is a model constant. The β model expresses the diffusion coefficient for Y_F as

$$\mu_{\text{eff}}/\sigma_{\text{F}} = \overline{\rho} D_\beta = \overline{\rho} C_{\beta D} \, s \, \Delta , \qquad (3.14)$$

where $C_{\beta D}$ is a model constant.

The model parameters $C_{\beta w}$ and $C_{\beta D}$ must satisfy

$$C_{\beta w} C_{\beta D} = \Lambda , \qquad (3.15)$$

where $\Lambda = D_\beta W/s^2$ is an eigenvalue of the 1D steady transport equation for the progress variable with the source term from Equation (3.11), and $\Lambda^{-1/2}$ is a non-dimensional burning velocity. Following the analysis of Catlin and Lindstedt (1991) and Arntzen (1998), the eigenvalue Λ can be expressed as a function of $(\sigma - 1) c_q$. Since $(\sigma - 1) c_q$ is fixed, Λ is everywhere constant.

Together with the critical progress variable, c_q, the parameters $C_{\beta w}$ and $C_{\beta D}$ determine the numerical flame thickness. The width of the flame zone is defined to avoid unwanted numerical diffusion and artificial increase of the reaction rate during simulation of the flame propagation. The model parameters are set so that the flame thickness becomes 3-5 control volume lengths in the direction of flame propagation. These settings reproduced the input burning velocity s with sufficient accuracy in a series of tests involving flame propagation in idealised scenarios, cf. (Arntzen, 1998). In FLACS simulations of realistic gas explosions, the input burning velocity s is derived from empirical correlations that depend on variables characterising the local flow regime and mixture properties. The correlations used in the standard version of FLACS (Gexcon, 2016) are presented in Section 3.2.2.

If numerical diffusion effects are negligible, the output burning velocity from the flame model should be unchanged for fixed Λ if $C_{\beta D}$ is increased, and $C_{\beta w}$ is simultaneously reduced to satisfy $C_{\beta w} C_{\beta D} = \Lambda$. In order to test the performance of the flame model, Vik (2014) presented a range of nominally one-dimensional test cases, and analysed the accuracy of the output burning velocity systematically for a range of fixed input burning velocities. Tests were performed both with standard settings (giving a flame thickness of 3-5 control volumes), and with an increased value of $C_{\beta D}$, resulting in a thicker flame zone. The tests where the time resolution was set to the recommended values for performing efficient simulations (these settings are described in

Section A.4) the thickened and the standard flame gave similar results. However, for increasing resolution in time, the convergence behaviour of the burning velocity from the thickened flame towards the input burning velocity was significantly better than that produced by the standard flame.

In standard versions of FLACS, using grid cells with characteristic lengths of less than 2 cm for explosion simulations is not recommended. For this range of cell sizes, significant grid dependency has been observed (Skjold et al., 2013b). This is likely due to grid dependency originating from the turbulence model, together with the model parameter settings in the combustion model being optimised for coarser grid resolutions. Increasing the flame thickness when refining the computational grid conserves the structure of the flame relative to the geometry, and may lead to more robust results and less grid dependency. This approach was tested in the grid dependency study in Paper 2 of the present thesis.

3.2.2 Burning velocity correlations

The numerical flame model presented in Section 3.2.1 requires an input burning velocity s. In FLACS, s is determined from empirical expressions. These correlations depend on the properties of the flammable mixture and the flow regime in each control volume, for each time step. Different correlations are defined for the *laminar*, *quasi-laminar* and *turbulent* regimes of flame propagation.

In the following, the settings used in standard releases of FLACS up to version 10.5r1 (Gexcon, 2016) are presented, as these constitute the starting point for the analysis and modelling approaches described in the present dissertation.

Laminar burning velocity

FLACS uses a library of literature values to represent u_l as a function of the equivalence ratio ϕ (cf. Section 2.1). Mixtures of different gas types are treated by computing the volume-weighted average, and u_l is initially corrected for the presence of additional inert gases or oxygen in the atmosphere, initial pressures and/or temperatures deviating from standard atmospheric values.

By assuming isentropic compression, pressure and temperature effects on the laminar burning velocity can be reformulated to only explicitly depend on the pressure. Hence, Arntzen (1998) expressed the laminar burning velocity during simulation in FLACS as

$$u_l = u_l^0 \left(\frac{p}{p_0} \right)^{\gamma_p} ,$$

where u_l^0 is the initial laminar burning velocity, p_0 is the initial pressure, and the constant γ_p depends on the fuel type.

The values for u_l in the standard releases of FLACS are not all consistent with the values found in the recent combustion literature, see e.g. (Ranzi et al., 2012). In particular, the laminar burning velocity for methane-air mixtures has been artificially enhanced, presumably to improve model performance for a set of large-scale experiments involving natural gas, see e.g. (Al-Hassan and Johnson, 1998; Foisselon et al., 1998; Selby and Burgan, 1998). This feature leads to a misrepresentation of the reactivity of methane-air mixtures, in comparison to that of e.g. propane-air mixtures.

Therefore, as part of the work presented in Chapter 4 and in Paper 2, the library values for the laminar burning velocities of methane and propane were updated to better reflect the difference in reactivity between the two fuels. This burning velocity modification was used together with other developments in Paper 2 (for propane-air) and in Section 6.2 (for natural gas-air with more than 90 % methane in the fuel component).

Quasi-laminar burning velocity

An empirical model for the quasi-laminar burning velocity u_{ql} controls the initial phase of flame propagation, as well as flame propagation through regions with very low turbulence levels. The expression for u_{ql} in FLACS (Gexcon, 2016) is given as

$$u_{ql} = u_l \left(1 + C_{ql} \left(\min\left[1, r_f/3\right]\right)^a\right) , \tag{3.16}$$

where C_{ql} is a fuel-dependent empirical constant, r_f is the flame radius and a is a model constant. Based on gas explosion experiments performed at CMI as part of the Gas Safety Programme (GSP) 90-92 (Arntzen, 1998), the radius exponent a was set to 0.5.

In Equation (3.16), the increase in the quasi-laminar burning velocity with r_f is limited to a flame radius of 3 m. Furthermore, C_{ql} does not vary with the equivalence ratio of the mixture, and a is a fixed model constant for all fuel types and concentrations. Chapters 4 and 6 and Paper 2 of the present thesis discuss alternative models for u_{ql}.

Turbulent burning velocity

The turbulent burning velocity u_t in FLACS for high stretch rates is governed by the expression by Bray (1990), which correlates 1650 separate measurements of turbulent burning velocities for premixed gaseous mixtures. The burning velocity is expressed in terms of the Karlovitz stretch factor $K = 0.157 \left(u'/u_l\right)^2 \left(u'\ell_I/\nu\right)^{-0.5}$ and the rms (root mean square) turbulence velocity fluctuation u' according to

$$u_t = 0.875 \, u' \, K^{-0.392} . \tag{3.17}$$

Alternatively, u_t from Equation (3.17) can be expressed in terms of u', an integral length scale ℓ_I defined as

$$\ell_I = 0.202 \frac{k^{1.5}}{\varepsilon}, \tag{3.18}$$

the laminar burning velocity u_l (including pressure, temperature and concentration effects as described above), and the kinematic viscosity ν, according to

$$
\begin{aligned}
u_t &= 0.875 \, u' \, K^{-0.392} , \\
&= 0.875 \, u' \left[0.157 \left(\frac{u'}{u_l}\right)^2 \left(\frac{u'\ell_I}{\nu}\right)^{-0.5}\right]^{-0.392} \\
&= 1.81 \, u'^{\,0.412} \, u_l^{\,0.784} \, \ell_I^{\,0.196} \, \nu^{\,-0.196} .
\end{aligned} \tag{3.19}
$$

For sufficiently high values of K, quenching of the turbulent flame brush commences. The limit for turbulent burning velocity increase with u' is set to $K = 1$. For low turbulence levels, the turbulent burning velocity is given by Arntzen (1998) as

$$u_t = 0.96 \, u'^{\,0.912} \, u_l^{0.284} \, \ell_I^{0.196} \, \nu^{-0.196} + u_l \,. \tag{3.20}$$

In the FLACS solver, pressure effects on ν are neglected in the turbulent burning velocity correlations, i.e. in equations (3.19) and (3.20), the kinematic viscosity ν is assumed to be a fixed constant. Chapters 4 and 6 and Paper 2 of the present thesis discuss alternative models for u_t.

Modelling the combustion length scale

The standard releases of FLACS (up to version 10.5) (Gexcon, 2016) model the integral length scale ℓ_I used as input to the burning velocity correlations, cf. equations (3.19) and (3.20), as a function of either the distance from the ignition point, r_f, or a length scale characterising the geometric extent of a confining geometry, ℓ_{lim}, according to

$$\ell_I = \min \left(C_{r_f} r_f, C_{\ell_{lim}} \ell_{lim} \right), \tag{3.21}$$

where C_{r_f} and $C_{\ell_{lim}}$ are model constants. If nothing else is specified in the following chapters, this combustion length scale model has been used to perform the simulations.

For the modelling work presented in Chapter 6, an updated framework for representing the combustion length scale has been applied. For the updated model results, a scaled version of the length scale ℓ derived from the k-ε model is used as input to the burning velocity model, rather than the length scale from Equation (3.21). The updated model is a result from JIP MEASURE (Skjold et al., 2017a). Developing combustion length scale models for turbulent combustion is not the focus of the present doctoral study. The model results and developments presented in the thesis, and the associated conclusions, are considered valid independently of changes to this specific model.

Chapter 4

Intrinsic flame instabilities and Markstein number effects

This chapter focuses on the effect of *intrinsic flame instabilities*, i.e. instabilities that occur because a freely expanding flame front is inherently unstable. Furthermore, the present chapter explores how the physicochemical properties of a premixed fuel-air mixture that influence the growth rate of intrinsic instabilities also affect the rate of turbulent combustion. These topics are highly relevant for addressing both aspects of the research question *"how can the sub-grid representation of flame acceleration mechanisms due to instability effects and flow past obstructed regions be improved in a CFD tool used for consequence assessment of gas explosions?"*. In particular, the chapter expands on the topics addressed in Paper 1 and Paper 2 of the present thesis. Meanwhile, the general theory concerning stability analysis and turbulent combustion in the present chapter is also highly relevant for discussing the findings of Paper 3 and Paper 4. Chapter 5 gives an extended analysis of the results from Paper 3 and Paper 4; these publications are therefore not reviewed in detail here.

Performing systematic validation against experiments is crucial for the further development of sub-grid models accounting for flame instabilities and turbulent combustion. Access to appropriate, high-quality experimental data, and careful analysis of the explosion mechanisms in the experiments, are prerequisites for doing meaningful consequence modelling of gas explosions. The first paper of the thesis constitutes part of this effort, and thus provides motivation for the work undertaken in the present doctoral study.

Gas explosion experiments conducted in large-scale vented enclosures provide challenging validation cases for investigating how a consequence model represents different physical phenomena associated with flame instabilities and turbulent combustion. The CFD tool FLACS has mainly been developed for predicting the effects of explosions in densely congested areas, where flow and flame front interactions with complex sub-grid obstructions constitute the main flame acceleration mechanism. It is therefore a valuable exercise to analyse the performance of the model in, for example, enclosures with a low degree of congestion, where other phenomena may govern the flame propagation and overpressure generation.

To this end, Paper 1 presents experimental and model results from an extensive campaign involving a series of explosion experiments performed in a large–scale empty, vented enclosure. The experimental configuration was, to the authors' knowledge,

unique; the enclosure was divided in two chambers separated by a narrow doorway (called a "twin-compartment" configuration). The analysis in the paper focuses on the representation of the explosion mechanism, timing of events and the maximum obtained explosion overpressure. Based on the analysis, Paper 1 proposes that model performance may be improved by (i) introducing updated sub-grid models for the initial phase of flame propagation, where intrinsic instabilities govern the flame acceleration, and (ii) by including the effect of instabilities developing on an accelerating flame front due to the Rayleigh–Taylor instability. Furthermore, the results in Paper 1 suggest that (iii) changing how the combustion rate responds to the turbulence generated by flow through vent openings may improve the representation of the explosion mechanisms. The present chapter expands on topics (i) and (iii), while topic (ii) is addressed in Chapter 5.

The majority of large-scale gas explosion experiments involving hydrocarbons found in the literature have been performed using near-stoichiometric fuel-air mixtures, as these often have the highest laminar burning velocities and are assumed to lead to the most severe consequences. Additionally, close to the stoichiometric equivalence ratio, small perturbations in the fuel concentration result in relatively small perturbations in the laminar burning velocity. Hence, the uncertainty associated with the laminar burning velocity for near-stoichiometric fuel-air mixtures is less than for mixtures that are leaner or richer. These experiments form the validation basis for the sub-grid models in CFD tools used for simulating gas explosions. To improve the validity of sub-grid models for more general scenarios, it is crucial to extend the matrix of gas explosion experiments to a wider range of fuel-air concentrations. This work would complement the earlier studies by e.g. van Wingerden and Zeeuwen (1983a), Hjertager et al. (1988) , Skjold et al. (2014a), Bauwens et al. (2012) and Bauwens et al. (2015).

This chapter and Paper 2 discuss how the models accounting for flame acceleration in both the initial (laminar and quasi-laminar) phase of a gas explosion and the turbulent regime can be improved in the CFD tool FLACS, cf. Section 3.2.2. To support this investigation, Paper 2 presents results from an experimental campaign comprising 42 tests that were designed, performed and analysed as part of the doctoral study. In this campaign, the effect of varying the fuel concentration in a propane-air mixture, thus effectively changing the Markstein number of the mixture, was explored for different flow regimes. Recent publications by Bradley et al. (2005, 2013, 2011a) suggest that the physicochemical properties that govern the onset and appearance of intrinsic instabilities, expressed in terms of the mixture's Markstein number, also affect the rate of turbulent combustion. Paper 2 compares the experimental results with model predictions from a development version of the CFD tool FLACS, where alternative sub-grid models for premixed combustion have been implemented. The present chapter significantly expands on the theoretical background for this work.

Additional results from simulations of vented explosions, using the new developments introduced in Paper 2 and in the present chapter, are presented in Chapter 6. All experiments that were simulated in Chapter 6 were performed by other research groups. In Section 6.2, the alternative models for premixed combustion explored by Paper 2 are also applied to key experiments from the campaign in Paper 1. Furthermore, Chapter 6 tests a sub-grid model for the Rayleigh–Taylor instability (described in Chapter 5) for the experiments in Paper 1. The work presented in Paper 1, Paper 2 and Chapter 6 thus demonstrates how validation against experiments can support the development of

improved sub-grid models in CFD tools.

4.1 Instabilities – definitions and overview

A freely expanding flame is intrinsically unstable. The hydrodynamic instability, alternatively termed the Landau–Darrieus (LD) instability, induces a cellular structure on the initially smooth surface of a freely propagating laminar flame front. The flame can be stabilised or further destabilised by thermal–diffusive effects, depending on the physicochemical properties of the mixture, the pressure level, etc. These effects are termed *intrinsic instabilities* (Ciccarelli and Dorofeev, 2008).

Together with turbulence production in shear layers from flow past obstructions, fluid flow instabilities play an important role for the flame acceleration in gas explosions (Ciccarelli and Dorofeev, 2008; Oran, 2015). When the flame propagates through areas with confinement and/or obstructions, the Rayleigh–Taylor (RT), Kelvin–Helmholtz (KH), Bénard–von Kármán (BVK), Richtmyer–Meshkov (RM), and acoustic instabilities may further increase the flame surface area and the overall combustion rate. The mechanisms are termed *geometry-induced instabilities*, as the presence of confinement and/or congestion is normally required for these to have an appreciable effect on the flame acceleration.

In this and subsequent chapters, the general term *instabilities* will refer to narrow-band disturbances with coherent structures. The instabilities are defined in contrast to the broadband range of disturbances on a wide range of temporal and spatial scales that characterises turbulent flow (Lieuwen, 2012). Meanwhile, as discussed in Paper 3 and Section 5.3, broadband turbulence can be an important secondary effect of coherent instabilities.

Finally, the term *flame instabilities* is used for instability effects that are triggered by and linked directly to the presence of a flame zone releasing chemical energy. In this respect, flame instabilities are more specifically termed than general fluid flow instabilities. For example, the BVK instability discussed in Chapter 5 is a fluid flow instability that is not directly triggered by the presence of a premixed flame zone.

4.2 Stability analysis and decomposition of disturbances

This section provides a brief introduction to linear flow stability analysis and the decomposition of disturbances. The concepts are used for discussing several flame acceleration mechanisms both in the present chapter and in Chapter 5.

To be consistent with Section 2.8, averaged values (e.g. in time) are denoted with an overbar, e.g. $\overline{\Phi}$, while fluctuations are denoted with a prime, e.g. Φ'. However, it is often relevant to differentiate the fluctuations further, and categorise them into (i) random fluctuations $\breve{()}'$ and (ii) quasi-deterministic fluctuations $< ()' >$, i.e. $\Phi' = \breve{\Phi}' + < \Phi' >$. Here, $<>$ denotes the ensemble average over a number of repeated trials. This decomposition is relevant e.g. for studying coherent vortex shedding due to the BVK instability in high-Reynolds number flows, where periodic oscillations are superimposed on a background of fine-scale turbulence (cf. Section 5.3). However,

experimental differentiation between fluctuation types will often depend significantly on the applied method, and is not straightforward (Lieuwen, 2012).

In order to study the evolution of disturbances, it is often convenient to expand the flow quantities of interest, Φ, in a Taylor series around the undisturbed base state, Φ^0, e.g. $\Phi = \Phi^0 + \Phi^1 + \Phi^2 + ...$, where $\Phi^0 >> \Phi^1 >> \Phi^2$, etc. The first order fluctuation Φ^1 is linear in the disturbance amplitude, a_d, while $\Phi^2 + \Phi^3 + ...$ represent higher order terms on the order of a_d^2, a_d^3, etc. Unlike the time average, $\overline{\Phi}$, the base value Φ^0 and the perturbation terms Φ^1, Φ^2, etc. are not experimentally available. However, the decomposition is useful for studying the stability of different flows analytically.

In *linearly stable* or *linearly unstable* systems, infinitesimal disturbances decay or grow, respectively. In a *non-linearly unstable* system, only disturbances exceeding a certain critical value will grow. First order perturbations are often assumed to be on the form $\Phi^1 = a_\Phi e^{ik_w x_1} e^{-i\omega t}$, where $k_w = k_{w,r} + ik_{w,i}$ is a complex wave number, and $\omega = \omega_r + i\omega_i$ is a complex frequency. To determine temporal linear instability, the complex growth rate ω_i must be evaluated for each real wave number $k_{w,r}$. If the maximum value of ω_i is positive, the flow is linearly unstable, while if the maximum value of ω_i is negative, the flow is linearly stable.

In a *convectively unstable flow*, disturbances grow as they propagate downstream, and eventually propagate out of the flow domain. In contrast, in an *absolutely unstable flow*, disturbances grow exponentially in time at the point where they were initiated, and eventually exist everywhere in the flow domain. One can determine whether a linearly unstable flow is convectively or absolutely unstable by solving for the combination of $k_{w,0}$ and ω_0 where both the dispersion relation (which relates the wave number of a wave to its frequency), $D(k_{w,0}, \omega_0)$, and the derivative of the dispersion relation with respect to k_w, $\partial D / \partial k_w (k_{w,0}, \omega_0)$, is zero (Lieuwen, 2012). If the $\omega_{i,0}$ satisfying this equation is larger than zero, the flow is absolutely unstable. If $\omega_{i,0}$ is less than zero, the flow is convectively unstable.

Rayleigh's theorem states that a necessary (but not sufficient) condition for temporal instability in inviscid flows is that the mean velocity profile has an inflection point (Lieuwen, 2012). Flows without inflection points are inviscidly stable, but can be destabilised by viscous and non-linear effects. Meanwhile, flow configurations such as mixing layers, jets or wakes have inflection points in their mean velocity profiles, and may therefore be destabilised by inviscid mechanisms alone. In flows such as jets and wakes, there are at least two separated sheets of vorticity present in the flow. Each vortex sheet induces motion on itself, as well as on the other vortex sheet (Abernathy and Kronauer, 1962). The instability of a bluff-body wake is discussed further in Section 5.3 and in Paper 3.

The methods and the definitions outlined here are used to analyse intrinsic instabilities in sections 4.3.2 and 4.3.4, and to study geometry-induced instabilities in Chapter 5. The results from the stability analyses can be directly related to the observed physical phenomena, and are therefore highly useful for understanding and supporting the relevant modelling approaches.

4.3   Intrinsic flame instabilities

4.3.1   Landau–Darrieus and thermal–diffusive instabilities

An outwardly propagating spherical flame is unstable for any expansion ratio $\sigma = \rho_u/\rho_b > 1$, where ρ_u and ρ_b are the densities of the reactants and the combustion products, respectively. The Landau–Darrieus (LD) or hydrodynamic instability is caused by the expansion of gas through the flame front (Darrieus, 1938; Landau, 1944), and results in the appearance of a cellular structure on the surface of the propagating flame. In practice, the cellular structure appears at a certain critical flame radius r_f^{cr}, as the spherical flame may be stabilised by initially high flame stretch rates (Beeckmann et al., 2017; Bradley, 1999). The physical mechanisms driving the instability are described in Section 4.3.2.

Laminar premixed flames are in general also subject to thermal–diffusive effects, affecting both the onset and appearance of flame cellularity (Barenblatt et al., 1962; Sivashinsky, 1977; Williams, 1985). The effects originate from imbalances between the thermal and mass diffusivity of the mixture. If a planar flame front is perturbed, such as in Figure 4.1, the part of the flame zone which is convex to the reactants (i.e. extending into the fresh mixture) releases more heat than a planar flame. This will in turn cool the flame and lead to a reduced combustion rate in the convex region, relative to that of a planar flame front. For the regions that are concave relative to the reactants (i.e. extending into the combustion products), the opposite effect is seen, i.e. the combustion rate will be enhanced relative to that of a planar flame. Consequently, thermal diffusion works against the perturbations and has a *stabilising* effect on the perturbed flame front. In contrast, diffusion of the limiting component of the combustion reaction will be increased in the convex parts of the flame front relative to the concave regions, thus promoting combustion in the regions that curve into the reactants relative to the regions that curve into the products. Molecular diffusion therefore has a *de-stabilising* effect on the perturbed flame front. In effect, the observed instability depends on the relationship
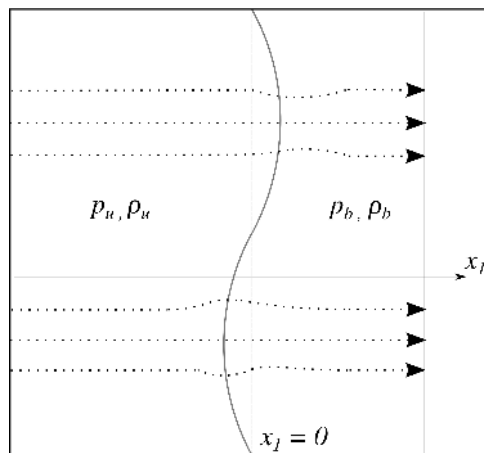
Figure 4.1: A perturbed flame front. The dashed curves represent streamlines. Reactants are on the left hand side and combustion products are on the right hand side of the flame front.

between the thermal diffusivity $\mathcal{D}_{th}$ and mass diffusivity $\mathcal{D}$ of the mixture, expressed by the Lewis number, $Le = \mathcal{D}_{th}/\mathcal{D}$. For $Le > 1$, thermal–diffusive effects have a stabilising effect on a perturbed flame front, while for $Le < 1$, the thermal–diffusive effects will further destabilise the flame.

The Lewis number generally varies with mixture composition. When the lighter component of a mixture is deficient, thermal–diffusive effects promote flame front instability. Consequently, for propane and higher hydrocarbons mixed with air, fuel-rich mixtures ($\phi > 1$) are more prone to instability than fuel-lean mixtures ($\phi < 1$). For hydrogen-air mixtures, the opposite is true, as the oxidiser then constitutes the heavier component.

The LD and thermal–diffusive instabilities are termed *intrinsic*, as they are inherently associated with outwardly propagating premixed flame fronts (Ciccarelli and Dorofeev, 2008). Intrinsic instabilities are in particular considered important for the initial phase of flame propagation, as the transition to cellularity is associated with a marked increase in flame surface area and burning velocity. The degree to which they affect the rate of flame acceleration depends on the specific scenario, i.e. geometry layout, mixture properties, initial pressure and temperature, etc. Geometry-induced instabilities (defined in Section 4.1) are normally considered to constitute stronger mechanisms. Meanwhile, for gas explosions in regions with a low degree of congestion, intrinsic instabilities may completely dominate the flame acceleration.

Furthermore, recent research suggests that thermal–diffusive effects are important also for turbulent flame propagation (Bradley et al., 2005, 2013, 2011a). The observed onset and growth rate of intrinsic instabilities are closely linked to the value of the Markstein length $\mathcal{L}$ or the Markstein number $Ma = \mathcal{L}/\delta_l$ (Markstein, 1951) of the mixture (Clanet and Searby, 1998; Searby and Quinard, 1990; Truffaut and Searby, 1999), where δ_l is the laminar flame thickness. These quantities are defined in Section 4.3.3, and their importance for characterising flame acceleration in different flow regimes is discussed in sections 4.3.3 through 4.5.2.

4.3.2   The stability analysis of Landau

The original analysis of the hydrodynamic instability performed by Landau (1944) is used in the following as a reference for discussing several instability mechanisms. For example, an extension of the analysis has been used to model the growth rate of the RT instability (cf. Section 5.4).

Landau (1944) originally analysed the hydrodynamic instability for a simplified system: a planar flame front located in a stationary fuel flow, where viscosity and compressibility effects are neglected, and the gas densities at each side of the flame front are assumed to be different and constant (Zeldovich et al., 1985). Conservation of continuity and momentum (cf. equations (2.9) and (2.10)) can therefore expressed as

$$\frac{\partial u_i}{\partial x_i} = 0 \, , \tag{4.1}$$

$$\frac{\partial u_i}{\partial t} + u_j \frac{\partial u_i}{\partial x_j} = -\frac{1}{\rho} \frac{\partial p}{\partial x_i} \, . \tag{4.2}$$

The coordinate system is attached to the (unperturbed) flame surface, which is located at $x_1 = 0$, cf. Figure 4.1. In the following, the variables with a subscript u denote the

state in the reactants, while variables with a subscript b are defined in the combustion products. Variables with a superscript 0 denote stationary values, i.e. the undisturbed base state, while variables with a superscript 1 represent small, non-stationary, first order perturbations. The expansion ratio is defined as $\sigma = \rho_u^0/\rho_b^0$. In the reactants, $u_1^0 = u_n$, where u_n is the stretched burning velocity, while $u_2^0 = u_3^0 = 0$, $\rho^0 = \rho_u$ and $p^0 = p_u$. In the combustion products, $u_1^0 = \sigma u_n$, $u_2^0 = u_3^0 = 0$, $\rho^0 = \rho_u/\sigma$ and $p^0 = p_b$.

The perturbations to the stationary base state are $u_1^1(x_1, x_2, t)$, $u_2^1(x_1, x_2, t)$ and $p^1(x_1, x_2, t)$ such that the sought solutions (for both reactants and products) are on the form

$$u_1 = u_1^0 + u_1^1(x_1, x_2, t) \ , \tag{4.3}$$

$$u_2 = u_2^0 + u_2^1(x_1, x_2, t) \ , \tag{4.4}$$

$$p = p^0 + p^1(x_1, x_2, t) \ . \tag{4.5}$$

The stability analysis is asymptotic, i.e. the perturbations are assumed to arise after an infinite time, from $t = -\infty$, from unperturbed motion at $x = -\infty$.

Equations (4.3)-(4.5) are inserted into equations (4.1)-(4.2). As the perturbations are assumed very small, non-linear terms in the first order perturbations can be neglected, resulting in

$$\frac{\partial u_1^1}{\partial x_1} + \frac{\partial u_2^1}{\partial x_2} = 0 \ , \tag{4.6}$$

$$\frac{\partial u_1^1}{\partial t} + u_1^0 \frac{\partial u_1^1}{\partial x_1} = -\frac{1}{\rho^0}\frac{\partial p^1}{\partial x_1} \ , \tag{4.7}$$

$$\frac{\partial u_2^1}{\partial t} + u_1^0 \frac{\partial u_2^1}{\partial x_1} = -\frac{1}{\rho^0}\frac{\partial p^1}{\partial x_2} \ . \tag{4.8}$$

From equations (4.6)-(4.8), it can be found that p^1 satisfies the Laplace equation, i.e.

$$\frac{\partial^2 p^1}{\partial x_1^2} + \frac{\partial^2 p^1}{\partial x_2^2} = 0 \ . \tag{4.9}$$

A solution of Equation (4.9) on the form

$$p^1 = a_p e^{n x_1} e^{i k_w x_2} e^{\omega^* t} \ , \tag{4.10}$$

where $\omega^* = -i\omega$ is the growth rate of the perturbations in time, k_w is the wave number of the perturbation in the x_2-direction, and n denotes the growth rate of the perturbation in the x_1-direction, is sought. The temporal linear stability analysis will therefore focus on evaluating the real part of ω^* for each real wave number $k_{w,r}$. From inserting (4.10) into (4.9), $n = \pm k_w$. The perturbations are assumed to be zero infinitely far away from the flame front, consequently, $n = k_w$ in the reactants, and $n = -k_w$ in the combustion products.

Equation (4.10) can be inserted into equations (4.6)-(4.8) to find general solutions for u_1^1 and u_2^1. By assuming again that perturbations are zero infinitely far away from the flame front, and by applying the continuity equation to reduce the number of constants,

specific solutions for u_1^1 and u_2^1 in both the reactants and combustion products can be found. They read

$$u_{1,u}^1(x_1,x_2,t) = -\frac{a_1 k_w}{\rho_u \left(\omega^* + u_u^0 k_w\right)} e^{k_w x_1} e^{ik_w x_2 + \omega^* t} \,, \tag{4.11}$$

$$u_{2,u}^1(x_1,x_2,t) = -\frac{ia_1 k_w}{\rho_u \left(\omega^* + u_u^0 k_w\right)} e^{k_w x_1} e^{ik_w x_2 + \omega^* t} \,, \tag{4.12}$$

$$p_u^1(x_1,x_2,t) = a_1 e^{k_w x_1} e^{ik_w x_2 + \omega^* t} \,, \tag{4.13}$$

in the reactants and

$$u_{1,b}^1(x_1,x_2,t) = \left(be^{-\frac{\omega^*}{u_b^0} x_1} + \frac{a_2 k_w}{\rho_b \left(\omega^* - u_b^0 k_w\right)} e^{-k_w x_1} \right) e^{ik_w x_2 + \omega^* t} \,, \tag{4.14}$$

$$u_{2,b}^1(x_1,x_2,t) = \left(\frac{\omega^* b}{ik_w u_b^0} e^{-\frac{\omega^*}{u_b^0} x_1} - \frac{ia_2 k_w}{\rho_b \left(\omega^* - u_b^0 k_w\right)} e^{-k_w x_1} \right) e^{ik_w x_2 + \omega^* t} \,, \tag{4.15}$$

$$p_b^1(x_1,x_2,t) = a_2 e^{-k_w x_1} e^{ik_w x_2 + \omega^* t} \,, \tag{4.16}$$

in the combustion products, where a_1, a_2 and b are arbitrary constants (Zeldovich et al., 1985).

The perturbation of the flame front $x_f(x_2,t)$ is assumed to sinuosoidal with an initial amplitude of d, on the form

$$x_f(x_2,t) = de^{ik_w x_2 + \omega^* t} \,. \tag{4.17}$$

Assuming that the flame front propagates with a constant speed, the following conditions must be met at the flame interface, $x_1 = 0$: $u_{1,u}^1 = u_{1,b}^1 = \partial x_f/\partial t$, $u_{2,u}^1 + u_{1,u}^0 \partial x_f/\partial x_2 = u_{2,b}^1 + u_{1,b}^0 \partial x_f/\partial x_2$ and $p_u^1 = p_b^1$. From these boundary conditions, and equations (4.11)–(4.16), a solution for the temporal growth rate ω^* can be found according to

$$\frac{\omega^*}{k_w u_n} = -\frac{\sigma \left(1 \pm \sqrt{1 + \sigma - 1/\sigma} \right)}{\sigma + 1}. \tag{4.18}$$

When $\sigma > 1$, the negative root of Equation (4.18) always leads to a real $\omega^* > 0$, or equivalently an imaginary ω, where $\omega_i > 0$, for which small perturbations grow without limit. For $\sigma = 1$, i.e. for $\rho_u = \rho_b$, the temporal growth rate of the perturbations is zero.

The physical interpretation of the result by Landau (1944) is that an infinitesimally thin flame surface is unconditionally unstable with respect to small perturbations of all wavelengths. Furthermore, since ω^* (as defined in this analysis) is always real, the perturbation develops as a standing wave and does not propagate along the flame front. An alternative physical understanding of the hydrodynamic instability is provided by the streamline visualisation in Figure 4.1. The streamlines passing through the flame converge before the concave parts of the surface (relative to the reactants) and diverge before the convex parts. Hence, the pressure decreases before the convex parts of the flame surface and increases before the concave, sustaining and enhancing the original perturbation (Bradley, 1999).

From Equation (4.18), it is clear that long wavelength perturbations (for which k_w is small) grow more slowly than perturbations with short wavelengths. However, the present linear stability analysis is not valid for perturbations with a wavelength on the order of the flame thickness, as it assumes an infinitesimally thin flame surface. Since the shortest wavelengths have the most significant growth rate from Equation (4.18), the analysis must be extended to take into account the effect of the thermal–diffusive structure of a stretched flame front. This effect is important for the observed flame acceleration that the instability induces, and is included in the following sections.

4.3.3 The effect of flame surface stretch on flame propagation

The *stretch rate* κ acting on a material flame surface describes the rate of surface area change per surface area, $\kappa = 1/A\,(dA/dt)$. A flame propagating in a non-uniform flow will experience stretch due to flame curvature, flow strain and unsteadiness. This changes both the surface area of the flame and the burning velocity (Williams, 1985). Markstein (1951) suggested that the local burning velocity would vary linearly with the local curvature. Later, several theoretical studies showed that the stretched flame speed u_n varies linearly for sufficiently small values of strain and curvature (Clavin, 1985; Clavin and Williams, 1982; Frankel and Sivashinski, 1983; Matalon and Matkowsky, 1982).

The stretched laminar burning velocity u_n can be expressed in terms of the unstretched laminar burning velocity u_l, the Markstein length $\mathcal{L}$ and the stretch rate κ according to

$$u_n = u_l - \mathcal{L}\,\kappa \,. \tag{4.19}$$

Markstein lengths can be defined relative to the unburnt reactant mixture, $\mathcal{L}_u$, and the combustion products, $\mathcal{L}_b$. However, it is crucial to note that $\mathcal{L}_u$ and $\mathcal{L}_b$ are, in general, neither equal nor proportional to each other (Davis et al., 2002).

The Markstein number $Ma = \mathcal{L}/\delta_l$ is obtained if the Markstein length is normalised by the flame thickness, δ_l. The Markstein number thus embodies the combined influence of flame stretch and thermal–diffusive effects on laminar flame propagation. The unstretched laminar burning velocity u_l can alternatively be expressed in terms of u_n, the Karlovitz stretch factor K (cf. Section 3.1.2) and Ma according to

$$\frac{u_l - u_n}{u_l} = K\,Ma \,. \tag{4.20}$$

From Equation (4.20), it is clear that an initial perturbation in the flame front that increases the (positive) local curvature and strain rate will lead to a reduced burning rate in the convex part of the flame (extending into the reactant mixture) for *positive* values of Ma. *Negative* values of Ma will have the opposite effect on the local burning velocity in the convex part of the flame, hence, the initial perturbation will be enhanced. By this mechanism, thermal–diffusive effects may stabilise or enhance the underlying LD instability, i.e. the effect of Ma on flame stability is closely linked to that of the Lewis number. From experimental studies, mixtures with negative values of Ma, such as fuel-lean hydrogen-air mixtures, are known to be highly prone to develop the cellular structure associated with intrinsic instabilities (Law, 2006).

Bradley et al. (1992) expressed flame stretch as

$$\kappa = \kappa_c + \kappa_s = \frac{u_n}{r} + \left(\frac{\mathbf{u} \cdot \mathbf{n}_f}{r} + \nabla_t \mathbf{u} \right) , \qquad (4.21)$$

where r is the radius of curvature, $\mathbf{u} \cdot \mathbf{n}_f$ is the fluid velocity component normal to the flame surface, and $\nabla_t \mathbf{u}$ is the fluid velocity gradient tangential to the flame surface. The first term on the right hand side of Equation (4.21), κ_c, represents stretch effects associated with flame front curvature, while the bracketed term, κ_s, represents the effect of strain due to the flow field. For example, for spherical, outwardly propagating laminar flames, the stretch rate is positive, generated only by curvature, and can be expressed in terms of the flame radius r_f as

$$\kappa = \frac{1}{A} \frac{dA}{dt} = \frac{2}{r_f} \frac{dr_f}{dt} . \qquad (4.22)$$

The stretched laminar burning velocity u_n can alternatively be expressed in terms of the unstretched laminar burning velocity u_l, the laminar Karlovitz stretch factors due to flame curvature $K_{lc} = \kappa_c \left(\delta_l / u_l \right)$ and flow strain $K_{ls} = \kappa_s \left(\delta_l / u_l \right)$, together with the Markstein numbers related to the curvature, Ma_c, and the strain rate, Ma_s, according to (Bradley et al., 2011c; Clavin, 1985)

$$\frac{u_l - u_n}{u_l} = K_{lc} Ma_c + K_{ls} Ma_s . \qquad (4.23)$$

When the flamelet concept is used for turbulent premixed combustion modelling, accounting for stretch effects is important both in the laminar and turbulent regime of flame propagation (see Section 3.1.2). In turbulent flames, both negative and positive stretch rates exist locally in the flame structure (Poinsot and Veynante, 2011).

4.3.4   Accounting for thermal–diffusive effects

The linear stability analysis of Landau (1944) (cf. Section 4.3.2) for a planar flame only includes hydrodynamic effects on an infinitesimally thin flame front, and is therefore not accurate for perturbations with wavelengths approaching the order of the flame thickness. This can be addressed by including the Markstein length of the flame front in the analysis.

The solutions for the equations of motion, equations (4.11)–(4.16), remain the same, however, the boundary conditions of the problem change. Equation (4.19) can be rewritten in terms of the curvature of the flame front, which can be replaced by $\partial^2 x_f / \partial x_2^2$ for small perturbations in the present system, i.e.

$$u_n = u_l \left(1 - \mathcal{L} \frac{\partial^2 x_f}{\partial x_2^2} \right) .$$

The kinematic boundary conditions from the analysis in Section 4.3.2 are replaced by $u_{1,u}^1 = \partial x_f / \partial t - \mathcal{L} u_l \, \partial^2 x_f / \partial x_2^2$ and $u_{1,b}^1 = \partial x_f / \partial t - \mathcal{L} \sigma u_l \, \partial^2 x_f / \partial x_2^2$. The pressure perturbations at the flame front are no longer equal in the reactants and products, so the

dynamic boundary condition becomes $p_u^1 - p_b^1 = -2\rho_u u_l^2 (\sigma - 1)\mathcal{L} \partial^2 x_f / \partial x_2^2$. Following the procedure outlined in Section 4.3.2, a new dispersion relation for ω^* can be found:

$$\frac{\omega^*}{k_w\,u_n} = -\frac{\sigma\left(1 + Ma\,k_w\delta_l \pm \sqrt{1 + \sigma - 1/\sigma + Ma\,k_w\delta_l\left(Ma\,k_w\delta_l - 2\sigma\right)}\right)}{\sigma + 1}\,. \quad (4.24)$$

It is interesting to investigate the behaviour of Equation (4.24) for different values of Ma. For $Ma = 0$, the Landau model in Equation (4.18) is retained, and the real part of ω^* increases linearly with the wave number k_w of the perturbation. For $Ma > 0$, the dependency of ω^* on k_w is weaker, and there exists a maximum wave number k_w^{max} for which the growth rate reaches its maximum value. For $k_w > k_w^{max}$, the real part of ω^* decreases for increasing k_w, and reaches zero for some critical wave number k_w^{cr}. Perturbations with wave numbers larger than k_w^{cr}, i.e. with wavelengths smaller than $2\pi/k_w^{cr}$, are stable. For $Ma < 0$, the dependency of ω^* on k_w is more significant, and there does not exist a limit k_w^{cr} for which smaller wavelengths are stabilised.

In the framework of this theory, it is therefore possible to explain why short-wavelength perturbations in practice are stabilised (for example in the very initial phase of spherical flame propagation), and why flames with $Ma < 0$ are observed to transition to the cellular regime at an earlier stage than flames with $Ma > 0$. In effect, Ma implicitly accounts for the effect of viscosity, thermal conductivity, mass and heat diffusivity (including Lewis number effects) on flame stability (Zeldovich et al., 1985).

4.3.5   Intrinsic instabilities and spherical flame propagation

The theory in sections 4.3.2 and 4.3.4 has been developed for planar flames. In most accident scenarios relevant for industrial applications, three-dimensional, outwardly propagating spherical flames are of interest.

For initially quiescent, spherical flames, several propagation regimes can be observed. In the early stages of flame propagation, the flame is laminar and stable. For highly unstable mixtures this regime may be extremely short-lived, as the flame surface will develop "cracks", and cell formation will commence almost immediately after ignition. At the point where the flame surface becomes fully cellular, the flame front accelerates. The flame surface area and speed continues to grow in the cellular regime. Meanwhile, for outwardly propagating spherical flames, the onset of instability occurs significantly later than what the linearised theory for planar flames predicts. For a spherical flame to change its shape due to the hydrodynamic instability, the growth rate of the amplitude of the perturbations needs to be larger than the growth rate of the flame radius itself. If this criterion is not satisfied, the perturbations will effectively be smoothed out (Bradley, 1999; Zeldovich et al., 1985).

Bechtold and Matalon (1987) used the linearised equations for an expanding spherically symmetric flame to analyse the instability growth rates of spherical flames. In their theory, perturbations are expanded in spherical harmonic series and specific wavelengths increase in proportion to the radius of the sphere. Stability is investigated for all possible modes, these are denoted n. Transitions between the different regimes of spherical flame propagation are given in terms of the Peclet number Pe, defined as the flame radius r_f normalised by the flame thickness δ_l.

Bechtold and Matalon (1987) expressed the dimensionless amplitude a of the perturbation relative to the flame front as

$$a = a_0 \left(r_f / r_f^0 \right)^{\omega \left(1 + \Omega / Pe \ln \left(r_f / r_f^0 \right) \right)} , \qquad (4.25)$$

where a_0 is the initial dimensionless amplitude of the perturbation, ω is the growth rate parameter accounting for the LD instability, depending solely on σ, and Ω is a growth rate parameter that depends on both Ma and the expansion ratio σ. Equation (4.25) is valid after the flame has propagated to a radius r_f, larger than the initial radius r_f^0, which is in turn significantly larger than the flame thickness δ_l. The parameters ω and Ω are expanded in series of spherical harmonic integers, or wave numbers $n = (2\pi Pe)/\lambda^\ell$, where λ^ℓ is the dimensional wavelength λ normalised by δ_l.

The logarithmic growth rate of the perturbation amplitude with respect to Pe, $\overline{A}(n)$, can be found from Equation (4.25):

$$\overline{A}(n) = \frac{d \ln(a/a_0)}{d \ln Pe} = \omega \left(1 - \frac{\Omega}{Pe} \right) , \qquad (4.26)$$

where a negative value of $\overline{A}(n)$ denotes a stable flame, and a positive value denotes an unstable flame. The first term on the right hand side of Equation (4.26) represents the effect of the LD instability, while the second term incorporates the effect of flame thermal–diffusivity. As in the analysis for a planar flame, for $\sigma = 1$, the flame front is unconditionally stable with respect to the LD instability.

Sufficiently high values of Ma also have a stabilising effect on the spherical flame front. Bradley (1999) observed that for a spherical flame propagating through a mixture with $\sigma = 6$ and $Ma = 1.4$, thermal–diffusive effects were destabilising for all wave numbers n at $Pe = 200$, while for a spherical flame at $Pe = 300$, with $\sigma = 6$, $Ma = 4$, the thermal–diffusive effects completely stabilised the underlying hydrodynamic instability. However, at a larger radius ($Pe = 600$), the latter mixture exhibited a range of unstable values of n (i.e. n for which $\overline{A}(n) > 0$). Bradley (1999) denoted the lower wave number limit of the unstable range as n_l and the upper limit as n_s. Consequently, for this spherical flame, there exists a critical Peclet number, Pe^{cr}, between $Pe = 300$ and $Pe = 600$ (and a corresponding n^{cr}) for which the flame becomes unstable.

For increasing Pe, the smallest unstable wave number n_l becomes constant. In effect, the largest unstable wavelength λ_l^ℓ increases linearly with Pe, or equivalently, the flame radius r_f. At the largest unstable wavelengths, the flame stretch rate is too low for the thermal–diffusive effects to stabilise the LD instability, and smaller wavelength perturbations are generated on the surface of the larger cells. If these wavelengths are unstable as well, further perturbations of even smaller wavelengths will develop. Unstable perturbations grow until they are stabilised by non-linear effects, such as flame annihilation at cusps between the convex regions of the flame surface (Gostintsev et al., 1988; Zeldovich et al., 1985).

The smallest unstable wavelength λ_s^ℓ, associated with the stabilising influence of thermal–diffusive effects at high flame stretch rates, is constant with increasing Pe. The cascade of unstable wavelengths is terminated at this scale. *The flame surface therefore develops a fractal character, with an inner cut-off length scale of λ_s^ℓ and outer cut-off length scale of λ_l^ℓ* (Bradley, 1999). This observation is used to derive correlations for the flame acceleration in the cellular regime.

4.4 Modelling the cellular regime of flame propagation

The Landau–Darrieus and thermal–diffusive instabilities can be the primary mechanisms of flame acceleration in gas explosions with low degrees of congestion. For modelling explosions following releases of flammable gases or liquids at onshore facilities, where flame propagation often occur through extended sparsely congested regions, it can be crucial to account for these effects. Accurate representation of cellular flame propagation is also important for simulating the initial phase of gas explosions. In particular, the pressure-time histories of vented explosions in empty enclosures, such as those modelled in Paper 1 and Chapter 6, will greatly depend on the flame speed in the cellular regime. The CFD tool FLACS represents cellular flame propagation through the correlation for the quasi-laminar burning velocity, u_{ql} (cf. Section 3.2.2).

Although the linear stability analyses in sections 4.3.2, 4.3.4 and 4.3.5 are useful for understanding the physical mechanisms, they cannot represent non-linear processes such as flame surface removal at cusps between cells. Cellular flame acceleration in spherical flames is most often characterised by assuming that the flame surface develops a fractal pattern (Bauwens et al., 2015; Bradley, 1999; Bradley et al., 2001; Gostintsev et al., 1988). Based on this assumption, the ratio of flame surface area with a resolution of the inner cut-off wavelength λ_s^ℓ, A_{fs}, to that with a resolution of the outer cut-off wavelength λ_l^ℓ, A_{fl}, is given by

$$\frac{A_{fs}}{A_{fl}} = \left(\frac{\lambda_l^\ell}{\lambda_s^\ell}\right)^{D-2} , \qquad (4.27)$$

where D is the fractal dimension of the surface. Sreenivasan et al. (1989) and Bradley (1999) suggested a fractal dimension D of $7/3$. For sufficiently large values of Pe, the ratio of the flame speed S for a wrinkled spherical flame and the flame speed for a smooth, laminar flame S_l of equal radius can be expressed as

$$\frac{S}{S_l} = \frac{A_{fs}}{A_{fl}} . \qquad (4.28)$$

At the point where the outwardly propagating spherical flame becomes fully cellular, the flame front accelerates. In practice, this transition occurs at Pe_{obs}^{cr}, which is generally larger than the critical Peclet number Pe^{cr} predicted by the linearised analysis by Bechtold and Matalon (1987). According to Bradley (1999), the expression for the flame speed in the cellular regime, equations (4.27) and (4.28), can be corrected by a factor f to account for the fact that the flame acceleration occurs at Pe_{obs}^{cr} rather than the theoretical Pe^{cr}. From experimental data, Bradley et al. (1998b) and Gu et al. (2000) correlated the observed critical Peclet number Pe_{obs}^{cr} for which the flame surface became fully cellular with the Markstein number of the mixture according to

$$Pe_{obs}^{cr} = 177Ma + 2177 , \text{ for } -5 < Ma < 8 , \qquad (4.29)$$

i.e. they observed that Pe_{obs}^{cr} increased linearly with increasing Ma.

Gostintsev et al. (1988) presented an analysis of several large-scale unconfined gas explosion experiments. They expressed the flame radius r_f for a freely propagating spherical flame as a function of time

$$r_f = r_f^0 + Ct^b , \qquad (4.30)$$

where r_f^0 is a critical flame radius for the onset of the self-similar propagation regime, C is a mixture specific constant and b is related to the fractal dimension D of the flame surface as $D = (3b - 1)/b$. Gostintsev et al. (1988) originally suggested an exponent b of 1.5; the exponent has since been found to vary from $1.2 - 1.5$, by e.g Gostintsev et al. (1999) and Pan and Fursenko (2008). Differentiating and rearranging Equation (4.30) gives an expression for the flame velocity according to

$$\frac{dr_f}{dt} = bC^{\frac{1}{b}} \left(r_f - r_f^0\right)^{(b-1)/b} . \tag{4.31}$$

A time exponent of 1.5 in Equation (4.30) leads to a flame speed that grows with the flame radius as $r_f^{1/3}$.

The correlation in Equation (4.30), proposed by Gostintsev et al. (1988), is valid only from Peclet numbers significantly larger than Pe^{cr}. The authors associated the self-similar regime with a transition to turbulent flame propagation. However, Bradley (1999) and Bradley et al. (2001) associated correlations on the form of Equation (4.30) with the regime of fully developed cellular flame propagation, observing this regime to occur in large-scale experiments at smaller values of Pe than those reported by Gostintsev et al. (1988). The flame radius from which the self-similar regime of flame propagation is realised, r_f^0, is often set to zero in equations (4.30) and (4.31). Bauwens et al. (2015) argued that this assumption is invalid, as the condition $r_f \gg r_f^0$ has not been satisfied in most studies.

Bauwens et al. (2015) analysed a series of experiments in a 64 m³ vented vessel, focusing on the growth rate of the LD instability during the first 1.2 m of undisturbed, constant pressure spherical flame propagation. The authors found that the observed flame speed versus flame radius for a range of propane-air mixtures, with equivalence ratios varying from $0.9 - 1.6$, exhibited a self-similar oscillation associated with the periodic growth and saturation of a narrow range of length scales following each new generation of cell formation. Specifically, they observed that after propagating a short distance as a smooth spherical flame from the ignition point, the first generation of cells appeared on the flame surface. The length scale of the cells was uniform, although richer mixtures (with lower values of Ma) exhibited smaller cells than the leaner mixtures. The first appearance of the cellular structure was accompanied by a significant increase in the flame velocity. According to Bauwens et al. (2015), for most of the equivalence ratios, the acceleration subsequently declined, and the flame velocity obtained a local maximum. After a slight decrease in flame velocity, the appearance of the next generation of cells lead to further flame acceleration. The process repeated itself with the appearance of each new cell generation. The critical values of Pe recorded by Bauwens et al. (2015) were found to increase roughly with increasing Ma, consistently with the correlations by Bradley et al. (1998b) and Gu et al. (2000), cf. Equation (4.29).

From the observed oscillatory behaviour, Bauwens et al. (2015) expressed the fractal increase in flame surface area and its effect on the quasi-laminar flame speed S_{ql} as

$$\frac{S_{ql}}{S_l} = \left(\frac{r_f}{r_f^0}\right)^{\zeta} , \tag{4.32}$$

where the fractal excess ζ is computed based on the relative increase in flame surface area by each successive generation of cells and the corresponding increase in normalised flame radius. Mixture-dependent values of ζ were thus obtained; ζ was found to be approximately constant (≈ 0.18) for propane-air mixtures with $\phi < 1.3$, and increased towards 0.3 for richer mixtures (with decreasing Ma). If Equation (4.32) is integrated to retain $r_f(t)$, a correlation on the form of Equation (4.30) is obtained according to

$$r_f(t) = r_f^0 \left((1 - \zeta) S_l t / r_f^0 \right)^{1/(1-\zeta)} . \tag{4.33}$$

Bauwens et al. (2015) found that Equation (4.33) gave reasonable agreement with the experimental data. This further corroborates the fractal assumption.

Bradley et al. (2001) observed dominant cell sizes ranging from 0.1 to 0.4 m in a series of large-scale explosions involving near-stoichiometric mixtures of methane-air and propane-air under atmospheric conditions. These observations were reported for the established cellular regime, with r_f growing from 1 to 3 m, and were found to be in agreement with the theoretical framework presented in Section 4.3.5. The dominant cell sizes observed in videos are expected to correspond to the wavelength where the growth rate of the instability is at its maximum, λ^{max}.

Bauwens and Dorofeev (2011) and Bauwens et al. (2011) performed CFD simulations of a series of gas explosions in the 64 m^3 vented enclosure, within a large-eddy simulation (LES) framework (Weller et al., 1998a,b). They assumed that flame wrinkling due to the hydrodynamic instability would be resolved in gas explosion simulations with methane-air and propane-air when applying a uniform grid resolution of 0.05 or 0.1 m. The lower cut-off scale λ_s of the fractal flame surface, which is imposed by thermal–diffusive effects, must be resolved.

However, for a 18 % hydrogen-air mixture, with a lower cut-off length scale of λ_s approximated to 7 mm, Bauwens et al. (2011) found it necessary to include sub-grid fractal flame surface area from the intrinsic instabilities. Since applying a fixed lower cut-off length scale is associated with some uncertainty, a model constant was required to ensure a satisfactory representation of the initial flame speed. The upper unstable wavelength, λ_l, was generally assumed to be resolved on the grid. The wavelength λ_l is associated with the lower wave number limit n_l, which is approximately constant in the cellular regime – with a typical value on the order of 10. The wave number represents the number of wavelengths of a particular value around the flame circumference. As λ_l grows proportionally to the flame radius, the assumption by Bauwens and Dorofeev (2011) that this wavelength will be resolved with a grid resolution of 0.05 or 0.1 m seems reasonable.

4.4.1 Modelling approach in FLACS

The expression for the quasi-laminar burning velocity u_{ql}, accounting for flame propagation in the cellular regime in standard releases of FLACS (Gexcon, 2016), is

$$u_{ql} = u_l \left(1 + C_{ql} \left(\min \left[1, r_f/3 \right] \right)^a \right) , \tag{4.34}$$

where C_{ql} is a fuel-dependent empirical constant, r_f is the flame radius and a is a model constant (cf. Section 3.2.2). Based on gas explosion experiments performed at CMI as

part of GSP 90-92, the radius exponent a in Equation (4.34) was set to a constant value of 0.5 (Arntzen, 1998).

Apart from the dependencies on the equivalence ratio, pressure and temperature that are included in the laminar burning velocity in FLACS, the flame acceleration given by Equation (4.34) (including the constant C_{ql}) does not depend on changes in physico-chemical properties of the mixture, e.g. with varying ϕ. Meanwhile, it is clear from the present discussion that the burning velocity in the quasi-laminar regime may vary significantly with changes in the Markstein number, i.e. with varying fuel concentration, pressure level, etc. (Bechtold, 2001; Bradley et al., 2007). Furthermore, these effects will be distinct for different types of fuel. Consequently, introducing a dependency on Ma to the model for u_{ql} would constitute an improved representation of intrinsic instabilities in the CFD tool FLACS.

However, the grid resolution normally applied in FLACS simulations of realistic accident scenarios excludes the possibility of correctly reproducing intrinsic instability effects on-grid, also in the established cellular regime. From the present discussion, it is assumed that the formation of a cellular structure on the flame surface from a cascade of unstable length scales in practice cannot be resolved by FLACS. The formation and cracking of cells due to intrinsic instabilities is a highly complex, non-linear process. The 'thickened flame' approach for modelling the flame zone, described Section 3.2.1, is formulated to give a representative overall burning velocity. The approach does not accurately represent the structure of a premixed flame front.

For simulating large-scale gas explosions, grid cell sizes on the order of 1 m are most often required to obtain reasonable simulation times. In practice, it is seldom feasible to apply a finer resolution than 0.05 m. Indeed, for a resolution of 0.05 m, the numerical flame thickness would extend between $0.15 - 0.25$ m. This will effectively dampen any instability forming on these length scales – such as the dominant grid cell sizes observed by Bradley et al. (2001), or λ_l for flame radii up to at least 2.5 m. Hence, it is assumed that flame acceleration in the cellular regime must be represented by a sub-grid model in FLACS, regardless of the applied grid resolution.

Presuming that all effects from intrinsic instabilities occur sub-grid, the fractal model for quasi-laminar flame propagation given by Equation (4.32) was implemented in a development version of FLACS for Paper 2 and Chapter 6 of the present thesis, i.e.

$$u_{ql} = u_l \left(\frac{r_f}{r_f^0} \right)^{\zeta} , \tag{4.35}$$

where r_f^0 is the estimated flame radius for the onset of the cellular regime, and ζ is the fractal excess. In Equation (4.35), r_f^0 and ζ depend on the fuel type and equivalence ratio, ϕ.

For the modelling work in Paper 2, the updated model for u_{ql} applies the data for propane-air flames from Bauwens et al. (2015), for equivalence ratios between 0.9 and 1.5. Corresponding measurements for hydrogen-air and methane-air mixtures, reported by Bauwens et al. (2017a,b), were used to extend the model for the simulations in Chapter 6.

Chapter 6, Section 6.1 presents model results for experimental campaigns performed in a 64 m^3 vented explosion chamber. The experiments were described by

Bauwens et al. (2011), Chao et al. (2011), Bauwens et al. (2012) and Bauwens and Dorofeev (2014). Fuel–lean hydrogen-air mixtures were used in all these tests. The concentration varied between 12 vol.% and 19 vol.% hydrogen in air, corresponding to equivalence ratios between 0.33 and 0.56. In addition to the arguments based on the analysis of physical phenomena presented in this chapter, implementing Equation (4.35) was motivated by the unsatisfactory representation of the initial flame propagation reported in Paper 1. The updated burning velocity model was therefore also tested for key experiments from Paper 1 in Section 6.2.

In contrast to Equation (4.34), the parameters of the alternative burning velocity model in Equation (4.35) depend on the equivalence ratio of the mixture, thus accounting for *Ma*-effects from varying mixture composition. Furthermore, Equation (4.35) does not restrict the flame acceleration generated by intrinsic instabilities to the first three meters of flame propagation, to be consistent with results from the analysis by e.g. Gostintsev et al. (1988) and Bradley (1999).

The effect of pressure on the growth rate of the instabilities was assumed to be negligible for the validation cases presented in Paper 1, Paper 2 and Chapter 6. Pressure effects on r_f^0 and ζ were therefore not included in the development version of FLACS used for the present doctoral study. This assumption is also valid for a range of applications, such as explosions following accidental releases under atmospheric conditions.

The modelling work performed for Paper 2 and Chapter 6 also includes an updated formulation of the turbulent burning velocity, expressed in terms of the mixture's Markstein number. This model is described in sections 4.5 and 4.6.

4.5   Representing the effect of turbulence on combustion

The modelling of turbulent premixed combustion involves representing the complex two-way coupling between the flame front and the local turbulence structures in the reacting flow. By analogy with the laminar burning velocity, the *turbulent burning velocity* u_t can be defined to be a basic characteristic of premixed turbulent combustion (Bray, 1990). A range of expressions relating the variables that characterise turbulence to the burning rate have been proposed for the different regimes of premixed combustion. Overviews of such correlations are presented by e.g. Lipatnikov and Chomiak (2002) and Dahoe et al. (2013). The CFD tool FLACS uses burning velocity correlations to close the system of equations describing premixed combustion, since this approach makes it possible to achieve practical simulation times for a wide range of gas explosion scenarios.

However, there are significant uncertainties associated with simple correlations – and with Reynolds averaged Navier-Stokes equations (RANS) modelling of premixed turbulent combustion in general. For example, the experiments on which many of the correlations are based have been performed at scales significantly smaller than the scales of the scenarios where they are ultimately applied. Furthermore, turbulence measurements in highly transient flows driven by gas explosions are rare. This implies that the validity of the modelled turbulence variables provided as input to the correlations is highly uncertain. Examples of relevant studies involving such measurements are described by Kong and Sand (1996), Lindstedt and Sakthitharan (1998) and Hjertager et al. (1988).

4.5.1   Fractal models for turbulent flame propagation

Damköhler (1940) studied the influence of the turbulence length scale and laminar flame thickness on the ratio of turbulent to laminar burning velocity. Damköhler suggested an indefinite increase of the turbulent burning velocity u_t with an increasing turbulence velocity u', i.e. neglecting the occurrence of flamelet quenching. This trend can be derived from assuming that the turbulent flame surface is a constant scalar surface wrinkled by all self-similar scales in the turbulent flow, down to the Kolmogorov microscale η. The ratio of the wrinkled flame surface area A_f^t to that with a resolution of ℓ_I, $A_f^{\ell_I}$, can be expressed as

$$\frac{A_f^t}{A_f^{\ell_I}} = \left(\frac{\ell_I}{\eta}\right)^{D-2} , \tag{4.36}$$

where D is the fractal dimension of the surface (Bradley, 1992; Mandelbrot, 1975). Sreenivasan et al. (1989) proposed a fractal dimension of the material surface of $7/3$. If one assumes that, for a flame surface, the inner cut-off scale should be the Gibson scale of turbulence ℓ_G instead of η, together with $D = 7/3$, the turbulent burning velocity can be expressed as

$$\frac{A_f^t}{A_f^{\ell_I}} = \frac{u_t}{u_l} \approx 1.52 \frac{u'}{u_l} . \tag{4.37}$$

Equation (4.37) assumes that u_t is independent of chemical kinetics, i.e. that the effect of the turbulence is merely to wrinkle the laminar flamelets without changing their structure.

Since the expression in Equation (4.37) does not consider flame stretch, it is not applicable to all regimes of the Borghi diagram, cf. Figure 3.1 in Section 3.1.2. Separate correlations for different premixed combustion regimes should therefore be combined when modelling flame propagation for a wide range of flow conditions.

Correlations based on fractal considerations may be appropriate for low stretch rate regimes. Equation (3.20), accounting for the turbulent burning velocity u_t for low stretch rates in standard releases of FLACS (cf. Section 3.2.2), has a high dependency on u'. The correlation gives similar results as the fractal-based expression proposed by Gülder (1991). However, recent validation work shows that changes to the low stretch rate correlation have a minimal impact on FLACS simulation results (Skjold et al., 2017a). The low-turbulence correlation is therefore not considered further in the present doctoral study.

4.5.2   Stretch rate based correlations

The laminar flamelets in a turbulent flow are exposed to flame stretch due to both flame curvature and aerodynamic strain. As for laminar flames (cf. Section 4.3.3) the stretch rate κ working on the flamelets can be expressed as a combination of these effects according to

$$\kappa = \kappa_c + \kappa_s ,$$

where κ_c and κ_s are the stretch rates due to flame curvature and aerodynamic strain, respectively. The distribution of κ_c and κ_s in turbulent flames can be represented as

probability density functions, see e.g. (Bradley et al., 2005). Both positive and negative stretch rates are present in the turbulent flame brush.

Karlovitz et al. (1953) described flame extinction in terms of the flame stretch rate. The Karlovitz stretch factor K used for turbulent premixed combustion expresses the stretch rate on a randomly orientated surface in isotropic turbulence normalised by the chemical timescale, as described in Section 3.1.2.

Bray (1990) presented a correlation based on the 1650 separate measurements of turbulent burning velocities for premixed gaseous mixtures consolidated by Abdel-Gayed et al. (1987). The turbulent burning velocity u_t was expressed in terms of K and the turbulence velocity fluctuation u', on the general form

$$u_t = \alpha \, u' \, K^{-\beta} \ . \tag{4.38}$$

where $C_k = 0.157$ in the expression for K:

$$K = C_k \left(\frac{u'}{u_l}\right)^2 \left(\frac{u'\ell_I}{\nu}\right)^{-0.5} \ . \tag{4.39}$$

Based on the experimental measurements, Bray (1990) set the constants α and β in Equation (4.38) to 0.875 and -0.393, respectively. This correlation is currently used in standard releases of FLACS to model high stretch rate flame propagation for all mixtures, regardless of fuel type and concentration (cf. Section 3.2.2).

Bradley et al. (1992) derived a correlation from the same data set on the same general form as Equation (4.38), also incorporating Le, according to

$$u_t = \alpha \, u'_k \, (KLe)^{-\beta} \ . \tag{4.40}$$

In Equation (4.40), $\alpha = 0.88$ and $\beta = -0.3$, and u' is replaced with an effective turbulence velocity fluctuation u'_k, representing the part of the turbulence spectrum that acts on the flame kernel – tending towards u' as the flame propagates.

In analogy to Equation (4.23), Bradley et al. (1996) defined the Markstein numbers Ma_{cr} and Ma_{sr}, associated with the stretched burning velocity u_{nr}, according to

$$\frac{u_l - u_{nr}}{u_l} = K_c Ma_{cr} + K_s Ma_{sr} \ . \tag{4.41}$$

Here, u_{nr} expresses the rate of generation of combustion products associated with the flame front, and K_c and K_s are the Karlovitz stretch factors due to flame curvature and flow strain, respectively. Bradley et al. (2005) presented turbulent burning velocities for a range of methane-air and propane-air mixtures at 100 kPa and 300 K. The mixtures had equivalence ratios varying from 0.55 to 1.4 for methane and 0.7 to 1.3 for propane, corresponding to positive values of Ma_{sr} varying between approximately 1 and 6. The turbulent burning velocities of these mixtures were correlated with the quantities K, (KLe) or (KMa_{sr}). The authors demonstrated that the correlations progressively improved with improving allowances for thermo–diffusive effects, whereas correlating the turbulent burning velocity with (KMa_{sr}) gave the best result.

Based on a considerable amount of experimental data, Bradley et al. (2011b) and Bradley et al. (2013) published updated correlations on the form of Equation (4.38),

where α and β were explicitly expressed in terms of Ma_{sr} according to

$$u_t = \alpha\, u_k'\, K^{-\beta} \, , \tag{4.42}$$

$$\alpha = 0.023\,(30 - Ma_{sr}) \text{ and } \beta = 0.0103\,(Ma_{sr} - 30) \text{ if } Ma_{sr} > 0 \, , \tag{4.43}$$

$$\alpha = 0.085\,(7 - Ma_{sr}) \text{ and } \beta = -0.0075\,(Ma_{sr} + 30) \text{ if } Ma_{sr} < 0 \, , \tag{4.44}$$

setting C_k to 0.25 in the expression for K (cf. Equation (4.39)). The correlations (4.42)-(4.44) were based on data from a fan-stirred spherical bomb using the implosion technique described by Bradley et al. (2011b). Data for mixtures with methane, hydrogen, 90 % methane - 10 % hydrogen, toluene, *i*-octane with air at a range of equivalence ratios and pressures from 1-35 bar, resulting in Ma_{sr} ranging from -23 to 5, were correlated to give equations (4.42)-(4.44). Curvature effects were neglected in Equation (4.42), as flame stretch due to aerodynamic strain can be assumed to dominate in turbulent flames. Hence, α and β in Equation (4.42) are functions of the strain rate Markstein number Ma_{sr} alone.

Figure 4.2 shows strain rate Markstein numbers Ma_{sr} for methane-air (Bradley et al., 1996), propane-air (Bradley et al., 1998a) and hydrogen-air (Bradley et al., 2007), for a range of equivalence ratios and different pressure levels. An alternative set of Ma from Taylor (1991) is also plotted in Figure 4.2 (right). Figure 4.2 shows that fuel-rich propane-air mixtures ($\phi > 1.4$) and fuel-lean hydrogen-air mixtures ($\phi < 0.6$) are characterised by negative values of Ma_{sr} at atmospheric pressure levels. Furthermore, the figure shows that Ma_{sr} may vary significantly with pressure.
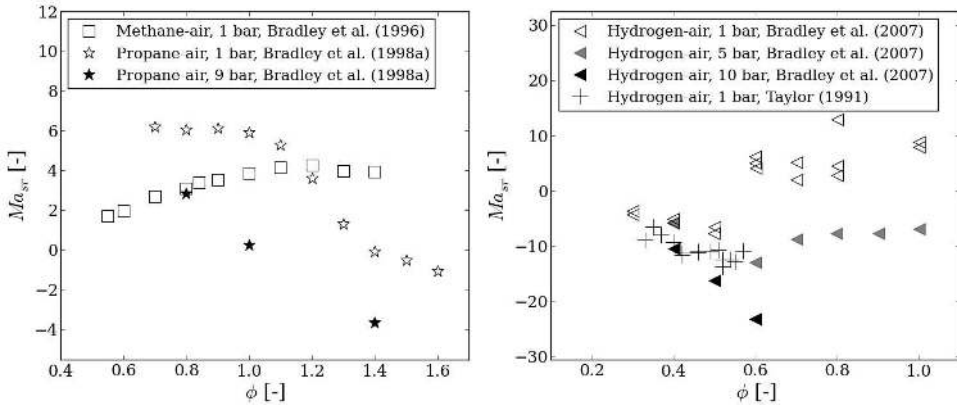
Figure 4.2: Markstein numbers for methane-air and propane-air at $T = 300$ K (Bradley et al., 1996, 1998a) (left) and hydrogen-air at $T = 365$ K (Bradley et al., 2007) and $T = 300$ K (Taylor, 1991) (right).

Overall, Equation (4.42) constitutes a more general correlation than Equation (4.38) (where the values for α and β are fixed), as it accounts for changes to the physico-chemical properties of the mixture e.g. with variations in fuel type and equivalence ratio. Perturbations in the values of Ma_{sr} in Equation (4.42) effectively change how u_t responds to variations in the turbulence variables, u' and ℓ_I, the laminar burning velocity u_l, and the kinematic viscosity ν. The dependence of u_t on u' is generally more pronounced when applying the formulation by Bradley et al. (2013) rather than the

correlation by Bray (1990), and this behaviour agrees better with trends reported by the general combustion literature (Dahoe et al., 2013; Lipatnikov and Chomiak, 2002; Skjold et al., 2013a).

4.6 Modelling Markstein number effects

Figure 4.3 illustrates how the turbulent burning velocity predicted by Equation (4.38) (currently used in standard releases of FLACS) and the Ma-dependent correlation in Equation (4.42) varies with the ratio u'/u_l and the integral length scale of turbulence ℓ_I, for different values of Ma_{sr}. Hydrogen-air mixtures with equivalence ratios ϕ of 0.5, 0.7 and 1.0, i.e. $Ma_{sr} \approx -10, 5$ and 9 at atmospheric pressure, are used to visualise the differences in combustion rates with varying values of Ma_{sr}.

Figure 4.3a shows that the burning velocity correlation by Bray (1990) (green surface) results in higher combustion rates than the correlation by Bradley et al. (2013) (red surface) for high values of u' and ℓ_I (i.e. u'/u_l approaching 40 and ℓ_I approaching 1), for $Ma_{sr} \approx 9$. The opposite trend is seen for high values of u' and ℓ_I in Figure 4.3b, where u_t is visualised for a hydrogen-air mixture with $\phi = 0.7$ and $Ma_{sr} \approx 5$. Overall, the burning velocities from the two correlations are comparable for a wide range of turbulence levels for this particular mixture.

Figure 4.4 compares the turbulent burning velocities predicted by Bray (1990) (solid lines) with that derived from Bradley et al. (2013) (dashed lines) as a function of u', for a fixed ℓ_I of 0.001 m (left) and 0.1 m (right). When $\ell_I = 0.001$ m (cf. Figure 4.4 (left)), the correlation by Bray (1990) predicts higher burning velocities than the correlation by Bradley et al. (2013) for $u' < 15$ m/s and $Ma_{sr} \approx 9$. Meanwhile, Figure 4.4 (right) shows that the correlation by Bray (1990) consistently gives higher burning rates than the correlation by Bradley et al. (2013) when $\ell_I = 0.1$ m and $Ma_{sr} \approx 9$. Figure 4.4 (left) shows that for a fixed ℓ_I of 0.001 m and $Ma_{sr} \approx 5$, Bray (1990) predicts higher burning rates for $u' < 3$ m/s, while for a fixed ℓ_I of 0.1 m in Figure 4.4 (right), Bray (1990) gives higher burning velocities for $u' < 12$ m/s.

For $Ma_{sr} \approx -10$, Figure 4.3c shows that the burning rates in the flamelets predicted by the correlation in Equation (4.42) generally are enhanced compared to the correlation in Equation (4.38), in particular for high values of ℓ_I and u'. Hence, when modelling gas explosions in densely congested regions, Equation (4.42) will likely result in significantly higher overpressures than Equation (4.38) for the mixture plotted in Figure 4.3c. Figure 4.4 shows the same trend for both $\ell_I = 0.001$ m (left) and $\ell_I = 0.1$ m (right). This is consistent with observations made e.g. by Bradley et al. (2005): mixtures characterised by negative Markstein numbers exhibit higher burning rates when exposed to positive stretch rates, are less likely to quench at high stretch rates, and are more prone to develop flame instabilities than mixtures with positive Markstein numbers.

4.6.1 Modelling approach in FLACS

In standard releases of FLACS (Gexcon, 2016), a Lewis number dependent correction is applied directly to the laminar burning velocity of hydrogen-air mixtures to account for thermal–diffusive effects in both the quasi-laminar and turbulent regime of flame
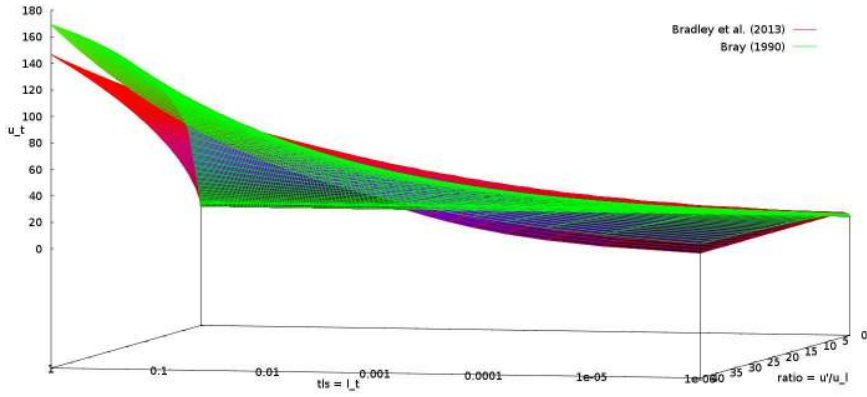
(a) $\phi = 1.0$, $Ma_{sr} \approx 9$, $u_l \approx 2.13$ m/s.
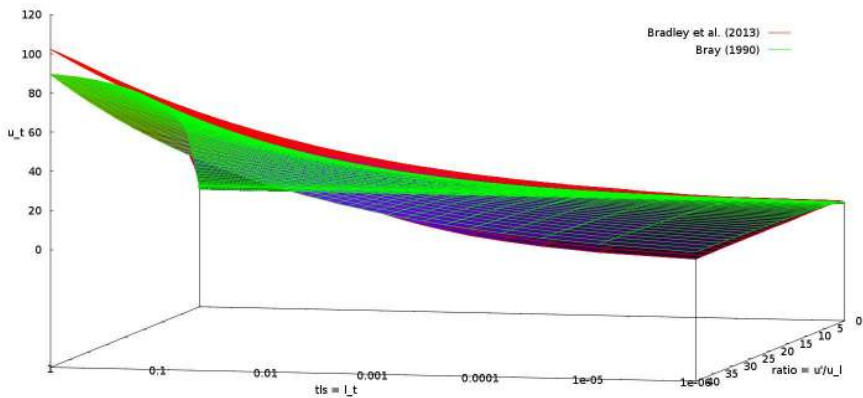
(b) $\phi = 0.7$, $Ma_{sr} \approx 5$, $u_l \approx 1.25$ m/s.
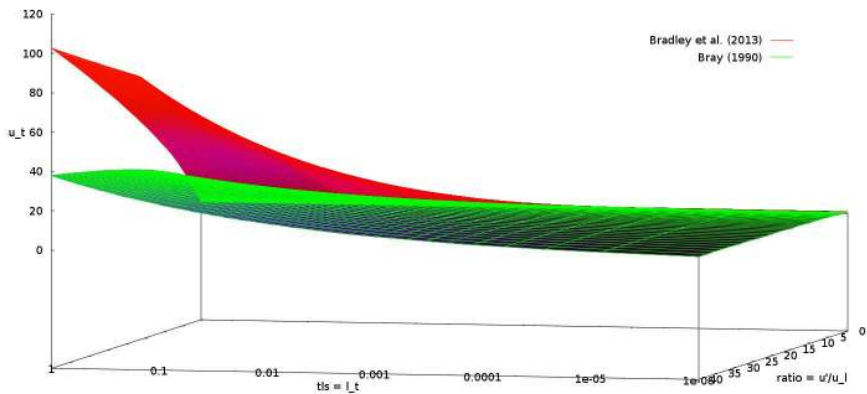
(c) $\phi = 0.5$, $Ma_{sr} \approx -10$, $u_l \approx 0.61$ m/s.

Figure 4.3: Burning velocities from Bray (1990) and Bradley et al. (2013) as a function of u'/u_l and ℓ_I (axis denoted "tls=l_t") for hydrogen-air mixtures with different values of the equivalence ratio ϕ.
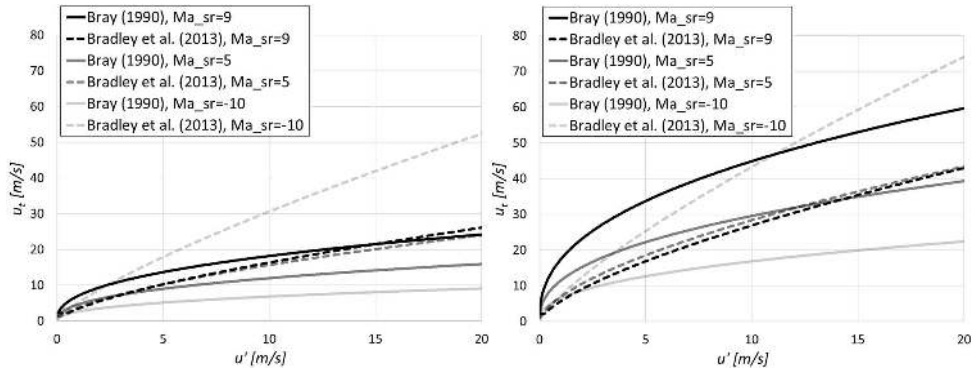
Figure 4.4: Burning velocities from Bray (1990) and Bradley et al. (2013) as a function of u' for hydrogen-air mixtures with different values of Ma_{sr} and u_l, for $\ell_I = 0.001$ m (left) and $\ell_I = 0.1$ m (right).

propagation (Middha, 2010). Figure 4.5 shows the corrected laminar burning velocity for hydrogen-air mixtures (grey line) together with the uncorrected values of u_l from FLACS (black line). The uncorrected laminar burning velocity agrees well with the values for u_l presented by Taylor (1991) (white dots). The correction enhances u_l for $\phi < 1.0$, while reducing the burning velocity for $\phi > 1.0$, to account for thermal–diffusive effects with varying Lewis or Markstein numbers. The same correction is applied to hydrogen-air mixtures in all versions of standard FLACS that are used in the present thesis. However, Lewis or Markstein number effects may have a different influence on the burning rate in different combustion regimes. For example, adjusting the laminar burning velocity in the correlation (4.38) with fixed values for α and β will not change the dependence of the turbulent burning velocity on the turbulence parameters u' and ℓ_I. Standard versions of FLACS do not apply Lewis number-dependent corrections for the laminar burning velocity of any other fuel-air mixture than hydrogen, although the variations in Ma_{sr} with changes in ϕ shown in Figure 4.2 suggest that these effects are appreciable also for propane-air explosions.

Figure 4.6 shows the turbulent burning velocities predicted by equations (4.38) and (4.42) for propane-air mixtures with ϕ of 1.0 and 1.4, corresponding to Ma_{sr} of about 6 and -0.1, respectively. For the two mixtures plotted in Figure 4.6, the same overall trends are observed: the correlation by Bradley et al. (2013) predicts somewhat higher burning velocities than the correlation by Bray (1990) for a wide range of turbulence levels. This behaviour is particularly pronounced for high values of ℓ_I and u'. Furthermore, the enhancement of the combustion rates for the mixture with $\phi = 1.4$ as predicted by Equation (4.42), relative to that predicted by Equation (4.38) (cf. Figure 4.6b), is more marked than for the mixture with $\phi = 1.0$ (cf. Figure 4.6a).

Figure 4.7 compares the turbulent burning velocities predicted by Bray (1990) (solid lines) with that derived from Bradley et al. (2013) (dashed lines) as a function of u', for a fixed ℓ_I of 0.001 m (left) and 0.1 m (right). For $Ma_{sr} = -0.1$, Figure 4.7 confirms that the correlation by Bradley et al. (2013) gives higher combustion rates for both values of ℓ_I. Figure 4.7 (left) shows that the correlation by Bray (1990) gives a slightly higher burning velocity than the correlation by Bradley et al. (2013) for $u' < 1$ m/s when
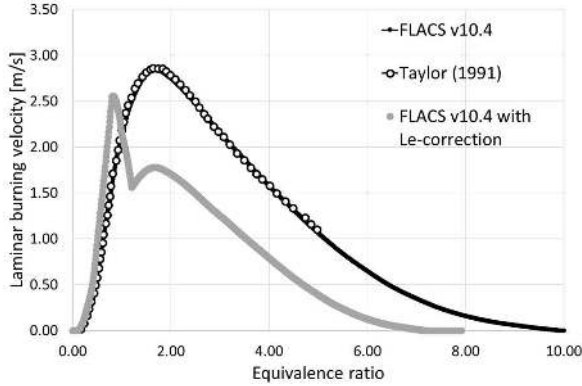
Figure 4.5: Laminar burning velocities for hydrogen-air mixtures from Taylor (1991) and the standard release FLACS v10.4, both the uncorrected data set (labelled "FLACS v10.4") and the Lewis number corrected data, used in the combustion model (labelled "FLACS v10.4 with Le-correction").

$\ell_I = 0.001$ m and $Ma_{sr} = 6$. The same trend is seen for $u' < 4$ m/s when $\ell_I = 0.1$ m and $Ma_{sr} = 6$ (cf. Figure 4.7 (right)).

Paper 2 of the present thesis describes an experimental campaign designed to provide validation data for a Markstein number-dependent burning velocity model. Further experimental work is needed to support the development of improved sub-grid models for non-stoichiometric mixtures. The objective of the campaign in Paper 2 was to investigate flame acceleration in regimes with both low and high stretch rates, for two different spatial scales. Consequently, experiments were performed in two vented channels of dimensions 1.5 m × 0.3 m × 0.3 m (small-scale) and 6.0 m × 1.2 m × 1.2 m (medium-scale). Experiments were performed in empty versions of both chambers to study flame propagation in the quasi-laminar regime of flame propagation. Five rectangular obstructions (cf. Appendix B and Paper 2) were then added to each explosion chamber to investigate the effect of varying the mixture concentration for explosion tests involving turbulent flame propagation, i.e. producing higher flame speeds and overpressures. These two setups (empty and with five rectangular obstructions inserted) were identical for both the small-scale and the medium-scale chamber, so as to study the scaling effect on explosion overpressures for different regimes of flame propagation. Finally, to investigate Markstein number effects for explosions with even higher flame acceleration rates, 4 grids, each consisting of 6 circular obstructions, were inserted in the medium-scale channel (cf. Figure 1.4). The variation in the Markstein number of the flammable mixture was achieved by changing the equivalence ratio of the propane-air mixture between 0.7 and 1.7. According to Figure 4.2, this corresponds to a variation in Ma_{sr} from ≈ 6 to ≈ -1. Appendix B includes additional details on the experimental setup.

For Paper 2, the Ma_{sr}-dependent correlation by Bradley et al. (2013) was implemented in a development version of FLACS. The correlations (4.42)-(4.44) are valid for $K > 0.05$, and replaced Equation (4.38) with α and β as defined by Bray (1990). The quench criterion was updated according to the recent setting of C_k to 0.25 in the expression for K (cf. Equation (4.39)). In their experiments, Abdel-Gayed et al. (1987)
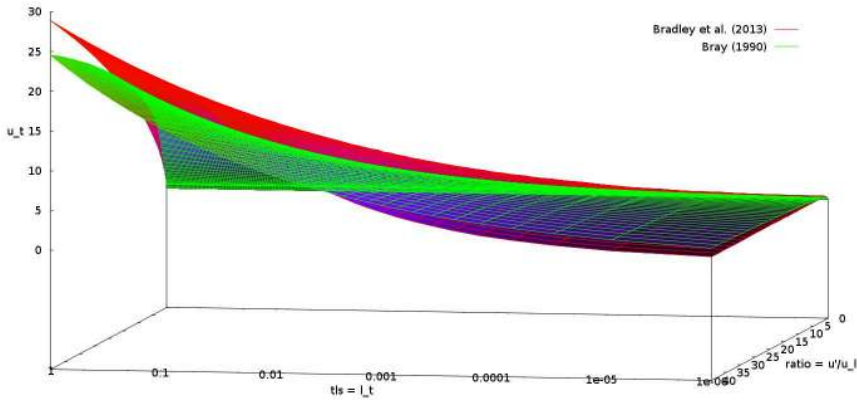
(a) $\phi = 1.0$, $Ma_{sr} \approx 6$, $u_l \approx 0.42$ m/s.
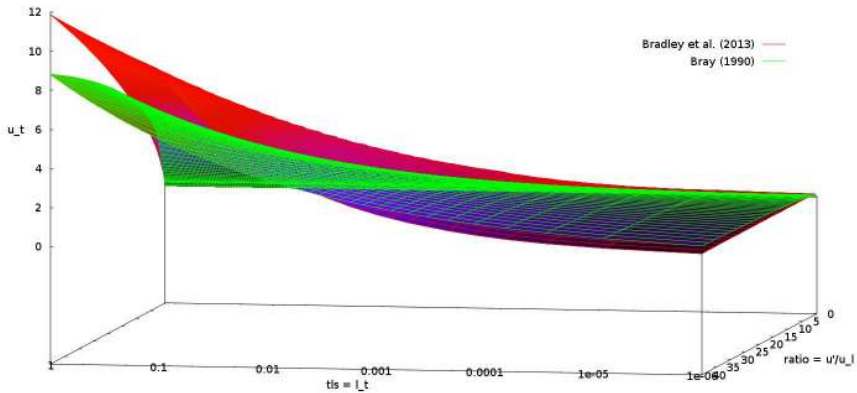
(b) $\phi = 1.4$, $Ma_{sr} \approx -0.1$, $u_l \approx 0.18$ m/s.

Figure 4.6: Burning velocities from Bray (1990) and Bradley et al. (2013) as a function of u'/u_l and ℓ_I (axis denoted "tls=l_t") for propane-air mixtures with different values of the equivalence ratio ϕ.

experienced significant quenching at $KLe = 1.5$, for high Re. Bradley et al. (1992) indicated a quenching limit of $KLe = 6.0$. Findings from direct numerical simulations (Poinsot et al., 1991) suggest that the quenching limit may be located around $K \approx 25$, near the border between the "thin reaction zones" and "distributed reaction zones" regimes of Peters (2013), where the smallest turbulence eddies start to penetrate the reaction zone. Bradley et al. (2013) demonstrated that the critical stretch rate for flame quenching depends significantly on the local Markstein number. In summary, there are considerable uncertainties associated with the use of a quenching limit for turbulent premixed combustion. For the Markstein-number dependent burning velocity model used in Paper 2, the limit for burning velocity increase with u' was set to $K = 1.5$.

Together with the correlation in Equation (4.42), the fractal model from Section 4.4, Equation (4.35), was implemented for the cellular phase of flame propagation, using the
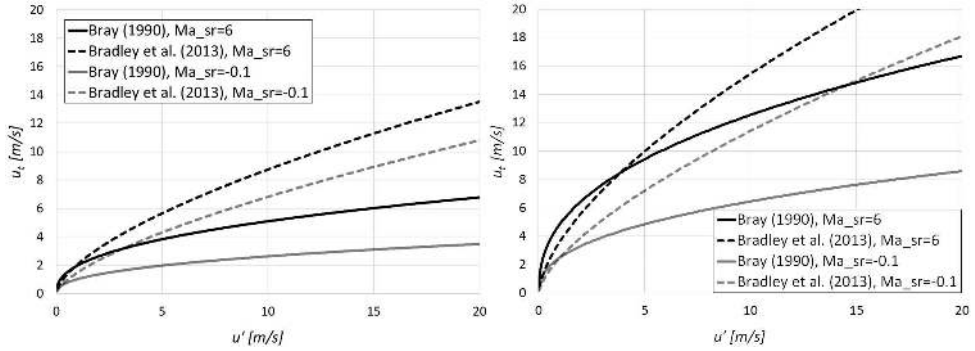
Figure 4.7: Burning velocities from Bray (1990) and Bradley et al. (2013) as a function of u' for propane-air mixtures with different values of Ma_{sr} and u_l, for $\ell_I = 0.001$ m (left) and $\ell_I = 0.1$ m (right).

experimental data presented by Bauwens et al. (2015). The low stretch rate correlation in Equation (3.20) was retained.

Paper 2 discusses validation results from the updated model together with results obtained with the corresponding standard version of FLACS. An overall summary of the results is given here. The maximum overpressures predicted by the standard FLACS release (denoted 'SBV') and the development version of FLACS using the Markstein number-dependent burning velocity model (denoted 'MBV') are plotted in Figure 4.8 together with the corresponding experimental values. Figure 4.8 (left) shows a *scatter plot* of the maximum overpressures. The *parabola plot* in Figure 4.8 (right) visualises the *geometric mean bias* (MG) and *variance* (VG) of the data sets in Figure 4.8 (left), i.e. the tendency of each model version to systematically over- or under-predict the overpressure, and the degree of scatter around a mean value for the model predictions, respectively. MG and VG are defined in Paper 2 and Chapter 6, Section 6.1.3.
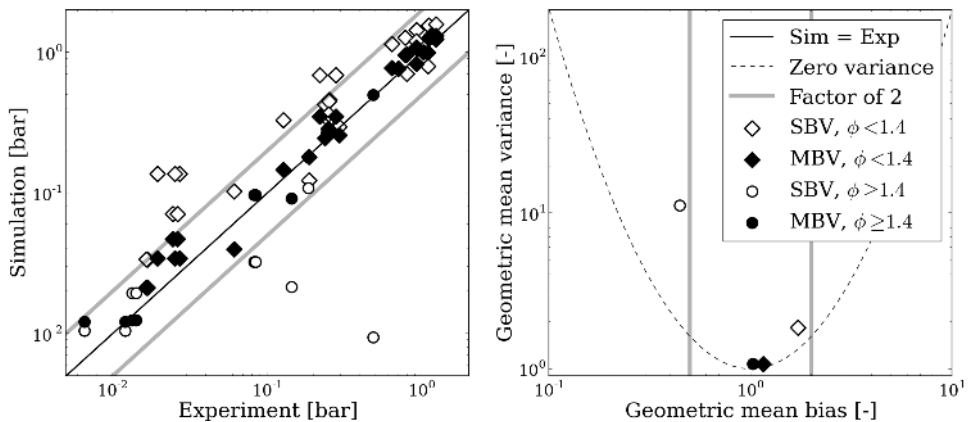
Figure 4.8: Scatter plot (left) and parabola plot (right) of simulated and experimental maximum overpressures from the study in Paper 2. Propane-air mixtures with ϕ varying between 0.7 and 1.7 were used in the experimental campaign. Note that the legend applies to both sub-plots.

Figure 4.8 shows that both models give acceptable predictions of the experimental maximum overpressures for propane-air mixtures with $\phi < 1.4$. For fuel-rich mixtures with $\phi > 1.4$ and $Ma_{sr} < 0$, the standard burning velocity model generally under-predicts the maximum overpressures. However, the Markstein number-dependent burning velocity model gives improved results for these mixtures, consistently predicting overpressures within ± 10 % of the experimental values. In addition to assessing model performance in terms of the maximum overpressure, Paper 2 presents a detailed analysis of the pressure-time curves and flame speeds versus distance from ignition. The analysis shows that the development version of FLACS using the MBV combustion model generally gives a more representative flame speed in the initial phase of flame propagation than that predicted by the standard FLACS release.

Similar to fuel-rich propane-air mixtures, fuel-lean hydrogen-air mixtures (with $\phi < 0.6$) are characterised by negative Markstein numbers at atmospheric pressure. To further validate the updated combustion model, a series of experiments involving fuel-lean hydrogen-air explosions were simulated. The Markstein number-dependent combustion model used in Paper 2 was therefore extended to hydrogen-air mixtures with data from Bauwens et al. (2017a) and (Bradley et al., 2007). The results from this study are presented in Chapter 6, Section 6.1.

In Chapter 6, Section 6.2, the Markstein number-dependent combustion model is used to model the experiments from Paper 1 of the present dissertation. Paper 1 presents a series of large-scale natural gas-air experiments performed in an empty vented enclosure, with two compartments separated by a doorway. A total of 85 experiments were performed in the twin-compartment enclosure, and a selection of 22 experiments were analysed and modelled for Paper 1. These represent a wide range of configurations, resulting in explosion overpressures ranging from 0.04 to 0.46 bar. For the tests considered in Paper 1, both chambers were either half-filled or completely filled with a 10 vol.% natural-gas mixture in air. The ignition point was either located at the centre of the back wall (opposite of the vent opening) or in the centre of the left chamber. Furthermore, the effect on the explosion mechanism of inserting a light-weight, initially closed door in the doorway between the rooms was investigated.

The pressure-time history in these experiments generally displayed two distinct pressure peaks. The first pressure peak was always associated with the removal of one or both of the explosion relief vent panels. The second pressure peak was found to be more complex in origin – its magnitude varying with the vent configuration and degree of filling. Sometimes, the second pressure peak was significantly enhanced by the presence of the interconnecting door.

The vent panels and the door in the experiments were modelled as "pressure relief panels" in FLACS for Paper 1, i.e. as regions with an area porosity varying in time in response to the explosion, according to a designated panel type, weight and failure pressure. The pressure relief panel model used in the FLACS simulations to model the opening and closing of the interconnecting door between the compartments is a highly simplified approach, and will therefore not always give an exact representation when the results are sensitive to how the door opens. This likely was the case for several of the experiments in Paper 1, for which the second pressure peak was under-predicted. Furthermore, the standard version of FLACS used in Paper 1 was found to persistently over-predict the rate of combustion in the very early stages of the explosion, i.e. during the period when the flame propagation is in the quasi-laminar propagation mode. This

fed through to the earlier occurrence of subsequent events.

Paper 1 concludes that an improved representation of the quasi-laminar burning velocity would be necessary to improve model performance for these experiments. Additionally, for the mixtures used in Paper 1, the Markstein-number dependent combustion model gives a higher sensitivity of the burning velocity to the turbulence velocity fluctuation u', which could improve the representation of the second pressure peak. To investigate this, the Markstein number-dependent combustion model proposed by Paper 2 was extended to natural gas-air mixtures for the modelling work in Chapter 6. The model uses data from Bradley et al. (1996) for methane-air mixtures and data from Tseng et al. (1993) for ethane-air mixtures. The natural gas mixture was assumed to be composed of methane, ethane and propane only, neglecting the smaller quantities of heavier components in the mixture. A simple, volume-fraction weighted mixing rule was implemented to obtain the necessary parameters for both the quasi-laminar and turbulent burning velocity models. The values for Ma_{sr} resulting from this simplified approach were found to be reasonable when compared to both the experimental and simulated data presented by Johnson and Cleaver (2002).

Finally, Paper 1 proposes that the tests where the second pressure peak is sensitive to the presence of the interconnecting door could be better represented in FLACS if a sub-grid model for the Rayleigh–Taylor instability is included. Section 5.4 addresses the modelling of this effect. Selected results from applying the findings of both Paper 2 and Section 5.4 to the experiments in Paper 1, together with an extended discussion, are presented in Chapter 6, Section 6.2.

4.6.2   Uncertainties associated with the Markstein number

The Markstein number is defined as the Markstein length normalised by the flame thickness, $Ma = \mathcal{L}/\delta_l$ (cf. Section 4.3.3). The values of the Markstein length can be determined experimentally by plotting the speed of a spherical flame as a function of the stretch rate, and extrapolating to a stretch rate of zero. Thus, the unstretched laminar burning velocity u_l can be found directly, while the gradient of the flame speed is the Markstein length $\mathcal{L}$. This procedure should preferably be performed before the flame front becomes unstable. After the onset of instability, the method must correct for flame acceleration associated with the cellular regime. However, at higher pressures, the flame front becomes cellular almost from the point of ignition. Consequently, it is more challenging to measure u_l and $\mathcal{L}$ for such conditions (Bradley et al., 2007).

Additional uncertainty is associated with the normalisation of $\mathcal{L}$ with the flame thickness to obtain Ma (Beeckmann et al., 2017). For example, the use of the approximation $\delta_l = \mathcal{D}_{\text{th}}/u_l$, where $\mathcal{D}_{\text{th}}$ is the thermal diffusivity, versus $\delta_l = \nu/u_l$, where ν is the kinematic viscosity, leads to discrepancies. Furthermore, using such simplified approximations for the flame thickness in itself introduces significant uncertainty.

Bradley et al. (2013) estimated error bands of approximately ± 1 on their measured Ma_{sr}. However, the uncertainties associated with using Markstein numbers in burning velocity models are likely more significant. In particular, when comparing and applying values of Ma, it is crucial to know how they have been estimated (Davis et al., 2002). Values for Ma_{sr} determined by the approaches described by Bradley et al. (1996, 1998a, 2007) are not readily available for all fuels; strictly, when using alternative data sets for Ma, the correlations may therefore not be valid. Hence, introducing Markstein

number effects to a model for premixed turbulent combustion can be viewed as a way of representing certain trends (e.g. with varying mixture composition), rather than as an exact quantification of the physicochemical effects.

4.7   Summary

The present chapter presents the theory underpinning the sub-grid models that were implemented in FLACS as part of the present doctoral study. A thorough understanding of the physical mechanisms driving flame acceleration is crucial for performing meaningful sub-grid modelling, in particular for CFD tools that apply a relatively coarse resolution compared to the scales of the governing physical phenomena.

For initially quiescent, spherical flames, several propagation regimes can be observed. In the early stages of flame propagation, the flame is laminar and stable. For highly unstable mixtures this regime may be extremely short-lived, as the flame surface will develop "cracks", and cell formation will commence almost immediately after ignition. At the point where the flame surface becomes fully cellular, the flame front accelerates. The flame surface area and speed continues to grow in the cellular regime. Intrinsic instabilities can be the primary mechanisms of flame acceleration in gas explosions with low degrees of congestion. Furthermore, accurate representation of cellular flame propagation is important for simulating the initial phase of gas explosions. The stability analysis in sections 4.3.2, 4.3.4 and 4.3.5 can be directly related to the observed physical phenomena of intrinsic instabilities. The results from the analysis are therefore highly useful for understanding and developing modelling approaches to represent the quasi-laminar regime of flame propagation.

The physical interpretation of the results by Landau (1944), presented in Section 4.3.2, is that an infinitesimally thin flame surface is unconditionally unstable with respect to small perturbations of all wavelengths. Since the shortest wavelengths have the most significant growth rate from Equation (4.18), the analysis must be extended to take into account the effect of the thermal–diffusive structure of a stretched flame front. The stability analysis in Section 4.3.4 therefore includes thermal–diffusive effects, by introducing the Markstein length (or equivalently, the Markstein number Ma and the laminar flame thickness δ_l) of the flame front to the analysis. This theory explains why short-wavelength perturbations in practice are stabilised (for example in the very initial phase of spherical flame propagation), and why flames with $Ma < 0$ are observed to transition to the cellular regime at an earlier stage than flames with $Ma > 0$. In effect, Ma implicitly accounts for the combined effect of viscosity, thermal conductivity, mass and heat diffusivity (including Lewis number effects) on flame stability (Zeldovich et al., 1985).

Meanwhile, for outwardly propagating spherical flames, the onset of instability occurs significantly later than what the linearised theory for planar flames predicts. For a spherical flame to change its shape due to the hydrodynamic instability, the growth rate of the amplitude of the perturbations needs to be larger than the growth rate of the flame radius itself. The linearised stability analysis for spherical flames presented by Bechtold and Matalon (1987) (cf. Section 4.3.5) explains why the flame surface develops a fractal character in the quasi-laminar regime. This observation is used to derive correlations for the flame acceleration in the cellular regime, presented in Section 4.4.

Furthermore, Section 4.4 argues that all effects from cellular flame structure on the observed flame speed must be modelled in FLACS.

In conclusion, the theory in this chapter infers that introducing a dependency on Ma to the model for u_{ql} (used in the quasi-laminar regime of flame propagation) would constitute an improved representation of intrinsic instabilities in the CFD tool FLACS. Assuming that all effects from intrinsic instabilities occur sub-grid, the fractal model for quasi-laminar flame propagation given by Equation (4.32) was implemented in a development version of FLACS for the present thesis. This model is supported by high-quality experimental data (Bauwens et al., 2015, 2017a,b).

Mixtures characterised by negative Markstein numbers exhibit higher burning rates when exposed to positive stretch rates, are less likely to quench at high stretch rates, and are more prone to develop flame instabilities than mixtures with positive Markstein numbers. Enhanced burning rates are observed for mixtures with negative Markstein numbers in the turbulent regime of flame propagation. For modelling the turbulent burning velocity, Section 4.5 proposes that a stretch-based model is most appropriate for the applications of FLACS. Bradley et al. (2005) presented turbulent burning velocities for a range of methane-air and propane-air mixtures with varying equivalence ratios. The turbulent burning velocities of these mixtures were correlated with the quantities K, (KLe) or (KMa_{sr}). The authors demonstrated that the correlations progressively improved with improving allowances for thermo–diffusive effects, whereas correlating the turbulent burning velocity with (KMa_{sr}) gave the best result.

Based on a considerable amount of experimental data, Bradley et al. (2011b) and Bradley et al. (2013) published updated stretch-rate based correlations on the form of Equation (4.38), where α and β were explicitly expressed in terms of Ma_{sr}. Overall, the correlation by Bradley et al. (2013), Equation (4.42), constitutes a more general correlation than Equation (4.38) (implemented e.g. in the standard release FLACS v10.5, where the values for α and β are fixed), as it accounts for changes to the physicochemical properties of the mixture e.g. with variations in fuel type and equivalence ratio. This model was implemented in FLACS for the modelling work of the present thesis.

Due to uncertainties both associated with measuring and applying Ma_{sr}, introducing Markstein number effects to a model for premixed turbulent combustion can be viewed as a way of representing certain trends (e.g. with varying mixture composition), rather than as an exact quantification of the physicochemical effects. The Markstein number-dependent combustion model was validated using the experiments presented in Paper 2, Paper 1 and Chapter 6.

Chapter 5

Representing geometry-induced flame instabilities and turbulence production from vegetation

The present chapter expands on instability effects that are relevant for scenarios where the flow induced by flame acceleration interacts with geometry, such as partial confinement and obstacles. Particular emphasis is put on the Bénard–von Kármán (BVK) instability, occurring in the wake of bluff-bodies, and the Rayleigh–Taylor (RT) instability, which is triggered when a flame front accelerates over an obstacle or through a vent opening. For completeness, Kelvin–Helmholtz (KH) and acoustic instability effects are also addressed. Finally, the chapter discusses how flexible obstructions in the form of vegetation affect the turbulence production and flame acceleration in gas explosions, and how these effects can be modelled.

In summary, this chapter elaborates on the findings of Paper 3 and Paper 4, together with additional key mechanisms, to give a comprehensive overview of geometry-induced instability effects relevant for industrial-scale explosions. The topics listed above address both aspects of the research question *"how can the sub-grid representation of flame acceleration mechanisms due to instability effects and flow past obstructed regions be improved in a CFD tool used for consequence assessment of gas explosions?"*.

Although geometry-induced instabilities (cf. Section 4.1) constitute powerful flame acceleration mechanisms in gas explosions, previous studies of their representation in the CFD tool FLACS have been limited. For example, the BVK instability causes vortex shedding in bluff-body wakes for Reynolds numbers exceeding a certain value. Vortex shedding produces energetic, coherent structures that cannot be considered part of the broadband range of disturbances characterising turbulent flow (Lieuwen, 2012). It is clear that these structures will increase the flame surface area and thus contribute to the flame acceleration downstream of obstacles (Arntzen, 1998; Kong, 1996; Kong and Sand, 1996). However, data relevant for transient, explosion driven flow past different types of bluff-bodies appear to be extremely scarce. In order to develop improved models for the sub-grid representation of flame folding due to the BVK instability, more knowledge of its significance in industrial-scale gas explosions is needed.

Consequently, for Paper 3, an experimental campaign was performed to investigate the contribution of vortex shedding to the generation of overpressure in gas explosions

with a single obstacle inserted. Vortex shedding was observed in the baseline experiments, and then suppressed by two simple passive flow control methods. The most effective control method configuration in the experimental campaign reduced the maximum explosion overpressures by approximately 32 %. The results from Paper 3 can be used as input to sub-grid models for the generation of flame surface area downstream of obstructions in any PDR model system. This is discussed in sections 5.1 and 5.3.3. Moreover, the results trigger the question of whether suppression of vortex shedding could be used as an explosion mitigation method. To address this question, additional experimental work building on Paper 3 would be required, cf. Section 5.3.4.

In the experimental campaign performed for Paper 4, branches from different types of trees were inserted into a vented channel during a series of gas explosions. Thus, the geometric configuration in this campaign was significantly more complex than the configurations investigated in papers 1-3. In addition, the experiments in Paper 4 involved two-way fluid-structure interactions due to the presence of flexible obstructions. The investigation in Paper 4 was motivated by a need for a meaningful approach to represent the effect of vegetation on gas explosions in CFD tools based on the PDR concept. The need was identified in the aftermath of a severe explosion incident that occurred at the fuel storage depot Buncefield, UK, in 2005 (BMIIB, 2008), where the presence of vegetation was assumed to have caused flame acceleration and significant overpressures. A two-stage research project was initiated to investigate the explosion mechanism that led to the overpressure damage observed at Buncefield (SCI, 2009, 2014). The project involved both medium-and large scale experimental campaigns, involving gas explosions in extensive regions with vegetation, as well as modelling work.

Consequently, the experimental study in Paper 4 was conducted to (i) investigate whether the flexible response of tree branches to the flow would significantly reduce the overpressures, (ii) investigate to which degree the presence of foliage contributes to flame acceleration, and (iii) to support the development of a general sub-grid modelling approach to account for vegetation in industrial-scale gas explosions. The paper thus addresses two separate influences on flame propagation in obstructed regions that must be represented sub-grid by CFD tools based on the PDR concept. Section 5.6 discusses the findings of Paper 4.

5.1   Modelling flame surface area increase due to sub-grid obstacles

This section presents approaches to account for the generation of sub-grid flame surface area due to various physical phenomena in CFD models. The modelling approaches are referred to throughout the chapter.

5.1.1   The combustion model by Weller and co-workers

The combustion model by Weller et al. (1998a) has been used in several CFD tools, using both the RANS and LES framework – see e.g (Bauwens and Dorofeev, 2011) and (Puttock et al., 2014). This model is referred to in sections 5.1.2 and 5.4; a short presentation of the Weller model is therefore included here.

Weller et al. (1998a) presented a combustion model for use with LES that solves a transport equation for the fuel mass fraction Y_F,

$$\frac{\partial \overline{\rho} \widetilde{Y}_F}{\partial t} + \frac{\partial}{\partial x_j} \left(\overline{\rho} \widetilde{Y}_F \widetilde{u}_j \right) - \frac{\partial}{\partial x_j} \left(\overline{\rho} \mathcal{D} \frac{\partial \widetilde{Y}_F}{\partial x_j} \right) = -\overline{\rho_u} u_l \Xi_T \left| \frac{\partial \widetilde{Y}_F}{\partial x_j} \right| ,$$ (5.1)

where Ξ_T is the *sub-grid flame wrinkling factor*, $\overline{()}$ denotes a filtered variable, and $\widetilde{()}$ denotes a density-weighted filtered variable. The flame wrinkling factor Ξ_T represents the effect of turbulence on the burning velocity, and can be interpreted as the ratio between the turbulent and the laminar burning velocity. Weller et al. (1998a) suggested a separate transport equation for Ξ_T,

$$\frac{\partial \Xi_T}{\partial t} + u_j^s \frac{\partial \Xi_T}{\partial x_j} = G \Xi_T - R(\Xi_T - 1) + (\tau_s - \tau_t) \Xi_T ,$$ (5.2)

where u_j^s is the surface-filtered velocity of the flame, τ_s and τ_t are resolved strain rates, and

$$G = R \frac{2 \left(1 - \widetilde{Y}_F \right) (\Xi_{T,eq} - 1)}{1 + 2 \left(1 - \widetilde{Y}_F \right) (\Xi_{T,eq} - 1)} , \quad R = \frac{0.28}{t_\eta} \frac{\Xi_{T,eq}}{(\Xi_{T,eq} - 1)} .$$ (5.3)

In Equation (5.3), t_η is the Kolmogorov timescale, and $\Xi_{T,eq}$ is the equilibrium Ξ_T, given by a turbulent burning velocity correlation. Weller et al. (1998a) investigated the effect of replacing Equation (5.2) with the equilibrium expression, $\Xi_{T,eq}$. This simplified approach corresponds to the method currently used in FLACS (Gexcon, 2016) to account for the effect of turbulence on the flame speed, cf. Section 3.2.

Bauwens and Dorofeev (2011) extended the Weller model by introducing separate flame wrinkling factors accounting for the RT instability, Ξ_{RT}, and the LD instability, Ξ_{LD}. In addition, they introduced a separate transport equation for Ξ_{RT}. The contributions from Ξ_{RT} and Ξ_{LD} were multiplied with Ξ_T from Equation (5.2) to obtain a 'final' flame wrinkling factor Ξ, replacing Ξ_T in Equation (5.1).

Puttock et al. (2014) also adopted the Weller model for their PDR solver, and included a separate transport equation for flame surface area generation due to sub-grid obstacles. The authors argued that the flame surface area produced by sub-grid obstacles should be transported separately from that accounting for turbulence effects, since sub-grid obstacles produce flame surface area on different scales from those of turbulence, and exhibit different decay characteristics. Hence, they proposed to use a transport equation on the general form of Equation (5.2),

$$\frac{D \widetilde{\Xi}_S}{Dt} = G_S \Xi_S - R_S (\Xi_S - 1) ,$$ (5.4)

where Ξ_S is the flame wrinkling factor accounting for sub-grid obstacles, and G_S and R_S are the generation and the removal rates of Ξ_S, respectively. Puttock et al. (2014) expressed the generation of flame surface area G_S as

$$G_S = R_S \left(\frac{\Xi_{S,eq} - 1}{\Xi_{S,eq}} \right) ,$$ (5.5)

$$\Xi_{S,eq} = 1 + \max\left(C_1\sqrt{b_r}, \min\left(C_2\frac{|\mathbf{u}|}{u'}\sqrt{b_r}, C_3\right)\right) \times \min(n_r, 1) \,, \qquad (5.6)$$

where C_1, C_2 and C_3 are constants, b_r is the blockage ration in the direction of the flow, and n_r is the number of rows of obstacles in the direction of the flow.

5.1.2   Modelling approach in FLACS

In FLACS, unresolved geometry influences the rate of combustion through the modelled turbulence parameters that are used by the burning velocity model. The production term in the conservation equation for the turbulence kinetic energy, k, explicitly accounts for the turbulence produced by sub-grid objects in the source term P_k, cf. Equation (2.32). However, the presence of an object will contribute to enhanced flame surface area and higher flame speeds not only through increased turbulence production. The flame front will fold itself around the obstacle, generating additional flame surface area on the scale of the obstacle dimension. For sub-grid objects, this effect is not resolved, and must be modelled.

Arntzen (1998) argued that the increase in flame surface area $\left(\Delta A_f / A_f\right)$ from sub-grid obstacles can be represented by a factor Ξ_S, defined as

$$\Xi_S = 1 + \frac{\Delta A_f}{A_f} = 1 + C_{fl}\sqrt{U_c}\,\phi_i\,\mathcal{C}_i \,, \qquad (5.7)$$

where U_c is the downstream flow velocity normalised by the speed of sound, ϕ_i is a direction vector, and $\mathcal{C}_i$ denotes the total surface area of the 'ending walls' of the sub-grid obstructions for flow in the ith direction. $\mathcal{C}_i$ is only defined for objects with one or more ending walls in the present control volume. In Equation (5.7), C_{fl} is a model parameter, determined by validation against experiments. Equation (5.7) is similar to the equilibrium expression proposed by Puttock et al. (2014), cf. Equation (5.6).

The formulation in Equation (5.7) is based on the assumption that the flame surface area increase from the flame front folding around an obstacle is proportional to the size of the obstacle and the ratio of the downstream flow velocity to the turbulent burning velocity, U/u_t. A higher flow velocity relative to the burning velocity means that the flame surface structures from the interaction with the obstacle is transported further downstream before the wake is fully burnt. The concept can be visualised by considering an idealised channel where one end wall is removed, and study the two cases with (a) ignition at the closed wall of the channel (Figure 5.1a) and (b) ignition close to vent opening (Figure 5.1b). Furthermore, Arntzen (1998) approximated u_t by $C\sqrt{u_l U}$, where C is a constant, resulting in the dependence of Ξ_S on the normalised velocity $\sqrt{U_c}$ in Equation (5.7).

In FLACS, flame wrinkling due to sub-grid obstacles is taken into account by multiplying the resulting burning velocity from the burning velocity model, s_{bvm}, with the flame wrinkling factor Ξ_S from Equation (5.7), to give the final input burning velocity s to the flame model (cf. Section 3.2.1), i.e.

$$s = s_{bvm}\Xi_S \,. \qquad (5.8)$$

The flame surface area contribution from sub-grid obstacles is therefore computed and taken into account at every time step for each control volume where combustion takes place.

(a) Ignition at the closed end.


(b) Ignition at the open end.
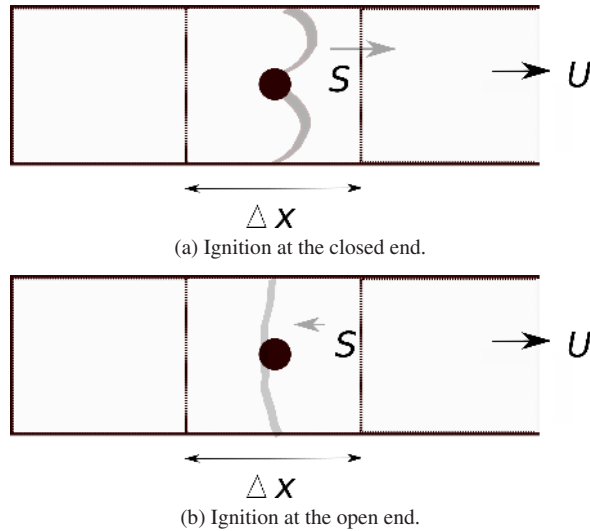
Figure 5.1: Idealised channel with the right end wall removed.

Equation (5.8) can in principle be extended with separate contributions accounting for different unresolved effects. Overall, using equilibrium expressions is a simplified and computationally more efficient alternative to solving separate transport equations for flame surface area generated by various physical phenomena.

5.2 The Kelvin–Helmholtz (KH) instability

Coherent vortical structures generated by fluid flow instabilities promote flame acceleration in gas explosions by enhancing the mixing rate between reactants and combustion products. Such coherent structures, frequently superimposed on broadband, fine-scale turbulence and acoustic disturbances, arise because the base flow configuration is unstable.

The Kelvin–Helmholtz (KH) or shear layer instability, and the Bénard–von Kármán (BVK) instability can be triggered by fluid shear or obstructions in the flow. Indeed, the KH instability will be present in bluff-body wakes together with the BVK instability for a wide range of Reynolds numbers and geometric configurations, also in gas explosion-driven flows (Prasad and Williamson, 1997). In the following section, the KH instability is studied analytically. The effect of the BVK instability on flame acceleration downstream of a bluff-body obstruction is investigated in Section 5.3.

5.2.1 Stability of a shear layer

Shear layers, or *mixing layers*, are regions where two fluid streams of different velocities or densities result in enhanced mixing in the transverse direction relative to the flow (Lieuwen, 2012). The stability analysis of a spatial mixing layer can be performed by considering a simplified shear layer with a base state on the form of a piecewise linear

velocity profile of thickness δ, given by

$$u_1^0(x_2) = \begin{cases} u_a^0 & , x_2 > \delta/2 \\ (u_a^0 + u_b^0)/2 + (u_a^0 - u_b^0)x_2/\delta & , |x_2| \leq \delta/2 \\ u_b^0 & , x_2 < -\delta/2 \end{cases} . \quad (5.9)$$

Figure 5.2 illustrates the simplified flow configuration in Equation (5.9).
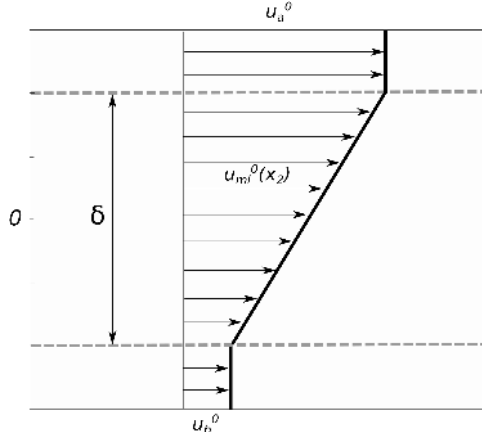
Figure 5.2: Velocity profile for the shear layer stability analysis. Figure reproduced from (Lieuwen, 2012).

Finding general solutions for the first order perturbations of the streamfunction Ψ^1 and the pressure p^1, and matching the conditions for the streamfunction and pressure at the interfaces between the different regions, i.e. at $x_2 = -\delta/2$ and $x_2 = \delta/2$, leads to the dispersion relation

$$D(k_w, \omega) = (k_w\delta)^2 \left(\frac{c_{ph}}{u_{av}} - 1\right)^2 - (\Delta u_1/2u_{av})^2 \left[(k_w\delta - 1)^2 - e^{-2k_w\delta}\right] = 0 . \quad (5.10)$$

In Equation (5.10), $u_{av} = (u_a^0 + u_b^0)/2$, $\Delta u_1 = u_a^0 - u_b^0$ and $c_{ph} = \omega/k_w$ is the complex phase speed. From Equation (5.10), a range of wave numbers k_w can be found for which the complex growth rate ω_i is positive. For these values of k_w, the first order disturbances grow in time. Hence, the flow in Figure 5.2 is linearly unstable.

Furthermore, it is possible to determine whether the flow is convectively or absolutely unstable with the method presented in Section 4.2. Assuming that $u_a^0 > u_b^0$, then if $\Delta u_1/2u_{av} = 1$ (or $u_b^0 = 0$), the complex growth rate $\omega_{i,0}$ is zero. Therefore, following the theory in Section 4.2, the shear layer is absolutely unstable when there is backflow, i.e. when $u_b^0 < 0$. When both layers are flowing in the same direction, or $u_b^0 > 0$, the shear layer is convectively unstable. Analysing continuous shear layer profiles gives similar results as for the simplified example in Figure 5.2 (Lieuwen, 2012).

5.2.2 Modelling the effect of the KH instability

The disturbances on the interface between two fluid streams of different velocity or density can first be observed as small-scale undulations. However, as the disturbances

grow, they cause the interface to 'roll up', pulling fluid from one side of the layer to the other side. The initially two-dimensional disturbances develop secondary instabilities as they are convected downstream, and the thickness of the shear layer increases.

Figure 5.3, taken from the experimental campaign in Paper 3, shows regions of enhanced combustion in the separated shear layers downstream of a circular cylinder inserted in a propane-air gas explosion. In the experiments described in Paper 3, the KH instability most likely contributed to the observed flame acceleration. Meanwhile, quantifying the isolated effect of KH instabilities in the separated shear layers is challenging, as these are not straightforward to suppress without removing the obstruction from the experimental setup.

The KH instability also occurs in free shear flows. For high Reynolds number flows, coherent structures are present together with the small-scale, broadband disturbances associated with turbulence. The turbulence can be considered as an added eddy-viscosity, contributing to the dissipation of the larger-scale structures and increasing the mixing rate in the shear layer (Gaster et al., 1985).
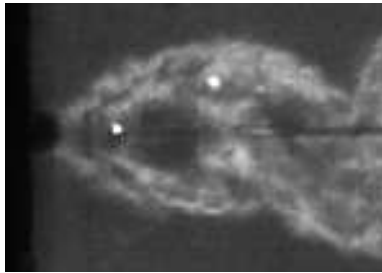

Figure 5.3: Regions of enhanced combustion are visualised by increased luminosity in the shear layers downstream of a bluff-body. The picture is taken from the experimental campaign in Paper 3.

Naturally, the KH instability is not resolved for objects that are represented sub-grid in models based on the PDR concept. Moreover, the spatial resolution of 0.05 - 1 m, which is typically used for simulating industrial-scale explosions with FLACS, will be insufficient for resolving the instability downstream of most on-grid objects. However, the model for production of turbulence kinetic energy in Equation (2.32) includes turbulence production from sub-grid objects. The sub-grid model parameters associated with the k-equation in FLACS, Equation (2.26), have been manually optimised against a number of gas explosion experiments to yield reasonable results for a wide range of configurations (Skjold et al., 2013b). The model accounts for an estimated total turbulence production from sub-grid objects, and may therefore implicitly account for KH instability effects on the flame acceleration as well. Similarly, the model for flame surface area production downstream of sub-grid obstacles, cf. Section 5.1.2, may also effectively include the influence of the KH instability in FLACS through manually optimised parameters.

Explicit modelling of the effect of the KH instability on flame acceleration in industrial-scale explosions is not considered further in the present thesis. Assessing the relative contribution of the instability, and how it is presently represented, would require significant additional efforts that are not feasible to undertake as part of the

present doctoral study.

5.3   The Bénard–von Kármán (BVK) instability

Paper 3 of the present thesis investigates an additional source of flame surface area from flow past bluff-bodies, produced by a process separate from that of turbulence generation. For a certain range of Reynolds numbers, the Bénard–von Kármán (BVK) instability results in *vortex shedding*. Vortex shedding occurs both in non-reacting and reacting bluff-body wake flows (Williamson, 1996; Zdravkovich, 1997, 2003). The instability introduces a strong periodicity in the velocity and pressure measurements immediately downstream of the bluff-body, and is associated with a significant increase in the form drag, enhanced mixing, as well as possible structural vibrations and noise. It is clear that vortex shedding will increase the flame surface area and thus contribute to the flame acceleration downstream of obstacles (Arntzen, 1998; Kong, 1996; Kong and Sand, 1996).

The BVK instability has been extensively studied for non-reacting flow (Roshko, 1993; Williamson, 1996), and in reacting flow for flame holder configurations in various combustor applications (Fureby, 2000; Hertzberg et al., 1991; Lieuwen, 2012). Kong and Sand (1996) and Kong (1996) measured and discussed vortex shedding in transient, explosion driven flow past various bluff-bodies. However, apart from the latter studies, data for scenarios relevant for industrial-scale gas explosions appears to be extremely scarce.

5.3.1   Theory and background

The circular cylinder has been widely studied in the field of fluid mechanics (Roshko, 1993; Williamson, 1996; Zdravkovich, 1997, 2003). For flow across a circular cylinder, the Reynolds number is defined as $Re = UD_{cyl}/\nu$, where U is the upstream flow speed, D_{cyl} is the diameter of the cylinder, and ν is the kinematic viscosity of the fluid. The two-dimensional flow around a circular cylinder can be represented by a thin viscous boundary-layer, surrounded by an external potential flow. Upstream of the highest point of the curved body, where the streamlines converge, the pressure gradient is favourable to the flow, i.e. it points in the opposite direction of the flow. However, downstream of the highest point of the curved body the streamlines diverge, giving rise to an adverse pressure gradient, i.e. a positive pressure gradient with respect to the flow direction. The boundary-layer experiences the same pressure as the external flow. If the adverse pressure gradient is sufficiently strong, the flow near the wall will decelerate faster than the external flow, and eventually reverses its direction leading to boundary-layer separation.

Following flow separation, free shear layers emanate from each side of the bluff-body. At *Re* from approximately $4 - 47$, the separated shear-layers roll up to form two counter-rotating steady laminar vortices behind the circular cylinder. When *Re* exceeds about 47, the two-dimensional wake becomes globally unstable and unsteady. The BVK instability is initially observed as a periodic oscillation of the laminar wake, producing two staggered rows of counter-rotating vortices in an anti-symmetric pattern. Regions of concentrated vorticity are then shed periodically from alternate sides of the

cylinder and convected downstream, forming a von Kármán vortex street. The vortex shedding is nominally two-dimensional in nature for $Re < 190$. At $Re \approx 190$, three-dimensional effects due to secondary instabilities become appreciable (Williamson, 1996).

The periodic oscillations persist, albeit with less coherence, as Re increases, and the three-dimensional structures become increasingly disordered. At $Re > 1200$, vortices generated by the convective Kelvin–Helmholtz instability in the separated shear layers start to appear (Bloor, 1964), cf. Section 5.2. The turbulence transition point in the shear layers move upstream towards the cylinder with increasing Re (Schiller and Linke, 1933). The boundary-layer around the circular cylinder itself undergoes transition to turbulence at $Re \approx 2 \times 10^5$. The more energetic turbulent boundary-layer can resist the adverse pressure gradient and hence separation for a longer time than the laminar boundary-layer. Consequently, the boundary-layer transition leads to less pressure deficiency across the cylinder, i.e. less form drag, and a narrower wake (Roshko, 1993). However, for $Re > 2 \times 10^5$, coherent vortex shedding can still be discerned (see e.g. the studies by Thomann (1959), Roshko (1961), Williamson (1996), and Rodríguez et al. (2015)). Figure 5.4 shows the von Kármán vortex street in the wake of circular cylinders for $Re = 300$ and $Re = 4000$.
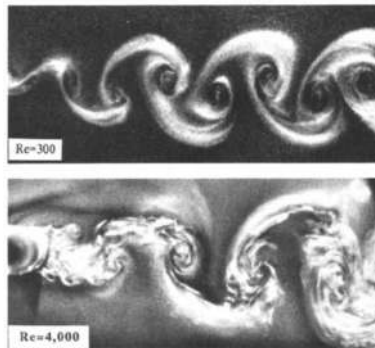

Figure 5.4: Visualisations of the von Kármán vortex street in the wake of circular cylinders for $Re = 300$ and $Re = 4000$, from Williamson (1996).

The flow oscillations due to two-dimensional vortex shedding can be characterised by the Strouhal number $St = fD/U$, where f is the shedding frequency, D is a characteristic diameter, and U is a characteristic velocity. For a circular cylinder, St can be expressed as a piecewise linear function of $1/\sqrt{Re}$ in the flow regimes from $47 < Re < 2 \times 10^5$ (Fey et al., 1998). Based on these relations, St varies between 0.18 and 0.21 for $1000 < Re < 2 \times 10^5$. For bluff-bodies with a square cross-section, the separation points are fixed at the sharp edges of the body, i.e. the position of the separation point does not move with varying Re. Vortex shedding is generated due to the same mechanisms. However, the shedding frequency f generally depends on the shape of the bluff-body.

The theory described above concerns vortex shedding in non-reacting, quasi-steady, uniform density flows. For bluff-bodies located inside a fuel-air cloud during a gas explosion, additional factors make the situation more complex. Combusting flows gen-

erally involve significant density gradients, which directly affect the stability of the bluff-body wake.

Yu and Monkewitz (1990) presented a local stability analysis for the two-dimensional wake behind a bluff-body with non-uniform density gradients. Figure 5.5 shows the 'top-hat' density and velocity profiles they used to perform the wake stability analysis.
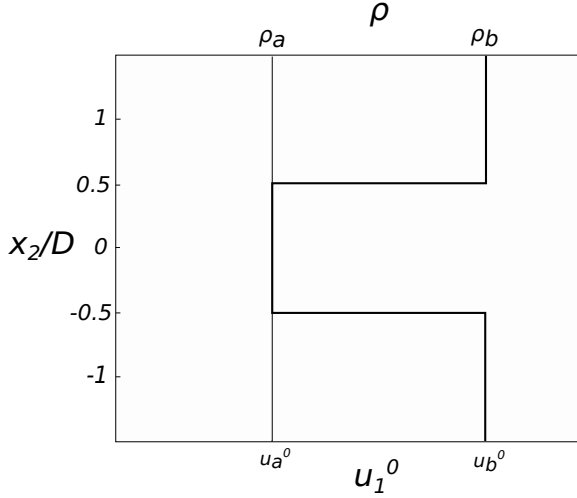

Figure 5.5: 'Top-hat' density and velocity profiles for the wake stability analysis by Yu and Monkewitz (1990). Figure reproduced from (Lieuwen, 2012).

In Figure 5.5, ρ_a and ρ_b denote the the density of the gases in the wake and the freestream, respectively, while u_a^0 and u_b^0 are the corresponding velocities. The backflow parameter χ is defined as

$$\chi = \frac{u_a^0 - u_b^0}{u_a^0 + u_b^0},$$ (5.11)

while the density ratio σ_ρ is defined as $\sigma_\rho = \rho_b/\rho_a$. Yu and Monkewitz (1990) derived a dispersion relation on the form of

$$\frac{1}{\sigma_\rho} \frac{\left[1 + \chi - \frac{1}{u_{av}} \frac{\omega}{k_w}\right]^2}{\left[1 - \chi - \frac{1}{u_{av}} \frac{\omega}{k_w}\right]^2} = -\frac{e^{(k_w D)/2} + se^{-(k_w D)/2}}{e^{(k_w D/2)} - se^{-(k_w D)/2}},$$ (5.12)

where $s = 1$ refers to the sinous instability mode, which is antisymmetric about the flow centreline, while $s = -1$ denotes the varicose instability mode, which is symmetric. In Equation (5.12), $u_{av} = \left(u_a^0 + u_b^0\right)/2$ is the average flow velocity, k_w is the wavenumber and ω is the angular frequency of the disturbance. The dispersion relation in Equation (5.12) can be used to determine regions of convective and absolute instability in terms of $1/\sigma_\rho$ and χ, according to the approach used in Section 5.2. For wake flow, where the backflow parameter χ is negative, absolute instability for the sinous mode occurs (approximately) when $\chi < -0.75$ and $1/\sigma_\rho > 1.0$. The sinous mode appears before the varicose mode of instability.

This local stability analysis shows that *the wake can be further destabilised if the fluid in the wake has a higher density than the approach flow*. Similarly, the presence of a heated, low-density wake stabilises the BVK instability, which is *the sinous, absolute instability occurring in the wake for high values of* $1/\sigma_\rho$ *and negative values of* χ. In the absence of the BVK instability, the wake will be dominated by fluctuations from the convectively unstable separated shear layers.

In the case of a gas explosion, the bluff-body wake initially consists of high-density reactants. However, as the flame propagates into the wake and folds itself around the obstruction, reactants burn, and the near-wake is filled with low-density combustion products. Due to the higher kinematic viscosity of the combustion products relative to the unburnt fuel-air mixture, Re at the circular cylinder will likely be somewhat lower after the flame has passed. Turbulence and unsteady flow structures that have formed in the reactant flow just prior to flame arrival will lead to flame acceleration in the bluff-body wake (Lindstedt and Sakthitharan, 1998; Moen et al., 1980). It is likely that flow structures due to the BVK instability generated in the uniform high-density reactants downstream of the obstacle will dominate the flame acceleration.

Furthermore, flow induced by flame propagation in a gas explosion will generally be transient. Lee and Budwig (1991) investigated vortex shedding in uniformly accelerating flow at $20 < Re < 330$, and found that the critical Re for the onset of the BVK instability increased with increasing flow acceleration. Flow deceleration had the opposite (destabilising) effect. However, the overall time to onset of the BVK instability decreased with increasing flow acceleration, and the temporal growth rate of the instability was approximately proportional to the applied flow acceleration.

As part of the GSP (1993-1996) and the EMERGE project, Christian Michelsen Research (CMR) evaluated drag, loading and turbulence velocities in the near-wake of circular and square cylinders (Kong, 1996; Kong and Sand, 1996; Mercx, 1996). Velocities were measured in both steady flow with Re varying between 1.4×10^4 and 7×10^4, and in transient, explosion driven flow with maximum upstream flow speeds comparable to those of the steady flows. In the transient experiments, the bluff-bodies were not inserted inside the premixed fuel-air cloud due to sensitivity of the LDA (Laser-Doppler anemometry) system to temperature changes, but in a test section downstream of the explosion.

The investigators observed significant effects from vortex shedding on the measured velocities in the near-wake of a single circular cylinder in both steady and transient flow. Furthermore, they found significant turbulence fluctuations also in the spanwise direction, indicating that three-dimensional effects in the near wake were non-negligible. The measured time-varying mean velocity due to vortex shedding in the transient flow was irregular, in contrast to the quasi-periodic variation in the steady flow conditions. In the transient case, the overall turbulence production was measured to be lower in the near-wake (two and four cylinder diameters downstream of the circular cylinder) compared to the corresponding steady configurations. However, the contributions from large-scale vortices were significant in this region for the transient case, so Kong and Sand (1996) suggested that the larger-scale coherent structures located there had not yet merged and dissipated to smaller-scale turbulence.

5.3.2 Experiments

For Paper 3, an experimental campaign was performed to quantify the contribution of vortex shedding to the flame acceleration downstream of bluff-body obstructions in gas explosions. The campaign was performed in a vented channel of dimensions 1.5 m × 0.28 m × 0.3 m. A near-stoichiometric propane-air mixture was used in all tests.

For small-scale rigs, it is possible to undertake a larger number of tests than for larger-scale experiments, i.e. perform repetitions, explore further parameter variations, etc. Furthermore, the initial conditions, in particular the composition of the fuel-air cloud, initial temperature and turbulence levels, are easier to control in a small vessel than in a larger chamber. For the tests performed for Paper 3, where the relative effect of vortex shedding to the flame acceleration and overpressure generation is investigated, excellent repeatability is crucial. For the baseline experiments, a single circular cylinder with an aspect ratio L_{cyl}/D_{cyl} of 17.8 was inserted in the channel. A single obstacle provides a clean setup, and is a natural starting point for further investigations. Subsequently, two different passive flow control methods were applied to the circular cylinder. Both methods are extensively referred to in the literature, and have been used in numerous studies for suppressing vortex shedding in bluff-body wakes, see e.g. (Choi et al., 2008; Zdravkovich, 2003). Furthermore, the methods are both relatively straightforward to apply.

For method (i), a splitter plate of varying length L_{sp} was inserted in the base region immediately downstream of the cylinder, and for method (ii), a helical steel wire of varying pitch P was added to the cylinder surface. The splitter plate prevents the separated boundary layers from interacting, thereby suppressing the BVK instability. The helical steel wire suppresses the instability by forcing the boundary-layer to separate inhomogeneously along the cylinder span, thus disrupting the two-dimensional nature of the instability. Meanwhile, both methods introduce additional shear layers to the flow. Appendix B and Paper 3 include further details on the experimental setup.

The paper compares the results from the baseline experiments to the results from tests where control methods were applied. Visualisations based on high-speed video recordings showed the flame propagation in each test. Figure 5.6a shows a snapshot of the flame position at the time of the maximum overpressure in a baseline test, where a clean, circular cylinder was inserted in the explosion rig. Regions of enhanced burning rates in the circular cylinder wake, resembling the von Kármán vortex street, could be observed in the baseline experiments. Both large-scale, coherent structures and regions of small-scale, broadband turbulence with intense combustion appeared to be present downstream of the obstruction, cf. Figure 5.6a. Figure 5.6b shows a snapshot at the time of the maximum overpressure for a test where a splitter plate of length $5D_{cyl}$ was inserted immediately downstream of the cylinder. When the applied control methods were successful, coherent shedding could not be discerned in the high-speed videos, and the circular cylinder wakes appeared significantly less energetic.

From the findings of Paper 3, vortex shedding appears to have a significant effect on the flame acceleration in bluff-body wakes. The most effective control method configurations in the experimental campaign reduced the maximum explosion overpressures by approximately 32 % and 25 % for methods (i) and (ii), respectively, while the corresponding reductions in maximum pressure impulse were 25 % and 16 %, respectively. The effect of the most efficient splitter plate (with $L_{sp} = 1.02D_{cyl}$) is visualised by the
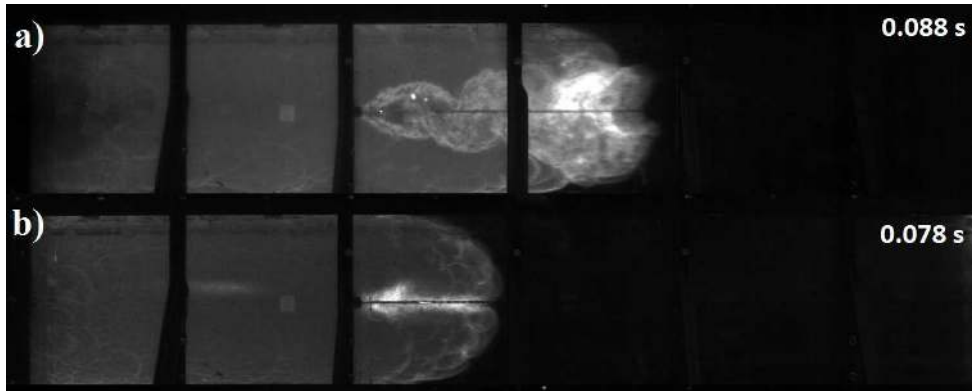
Figure 5.6: High-speed video frames taken at the time of maximum overpressure, a) reference case, and b) cylinder with splitter plate of length $5D_{cyl}$.

pressure-time curve in Figure 5.7a and the flame velocity vs. distance from the ignition point in Figure 5.7b. Paper 3 presents results and further analysis for the complete experimental matrix.
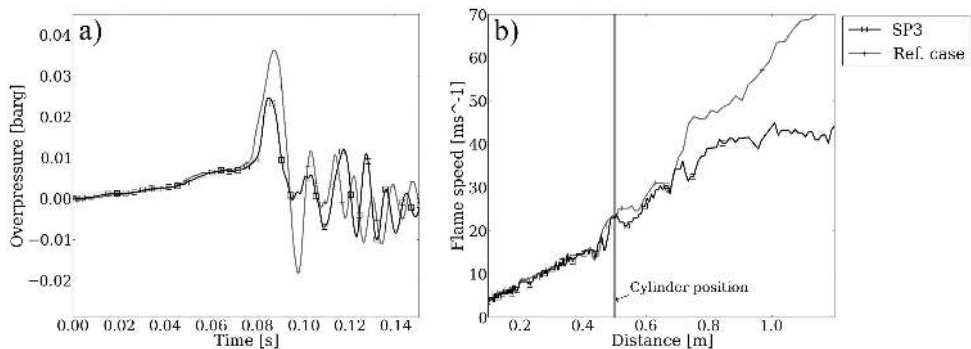

Figure 5.7: a) Overpressure-time history and b) flame speed vs. distance curves for a baseline test (denoted "Ref. case"), together with a test where a splitter plate was inserted, $L_{sp} = 1.02D_{cyl}$ (denoted "SP3").

Previous work corroborates the experimental findings. The characteristic length scales of vortices generated in the bluff-body wake determine how the flame zone and the turbulent flow field interact. Large-scale flow structures distort and increase the overall flame surface area, leading to an overall higher fuel consumption rate, while small-scale turbulence structures promote mixing in the flame brush and enhance the combustion rate locally. Most theoretical and experimental studies on turbulent premixed combustion relate the turbulent burning velocity u_t to the turbulence velocity fluctuations u', and express u_t as increasing with u' before quenching effects become important, cf. Section 4.5. For non-reacting flow past a bluff-body, where a splitter plate suppresses the vortex shedding, the highest values of the Reynolds stresses $-\overline{\rho u_i' u_j'}$ are found in the separated shear layers. In a bluff-body wake without a splitter plate, where vortex shedding dominates, the Reynolds stresses are generally higher

and more evenly distributed compared to the splitter plate case (Cantwell and Coles, 1983; Roshko, 1993). Furthermore, the energetic, large-scale structures generated by the BVK instability eventually break down into smaller-scale turbulence (Schadow and Gutmark, 1992). Therefore, coherent vortex shedding likely promotes combustion in the far-wake more efficiently than the less energetic separated shear layers. The video frames in Figure 5.6 seem to support this hypothesis. Observations from the experimental campaign in Paper 3 suggest that the mechanism is significant, cf. the overpressure reduction in Figure 5.7a.

5.3.3 Modelling the effect of vortex shedding

The BVK instability may occur naturally in CFD simulations, provided that the spatial and temporal resolution of the flow is sufficient. Arntzen (1998) observed vortex shedding in FLACS simulations for steady, uniform flow conditions, occurring in the wake of a circular cylinder resolved with three control volumes across the diameter. Skjold et al. (2017a) performed simulations of two fully resolved square cylinders in tandem in a steady, non-reacting flow with $Re = 4 \times 10^6$, and saw vortex shedding when the cylinders were resolved with more than four cells across the obstacle thickness. The unsteadiness of the wake seemed to increase with higher grid resolutions. Meanwhile, the ability of the CFD tool to represent vortex shedding in a transient flow, such as that generated by a gas explosion, was not investigated.

Narasimhamurthy (2015) presented FLACS simulations of a hypothetical case involving a narrow channel with several square cylinders placed along the channel centreline. Figures 5.8 and 5.9 show the geometry, where cylinders with cross-sections of 0.03 m × 0.03 m were inserted in a 9.0 m × 0.8 m × 0.8 m channel. Non-reacting transient flow was obtained by imposing a high-pressure region in the inner part of the channel at the beginning of the simulation. This initial condition resulted in very high flow acceleration rates and maximum flow speeds of ≈ 300 m/s over the obstructions. Figure 5.8 shows that vortex shedding occurs in the square cylinder wakes upstream of the propagating pressure front when using a grid resolution of 0.01 m, i.e. with three control volumes across the obstacle width. These results suggest that FLACS can reproduce vortex shedding also in highly transient flows. The modelled values for the turbulence velocity fluctuation, u', are not significantly higher than for the same configuration with a grid resolution of 0.09 m, where the obstructions are represented completely sub-grid, cf. Figure 5.9 (top). However, the distribution of u' is significantly different for the two grid resolutions.

Unfortunately, it is not straightforward to perform meaningful simulations of the gas explosion experiments in Paper 3. Resolving the circular cylinder sufficiently to be able to discern vortex shedding would require a uniform grid resolution with grid cell sizes less than 0.005 m. However, when using grid cells with characteristic lengths of less than 2 cm, the sub-grid models for turbulence and combustion in FLACS are known to over-predict the flame acceleration in gas explosion simulations (Gexcon, 2016), cf. Section 3.2.1. Alternatively, the circular cylinder would need to be represented completely sub-grid, and adding a splitter plate to the geometry would not give the desired effect. The BVK instability will obviously not be triggered for sub-grid objects in simulations of either steady or transient flow.

The following discussion is limited to modelling approaches for obstacles on the
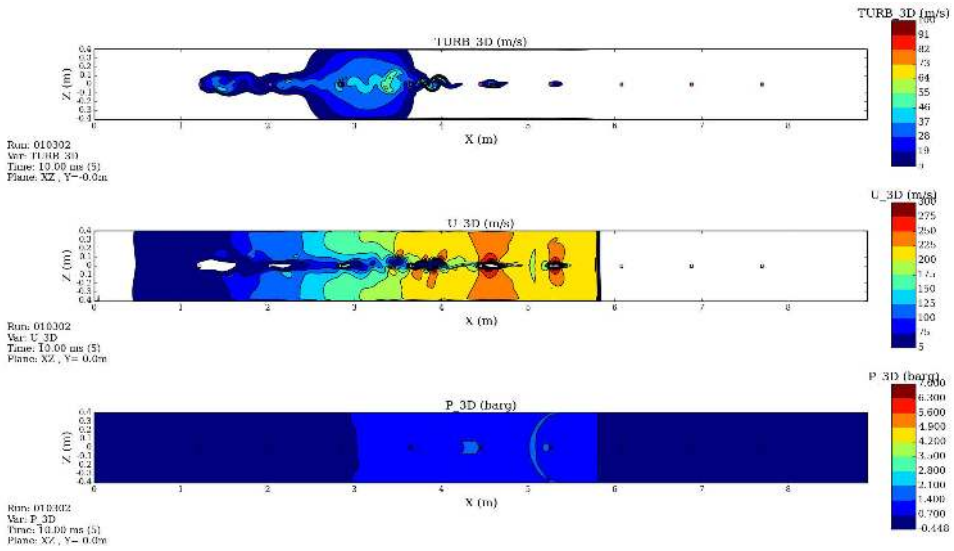
Figure 5.8: Simulation of transient, non-reacting flow past a row of square cylinders: turbulence velocity fluctuation, u' (top), flow velocity in the x_1-direction, u_1 (middle), and pressure, p (bottom), grid resolution of 0.01 m.
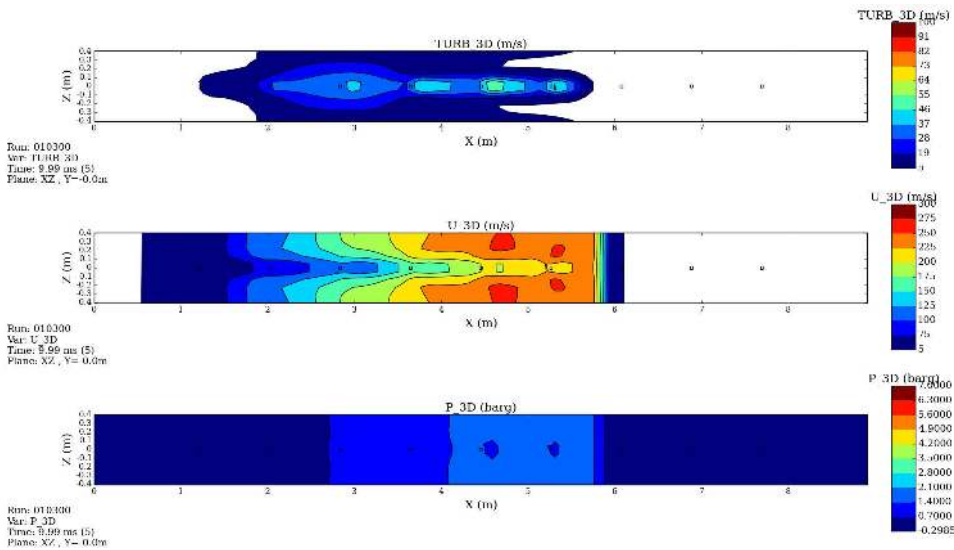
Figure 5.9: Simulation of transient, non-reacting flow past a row of square cylinders: turbulence velocity fluctuation, u' (top), flow velocity in the x_1-direction, u_1 (middle), and pressure, p (bottom), grid resolution of 0.09 m.

sub-grid scale. Section 5.1.2 showed that the flame surface area increase downstream of sub-grid obstacles in FLACS is represented by the flame wrinkling factor Ξ_S, defined

as

$$\Xi_S = 1 + \frac{\Delta A_f}{A_f} = 1 + C_{fl}\sqrt{U_c}\,\phi_i\,\mathcal{C}_i\,, \qquad (5.13)$$

where C_{fl} is a model parameter, U_c is the downstream flow velocity normalised by the speed of sound, ϕ_i is a direction vector, and $\mathcal{C}_i$ denotes the total surface area of the 'ending walls' of the sub-grid obstructions for flow in the ith direction. The parameter $\mathcal{C}_i$ is only defined for objects with one or more ending walls in the present control volume.

The model parameters in Equation (5.13) must account for a range of physical phenomena that cause complex changes in the flame surface structure as the flame front interacts with the obstacles and the downstream flow. For fixed geometry and grid settings, Ξ_S from Equation (5.13) will increase with an increasing Reynolds number. Meanwhile, the model only gives a *localised* contribution to the burning velocity, i.e. the effect of a sub-grid obstruction is only felt in the control volume where it is located. The experiments in Paper 3 indicate that an important effect of vortex shedding may be enhanced turbulence levels further downstream of the bluff-body, resulting from dissipation of the larger-scale, energetic structures. If the effect of unresolved vortex shedding should be accounted for through the modelling of Ξ_S, the flame wrinkling factor should be a transported quantity. The transport equation formulated by Puttock et al. (2014), Equation (5.4), based on the transport equation for flame surface area due to turbulence effects proposed by Weller et al. (1998a), may then be an attractive alternative to the equilibrium approach in Equation (5.13).

However, to model the generation and destruction rate of Ξ_S, extensive validation against relevant experiments would be required. Simulations performed with CFD models that resolve a wider range of the turbulence spectrum, e.g. LES models that resolve boundary-layers (Gourdain et al., 2009a,b), could provide further knowledge about the increase in flame surface area from obstacles in different flow regimes.

5.3.4   Relevance of the BVK instability for industrial-scale explosions

Paper 3 shows that vortex shedding triggered by the BVK instability is significant for the flame acceleration downstream of a bluff-body in a flow with *Re* increasing from $O\left(10^2\right)$ to $O\left(10^4\right)$, in a time interval of approximately 50 ms prior to flame arrival. Applying two different passive control methods to the circular cylinder in the experiments of Paper 3 successfully suppressed the instability and reduced the generated explosion overpressures by $25-30$ %. In addition to highlighting the importance of modelling this effect in the consequence analysis, the results trigger the question of whether suppression of vortex shedding could be used as a potential explosion mitigation method in process facilities.

The BVK instability is essentially two-dimensional in nature. However, in the experiments performed for Paper 3, the flame front approaching the cylinder originates from point ignition. The flame front initially has the shape of a half-ellipsoid, and therefore creates a three-dimensional flow field upstream of the cylinder in the initial phase of the explosion. In addition, boundary-layers are created as the flow is pushed along the channel walls, and the flow past the circular cylinder will likely be affected by end effects and various three-dimensional instabilities (Kong, 1996). For a circular cylinder with an aspect ratio of 17.8 in an accelerating flow, confining walls may delay the onset of BVK instability (Lee and Budwig, 1991). Still, the significant effect of applying

control methods developed for suppressing the nominally two-dimensional instability suggests that this instability can be important also in three-dimensional, transient flow fields. Therefore, based on the findings in Paper 3, vortex shedding will most likely occur also in gas explosion scenarios with higher values of Re. Indeed, as noted above, shedding has been observed in non-reacting flows with $Re > 2 \times 10^5$ (Rodríguez et al., 2015; Roshko, 1961; Thomann, 1959; Williamson, 1996). Wakes will interact when several obstructions are present in the flow.

The gas explosion experiments presented by Bauwens et al. (2010), performed in a 4.6 m × 4.6 m × 3.0 m vented enclosure, provide relevant test cases for investigating whether vortex shedding would play a role in more realistic scenarios (i.e. higher values of Re and several obstructions with interacting wakes). Here, one of these experiments, with a 5.4 m^2 vent opening and eight square obstacles inserted in the enclosure, is investigated. Figure 5.10a shows the configuration. For this test, a 4 vol.% propane-air mixture was ignited at the back wall of the enclosure, opposite of the vent opening. Bauwens et al. (2010) do not report any velocity fluctuation measurements from the explosion event itself (such measurements were performed prior to ignition). Meanwhile, the square obstacles can be resolved with grid resolutions that are within the applicable range for gas explosion simulations in FLACS. Additional experimental campaigns performed in this chamber are described in Section 6.1.

Figure 5.10b shows the pressure-time history for the selected test, together with results from a corresponding FLACS simulation. The pressure-time history is predicted by a development version of FLACS that includes key findings from the present doctoral study. This version of FLACS, denoted *FLACS v10.4-ma-rt*, applies the Markstein number-dependent burning velocity model discussed in Section 4.6 and Paper 2. Furthermore, the development version includes the effect of flame surface area increase due to the Rayleigh–Taylor instability, cf. Section 5.4.2 for further details. The pressure build-up and time of arrival of the main pressure peak is well reproduced by FLACS v10.4-ma-rt, indicating that the flow velocities induced by the flame propagation in the initial phase is representative of that observed in the experiment. However, the validity of a numerical investigation of the BVK instability in gas explosions depends on FLACS correctly reproducing the vortex shedding mechanism, which is highly uncertain.

Figure 5.11 presents additional results from the simulation that gave the pressure-time curve in Figure 5.10b. Figure 5.11a shows the distribution of combustion products, Figure 5.11b shows the distribution of velocity in the x_1-direction, u_1, and Figure 5.11c shows the turbulence velocity fluctuation, u', 300 ms after ignition. Shedding cannot be discerned downstream of the obstacles at this point in time, cf. figures 5.11b and 5.11c. Indeed, FLACS does not predict vortex shedding at any time during the simulation. In these simulations, the square cylinders are resolved with four control volumes across the obstacle width.

Figure 5.12 (left) shows u' for a simulation with a corresponding geometry to that used in Figure 5.11. However, for the simulation in Figure 5.12 (left), a uniform, steady inflow of 10 m/s is imposed as the boundary condition at the back wall of the chamber, and the flow is non-reacting. This results in a flow that represents an approximate average of the velocities in Figure 5.11b. The steady inflow conditions give a Reynolds number relative to the obstructions of approximately 2.5×10^5. At 3 s after the onset of the inflow, Figure 5.12 (left) shows that vortex shedding has not developed in the

(a) Geometry layout and ignition position.

(b) Pressure-time history, vent size 5.4 m^2, back ignition, 4 vol.% propane-air.
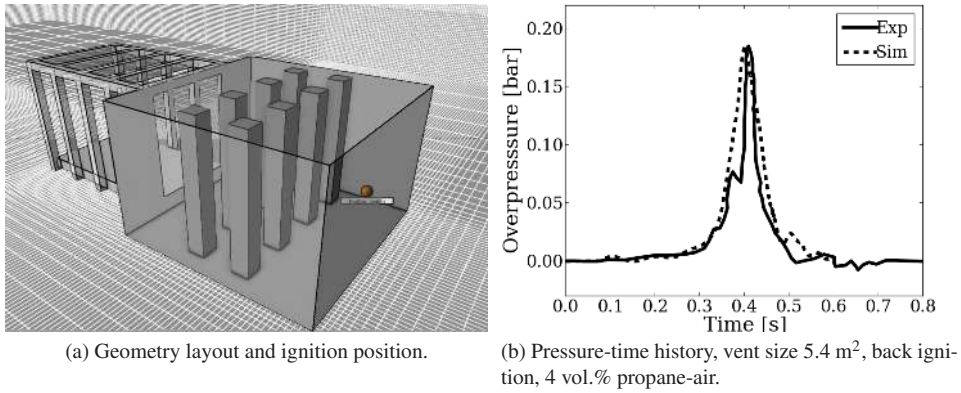
Figure 5.10: Representation of the 64 m^3 vented explosion chamber with obstacles used by (Bauwens et al., 2010) with FLACS v10.4-ma-rt, grid resolution of 0.1 m.

(a) Combustion products.

(b) Velocity in x_1-direction, u_1.

(c) Turbulence velocity fluctuation, u'.
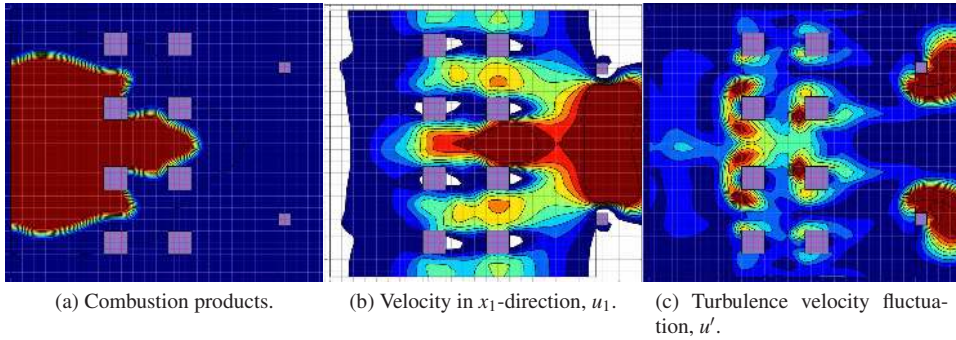
Figure 5.11: Two-dimensional cut planes from the FLACS simulation in Figure 5.10b, performed with a grid resolution of 0.1 m, 300 ms after ignition.

square cylinder wakes when a grid resolution of 0.1 m is used. Meanwhile, Figure 5.12 (right) shows that when a grid resolution of 0.05 m is applied to the same scenario (i.e. with eight control volumes across the obstacle width), vortex shedding does eventually develop in the simulation. For a grid resolution of 0.05 m, the onset of shedding occurs later than 300 ms after the onset of the inflow from the boundary, and the antisymmetric pattern is not fully developed until 400 ms after the onset of the inflow.

Figure 5.13 (right) shows that inserting splitter plates with the same length as the side wall of the square obstructions successfully suppresses the vortex shedding in the steady flow. The wakes in Figure 5.13 (right) are significantly less energetic than those in Figure 5.13 (left) (the corresponding scenario without splitter plates, same plot as in Figure 5.12 (right)).

Figure 5.14 shows results for the combustion products, u_1 and u', 300 ms after ignition for the same gas explosion scenario as in Figure 5.11, simulated with a grid resolution of 0.05 m. Here, vortex shedding has not developed in the square cylinder wakes. Indeed, the wake instability is not observed at any time during the simula-
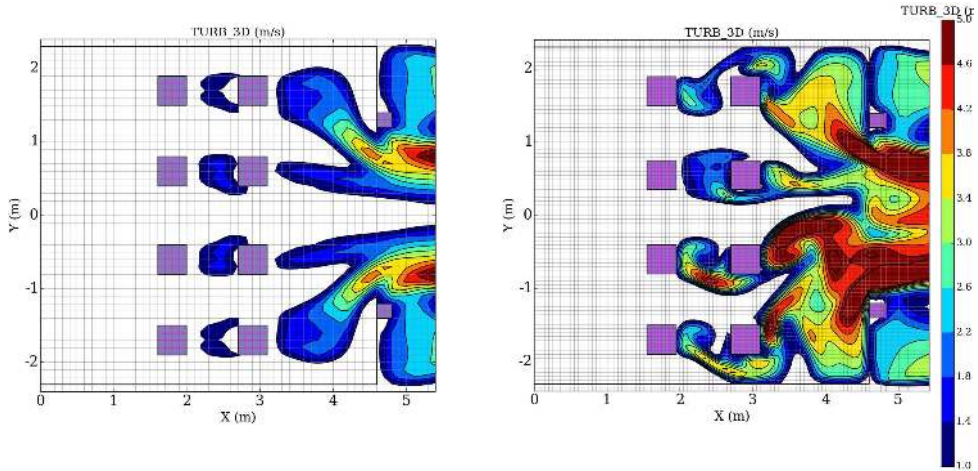
Figure 5.12: Simulations performed with a uniformly distributed, steady flow velocity (non-reacting flow), using a grid resolution of 0.1 m (left) and 0.05 m (right), 3 s after the onset of the inflow.
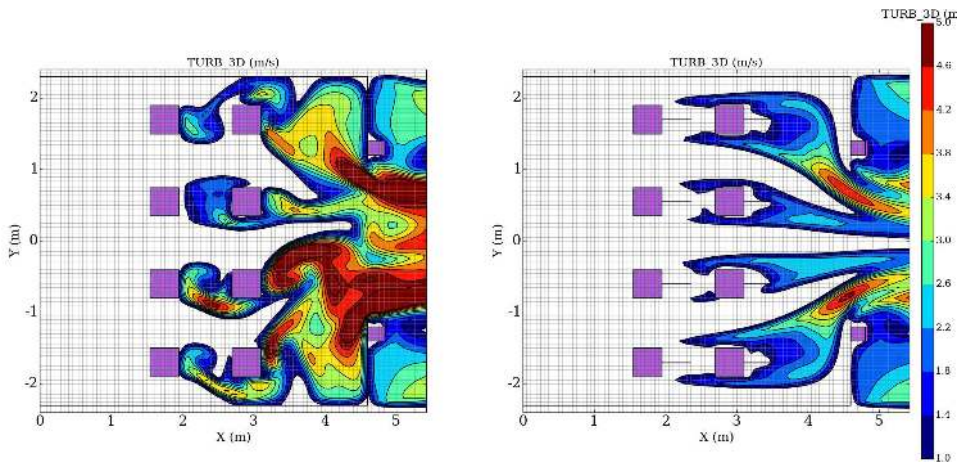
Figure 5.13: Simulations performed with a uniformly distributed, steady flow velocity (non-reacting flow), using a grid resolution of 0.05 m without splitter plates (left) and with splitter plates (right), 3 s after the onset of the inflow.

tion, even though figures 5.12 and 5.13 suggest that the spatial and temporal resolution should be sufficient. Hence, for the transient case with a non-uniform velocity profile and reacting flow, vortex shedding does not develop quickly enough to affect the simulation. However, the simulated behaviour does *not* prove that vortex shedding was not an important mechanism in the experiments performed by Bauwens et al. (2010).

To conclude, the FLACS simulations presented here are not able to confirm whether

(a) Combustion products.   (b) Velocity in x_1-direction, u_1.   (c) Turbulence velocity fluctuation, u'.
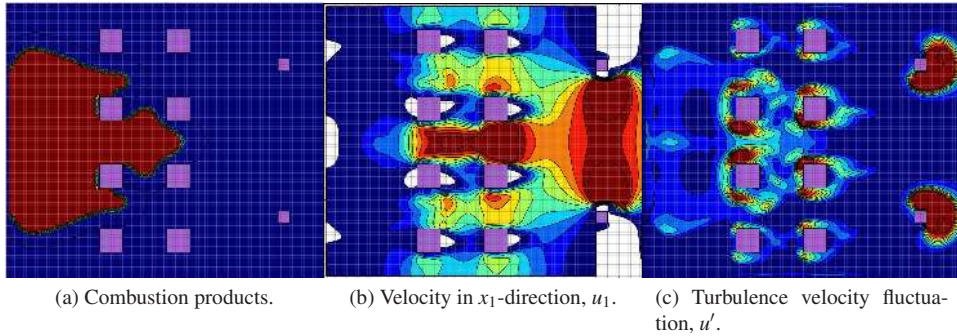
Figure 5.14: Two-dimensional cut planes from an explosion simulation performed with a grid resolution of 0.05 m, 300 ms after ignition.

the pressure-reducing effect of passive control methods would be significant in large-scale gas explosions with multiple obstacles. However, both of the passive control methods used in the experimental campaign of Paper 3 directly affect the global instability in the near-wake, rather than delaying the separation point, and should therefore be effective for a wide range of Re (Choi et al., 2008). For a single bluff-body obstruction, these control methods were able to reduce the maximum overpressures obtained in the explosion by $25 - 30$ %.

In order for a control method to be useful for reducing overpressures in a real accident, it must be independent of the flow direction. Consequently, a fixed splitter plate would be unpractical, while adding a structure to the surface of the obstruction to disrupt the two-dimensional nature of the instability (comparable to adding a helical steel wire as in Paper 3) may be feasible. To confirm whether such an approach could constitute a cost-effective risk-reducing measure in real process facilities would require a series of large-scale experiments, specifically designed to investigate this effect. The experiments should include both idealised, symmetric setups, such as the setup used by Bauwens et al. (2010), and more realistic, non-uniform geometry configurations. The effect of applying different control methods should be investigated for different ignition positions. However, such a large-scale campaign was not feasible to undertake as part of the present doctoral study.

5.4 The Rayleigh–Taylor (RT) instability

Significant mixing processes can arise from situations where fluids of different densities are moving relative to each other. The Rayleigh–Taylor (RT) instability is triggered when a lighter fluid is accelerated into a heavier fluid, for example when a flame front is accelerated over an obstacle or through a vent opening (Ciccarelli and Dorofeev, 2008; Oran, 2015). Similarly, the Richtmyer-Meshkov (RM) instability is triggered when a shock wave accelerates a perturbed interface between fluids of different densities. This mechanism corresponds to the RT instability for compressible flow. However, the RM instability has not been investigated further in the present doctoral study, as the analysis and representation of shock wave formation have not been considered feasible

to undertake within the present scope.

Strictly, the mechanism behind the RT instability will be active also for gas explosions involving more or less freely expanding flames in uncongested regions. The RT instability has been proposed as a source of flame-generated turbulence, through the baroclinic source term in the vorticity equation, by e.g. Bradley (1999); Khokhlov et al. (1996). Meanwhile, for the relatively modest acceleration rates associated with freely expanding spherical flames in gravity fields, the RT instability is normally not considered to contribute significantly to flame acceleration and overpressure generation. Following Ciccarelli and Dorofeev (2008), the RT instability is therefore discussed together with the other geometry-induced phenomena investigated in the present thesis.

In particular, the RT instability is considered an important source of flame surface area production in vented explosions (Bauwens et al., 2009a,b; Cooper et al., 1986; Solberg et al., 1981; Tsuruda and Hirano, 1987). The RT instability has been observed to cause enhanced flame wrinkling both as the flame front exits the vent opening, and during the subsequent Helmholtz oscillation phase when the chamber alternates between over- and under-vented states (Bauwens et al., 2009a; Cooper et al., 1986). In order to correctly represent the external explosion in simulations of vented scenarios, several researchers have suggested that including the RT instability effect is necessary, i.e. only modelling the effect of turbulence is insufficient (Bauwens et al., 2009b, 2011; Keenan et al., 2014). Vented explosions therefore provide useful validation cases for testing sub-grid models for the RT instability.

5.4.1 Stability analysis

The linearised growth rate of the RT instability can be studied analytically by including the effect of acceleration in the stability analysis of the perturbed flame front from sections 4.3.2 and 4.3.4 (Zeldovich et al., 1985). The solutions of the linearised system of equations for the perturbed variables, equations (4.11)–(4.16) remain the same if acceleration is included, while the dynamic boundary condition at the flame front becomes

$$p_u^1 - p_b^1 = (\rho_u - \rho_b)\,(\mathbf{a}\cdot\mathbf{n})\,x_f - 2\rho_u(u_n)^2(\sigma - 1)\mathcal{L}\frac{\partial^2 x_f}{\partial x_2^2}\;, \tag{5.14}$$

where $\mathbf{a}\cdot\mathbf{n}$ is the acceleration component of the flame front normal to the flame, and $\mathcal{L}$ is the Markstein length of the mixture.

Using this boundary condition in the stability analysis, the growth rate ω^* of the perturbation can be expressed as

$$\frac{\omega^*}{k_w u_n} = -\frac{\sigma\left(1 + Ma\,k_w\delta_l \pm \sqrt{1 + \sigma - 1/\sigma + Ma\,k_w\delta_l\,(Ma\,k_w\delta_l - 2\sigma) + \frac{\sigma^2 - 1}{\sigma^2}\frac{\mathbf{a}\cdot\mathbf{n}}{k_w(u_n)^2}}\right)}{\sigma + 1}\;,$$
$$\tag{5.15}$$

where Ma is the Markstein number of the mixture. By setting $\omega^* = 0$, the stability boundary and the critical wave number k_w^{cr} can be found as

$$k_w^{cr} = \frac{\sigma - 1}{4Ma\delta_l\sigma}\left[1 \pm \sqrt{1 + \frac{8Ma\delta_l\,(\mathbf{a}\cdot\mathbf{n})}{(\sigma - 1)(u_n)^2}}\right]. \tag{5.16}$$

From Equation (5.15), it is possible to find that perturbations that satisfy $k_w > k_w^{cr}$ are stable. For increasing acceleration, a wider range of wavelengths become unstable. Figure 5.15 shows how the critical wave number k_w^{cr}, determined by the positive root of Equation (5.16), grows with the acceleration $\mathbf{a} \cdot \mathbf{n}$.
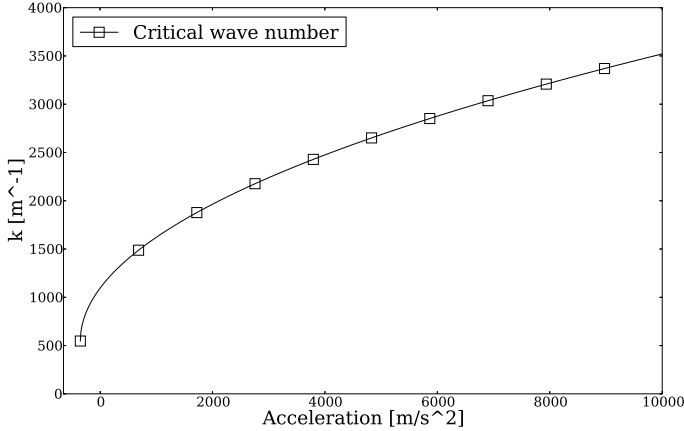

Figure 5.15: Critical wave number, k_w^{cr}, as a function of acceleration.

5.4.2 Modelling the effect of the RT instability

Bauwens et al. (2009b, 2011) presented results from a series of vented methane-air and hydrogen-air explosions, together with numerical results obtained with a LES solver using the flamelet model by Weller et al. (1998a) (cf. Section 5.1.1). The authors observed that the explosion history could not be sufficiently represented by turbulence effects alone. Consequently, Bauwens and Dorofeev (2011) and Bauwens et al. (2011) proposed to use Equation (5.15), expressing the linearised growth rate of intrinsic flame instabilities under the influence of acceleration, to formulate a separate transport equation for the flame surface area generated by the RT instability. This contribution was represented by the flame wrinkling factor Ξ_{RT}, and a transport equation for Ξ_{RT} was solved in addition to Equation (5.2).

By assuming that the RT and intrinsic instabilities occur for significantly different wave numbers, Bauwens et al. (2011) separated the growth rate for the two phenomena in Equation (5.15). Retaining only the last term of Equation (5.15) gives an expression for the linearised growth rate of perturbations due to acceleration, ω_{RT}, that can be written as

$$\omega_{RT} = \sqrt{k_{RT} \frac{\sigma - 1}{\sigma + 1} \mathbf{a} \cdot \mathbf{n}} \,, \tag{5.17}$$

where k_{RT} is a characteristic unstable wave number for the RT instability, chosen to be the wave number that gives the maximum growth rate. The normal vector for the flame surface, $\mathbf{n}$, is defined to point outwards, i.e. away from the combustion products, into

the reactants. A positive value for $\mathbf{a} \cdot \mathbf{n}$ signifies the acceleration of a low-density fluid into a higher-density fluid, which promotes the RT instability.

Furthermore, Bauwens and Dorofeev (2011) argued that the amplitude a_d of the disturbances can be assumed to be less than a quarter of a wavelength, $a_d << \pi/(2k_{RT})$ and that the amplitude decays in time as $da_d/dt = -2u_n \sigma a_d^2/(\pi/(2k_{RT}))^2$. The flame-wrinkling factor for the RT instability, Ξ_{RT}, is related to the amplitude a_d by $a_d = \pi/(2k_{RT})\sqrt{[\Xi_{RT} - 1]}$. Bauwens et al. (2011) used these assumptions to formulate a transport equation for Ξ_{RT} on the form

$$\frac{d\Xi_{RT}}{dt} = G_{RT}(\Xi_{RT} - 1) - R_{RT}(\Xi_{RT} - 1)^{3/2} , \qquad (5.18)$$

$$G_{RT} = 2\sqrt{k_{RT}\frac{\sigma - 1}{\sigma + 1}\mathbf{a} \cdot \mathbf{n}} , \qquad (5.19)$$

$$R_{RT} = 8\sigma u_n \frac{k_{RT}}{\pi} , \qquad (5.20)$$

where G_{RT} and R_{RT} are the generation and removal rate of flame wrinkling due to the RT instability, respectively. Bauwens and Dorofeev (2011) and Bauwens et al. (2011) subsequently used the separate flame wrinkling factors accounting for the RT instability, Ξ_{RT}, and the LD instability, Ξ_{LD}, to obtain the 'final' flame wrinkling factor Ξ for closing Equation (5.1) in the Weller model according to

$$\Xi = \Xi_T \, \Xi_{LD} \, \Xi_{RT} . \qquad (5.21)$$

In Equation (5.21), Ξ_T is the flame wrinkling factor representing turbulence effects, presented in Section 5.1.1.

Equations (5.18)-(5.20) were derived based on a simplified linear analysis, while the generation and destruction of flame surface area from the RT instability are highly non-linear processes. Meanwhile, Bauwens et al. (2011) argued that lack of non-linear effects can be compensated for by defining appropriate model constants in the transport equation for Ξ_{RT}. Consequently, they set the generation and removal rates G_{RT} and R_{RT} in equations (5.18) – (5.20) to mixture-dependent constants in their CFD model, and calibrated these against experimental results. They found that this approach gave reasonable representation of the external explosion for a wide range of methane-air, propane-air and hydrogen-air vented explosions.

Several publications, e.g. (Bauwens et al., 2010, 2012; Chao et al., 2011), describe a simplified analytical model developed by FM Global for estimating the magnitude of the different pressure peaks that occur in vented explosions. In this model, the RT instability contributes to the pressure peak generated by the external explosion. The modelling approach is based on the same linear stability analysis as used for the CFD modelling that resulted in equations (5.18)-(5.20). Meanwhile, the flame surface area in the simplified analytical model is assumed to grow linearly in time, i.e. $\Xi_{RT} = 1 + \Xi_{RT}^0 t$, where $\Xi_{RT}^0 = \sqrt{(k_{RT}a)}$, and a is the acceleration. Here, the characteristic wave number k_{RT} is determined by calibration against experimental data. In effect, k_{RT} becomes a model constant.

5.4.3 Modelling approach in FLACS

A simplified sub-grid model for flame wrinkling due to the RT instability based on the theory by Zeldovich et al. (1985) and the approach by Bauwens and Dorofeev (2011) (presented in sections 5.4.1 and 5.4.2) was implemented in a development version of FLACS as part of the present doctoral study. The model was formulated to be consistent with the current framework for modelling flame surface area generation due to sub-grid obstructions, cf. Section 5.1.2.

In the development version of FLACS, if the normal component of the flame front acceleration exceeds a certain limit a^{lim}, the flame wrinkling factor Ξ_{RT} is assumed to be approximated by

$$\Xi_{RT} = \min\left(\max\left[1, 1 + C_{RT}\sqrt{k_{RT}\left(\mathbf{a}\cdot\mathbf{n} - a^{lim}\right)}\right], \Xi_{RT}^{lim}\right) , \qquad (5.22)$$

where C_{RT} is a model constant, k_{RT} is a characteristic wave number for the RT instability, and Ξ_{RT}^{lim} is an upper limit for the enhancement in flame surface area due to the instability. The value for Ξ_{RT} from Equation (5.22) is computed at each time step, for each control volume where the flame front is present. Following the principle applied by Bauwens and Dorofeev (2011) and Puttock et al. (2014), the flame wrinkling factor Ξ_{RT} in FLACS is then multiplied with Ξ_S and the modelled burning velocity s_{bvm} to obtain the final input burning velocity s to the flame model according to

$$s = s_{bvm}\,\Xi_S\,\Xi_{RT} . \qquad (5.23)$$

Section 3.2 describes how FLACS applies the burning velocity s from Equation (5.23) to model premixed flame propagation.

When including the sub-grid model based on Equation (5.22) in FLACS, it is assumed that the effect of the RT instability is unresolved by the CFD model in all scenarios relevant for industrial-scale explosions. For the typical values of flame front acceleration obtained in gas explosions, $0 - 10\,000$ m/s^2, the wave number k_{RT} that corresponds to the perturbation wavelength of maximum growth rate typically varies between 200 and 2000 (SUSANA, 2016). These wave numbers correspond to wavelengths of approximately 0.03 m to 0.003 m. Perturbations on this scale are impossible to represent with a numerically thickened flame, using a grid resolution of $0.05 - 1$ m, cf. the discussion in Section 4.4.1.

The model approach described here is highly simplified. The stabilising effect of the RT mechanism on the flame surface is not accounted for, as Equation (5.22) only takes into account enhancement of the burning velocity due to the instability. Furthermore, the characteristic wave number k_{RT} is an empirical model constant representing a single unstable perturbation wavelength (chosen to be fixed to $k_{RT} = 1000$), while, naturally, a range of unstable wavelengths will be triggered on the flame surface.

Finally, the model assumes that the effect of the acceleration on the burning rate is localised and instant. To be consistent with the current approach for flame wrinkling in FLACS (Gexcon, 2016), cf. Section 5.1.2, flame surface area is not transported with the flow. A simplified equilibrium approach, as defined by Weller et al. (1998a), is used instead. A range of unresolved effects must therefore be represented by the model constants C_{RT}, k_{RT} and Ξ_{RT}^{lim} in Equation (5.22). The downstream flow will feel

the effect of an upstream burning velocity enhancement through transported quantities: velocities, pressure, turbulence parameters, etc.

Values for the model constants in Equation (5.22) were calibrated by simulating the experimental campaigns described by Bauwens et al. (2011), Chao et al. (2011), Bauwens et al. (2012), and Bauwens and Dorofeev (2014), involving vented fuel-lean hydrogen-air explosions for a range of experimental configurations (varying vent size, concentration, obstacle layout, etc.). Model results for these experiments, obtained by using the sub-grid model for the RT instability together with the Markstein number-dependent burning velocity model from Section 4.6, are presented in Chapter 6, Section 6.1.

Finally, the version of FLACS developed as part of the present thesis, incorporating both RT instability and Markstein number effects, was used to simulate key experiments from Paper 1 in Chapter 6, Section 6.2. Chapter 6 thus presents further analysis on the performance of equations (5.22) and (5.23) in FLACS.

5.5   Acoustic instabilities

Flame-acoustic interactions have been observed to produce significant pressure peaks in a number of experimental campaigns involving vented gas explosions, see e.g. (Bauwens et al., 2010; Cooper et al., 1986; van Wingerden and Zeeuwen, 1983a; Zalosh, 1979). Generally, flame-acoustic interactions are associated with gas explosions in geometries with a high degree of confinement. The explosion creates pressure waves that may be reflected by walls, excite structural vibrations and couple with the flame front dynamics, thus enhancing the combustion rate through a range of different instability mechanisms (Ciccarelli and Dorofeev, 2008; Clavin and Searby, 2016).

The pressure peaks generated by acoustic instabilities typically occur in the last phase of confined explosions: after the onset of external combustion for vented chambers, and either after or as the flame front approaches the chamber walls. Significant overpressures generated by acoustic flame instabilities are normally associated with explosions in empty enclosures, in particular with near-cubical, symmetric geometries. For these configurations, flame-acoustic interactions may completely dominate the pressure-time history. Meanwhile, the presence of obstacles and/or absorbing material significantly reduces the relative importance of flame-acoustic interactions (Bauwens et al., 2010; Cooper et al., 1986; van Wingerden and Zeeuwen, 1983a). For example, van Wingerden and Zeeuwen (1983a) presented results from a series of propane-air explosions performed in a 5.2 m^3 vented explosion vessel. They found that the high-frequency oscillations (≈ 200 Hz) corresponding to that of a standing acoustic pressure wave between the vessel walls were accompanied by a pressure peak that could be $6-7$ times higher than any other peak produced during the explosion. When all walls were lined with absorbing glass wool, the pressure peaks associated with flame-acoustic interactions were completely eliminated.

A series of publications describe the experimental campaigns conducted in the vented explosion chamber of dimensions 4.6 m × 4.6 m × 3.0 m located at the FM Global Research Campus (Bauwens et al., 2009a, 2010). The publications highlight the physical phenomena that produce several distinct pressure peaks in vented gas explosions. The effects on peak overpressures of varying the vent size (either 5.4 m^2 or

2.7 m^2), the ignition position ('back', 'centre' or 'front', with respect to the vent opening), and the effect of inserting eight square obstacles of dimensions 0.4 m × 0.4 m, spanning the vertical direction of the explosion chamber, were systematically investigated for near-stoichiometric propane-air mixtures (Bauwens et al., 2010). The authors found that the pressure peak generated by acoustic instabilities was particularly important for the experiments performed in empty enclosures. Furthermore, they reported that the peak was enhanced when the vent opening was smaller, and when using centre or front ignition. For these configurations, a larger amount of unburnt reactants was present inside the enclosure at the time the acoustic oscillations developed. Chao et al. (2011) reported quite considerable variations (±50 % between repeated tests) in the maximum overpressure due to flame-acoustic interactions.

Bauwens et al. (2009a) observed that acoustic oscillations of two different characteristic frequencies were produced during the explosions in the 64 m^3 vented chamber: (i) low-frequency oscillations matching the first fundamental mode of a wave propagating inside the chamber parallel to the vent opening ($\approx$ 100 Hz) followed by (ii) high-frequency vibrations corresponding to the natural frequency of various structural components of the chamber ($\approx$ 700 Hz). The most significant pressure rise in the chamber was associated with the development of the high-frequency oscillations. Furthermore, Bauwens et al. (2009a) performed CFD simulations where the walls of the enclosure were forced to oscillate with the frequency and the amplitude observed in the experiments, and found that this was a requirement for reproducing the pressure peak generated by high-frequency acoustics in the simulations. The high-frequency oscillations can only occur in CFD simulations where the structural response of the chamber is modelled.

Section 6.1 presents results from several experimental campaigns performed in the FM Global 64 m^3 vented explosion chamber, where pressure peaks due to acoustic instabilities were observed. The results are compared with FLACS simulations. However, as FLACS does not at present take into account explosion-generated structural vibrations, the pressure peak generated by flame-acoustic interactions cannot be reproduced. Modelling the effect of acoustic instabilities is not considered further in the present doctoral study, as their relevance for the realistic geometries normally encountered in industrial-scale explosions is assumed to be limited.

5.6   Representing the effect of vegetation in gas explosions

This section discusses how fractal-like, flexible obstructions in the form of vegetation affect the flame acceleration in gas explosions, expanding on the work performed for Paper 4 of the present thesis. The experimental campaign in Paper 4 studies the separate effects of flexibility and foliage. Thus, it addresses two separate influences on flame propagation in obstructed regions that must be represented sub-grid when modelled by a CFD tool based on the PDR concept.

Experiments with an idealised, symmetric geometry layout, such as that used in Paper 3, are highly useful for investigating and (as far as possible) isolating different physical mechanisms leading to flame acceleration in gas explosions. The majority of the large-scale gas explosion experiments commonly used for model validation have been performed in idealised geometries, involving fixed, solid obstacles. In most

cases, all obstructions used in a single test had the same physical dimensions (Bimson et al., 1993; Cronin and Wickens, 1986, 1988; Hjertager et al., 1988; Mercx, 1994, 1996; Pekalski et al., 2014; Tomlin et al., 2015; Wilkins et al., 1999). Notable exceptions are the experimental campaigns from the Blast and Fire Engineering for Topside Structures (BFETS) project phases 2 and 3 (Al-Hassan and Johnson, 1998; Evans et al., 1999; Selby and Burgan, 1998), involving realistic offshore module geometries, and the experiments performed as part of the Buncefield Project Phase 2, investigating flame acceleration through both confined and unconfined regions with vegetation (SCI, 2014). The background for performing experiments of the latter type is briefly summarised in the following section.

5.6.1 Background and motivation

On 11 December 2005, a devastating vapour cloud explosion occurred on the Buncefield oil storage depot in Hemel Hempstead, United Kingdom. The need for investigating the underlying mechanism of the event for future prevention was considered critical (Bradley et al., 2012). The report 'Buncefield Explosion Mechanism, Phase 1', prepared by the Steel Construction Institute (SCI) for the Health and Safety Executive (HSE) suggested that the dense vegetation in certain areas of the facility may have caused significant flame acceleration up to flame speeds where a deflagration to detonation transition (DDT) may occur. The occurrence of a DDT was necessary to explain the extensive pressure damage observed at Buncefield, and CFD simulations performed with EXSIM (SCI, 2009) and FLACS (Bakke, 2010; Gexcon, 2005) supported this scenario.

Bradley et al. (2012) summarised the analysis of the physical mechanism behind the Buncefield explosion together with related research findings. They concluded that one of the subjects needing further study after the first phase of the Buncefield project was *"...the mathematical modelling of explosions through densely packed, small-scale, flexible obstacles..."*. Furthermore, Bakke (2010) concluded that *"More research is needed, however, because even if FLACS predicts flame acceleration in dense vegetation, no evidence exists that applying the code to trees rather than rigid obstacles provides results of acceptable accuracy..."* after presenting the Buncefield explosion simulations. In some of the simulations of the accident performed with EXSIM, ethylene was used instead of propane to account for enhanced burning due to unresolved vegetation components (SCI, 2009).

The Buncefield project, Phase 2 (SCI, 2014), included a series of medium-and large-scale experiments where the effects of varying the type and density of trees or bushes on the flame acceleration in both semi-confined and unconfined gas explosions were studied. The congestion level in each test was characterised by the total length distribution of tree or bush components with different diameters. This study also entailed modelling with FLACS (Pedersen and Brewerton, 2014). Hence, there was a need for a consistent approach for how to account for the specific properties of vegetation in the simulations: (i) flexibility and (ii) the presence of foliage, which effectively consists of numerous small-scale components that cannot be described accurately nor resolved by a CFD tool based on the PDR concept.

Pedersen and Brewerton (2014) studied the effect of flexibility in structural response simulations performed with a simplified version of the 'Natabelle Projectile Simulator'

(Brewerton, 2001), which was written especially for the Buncefield project, and takes input from FLACS simulations. A similar analysis was done as part of the study of the Buncefield accident presented by Bakke (2010). The effect of flexibility was not studied experimentally. Meanwhile, the medium-scale experiments of the Buncefield Project, Phase 2, included a study of the effect of smaller twigs and leaves on the explosion mechanism for birches (SCI, 2014; van Wingerden and Wilkins, 2011). Some of the birches were trimmed to various degrees, where in 'trimming stage 1', components less than 2-3 mm were removed, while for 'trimming stage 2', components less than 4-8 mm were removed. Removing leaves and twigs less than 2-3 mm in diameter reduced the maximum overpressures significantly, by a factor of 2-3. When going from a full tree to 'trimming stage 1', the volume blockage in the volume occupied by the tree was reduced from approximately 0.28 % to 0.17 % (van Wingerden and Wilkins, 2011).

As an extension of these efforts, the experimental study in Paper 4 was conducted to (i) investigate whether the flexible response of tree branches to the flow would significantly reduce the overpressures, (ii) investigate to which degree the presence of foliage contribute to flame acceleration, and (iii) to support the development of a sub-grid modelling approach (based on the approach used by Bakke (2010) and Pedersen and Brewerton (2014)), accounting for flame propagation through regions of vegetation in gas explosions. The findings of Paper 4 therefore address the latter part of the research question of the present thesis: *"how can the sub-grid representation of flame acceleration mechanisms due to instability effects and flow past obstructed regions be improved in a CFD tool used for consequence assessment of gas explosions?"*.

Knowledge about the effect of vegetation on flame acceleration is not only applicable to the investigation of the Buncefield incident. Appropriate modelling guidelines are also relevant for risk assessment for onshore process facilities in general. Such facilities are frequently surrounded by trees and bushes e.g. for screening reasons (Johnson, 2010). Moreover, although the Buncefield incident was thought to be unique at the time, two incidents of the Buncefield type (i.e. involving massive releases of gasoline from storage tanks) have since occurred in San Juan (CSHIB, 2009) and in Jaipur (Johnson, 2009). Accidents where massive hydrocarbon releases happened in regions with vegetation include the events that occurred at Ufa, USSR, in 1989 (Makhviladze, 2011), Port Hudson, Missouri, US, in 1970 (NTSB, 1971) and Brenham, Texas, US, in 1992 (NTSB, 1992).

5.6.2   Experiments

For Paper 4, a series of tests were performed in a 1.5 m × 0.3 m × 0.3 m vented channel. The same experimental rig was used for the experiments presented in papers 2 and 3. The channel had a transparent front wall, allowing for high-speed video analysis of the flame propagation. Pressure-time histories were recorded in four different locations. Branches from Norway Spruce *(Pies abies)*, Mugo Pine *(Pinus mugo)* and Thuja *(Thuja occidentalis)* were inserted in the channel during a series of near-stoichiometric propane-air explosions. The effect of foliage was investigated by performing tests where all needles were removed from the spruce branches, while the effect of flexibility was studied by replacing the bare spruce branches with stainless steel models of similar structure. The steel branches provided the same blockage ratio and spatial distribution of obstructions as the real branches, but would not deform

when exposed to explosion-generated flow. Thuja and Norway Spruce were used in the large-scale experiments that inspired the small-scale study. The small-scale setup, using relatively few obstructions, made it possible to have detailed knowledge about the geometric configurations and initial conditions in the tests.

Figure 5.16a shows one spruce branch with needles, while Figure 5.16b shows three bare spruce branches inserted in the channel prior to testing. All branches were analysed in detail to find their total volume (including foliage when that was present) and the estimated drag area (length $\times$ diameter) of their separate components. The drag area analysis did not include needles. Meanwhile, due to the 'two-dimensional' nature of the branches, a photograph analysis could be performed, where the total two-dimensional area blockage ratio of each branch was estimated. This analysis thus provided a separate measure of the foliage. Paper 4 and Appendix B include further details on the measurements.

(a) Spruce branch with needles.

(b) Spruce branches without needles.
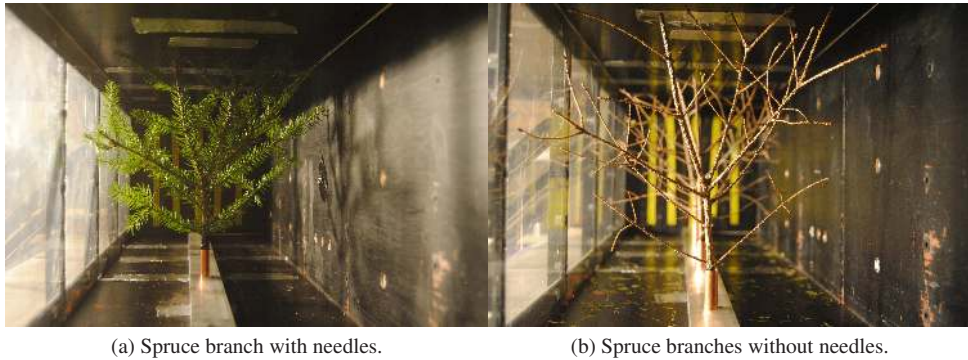
Figure 5.16: Spruce branches inserted in the experimental rig.

The main findings of the experimental campaign can be summarised as follows: (i) the presence of foliage on spruce branches was found to enhance the maximum overpressures by approximately a factor of three, relative to the tests with bare branches, (ii) inserting stainless steel models in the channel approximately doubled the peak overpressures compared to the tests with the corresponding flexible branches, (iii) the increase in overpressure with the presence of foliage corresponded better with the relative increase in area blockage ratio determined from two-dimensional photograph analysis compared with the increase in volume blockage. Figure 5.17 illustrates these effects on the overpressure-time development and flame speed as a function of distance from ignition. Although the steel branch test produces a comparable maximum overpressure to that obtained with flexible spruce branches with needles, the pressure impulse is enhanced when the small-scale obstructions are present. The needles likely generate numerous shear-layers prior to flame arrival that increase the combustion rates immediately downstream of the branch, as discussed in the following.

Tests with the alternative species of trees, pine and thuja, showed that the changes in maximum overpressures relative to the spruce branch tests also approximately scaled with the changes in area blockage ratio from the photograph analysis. However, it is not straightforward to separate the effects of varying flexibility and foliage for the inter-species comparison, as stainless steel models could not be made for these branches.

(a) Pressure-time curves.

(b) Flame speed vs. distance from ignition point. Position of branches marked with vertical grey lines.
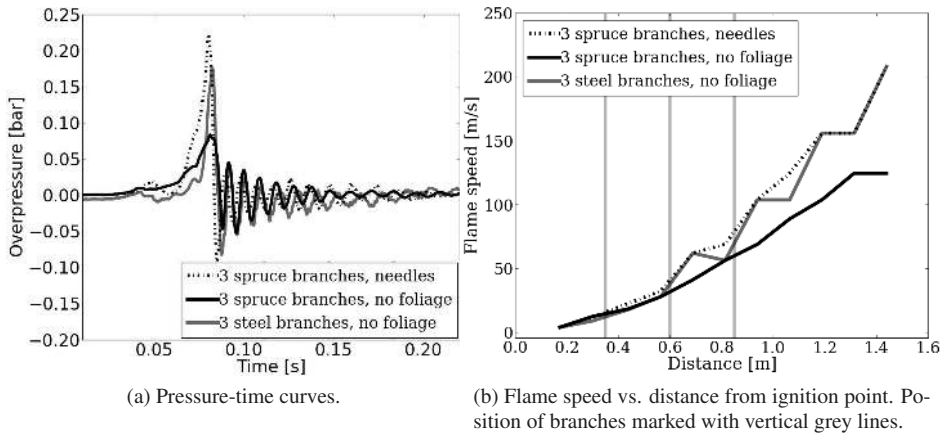
Figure 5.17: Effect of flexibility and foliage for three spruce branches.

The results from the small-scale experiments in Paper 4 suggest that obstructions of very small dimensions may contribute significantly to the overpressure generation in gas explosions. The observations are consistent with findings from direct numerical simulation and experimental studies of non-reacting and reactive flow past square fractal (self-similar) grids (Souloopoulos et al., 2013; Sponfeldner et al., 2015; Zhou et al., 2014). The turbulence diffusivity and scalar mixing rates in the region close to the fractal grid are enhanced when compared to the corresponding region downstream of a regular square grid of the same blockage ratio, where all components have the same dimensions. Souloopoulos et al. (2013) found that the turbulent burning velocity in pre-mixed flames stabilised downstream fractal grids on average was enhanced by 40 % compared to that obtained for a corresponding regular grid. The introduction of additional small-scale structures enhances the number of shear layers in the flow, and they interact in the region close to the grid. The turbulence field further downstream is still dominated by the largest geometry components present, creating large-scale energetic structures that do not dissipate close to the grid (Zhou et al., 2014).

Similar behaviour was observed in the experiments in Paper 3, where the additional shear layers introduced by adding a steel wire helix to the smooth cylinder enhanced combustion in the near-wake, immediately downstream of the cylinder (cf. Figure 11 of Paper 3). However, since the presence of the helix dampened the instability mechanism that produces larger-scale coherent structures further downstream of the obstruction, the overall flame acceleration and explosion overpressure became less than that obtained with a smooth cylinder.

5.6.3 Simulation approach in FLACS

The experimental work in Paper 4 entailed detailed characterisation of the obstructions that were used. However, constructing congestion blocks for modelling purposes that represent the actual branches is not a straightforward task. The degree to which a certain branch will act as a solid object in a gas explosion will depend upon the flow of the specific scenario. For example, for high flame speeds, the flexible obstruction

will have less time to respond to the explosion-generated flow and act more like a fixed obstacle than for low flame speeds.

Specifically, the turbulence generating capacity of a branch depends upon the relative velocity of the branch to the unburnt gas. In the initial forward flow of the unburnt gas, a soft branch will be accelerated by the flow so that it will not generate as much turbulence as a static branch. When the flame front arrives, the flow is still in the forward direction, and the relative velocity of the flow to a flexible branch is less than the absolute velocity. The proportion of reduction is a function of branch mass to drag area (diameter $\times$ length). As drag is proportional to the diameter D and mass to D^2, the larger diameter branch components move less, and the velocity reduction is smaller. Larger branch components will therefore behave more like fixed obstacles compared to smaller branch components.

The phases of the explosion that are important for the turbulence generation must also be identified. The reduction of the turbulence generating effect for branch size is important when the relative velocity for small branches is more or less the same as for the large branches during, approximately, the last 5 ms of the passage of the flame front (Pedersen and Brewerton, 2014). Therefore, a decision has to be made on a lower cut-off size, i.e. the smallest branch diameter where the turbulence generation is approximately equal to that of a fixed obstruction of the same diameter, or the largest diameter for which the turbulence generation can be neglected. As it is flow-dependent, the effective lower cut-off scale for turbulence generation may vary significantly between scenarios.

Consequently, the modelling methodology that is used to represent the sub-grid vegetation components in the FLACS simulations for Paper 4 is based on either the estimated *effective drag area* or the *effective volume* of the obstructions. The largest branch components are modelled explicitly, while the effective drag area or volume of the smaller scale twigs are represented by circular cylinders with appropriate diameters, evenly distributed over the volume that the branch is expected to occupy. The objective is to conserve the measured drag area or volume of the vegetation block that is expected to generate turbulence during the last 5 ms of the passage of the flame front. Accordingly, following the approach proposed by Pedersen and Brewerton (2014), the effect of flexibility is taken into account by assuming a lower cut-off scale of the vegetation components contributing to the turbulence generation. This changes the effective drag area or volume of the representative congestion blocks. Figure 5.18 shows the congestion blocks used for the modelling work in Paper 4.

For both the simulations of the small-scale experiments performed in Paper 4 and the medium- and large-scale experiments performed as part of the Buncefield project, Phase 2 (Pedersen and Brewerton, 2014), it was found that using the effective drag area of the vegetation block gave consistently better trends with varying congestion degree than using the effective volume. Paper 4 therefore presents simulation results where the effective drag area was used to construct the sub-grid congestion blocks.

Using three stainless steel branches instead of three bare spruce branches (cf. Figure 5.16b) enhanced the maximum overpressures in the experiments by approximately a factor of two. This trend is best reproduced in the FLACS simulations by assuming a lower cut-off scale for turbulence production of 2 mm, to account for the overall response of the branches to explosion wind. In reality, this effect would not be the same for all three branches. Indeed, Figure 5.17b shows that the flame acceleration
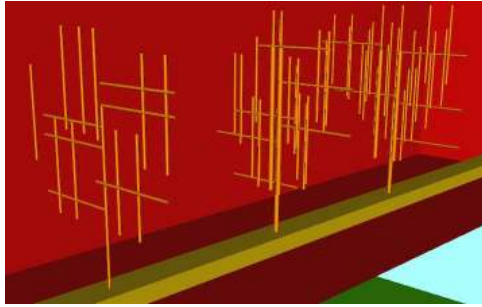
Figure 5.18: Congestion blocks representing spruce branches with foliage in the FLACS geometry.

downstream the first branch is practically identical for the steel model and the corresponding bare spruce branch, suggesting that the first branch acts more or less like a fixed object. This may be due to the initially low flow speeds being unable to bend the branch, combined with the fact that the first branch has less time to respond to the explosion-generated flow.

Pedersen and Brewerton (2014) described FLACS simulations of the experiments from the Buncefield project, Phase 2, where the effect on the explosion mechanism of removing leaves and smaller branches of birch (in different trimming stages) was investigated (cf. Section 5.6.1). These simulations were performed with a standard release of FLACS (Gexcon, 2012). By only accounting for the measured reduction in volume blockage for the first trimming stage, the overpressure trends with increased degree of trimming were not correctly reproduced in the simulations. For example, removing leaves and twigs with diameters less than 2-3 mm reduced the overpressures by a factor of 2-3 in the experiments, while in the simulations, the reduction in maximum overpressure was approximately 20 %. Hence, Pedersen and Brewerton (2014) concluded that the relative increase in flame acceleration due to small-scale vegetation components may not be completely captured by a methodology based on the increase in volume blockage.

Paper 4 applied an alternative strategy. The effect of foliage (only studied experimentally in Paper 4 for the spruce branches) was found to be represented most accurately by multiplying the effective drag area from the flexibility analysis with a 'foliage factor', based on the approximate average increase in cross-sectional area blockage of the spruce branches with needles, relative to the corresponding bare branches. For the spruce branches, this factor was approximately 3.5.

For more general use in consequence modelling for process facilities, it would be possible to estimate such foliage factors based on (a) the type of tree or bush, and (b) a visual interpretation of the density of foliage (e.g. depending on the season). Variations with criterion (b) could be divided into e.g. three categories, such as (1) 'none', (2) 'sparce' and (3) 'full'. Experiments with spruces and birches could then be used to find reference values for evergreens and deciduous plants, respectively.

However, there are considerable uncertainties associated with the modelling approach described here, as the relative contribution of flexibility will change with the flow regime. Furthermore, vegetation is by nature diverse, and general constants for

the 'foliage factor' may not exist. Nevertheless, the present sub-grid modelling approach was able to reproduce the trends observed in experiments. The findings provide useful guidance for how to account for congested regions consisting of vegetation at onshore process facilities.

5.7   Summary

The present chapter expands on the findings of Paper 3 and Paper 4, together with additional key mechanisms, to give an overview of geometry-induced instability effects relevant for industrial-scale explosions.

Flame wrinkling due to sub-grid obstacles in FLACS is taken into account by multiplying a *flame folding factor* with the burning velocity from the combustion model. This sub-grid model corresponds to the equilibrium approach investigated by Weller et al. (1998a). The flame surface area contribution from sub-grid obstacles is computed and taken into account at every time step for each control volume where combustion takes place. This model can in principle be extended with separate contributions accounting for different unresolved effects. Overall, using equilibrium expressions is a simplified and computationally more efficient alternative to solving separate transport equations for flame surface area generated by various physical phenomena.

In order to correctly represent the external explosion in simulations of vented scenarios, several researchers have suggested that including the RT instability effect on the flame surface area is necessary, i.e. only modelling the effect of turbulence is insufficient (cf. Section 5.4). The Rayleigh–Taylor (RT) instability is triggered when a lighter fluid is accelerated into a heavier fluid, for example when a flame front is accelerated over an obstacle or through a vent opening. The linearised growth rate of the RT instability can be studied analytically by including the effect of acceleration in the stability analysis of the perturbed flame front from sections 4.3.2 and 4.3.4. Following the approach suggested by Bauwens et al. (2011), assuming that the RT and intrinsic instabilities occur for significantly different wave numbers, the result from the analysis can be used to represent the linearised growth rate of perturbations due to acceleration. From the linearised growth rate, the increase in flame surface area due to the RT instability can be estimated. A model for flame surface area increase due to the RT instability, based on this correlation, was implemented in FLACS for the present doctoral study. The model was formulated to be consistent with the current framework for modelling flame surface area generation due to sub-grid obstructions (cf. Section 5.1.2). The approach assumes that non-linear effects can be represented by appropriate model constants.

Values for the RT model constants were calibrated by simulating the experimental campaigns described by Bauwens et al. (2011), Chao et al. (2011), Bauwens et al. (2012), and Bauwens and Dorofeev (2014), involving vented fuel-lean hydrogen-air explosions for a range of experimental configurations. Model results for these experiments, obtained by using the sub-grid model for the RT instability together with the Markstein number-dependent burning velocity model from Section 4.6, are presented in Chapter 6, Section 6.1. Additionally, the version of FLACS developed as part of the present thesis, incorporating both RT instability and Markstein number effects, was used to simulate key experiments from Paper 1 in Chapter 6, Section 6.2.

For a certain range of Reynolds numbers, the Bénard–von Kármán (BVK) instability results in vortex shedding downstream of bluff-bodies, cf. Section 5.3. The instability introduces a strong periodicity in the velocity and pressure measurements immediately downstream of the bluff-body, and is associated with a significant increase in the form drag, enhanced mixing, as well as possible structural vibrations and noise. It is clear that vortex shedding will increase the flame surface area and thus contribute to the flame acceleration downstream of obstacles. The KH instability will be present in bluff-body wakes together with the BVK instability for a wide range of Reynolds numbers and geometric configurations in gas explosion-driven flows. Assessing the relative contribution of the KH instability, and how it is presently represented, would require significant additional efforts that are not feasible to undertake as part of the present doctoral study. However, the stability analysis of shear layers, which is presented in Section 5.2.1, is used in the discussion of the BVK instability in Section 5.3.1.

The experimental campaign in Paper 3 of the present thesis investigates the effect of flame surface area generated by the BVK instability downstream bluff-body obstacles. From the findings of Paper 3, vortex shedding appears to have a significant effect on the flame acceleration in bluff-body wakes. The most effective vortex shedding suppression method in the experimental campaign reduced the maximum explosion overpressures by approximately 32 %, while the corresponding reduction in maximum pressure impulse was 25 %. Furthermore, the experiments in Paper 3 indicate that an important effect of vortex shedding may be enhanced turbulence levels further downstream of the bluff-body, resulting from dissipation of the larger-scale, energetic structures. If the effect of unresolved vortex shedding should be accounted for through the modelling of flame surface area downstream obstructions, the flame wrinkling factor should therefore be a transported quantity. Simulations performed with CFD models that resolve a wider range of the turbulence spectrum, e.g. high-fidelity LES models that resolve boundary-layers, could provide further knowledge about the increase in flame surface area from obstacles in different flow regimes.

Based on the findings in Paper 3, vortex shedding will most likely occur also in gas explosion scenarios with higher values of Re. The gas explosion experiments presented by Bauwens et al. (2010), performed in a 4.6 m × 4.6 m × 3.0 m vented enclosure, provide relevant test cases for investigating whether vortex shedding would play a role in more realistic scenarios (i.e. higher values of Re and several obstructions with interacting wakes). The present chapter analyses results from one of the geometrical configurations of this experimental campaign, inducing both a steady and a transient- gas explosion-driven flow field. In the FLACS simulations, vortex shedding occurs only for the scenario involving a steady flow. For the transient case with a non-uniform velocity profile and reacting flow, vortex shedding does not develop quickly enough to affect the simulation. The FLACS simulations presented in the present chapter are therefore not able to confirm whether the pressure-reducing effect of passive control methods would be significant in large-scale gas explosions with multiple obstacles. To confirm whether vortex shedding suppression could constitute a cost-effective risk-reducing measure in real process facilities would require a series of large-scale experiments, specifically designed to investigate this effect.

Flame-acoustic interactions have been observed to produce significant pressure peaks in a number of experimental campaigns involving vented gas explosions. However, modelling the effect of acoustic instabilities is not considered in the present doc-

toral study, as their relevance for the realistic geometries normally encountered in industrial-scale explosions is assumed to be limited. Nonetheless, Section 5.5 includes a brief discussion on these effects.

Finally, Section 5.6 discusses how fractal-like, flexible obstructions in the form of vegetation affect the flame acceleration in gas explosions, expanding on the work performed for Paper 4 of the present thesis. Thus, Paper 4 addresses two separate influences (flexibility and the presence of numerous small-scale obstacles) on flame propagation in obstructed regions that must be represented sub-grid when modelled by a CFD tool based on the PDR concept. The main findings of the experimental campaign in Paper 4 can be summarised as follows: (i) the presence of foliage on spruce branches was found to enhance the maximum overpressures by approximately a factor of three, relative to the tests with bare branches, (ii) inserting stainless steel models in the channel approximately doubled the peak overpressures compared to the tests with the corresponding flexible branches, (iii) the increase in overpressure with the presence of foliage corresponded better with the relative increase in area blockage ratio determined from two-dimensional photograph analysis compared with the increase in volume blockage. Foliage likely generates numerous shear-layers prior to flame arrival that increase the combustion rates immediately downstream of the branch. Similar behaviour was observed in the experiments in Paper 3, where the additional shear layers introduced by adding a steel wire helix to the smooth cylinder enhanced combustion in the near-wake.

The modelling methodology that is used to represent the sub-grid vegetation components in the FLACS simulations for Paper 4 is based on either the estimated *effective drag area* or the *effective volume* of the obstructions. The largest branch components are modelled explicitly, while the effective drag area or volume of the smaller scale twigs are represented by circular cylinders with appropriate diameters, evenly distributed over the volume that the branch is expected to occupy. The objective is to conserve the measured drag area or volume of the vegetation block that is expected to generate turbulence during the last 5 ms of the passage of the flame front. Accordingly, the effect of flexibility is taken into account by assuming a lower cut-off scale of the vegetation components contributing to the turbulence generation. This changes the effective drag area or volume of the representative congestion blocks. The effect of foliage (only studied experimentally in Paper 4 for the spruce branches) was found to be represented most accurately by multiplying the effective drag area from the flexibility analysis with a 'foliage factor', based on the approximate average increase in cross-sectional area blockage of the spruce branches with needles, relative to the corresponding bare branches.

Chapter 6

Additional model results

This chapter presents updated model results for a range of large-scale experimental campaigns conducted in vented enclosures. The simulations were performed with development versions of the CFD tool FLACS that include key findings from the present doctoral study. Specifically, the development versions of FLACS used throughout the chapter apply the Markstein number-dependent burning velocity model discussed in Section 4.6 and Paper 2. Furthermore, the present chapter investigates the effect of modelling additional flame surface area generated by the Rayleigh–Taylor instability, cf. Section 5.4.3.

The experiments presented in Section 6.1 involved a single-compartment 64 m^3 vented explosion chamber, in which the effect on the flame propagation and overpressure development of varying the vent size, the ignition point and the degree of congestion inside the chamber was systematically investigated (Bauwens et al., 2011, 2012; Bauwens and Dorofeev, 2014; Chao et al., 2011). A fuel–lean hydrogen-air mixture was used in all tests. The concentration was varied between 12 vol.% and 19 vol.% hydrogen in air, corresponding to equivalence ratios between 0.33 and 0.56. The range of different mixture concentrations was the main motivation for choosing these particular experiments to test the performance of the model system. Fuel-lean hydrogen–air mixtures in this concentration range are associated with negative Markstein numbers (cf. Figure 4.2) and significant variations in the laminar burning velocity. Furthermore, Bauwens et al. (2009b) and Bauwens et al. (2011) emphasise the importance of modelling the Rayleigh–Taylor instability to capture the external explosion for these configurations.

Section 6.2 presents updated model results from the experimental campaign described in Paper 1, obtained with the same development versions of the CFD tool FLACS as used in Section 6.1. The experimental campaign in Paper 1 provides a challenging validation case for assessing how a CFD tool represents the effects of flame instabilities and turbulence on the burning velocity in vented explosions. The campaign was performed in a twin-compartment enclosure – an explosion rig consisting of two separate vented chambers connected by a narrow doorway. When a gas explosion propagates from one room into another, explosion overpressures may be significantly higher than for an explosion in a single-compartment enclosure with similar total volume and vent size, due to additional turbulence and flame surface area production resulting from interactions between the chambers (Astbury et al., 1972, 1970; Rasbash et al., 1970). Paper 1 compares experimental and model results from this campaign. The paper con-

cludes that improving the representation of the cellular phase of flame propagation, as well as accounting for enhanced flame surface area due to the Rayleigh–Taylor instability, may improve model performance for certain configurations. Section 6.2 thus provides an extension of the work in Paper 1, demonstrating how systematic validation against experiments can be used for developing sub-grid models.

For Section 6.3, the FLACS versions that include key findings from the doctoral study were used for modelling a series of large-scale experiments performed as part of the Blast and Fire Engineering for Topside Structures (BFETS) project, Phase 3A (sponsored by the Health and Safety Executive). In rigs with a low degree of confinement and numerous obstructions of varying size, the effect of turbulence generated downstream obstructions, together with flame surface area increase due to flame folding around objects, is expected to govern the flame acceleration. The realistic offshore modules used in the BFETS Phase 3A campaign differ significantly from the layout of the vented explosions described in sections 6.1 and 6.2. Section 6.3 thus investigates whether the sub-grid models that were initially developed and validated for explosions with a high degree of confinement and idealised obstacle configurations could produce improved results also for explosions in complex geometries with a low degree of confinement. The results can be used to support further development of the model system.

In the following sections, the development version of FLACS applying the Markstein number-dependent model is termed *FLACS v10.4-ma*. When the sub-grid model for the RT instability is activated, the FLACS version is termed *FLACS v10.4-ma-rt*. The results are compared with simulations performed with the standard release *FLACS v10.4r2* (Gexcon, 2015), and in Section 6.2, also with *FLACS v9.1r3* (Gexcon, 2011), as this version was used in Paper 1. The standard FLACS releases are documented in chapters 2 and 3.

6.1 FM Global 64 m^3 vented chamber

Bauwens et al. (2011), Chao et al. (2011), Bauwens et al. (2012) and Bauwens and Dorofeev (2014) describe experimental campaigns conducted in the vented explosion chamber of dimensions 4.6 m × 4.6 m × 3.0 m located at the FM Global Research Campus. The publications highlight the physical phenomena that produce distinct pressure peaks in vented gas explosions. The effects on peak overpressures of varying the vent size (either 5.4 m^2 or 2.7 m^2), the ignition position ("back", "centre" or "front" with respect to the vent opening), the initial turbulence level, and the fuel concentration of hydrogen-air mixtures were systematically investigated. In addition, the experimental campaigns also investigated the effect of inserting eight square obstacles with cross-sections of 0.4 m × 0.4 m, spanning the vertical direction of the explosion chamber. Figure 6.1 shows a representative geometry and computational grid, as used in the FLACS simulations of these experiments. The same geometry was used for the modelling work in Section 5.3.4.

6.1.1 Description of physical phenomena

Bauwens et al. (2011) and Chao et al. (2011) investigated Lewis (or Markstein) number effects in the quasi-laminar and turbulent phase of flame propagation for fuel-lean
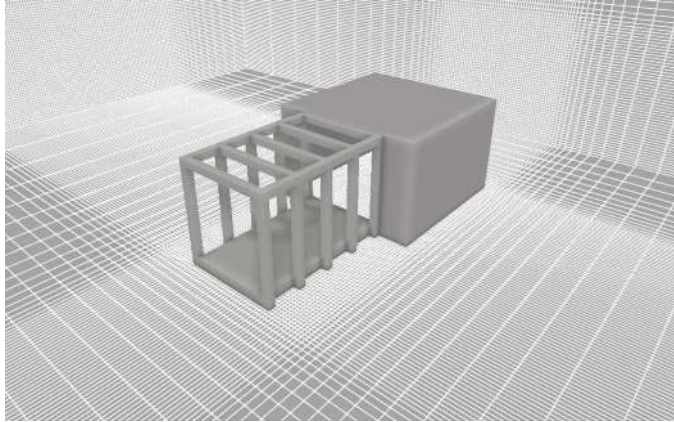
Figure 6.1: FM Global 64 m^3 vented chamber.

hydrogen mixtures (18 ± 0.5 vol.% hydrogen in air) by comparison with results for methane and propane-air mixtures with similar laminar burning velocities. For fuel-lean hydrogen-air mixtures, thermal-diffusive effects significantly enhance flame surface wrinkling due to the Darrieus–Landau instability, cf. Section 4.3. Furthermore, the dependency of the turbulent burning velocity on the turbulence velocity fluctuation u' changes with a varying Lewis number, or more rigorously, a varying Markstein number (cf. Section 4.5.2). These effects were also explored by Bauwens et al. (2012), presenting results for lean hydrogen-air mixtures with varying fuel concentrations (thus effectively varying the Lewis or Markstein number of the mixture). Bauwens and Dorofeev (2014) presented results for experiments where both the initial turbulence levels and hydrogen concentrations were varied systematically.

Overall, the pressure-time histories for tests in the empty enclosures exhibited two distinct peaks. The first pressure peak, denoted p_{ext}, was generated by the external explosion. An external explosion is obtained if sufficient unburnt mixture is pushed out of the vent opening prior to flame arrival at the vent; in particular, this may be significant for back and centre ignition. When the flame front reaches the vent opening, the external turbulent fuel-air cloud ignites. The overpressure generated by the external explosion reduces the rate of venting from the chamber. The Rayleigh-Taylor instability, occurring when a less dense fluid accelerates into a denser fluid, increases the flame surface area and promotes the mass combustion rate as the flame front exits the chamber (cf. Section 5.4). The Helmholtz (or "organ pipe") oscillations are initiated by the venting of combustion products. In the oscillation phase, the Rayleigh-Taylor instability will again be triggered on the flame surface, further promoting the combustion rate when the density gradient is accelerated in the unstable direction. The external explosion may or may not enhance the Helmholtz oscillations through the vent opening, depending on the timing of the external explosion relative to the phase of the oscillation. Variations in the magnitude of p_{ext} up to ±25 % between repeated tests were reported by Chao et al. (2011).

Flame-acoustic interactions (cf. Section 5.5) were found to generate the second pressure peak, denoted p_{vib}. Two distinct types of acoustics were identified in the present campaigns: (i) low-frequency oscillations matching the first fundamental mode

of a wave propagating inside the chamber parallel to the vent opening, assuming the chamber is filled with combustion products ($\approx$ 100 Hz) and (ii) high-frequency vibrations corresponding to the natural frequency of various structural components of the chamber ($\approx$ 700 Hz) (Bauwens et al., 2009a). The pressure peak p_{vib} particularly dominated for front-ignition, due to the relatively high amount of unburnt gas and large flame surface area present in the chamber at the time that acoustics developed. Furthermore, p_{vib} only seemed to be important for empty vented enclosures, since the presence of obstacles dampen flame-acoustics interactions. Chao et al. (2011) reported variations in p_{vib} of ± 50 % between repeated tests.

For the experiments with obstacles inserted, a third pressure peak, p_{obs}, was observed, corresponding to the time when the maximum flame surface area was reached inside the chamber. Chao et al. (2011) reported variations in p_{obs} up to ± 25 % between repeated tests. For some configurations (in particular for back ignition), the pressure peaks p_{ext} and p_{obs} were merged together, so that the separate contributions of the mechanisms could not be assessed.

6.1.2   Simulation results

Sensitivity studies

Simulations were performed using grid resolutions of 0.20 m or 0.10 m inside the chamber. The same grid refinement was used up to 4 m outside the vent opening to capture the external explosion, while a coarser (stretched) grid was applied outside the core domain (cf. Figure 6.1). The main features of the pressure-time curves were similar for both grid resolutions. However, a grid resolution of 0.10 m better resolves the flow features through the vent opening, and generally gives more accurate results than 0.20 m. The simulations in the following sections therefore apply a grid resolution of 0.10 m.

Figure 6.2a shows the maximum observed grid dependency of the peak overpressure for FLACS v10.4r2 (60 % higher overpressure for a grid resolution of 0.2 m compared with a grid resolution of 0.1 m), for a test with 18 % hydrogen-air, centre ignition, and a 5.4 m^2 vent opening. Figure 6.2b shows the corresponding grid sensitivity for FLACS v10.4-ma-rt, which generally is comparable to that observed for the standard version. Similar grid dependency was found for centre ignition, with a 2.7 m^2 vent opening, while the other configurations showed variations of less than 20 % with each refinement.

The sensitivity of the peak overpressures to the hydrogen concentration is significant around the reference concentration of 18 % hydrogen in air (used for all tests by Bauwens et al. (2011)). The maximum simulated overpressures vary with ± 25 % over the experimental uncertainty range of ± 0.5 vol.% hydrogen in air. The effect of varying the initial fuel concentration was studied in a dedicated test series (Bauwens et al., 2012); these experiments are included in the following analysis. The simulated maximum overpressures vary with < 1 % for perturbations in the initial turbulence velocity u' of ± 0.014 m/s (the expected level of accuracy for the measured values of u'). The initial value for the turbulence length scale in the simulations determines the initial conditions for the rate of dissipation of turbulence kinetic energy, ε, in the $k - \varepsilon$ model. The representation of the external explosion appears to be particularly sensitive to the

(a) Grid sensitivity for FLACS v10.4r2.   (b) Grid sensitivity for FLACS v10.4-ma-rt.
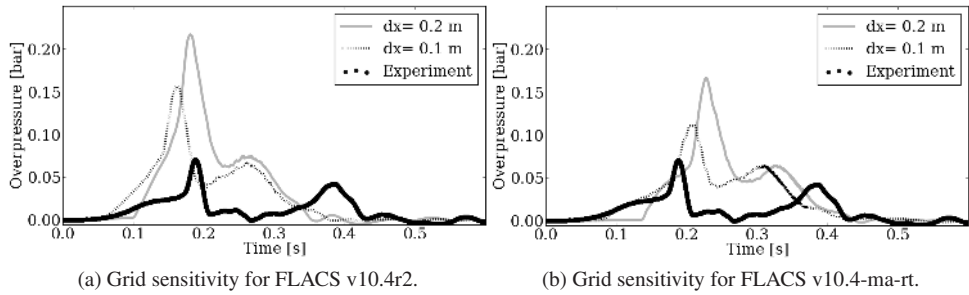
Figure 6.2: Pressure-time histories, vent size 5.4 m^2, centre ignition, 18 % hydrogen-air.

initial conditions for ε; a change in the turbulence length scale from 10 % to 20 % of the grid cell size can give an increase in maximum overpressure of 40 %. In the following analysis, the initial turbulence length scale is set to 10 % of the grid cell size in the core domain, following recommendations from previous validation studies (Gexcon, 2015).

Detailed analysis of selected experiments

Figure 6.3a shows the pressure-time curves for an experiment with back ignition and a 5.4 m^2 vent opening, while Figure 6.3b shows the corresponding flame speeds vs. distance from the ignition point. The vertical lines in Figure 6.3a mark the simulated flame arrival at the vent opening for each of the plotted FLACS versions. In Figure 6.3b, the vertical line marks the position of the vent.

FLACS v10.4r2 over-predicts the initial flame speed (up to 3 m from ignition) by 20-50 %, leading to an earlier and more significant pressure rise than in the experiments. The simulated rate of pressure rise decreases for a short period of time right after flame arrival at the vent opening, as low-density combustion products are vented from the chamber. Similar to the experiment, FLACS v10.4r2 subsequently produces a distinct pressure peak generated by the external explosion (occurring approximately 200 ms after ignition). As the flame front approaches and passes through the vent opening, the model persists in over-predicting the flame speed.

Overall, the pressure-time development given by FLACS v10.4-ma-rt in Figure 6.3a appears to be representative of that observed in the experiment. A closer investigation shows that before the flame front exits the vent opening, flame propagation is governed by the quasi-laminar burning velocity from the Markstein number-dependent combustion model. In this phase, FLACS v10.4-ma-rt accurately reproduces the flame speed. Meanwhile, as the flame propagates through the vent opening, the flame speed is over-predicted also by FLACS v10.4-ma-rt, cf. Figure 6.3b. In this phase, the acceleration of the flame front becomes significant – the sub-grid model for the RT instability therefore enhances the rate of turbulent combustion.

Figure 6.4a shows the pressure-time curves for the same test as in Figure 6.3a, obtained with the development version of FLACS *without* the contribution of the RT instability in the combustion model. Comparing figures 6.3a and 6.4a, it can be seen that the external explosion peak is less distinct when the RT instability effect is omitted.

(a) Pressure-time histories.

(b) Flame velocity vs. distance from ignition.
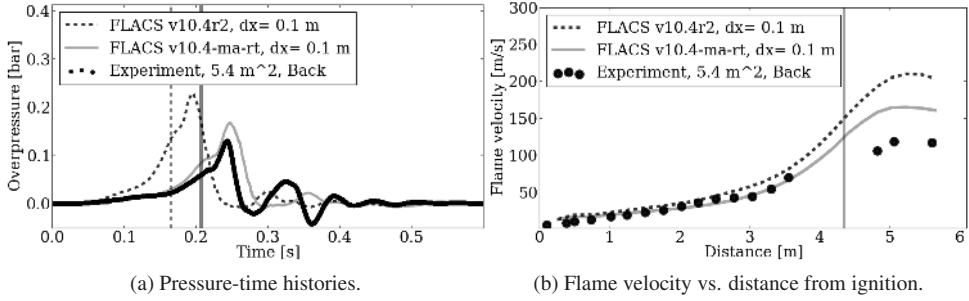
Figure 6.3: Vent size 5.4 m^2, back ignition, 18 % hydrogen-air, FLACS v10.4-ma-rt.

Meanwhile, Figure 6.4b shows that the flame speed through the vent opening is over-predicted, also without the contribution of the RT instability. It is not straightforward to identify what causes this behaviour from the available information on the experiments.


(a) Pressure-time histories.

(b) Flame velocity vs. distance from ignition.
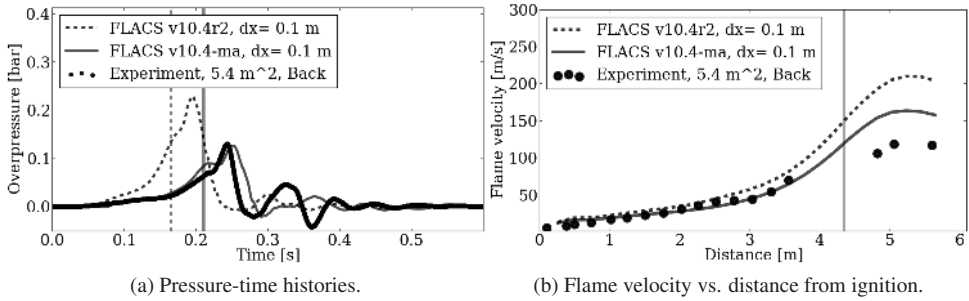
Figure 6.4: Vent size 5.4 m^2, back ignition, 18 % hydrogen-air, FLACS v10.4-ma.

Figure 6.5a shows the experimental and simulated pressure-time curves for a test with front ignition and a 2.7 m^2 vent opening, while Figure 6.5b shows corresponding results for a 5.4 m^2 vent opening. FLACS v10.4r2 closely matches the experimental results up to approximately 150 ms after ignition for both configurations. However, from 200 ms after ignition, the model predicts a more significant pressure rise than observed in the experiments, producing a pressure peak as the flame front reaches the chamber walls. These observations are consistent with the results for back ignition; FLACS v10.4r2 consistently over-estimates the flame speed throughout the explosion history.

FLACS cannot reproduce the coupling between acoustics in the chamber and its structure, and the subsequent enhancement of the flame surface area, as appropriate sub-grid models accounting for this effect currently are not implemented (cf. Section 5.5). Consequently, the model cannot reproduce p_{vib}, the main pressure peak occurring at approximately 600 ms in the front ignition experiments in Figure 6.5. Considering this, the Markstein number dependent burning velocity model employed by FLACS v10.4-ma likely produces flame speeds that agree well with the experiments for front ignition, up to the point in time when flame-acoustic effects start to dominate.

(a) Vent size 2.7 m^2. (b) Vent size 5.4 m^2.
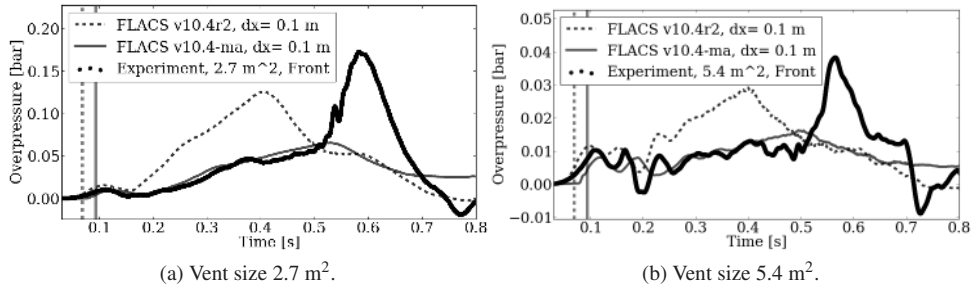
Figure 6.5: Front ignition, 18 % hydrogen-air.

Figure 6.6a shows the pressure-time curves for back ignition, with a 2.7 m^2 vent opening. FLACS v10.4r2 clearly over-predicts the rate of pressure rise in the initial phase of flame propagation, prior to flame arrival at the vent opening. The pressure-time development predicted by FLACS v10.4-ma is more representative of that observed in the experiment. However, both FLACS versions over-predict the combustion rate internally in the chamber, after the flame has exited the vent opening. The simulated maximum overpressures occur as the flame front reaches the chamber walls (and the maximum flame surface area is obtained).

Figure 6.6b shows the pressure-time curves for centre ignition, with a 5.4 m^2 vent opening. FLACS v10.4r2 predicts two distinct pressure peaks for this configuration; the first peak is due to the external explosion, while the second peak is produced as the flame reaches the chamber walls. The model significantly over-predicts the initial flame speed and the overpressure from the external explosion. For FLACS v10.4-ma, the over-prediction of the external explosion pressure is less significant, and from the rate of pressure build-up, the flame propagation before the flame exits the chamber seems to be well represented. The second pressure peak, obtained as the flame front reaches its maximum surface area inside the chamber, also occurs for this model version. The combustion rate inside the chamber is likely over-predicted by both FLACS versions after the external explosion, as the second pressure peak in the experiments is attributed purely to acoustic instabilities (Bauwens et al., 2011).

The experiments with obstructions cannot be analysed in detail, as the publications by Bauwens et al. (2011), Chao et al. (2011) and Bauwens et al. (2012) only list maximum overpressures for these configurations. The experiments are included in the overall analysis in Section 6.1.3.

6.1.3 Overall model performance

In this section, quantitative assessment of the model performance is summarised for FLACS v10.4r2, FLACS v10.4-ma and FLACS v10.4-ma-rt, following principles from the integrated validation framework presented by Hisken et al. (2016) and Skjold et al. (2013a). To perform quantitative assessment of the model performance, a set of *statistical performance measures* (SPM) are defined. According to Duijm and Carissimo (2002), SPM should provide (i) a measure of bias in model predictions, i.e. the tendency of a model to systematically over- or under-predict relevant variables, and (ii) a measure of the spread in predictions, i.e. the degree of scatter around a mean value.

(a) Vent size 2.7 m^2, back ignition.   (b) Vent size 5.4 m^2, centre ignition.
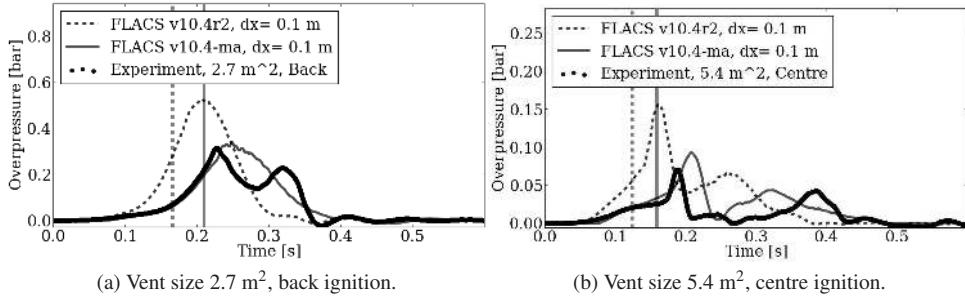
Figure 6.6: Pressure-time histories, 18 % hydrogen-air.

Two of the SPM discussed in the following are also used to assess model performance in Paper 1 and Paper 2 of the present thesis.

Figure 6.7 (left) shows a scatter plot of the maximum obtained overpressure, p_{max}, for all the relevant tests from (Bauwens et al., 2011, 2012; Bauwens and Dorofeev, 2014; Chao et al., 2011), for FLACS v10.4r2 and FLACS v10.4-ma. Figure 6.7 (right) shows the corresponding parabola plot (Hanna et al., 1991a,b; MEGGE, 1996; Tam and Lee, 1998) of the complete data set from Figure 6.7 (left). The parabola plot is a graphical presentation of the *geometric mean bias* (MG), defined as

$$MG = \exp\left[\langle \ln\left(x_p/x_o\right)\rangle\right] , \qquad (6.1)$$

where x_p is the predicted value of a relevant variable, x_o is the observed value, and $\langle\rangle$ is the arithmetic mean, plotted against the corresponding *geometric mean variance* (VG), defined as

$$VG = \exp\left[\langle \ln\left(x_p/x_o\right)^2\rangle\right] . \qquad (6.2)$$

Results are only included for tests where p_{vib} did not produce the maximum overpressure.
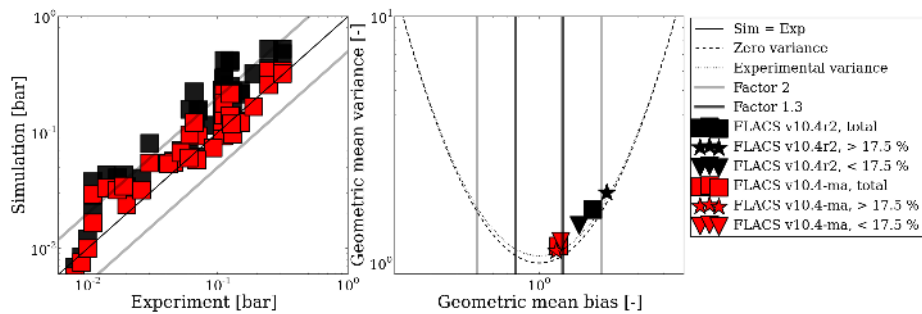
Figure 6.7: Scatter plot (left) and parabola plot (right) of p_{max}, for all tests in the campaigns by Bauwens et al. (2011), Chao et al. (2011), Bauwens et al. (2012) and Bauwens and Dorofeev (2014), for FLACS v10.4r2 and FLACS v10.4-ma.

The dashed parabola in Figure 6.7 (right) represents the curve of zero arithmetic variance, the line $MG = 1$ represents unbiased results; perfect agreement is therefore

represented by the point (1,1). The experimental variability for the maximum over-pressure is plotted in Figure 6.7 (right) together with the zero-variance parabola. The presentation of results should reflect model performance under the various initial and geometric conditions affecting the governing physical phenomena, to identify overall trends for the different configurations (Hisken et al., 2016). In Figure 6.7 (right), MG and VG for tests performed with a hydrogen concentration higher or lower than 17.5 % are plotted separately. Criteria for "excellent" (dark grey lines) and "acceptable" (light grey lines) model performance (in terms of MG), as suggested by Hisken et al. (2016), are also indicated in Figure 6.7 (right). Here, "excellent" model performance in terms of the validation target p_{max} from an experimental campaign is characterised by the measured variable being reproduced with $0.77 < MG < 1.3$ (i.e. a mean bias within a factor of 1.3), and $VG < 1.6$ ("factor two scatter"). For "acceptable" model perfor-mance, the measured p_{max} should be reproduced with $0.5 < MG < 2$ (i.e. a mean bias within a factor of two), and $VG < 3.3$ ("factor three scatter"). Figure 6.8 shows the corresponding results for FLACS v10.4r2 and FLACS v10.4-ma-rt.

In addition to MG and VG, the performance criterion $FAC2$, defined as *the fraction of the predictions, x_p, that are within a factor of 2 of the observed values, x_o*, is used. An "acceptable" value of $FAC2$ exceeds 50 %, while an "excellent" value of $FAC2$ exceeds 75 %.
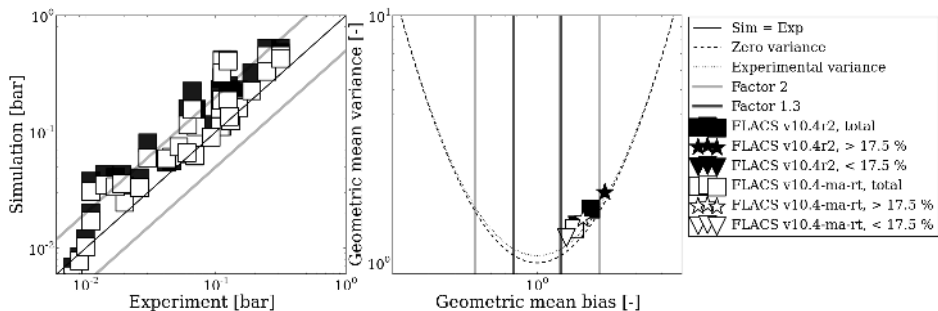

Figure 6.8: Scatter plot (left) and parabola plot (right) of p_{max}, for all tests in the campaigns by Bauwens et al. (2011), Chao et al. (2011), Bauwens et al. (2012) and Bauwens and Dorofeev (2014), for FLACS v10.4r2 and FLACS v10.4-ma-rt.

When considering the results from all campaigns with lean hydrogen-air mixtures from Bauwens et al. (2011), Chao et al. (2011), Bauwens et al. (2012) and Bauwens and Dorofeev (2014) together, the model performance for FLACS v10.4r2 is within the "acceptable" criteria, with $MG = 1.83$, $VG = 1.67$, and $FAC2 = 58$ %. However, Fig-ure 6.7 (right) shows that the maximum overpressures for mixtures with more than 17.5 % hydrogen are over-predicted compared with the leaner mixtures for FLACS v10.4r2, with $MG = 2.14$ and $FAC2 = 43$ %. This trend is significantly less pronounced for FLACS v10.4-ma, where all the maximum overpressures are within the criteria for "ex-cellent" model performance. For example, FLACS v10.4-ma predicts the overpressures from the experiments for mixtures with more than 17.5 % hydrogen with $MG = 1.21$, $VG = 1.12$ and $FAC2 = 100$ %.

The pressure-time curves in figures 6.3a and 6.4a suggest that including the sub-grid model for the RT instability improves the representation of the external explosion. This

mechanism is particularly important for enclosures with large vent openings, when the ignition point is positioned far from the vent. Meanwhile, the model for the RT instability does not seem necessary for reproducing the general overpressure levels in the present experiments with sufficient accuracy. The burning rates resulting from turbulence production by flow through vent openings and past walls seem to compensate for the lack of the RT effect in FLACS v10.4-ma. This may be partly explained by the presence of initial turbulence in the chamber, cf. the results in Section 6.2 for an initially quiescent mixture. Figure 6.8 shows that for FLACS v10.4-ma-rt, the maximum overpressures generally are somewhat over-predicted.

Overall, when compared with the standard FLACS release, the model developments from the present doctoral work improve model performance for the experimental campaigns described by Bauwens et al. (2011), Chao et al. (2011), Bauwens et al. (2012) and Bauwens and Dorofeev (2014). In particular, figures 6.7 and 6.8 show that FLACS v10.4-ma and FLACS v10.4-ma-rt better reproduce trends with variations in the mixture concentration than the standard release FLACS v10.4r2.

6.2 Twin-compartment enclosure

Paper 1 discusses the overpressure-generating mechanisms in a series of explosion experiments performed in a 44 m^3 vented enclosure. The campaign was conducted by British Gas in the early 1980s, however, the experimental results had not been published prior to the publication of Paper 1 in 2013. The objective of the campaign was to obtain data relevant for accidental gas explosions in typical UK homes. Therefore, the enclosure was divided into two 22 m^3 rooms, separated by a 1.98 m × 0.76 m doorway. Vent panels were installed on the front wall of each room (cf. Figure 6.9).
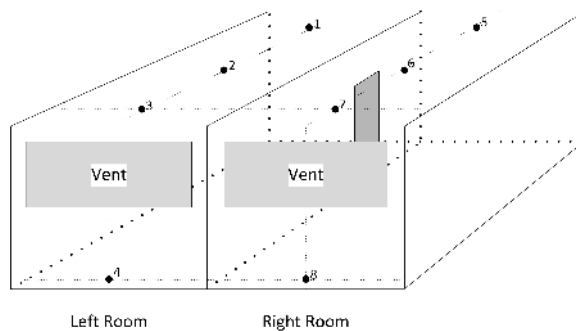

Figure 6.9: Sketch of the twin-compartment enclosure. Positions of pressure transducers are marked with black dots.

The majority of the experimental research related to vented explosions has been performed for single-compartment enclosures. The results from such campaigns demonstrated that the pressure-time history of a vented explosion in general will show a number of peaks, with different physical phenomena contributing to each peak (Bauwens et al., 2010; Butlin and Tonkin, 1974; Cooper et al., 1986; Harrison and Eyre, 1987; Solberg et al., 1981; van Wingerden, 1989; van Wingerden and Zeeuwen, 1983a,b).

Section 6.1.1 describes the physical mechanisms that typically govern the flame propagation in vented explosions. With several interconnected chambers present, the situation is even more complex. When a gas explosion propagates from one room into another, explosion overpressures may be significantly higher than for an explosion in a single-compartment enclosure of similar total volume and vent size, due to additional turbulence and flame surface area production resulting from interaction between the chambers (Astbury et al., 1972, 1970; Rasbash et al., 1970). The degree of interaction may depend significantly on the timing of pressure panel failure and the rate of turbulent combustion, therefore, such explosions are challenging to model with CFD tools that rely on sub-grid models for these processes.

A total of 85 experiments were performed in the twin-compartment enclosure, and a selection of 22 experiments were analysed and modelled in Paper 1. These represent a wide range of configurations, resulting in explosion overpressures ranging from 0.04 to 0.46 bar. For the tests considered in Paper 1, both chambers were either half-filled or completely filled with a 10 vol.% natural-gas mixture in air. The ignition point was either located at the centre of the back wall (opposite of the vent opening) or in the centre of the left chamber (termed the *ignition chamber* in the following). Furthermore, the effect on the explosion mechanism of inserting a light-weight, initially closed door in the doorway between the rooms was investigated.

For the purpose of the analysis, the tests were divided into three classes: the *Type A* experiments involved enclosures where the vent panels fitted in each room were of the same size (and consequently, nearly identical failure pressures), in the *Type B* experiments, the vent panel in the ignition chamber was larger than in the secondary chamber, while in the *Type C* experiments, the vent panel in the ignition chamber was smaller than in the connected room. The results showed that the relative size (and consequently the failure pressure) of the vent panels significantly affected the explosion mechanism and overpressures.

The following sections focus on how the model developments described in Paper 2 and chapters 4 and 5 of the present thesis affect simulations of a few selected tests from the experimental programme. The presented results are considered to be representative of the campaign. To support the discussion, Section 6.2.1 summarises the governing physical phenomena in the Type A, B and C experiments.

6.2.1 Description of physical phenomena

Paper 1 discusses the explosion mechanism in terms of the three experiment classes, types A, B and C. In almost all of the experiments, the explosion pressure-time profiles displayed two distinct peaks. The first peak (denoted p_1) was always associated with the removal of one or both of the vent panels (in either of the two compartments) and its magnitude was equal to or slightly greater than the failure pressure of the panel. The second pressure peak (denoted p_2) was found to be more complex in origin and significantly more variable in magnitude.

Except for the presence of the door, both compartments of the explosion rig were empty, i.e. no additional obstructions were present to promote flame acceleration. The response of the combustion rate to turbulence and large-scale unsteady flow structures generated by the flow of reactants through vent openings (under varying degrees of confinement), was the dominant overpressure-generating mechanism in all tests. In ad-

dition, pressure differences between the chambers that developed during the explosion were seen to push the flame front for several configurations. This further enhanced the combustion rate. As for single-compartment enclosures, the RT instability increases the flame surface area when the flame front is accelerated towards the reactant mixture, cf. Section 5.4. Intrinsic instability effects resulting in cellular flame propagation (described in Section 4.4) govern the initial pressure rise, and are therefore important for the timing of events in the explosion history.

Since the enclosures used for the experiments in Paper 1 were empty, flame-acoustic interactions may be expected to generate overpressure. Pressure oscillations were indeed recorded in a few tests, occurring well after p_1 and p_2. Meanwhile, the oscillations did not generate any significant pressure rise. Skippon (1985) suggested that acoustic instabilities may be inhibited by the asymmetry of the experimental configuration.

In the Type A experiments, p_1 was found to correspond to the almost simultaneous failing of both pressure relief panels, while p_2 was a result of turbulent combustion external to the explosion chamber. The pressure-time profiles were similar to those which likely would be generated in explosions in a single-compartment enclosure of the same total volume. In the Type A tests, the presence of the door (either open or closed) seemed to have little effect on the maximum overpressures.

For the Type B experiments, the pressure relief panel in the secondary enclosure had a higher failure pressure (and smaller size) than that in the ignition enclosure. Paper 1 proposes a likely explosion mechanism based on video analysis for a typical Type B test with a half-filled enclosure, a closed door, and back ignition. Figure 6.10 shows the outline of the flame front at different time steps for the analysed test. Approximately 150 ms after ignition, the door between the chambers opened, before any of the pressure relief panels failed, and the pressure began to equalise in the two enclosures. The flow through the doorway was seen to distort the flame, causing combustion to begin in the secondary enclosure before either of the vent panels failed. Meanwhile, the continued combustion and pressure increase in the ignition chamber caused the large panel of that enclosure to fail at approximately 265 ms, leading to a backflow into the ignition chamber through the door opening. In turn, this lead to a pressure drop in the secondary chamber, and subsequent flow back into that enclosure. Turbulent combustion in the secondary chamber led to a significant, rapid pressure rise there, eventually causing the smaller pressure relief panel to fail at approximately 410 ms after ignition.

In the Type B experiments, the presence of a closed door was found to significantly promote the combustion rate in the secondary enclosure. The opening process generated additional turbulence in the unburnt mixture. Combined with a higher failure pressure of the vent panel in the secondary enclosure than in the ignition chamber, leading to flame front reversals through the doorway (cf. Figure 6.10), this resulted in markedly higher overpressures than in the experiments with an initially open doorway. The RT instability probably further enhanced the flame surface area during this explosion phase. When the doorway was open from the time of ignition, the explosion mechanism was more similar to that observed in the Type A experiments (p_2 mainly generated by the external explosion).

The Type C experiments were characterised by a large vent panel of low failure pressure in the secondary enclosure, while the ignition enclosure was fitted with a smaller vent panel of higher failure pressure. Paper 1 discusses the likely explosion mechanism in the Type C experiments, based on analysis of videos and pressure-time curves, for
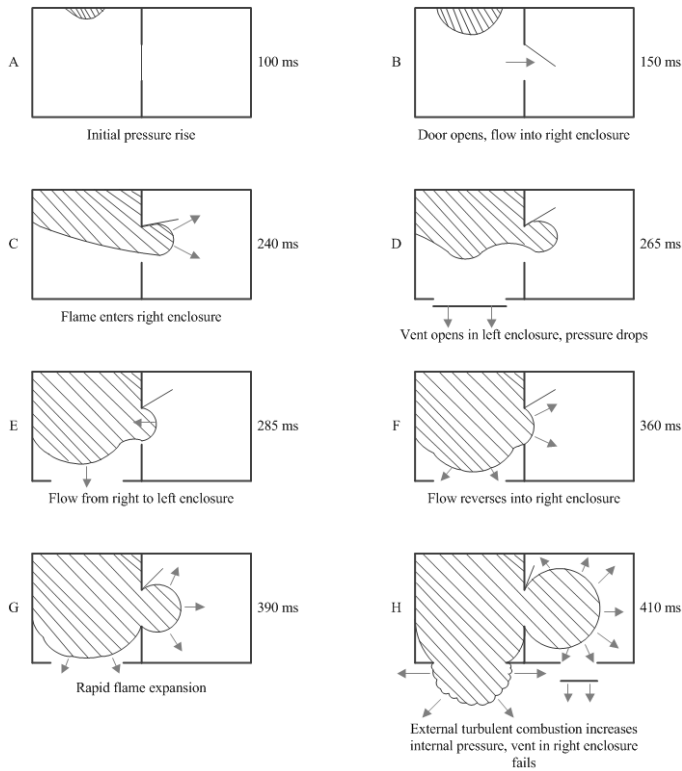
Figure 6.10: Likely explosion mechanism of a representative Type B experiment, half-filled enclosure, back ignition, closed door.

a representative test with a lightweight door fitted in the doorway between the chambers (cf. Figure 6.11). During the initial phase of flame propagation, prior to the failure of either of the panels installed at the front of the enclosure, the interconnecting door opened. At the onset of combustion in the secondary chamber, the large vent panel in that room failed. The subsequent flow out of the secondary chamber pushed the flame front towards the vent opening, promoting highly turbulent combustion and RT instability effects on the flame front. The pressure increase in the secondary enclosure, enhanced by the external explosion, subsequently generated a backflow into the ignition enclosure. Turbulent combustion under highly confined conditions led to significant overpressures also in the ignition enclosure, eventually causing the smaller vent panel there to fail. The Type C experiments involved the overall highest overpressures of the campaign.

For all configurations, when the ignition position was shifted from the back to the centre of the chamber, lower values of p_2 were recorded. Centre ignition led to a weaker external explosion, since less unburnt gas was expelled prior to flame arrival. Furthermore, centre ignition allowed for less flow of reactant mixture through the doorway prior to flame arrival, and consequently less turbulence generation before the onset of combustion in the secondary chamber.
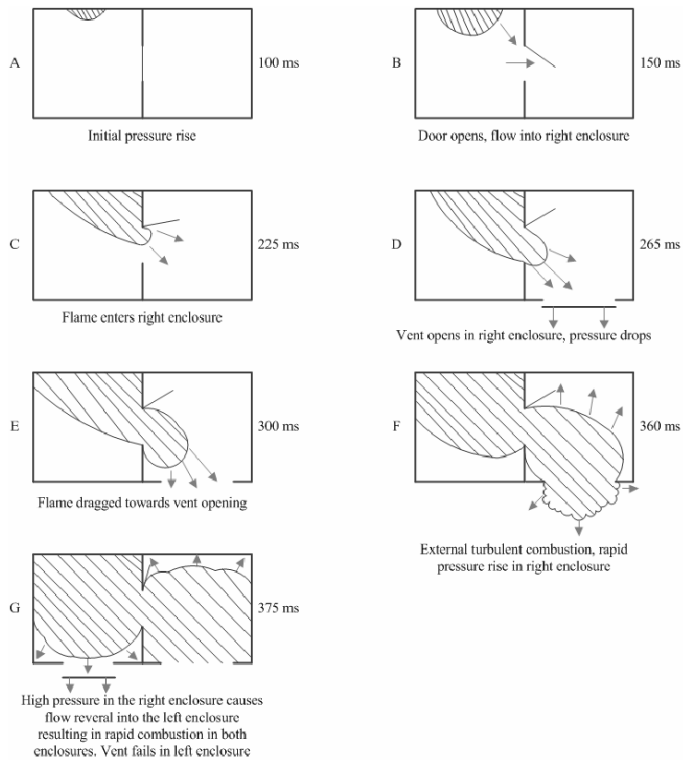
Figure 6.11: Likely explosion mechanism of a representative Type C experiment, half-filled enclosure, back ignition, closed door.

6.2.2   Simulation results

The specifications from the experiments were followed as closely as possible when the simulations were set up. Paper 1 describes the setups – all details are therefore not repeated here.

The vent panels and the door in the experiments were modelled as "pressure relief panels" in FLACS, i.e. as regions with an area porosity varying in time in response to the explosion, according to a designated panel type, weight and failure pressure. Due to the narrow doorway and small vent openings of the geometry, it is necessary to use a grid resolution of 0.05 m to resolve the flow sufficiently. Applying grid cells with characteristic dimensions of less than 0.05 m was found to be prohibitive, due to long simulation times. The analysis in this section (as well as in Paper 1) is therefore performed for a grid resolution of 0.05 m. The simulation setups used to produce the updated results were as similar as possible to those used in Paper 1.

The analysis of the simulation results is complicated by improvements related to the calculation of partial porosities and sub-grid turbulence production introduced in FLACS version 10. The development versions of FLACS that include sub-grid models from chapters 4 and 5, FLACS v10.4-ma-rt and FLACS v10.4-ma, builds on version 10, while the simulations in Paper 1 were performed with FLACS version 9. The turbulence production from partially porous regions in this and earlier versions was found to be

artificially enhanced for a few sensitive scenarios, leading to unphysical results for highly reactive fuels, such as hydrogen. For that reason, the model for turbulence production from sub-grid objects in Equation (2.32) was updated in version 10, together with the pre-processor that computes porosities. The turbulence production from the vent panels is therefore slightly different for the two versions. Consequently, some of the results obtained with FLACS v10.4-ma-rt are also compared with results obtained with FLACS v10.4r2 in the following (so as to be consistent with the analysis in Section 6.1). Finally, in contrast with the analysis in Section 6.1.2, the discussion focuses on the performance of FLACS v10.4-ma-rt, rather than FLACS v10.4-ma. Accounting for the RT instability in the combustion model was found to be necessary to reproduce the pressure peak due to the external explosion in the twin-compartment experiments (as illustrated in Figure 6.12b). This is discussed further in the following sections.

Analysis of the Type A experiments

Figures 6.12a and 6.12b show the pressure-time curves for a representative pressure transducer located in the ignition chamber for two Type A tests, with back ignition, completely filled with natural gas-air, and an open and closed doorway, respectively. Simulation results from FLACS v9.1r3 (used in Paper 1), FLACS v10.4r2 and FLACS v10.4-ma-rt (including developments from the present thesis) are plotted together. In Figure 6.12b, the pressure-time history from FLACS v10.4-ma is also included, for comparison with FLACS v10.4-ma-rt. The vertical dark grey dashed and solid lines represent the failure of the pressure relief panels and the arrival time of the flame at the vent opening in the FLACS v10.4-ma-rt simulations, respectively. These lines are only drawn for the enclosure (ignition or secondary) whose pressure-time development is plotted. Correspondingly, the vertical light grey dashed and solid lines represent the beginning of the vent breaking process and time of arrival of the flame at the vent opening in the experiments, respectively. The latter information is not always available, due to occasional video failure. Where only one plot is shown for an experiment, the events in both chambers were simultaneous.


(a) Full enclosure, back ignition, open door.   (b) Full enclosure, back ignition, closed door.
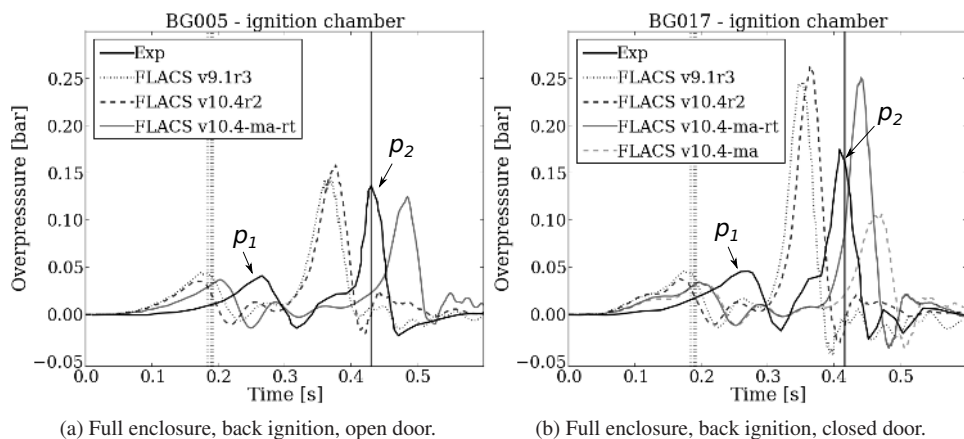
Figure 6.12: Pressure-time histories for two representative Type A experiments.

All FLACS versions predict a higher peak value of p_2 when the door is closed (Figure 6.12b), compared to the test where the doorway is initially open (Figure 6.12a). This effect was less pronounced in the experiments, where the closed door appeared to enhance the duration of the pressure peak (i.e. the pressure impulse) rather than the maximum overpressure. However, all FLACS versions in Figure 6.12b predict a significant pressure rise before flame arrival at the vent opening when the door is initially closed, which is consistent with experimental observations (flame arrival at the vent is only plotted for FLACS v10.4-ma-rt). FLACS v9.1r3 and FLACS v10.4r2 give relatively similar results for these configurations. It is clear from Figure 6.12b that the development version of FLACS that does not include the effect of the RT instability, FLACS v10.4-ma, under-predicts the magnitude of p_2.

Furthermore, figures 6.12a and 6.12b show that the time-of-arrival of p_2 predicted by FLACS v10.4-ma-rt and FLACS v10.4-ma is delayed relative to p_1, when compared with the experimental pressure-time histories and the results from the standard FLACS versions. The Markstein number-dependent burning velocity model described in Chapter 4, employed by FLACS v10.4-ma-rt and FLACS v10.4-ma, results in lower values for the laminar and quasi-laminar burning velocity for near-stoichiometric natural gas-air mixtures than those obtained with FLACS v9.1r3 and FLACS v10.4r2. The laminar burning velocity for methane in the standard releases has been artificially enhanced, presumably to compensate for insufficient representation of other flame acceleration mechanisms (cf. Section 3.2.2). The values employed by FLACS v10.4-ma-rt and FLACS v10.4-ma are more representative of measurements found in literature, see e.g. (Ranzi et al., 2012). While this results in FLACS v10. 4-ma-rt and FLACS v10.4-ma predicting a more representative flame acceleration and pressure development in the initial phase, it likely also contributes to the delayed arrival of p_2 for these versions.

Figure 6.13a compares the turbulent burning velocity predicted by the combustion model developed in Chapter 4 with that predicted by the correlation used in standard releases of FLACS. Figure 6.13a shows u_t computed specifically for a 10 vol.% natural gas-air mixture, as a function of u'. For this specific set of experiments, the length scale used as input to the combustion model was somewhat higher for FLACS v9.1r3 and FLACS v10.4r2 than for FLACS v10.4-ma-rt and FLACS v10.4-ma. Figure 6.13a therefore shows u_t plotted for a fixed length scale of 0.1 m for the correlation by Bray (1990), and 0.02 m for the correlation by Bradley et al. (2013) (cf. Section 3.2.2). These values are representative for the difference in length scales between the model versions. The figure shows that for relatively low turbulence levels ($u' < 10$ m/s), the burning velocity correlation from Bray (1990) (used in FLACS v9.1r3 and FLACS v10.4r2) predicts higher burning velocities than the correlation by Bradley et al. (2013) (used in FLACS v10.4-ma-rt and FLACS v10.4-ma). For higher turbulence levels, the opposite is true. Figure 6.13b shows the simulated u' for the test plotted in Figure 6.12b, 412 ms after ignition, just before the onset of the external explosion. In the earlier phases of the explosion history, the simulated u' from FLACS v10.4-ma-rt is indeed in the range where the correlation by Bradley et al. (2013) would predict lower burning velocities, thus further contributing to the delayed time-of-arrival of p_2. Meanwhile, Figure 6.12b shows that the contribution of the RT instability model leads to a somewhat earlier pressure build-up of p_2 for FLACS v10.4-ma-rt than for FLACS v10.4-ma. Furthermore, the sub-grid model for the RT instability seems to be required to produce representative maximum overpressures from the external explosion.

(a) Values of u_t for the turbulent burning velocity correlations from Bray (1990) (used in FLACS v9.1r3 and FLACS v10.4r2) and Bradley et al. (2013) (used in FLACS v10.4-ma-rt and FLACS v10.4-ma).

(b) Turbulence velocities u' before onset of the external explosion, full enclosure, back ignition, closed door.
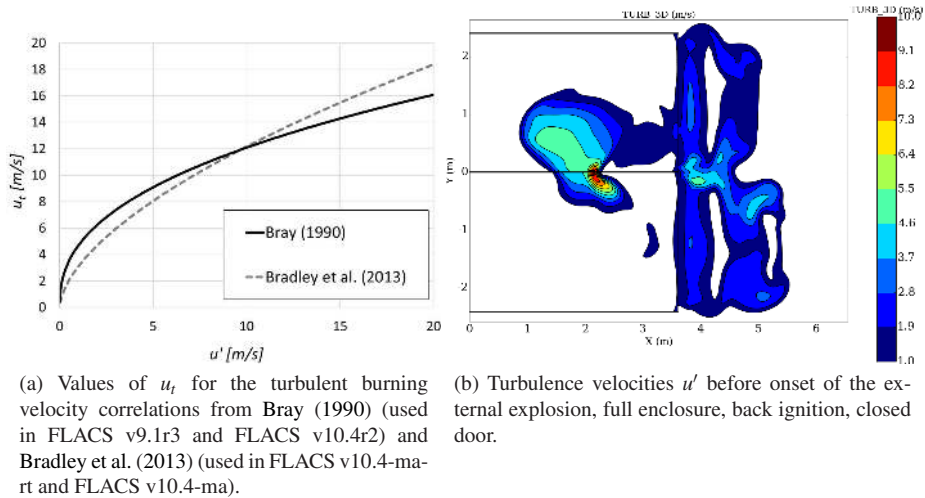
Figure 6.13: Analysis of turbulent burning velocities, u_t, and simulated turbulence velocity fluctuations, u'.

Figures 6.14a and 6.14b show the pressure-time curves for a representative transducer in the secondary chamber for two Type A tests, both with centre ignition, an open doorway, half-filled and completely filled with natural gas-air, respectively. The figures compare results from FLACS v9.1r3 with results from FLACS v10.4-ma-rt. Since the ignition source was located significantly closer to the vent panel in the ignition chamber in these tests, overpressures from two separate external explosion events were recorded. Both experiments generated two separate peaks following p_1, the first, p_{2a}, was attributed to the external explosion outside the ignition chamber, the second, p_{2b}, to the external explosion outside the secondary chamber.

FLACS v9.1r3 produces two distinct pressure peaks for the completely filled enclosure in Figure 6.14b, while over-predicting the overpressures produced by the external explosions somewhat. The double-peak structure is less marked for the half-filled enclosure in Figure 6.14a. FLACS v10.4-ma-rt reproduces the double-peak structure for the test with a half-filled enclosure in Figure 6.14a. For the test in Figure 6.14b, the onset of the external explosion outside the ignition chamber as predicted by FLACS v10.4-ma-rt starts at approximately 300 ms after ignition, while flame arrival at the secondary vent opening occurs 320 ms after ignition. As the pressure generation following the two events are merged together, a clear double-peak structure cannot be discerned in the FLACS v10.4-ma-rt simulation.

The same trends as observed in figures 6.12a and 6.12b are seen also in figures 6.14a and 6.14b. The initial phase of flame propagation is better represented by FLACS v10.4-ma-rt than by FLACS v9.1r3, while the time-of-arrival of p_{2a} and p_{2b} from the development version is over-predicted relative to that of p_1. This is most likely explained by the same mechanisms that were proposed for the tests in figures 6.12a and 6.12b. Additionally, lower flame acceleration rates lead to less contribution from the RT instability model in the centre ignition tests, relative to the back ignition tests.

The findings of Paper 1 are consistent with the results presented here for the Type

(a) Half-filled enclosure, centre ignition, open door.　　(b) Full enclosure, centre ignition, open door.
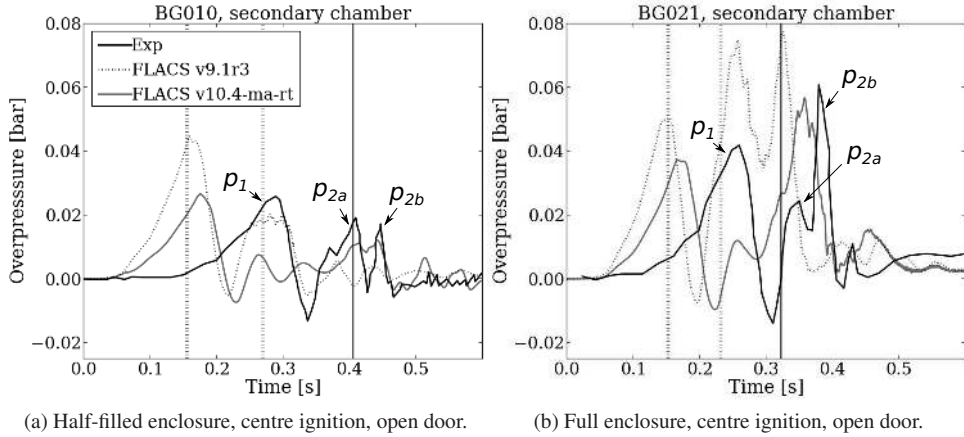
Figure 6.14: Pressure-time histories.

A experiments. Paper 1 observes that the initial flame speeds for FLACS v9.1r3 generally are over-predicted, leading to an earlier pressure rise in the simulations compared with that recorded in the experiments. The Markstein number-dependent combustion model described in Chapter 4, used by FLACS v10.4-ma-rt and FLACS v10.4-ma, seems to give more representative initial flame speeds. Lower flame speeds result in less overshoot of the panel opening pressures, producing a lower value of p_1. Generally, this behaviour represents an improvement of the simulation results obtained with FLACS v10.4-ma-rt relative to those obtained with FLACS v9.1r3.

However, for the Type A experiments, p_1 as predicted by FLACS v10.4-ma-rt still occurs before the corresponding pressure peak is observed in the experiments. This may be caused by the numerical representation of ignition, which most likely does not reproduce the experimental ignition process exactly. It is not straightforward to analyse this further, without additional information about the initial conditions, and, preferably, access to high-quality video recordings from inside of the explosion chambers.

The pressure peak produced by the external explosion, p_2, generally arrives later (relative to p_1) in the simulations with FLACS v10.4-ma-rt than observed in the experiments. This may be due to insufficient representation of the sub-grid turbulence production from the simplified models accounting for pressure relief panels. Meanwhile, once flame acceleration is triggered, representative maximum overpressures are produced for most Type A tests.

Analysis of the Type B experiments

Figure 6.15 shows pressure-time curves for a typical Type B test with a half-filled enclosure, back ignition, and a closed door between the chambers. Paper 1 analyses the simulation of the test in Figure 6.15 in terms of the position of the flame front at different time steps for FLACS v9.1r3, cf. Figure 9 in Paper 1. Figure 6.16 shows corresponding plots for FLACS v10.4-ma-rt.

According to Paper 1, the interconnecting door opened at 150 ms after ignition in the experiment (cf. Figure 6.10). While the door fails at approximately 60 ms in the
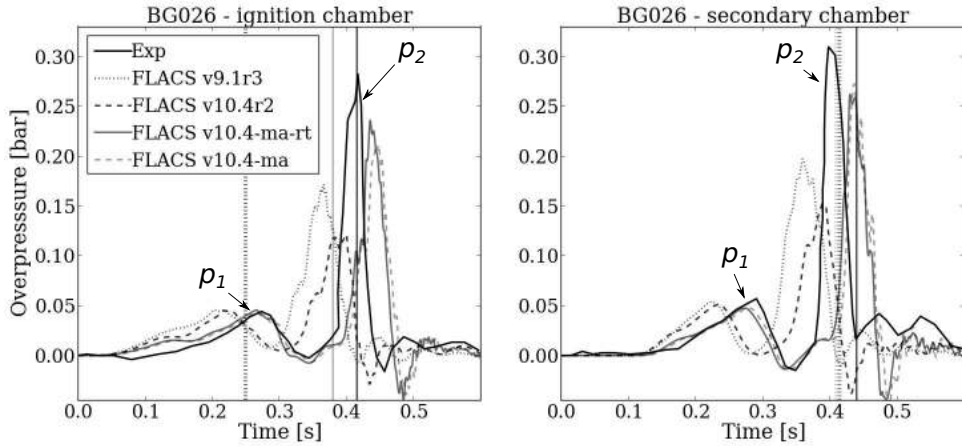
Figure 6.15: Pressure-time histories recorded in both chambers for a Type B experiment, half-filled enclosure, back ignition, closed door.
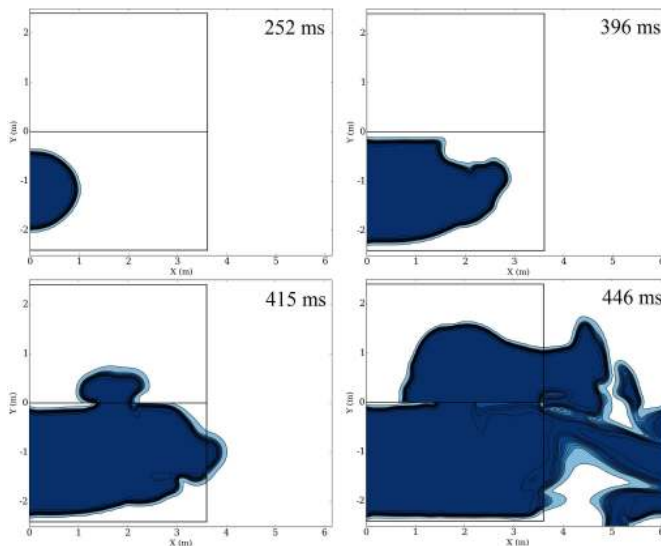

Figure 6.16: Simulated flame position for a Type B experiment, half-filled enclosure, back ignition, closed door. Simulation performed with FLACS v10.4-ma-rt.

simulations performed with FLACS v9.1r3, FLACS v10.4-ma-rt predicts that the door will start to open at approximately 110 ms. Furthermore, the dashed vertical lines in Figure 6.15 show that FLACS v10.4-ma-rt predicts the failure of both pressure relief panels at approximately the same time as recorded in the experiment. Consequently, the simulated time-of-arrival of p_1 agrees well with the experiment.

After the failure of the door in the simulations, the pressure in the two enclosures starts to equalise by a flow of reactant mixture from the ignition chamber into the secondary chamber. However, before the simulated flame front is able to propagate to the

door opening, the large pressure relief panel in the ignition enclosure fails. The premature breaking of the pressure panel in the ignition chamber with respect to the onset of combustion in the secondary chamber leads to a history of events that differs somewhat from that in the experiments (plotted in Figure 6.10). The flow through the doorway reverses as the venting of the ignition chamber increases, pushing the flame front away from the door opening (cf. Figure 9 in Paper 1 and Figure 6.16, at 396 ms). This behaviour is observed for all FLACS versions plotted in Figure 6.15, i.e. in the simulations, combustion never occurs in the right chamber before the left vent panel fails. For FLACS v10.4-ma-rt, the simulated flame propagates into the secondary chamber at the onset of the external explosion, cf. Figure 6.16, at 415 ms. Turbulent combustion in this chamber then generates p_2. When compared with the simulated flame propagation from FLACS v9.1r3, visualised in Figure 9 of Paper 1, this behaviour more closely represents that observed in the experiment (cf. Figure 6.10).

The shift in timing of events has a more significant effect on the pressure-time curves in the Type B experiments, than for the Type A experiments, due to the importance of door-generated turbulence. The p_2 produced by all FLACS versions plotted in Figure 6.15 have a longer duration than in the experiment, while the corresponding maximum overpressures are under-predicted. Meanwhile, the magnitude of p_2 as predicted by FLACS v10.4-ma-rt and FLACS v10.4-ma agrees significantly better with that recorded in the experiment, compared with p_2 from FLACS v9.1r3 and FLACS v10.4r2. As observed for the Type A experiments, the time-of-arrival of p_2 for FLACS v10.4-ma-rt and FLACS v10.4-ma is over-predicted.

Paper 1 suggests that the sub-grid turbulence production from the opening of the door as predicted by FLACS v9.1r3 is insufficient to compensate for the lack of several flame front and flow reversals through the doorway for the Type B experiments (cf. Figure 6.10). Figure 6.17a shows the turbulence velocity u' as predicted by FLACS v10.4-ma-rt in a representative cut-plane 396 ms after ignition (just prior to flame entry into the secondary chamber) for the same test as in figures 6.15 and 6.16. At this point in time, the predicted turbulence velocities generated by reactant flow through the doorway are less than 6 m/s, resulting in a modest flame acceleration through the door opening.

Furthermore, Paper 1 suggests that a sub-grid model including RT instability effects may improve the representation of p_2 in the Type B experiments. The sub-grid model for the RT instability (cf. Section 5.4.2) is included in FLACS v10.4-ma-rt, and the contribution from this model in terms of Ξ_{RT} at 418 ms after ignition is visualised in Figure 6.17b. As expected, the acceleration of the flame front through the doorway and vent opening triggers the contribution to the flame surface area from the RT instability. However, this effect alone is insufficient to ensure an equally rapid pressure build-up for p_2 as measured in the experiments – this would likely require higher initial flame acceleration rates, induced by sub-grid turbulence production.

Higher turbulence levels obtained in the secondary enclosure in the subsequent explosion phase result in the enhanced magnitude of p_2 predicted by both FLACS v10.4-ma-rt and FLACS v10.4-ma, relative to the standard releases. The role of the RT instability does not appear to be crucial for generating p_2 when the mechanism behind this pressure peak is turbulent combustion under a high degree of confinement, such as in the Type B experiments with an initially closed door. Meanwhile, as observed in Figure 6.15, the contribution of the RT instability model in FLACS v10.4-ma-rt gives an

earlier pressure rise relative to p_1 than that predicted by FLACS v10.4-ma.

(a) Turbulence velocity u', 396 ms after ignition.

(b) Contribution of RT instability model, Ξ_{RT}, 418 ms after ignition.
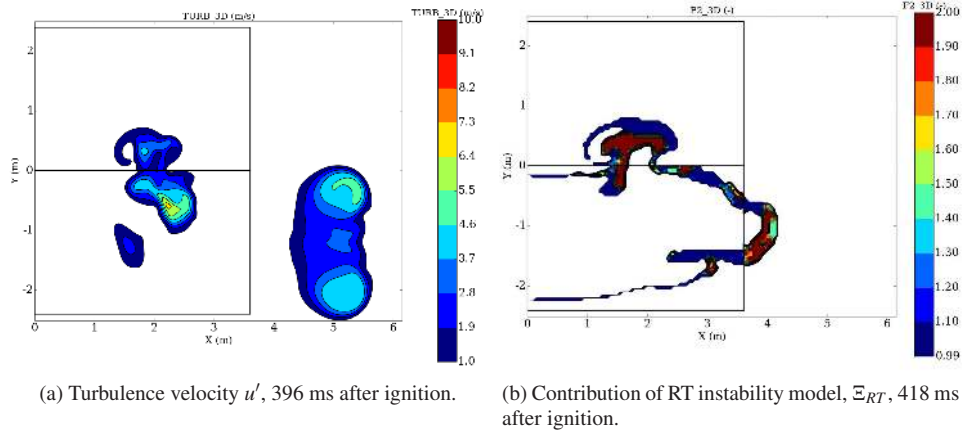
Figure 6.17: Type B experiment, half-filled enclosure, back ignition, closed door. Simulation performed with FLACS v10.4-ma-rt.

Figure 6.18 shows the results from a Type B test with a configuration corresponding to that of the test plotted in Figure 6.15, with centre ignition instead of back ignition. Overall, the same trends as for back ignition are seen for this configuration; the initial flame speed and time-of-arrival of p_1 is more accurately predicted by FLACS v10.4-ma-rt than by FLACS v9.1r3. However, in this test, the predicted time of arrival of p_2 relative to p_1 is similar for both FLACS versions.

In the experiment, a double-peak was recorded in the ignition chamber after p_1, see Figure 6.18 (left). The first of these peaks was due to the external explosion outside the ignition chamber, closely followed by p_2, generated by turbulent combustion in the secondary chamber. For both FLACS simulations, these separate events cannot be clearly discerned in the pressure-time history. As for back ignition (cf. Figure 6.15), the rate of turbulent combustion in the secondary chamber appears to be under-predicted by both FLACS v10.4-ma-rt and FLACS v9.1r3. Meanwhile, FLACS v10.4-ma-rt produces a p_2 that is more representative of that recorded in the experiment.

Analysis of the Type C experiments

Overall, FLACS v9.1r3 reproduces the maximum overpressures of the Type C experiments within ± 50 % – although with a bias towards under-prediction, see figures 16 and 17 in Paper 1. Similar to the Type A and Type B experiments, panel failure in the FLACS v9.1r3 simulations occurs significantly earlier (in terms of how far the flame front has progressed), compared with the experiments. Meanwhile, the pressure-generating mechanism for the Type C experiments appears to be relatively insensitive to the shift in timing of events.

Figure 6.19 shows updated pressure-time curves for a typical Type C test half-filled with a 10 vol.% natural gas-air mixture, with back ignition and a closed door. Figure 6.20 shows the flame position at selected time steps for the same test, simulated with
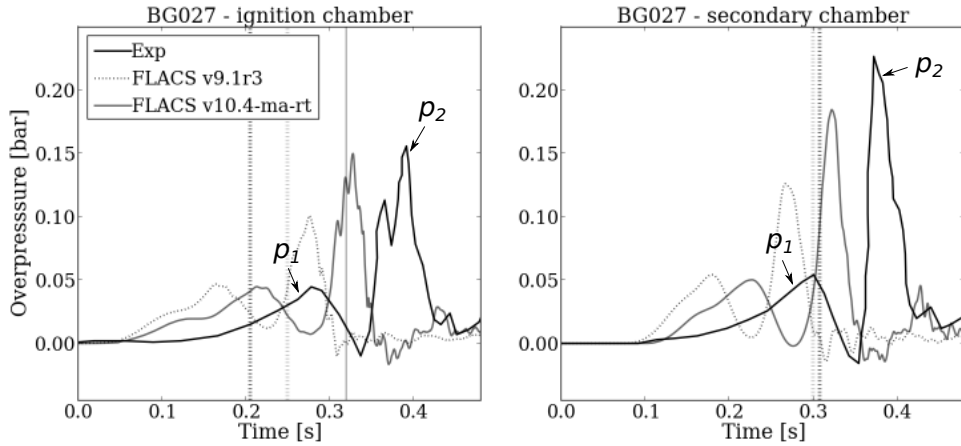
Figure 6.18: Pressure-time histories for a Type B experiment, half-filled enclosure, centre ignition, closed door.

FLACS v10.4-ma-rt. The corresponding plots for FLACS v9.1r3 can be found in Figure 14 in Paper 1. As for the majority of the simulated Type A and Type B experiments, FLACS v10.4-ma-rt predicts an initial pressure rise that is more representative of that observed in the experiment, when compared with the standard releases. Furthermore, the time-of-arrival of the second pressure peak, p_2, is over-predicted by FLACS v10.4-ma-rt and FLACS v10.4-ma. For the test in Figure 6.19, FLACS v10.4-ma-rt gives a magnitude of p_2 which agrees well with the experiment, while the pressure impulse is somewhat over-estimated. Figures 6.19 and 6.20 show that in contrast with the corresponding FLACS v9.1r3 simulation (cf. Figure 13 in Paper 1), FLACS v10.4-ma-rt does not predict failure of the vent panel in the ignition enclosure before the onset of the external explosion outside the secondary enclosure. This leads to a simulated explosion mechanism that more closely represents that observed in the experiments, cf. Figure 6.11.

Figure 6.21 (left) shows u' in a representative cut-plane just after the flame front has exited the vent opening of the secondary chamber, while Figure 6.21 (right) shows the corresponding distribution of Ξ_{RT}. The simulation was performed with FLACS v10.4-ma-rt. Figure 6.21 (left) together with Figure 6.13a indicate that the turbulence production in the later stages of the explosion history will result in a turbulent burning velocity that is higher when computed from the correlation by Bradley et al. (2013), used in FLACS v10.4-ma-rt and FLACS v10.4-ma, than from the combustion model used in the standard FLACS releases. The RT instability model (cf. Figure 6.21 (right)) further enhances the burning velocity in the Type C experiments as the flame is accelerated through the secondary chamber towards the larger vent opening. The combined contributions from these two sub-grid models result in the enhanced magnitude of p_2 in Figure 6.19, while the delayed time-of-arrival of the pressure peak is likely explained by the same mechanisms as for the Type A and B experiments. However, Figure 6.19 shows that including the sub-grid model for the RT instability somewhat improves the prediction of both the time-of-arrival and magnitude of p_2.
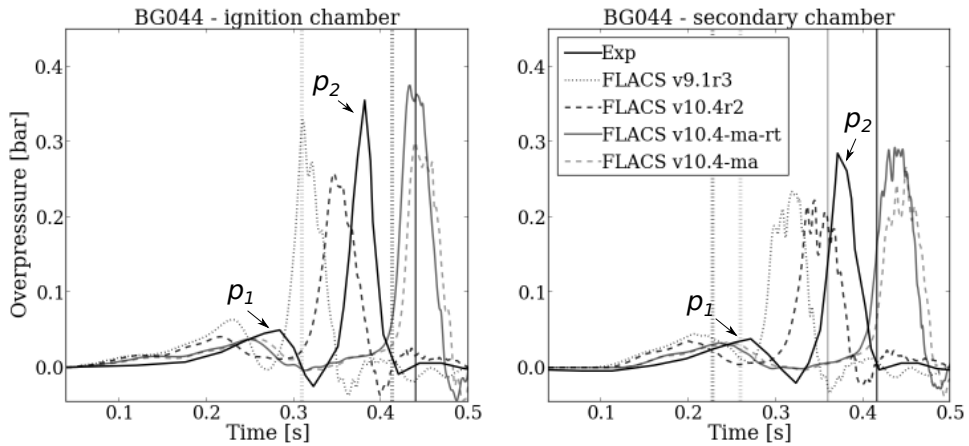
Figure 6.19: Pressure-time histories for a Type C experiment, half-filled enclosure, back ignition, closed door.
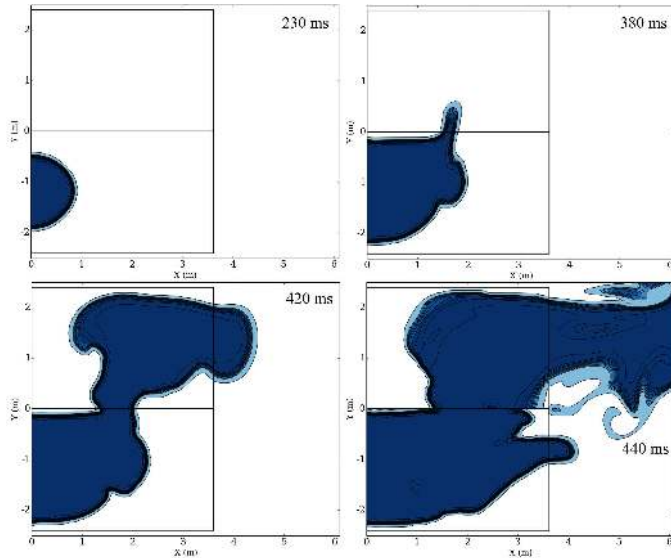

Figure 6.20: Flame position for a Type C experiment, half-filled enclosure, back ignition, closed door. Simulation performed with FLACS v10.4-ma-rt.

6.2.3 Overall model performance

The experimental campaign described in Paper 1 provides challenging validation cases for assessing how a CFD tool represents the effects of flame instabilities and turbulence on the burning velocity in vented explosions. Inherent variability in initial and boundary conditions in the experiments, combined with the sensitivity of the explosion mechanism to the timing of subsequent events, further complicate the analysis. Paper 1 emphasises that the CFD tool FLACS mainly has been developed for predicting the consequences of explosions in congested rigs, where the flow and flame front inter-
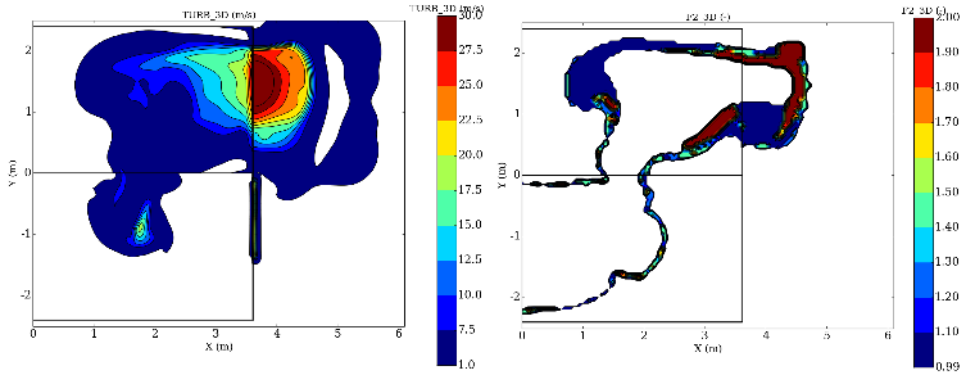
Figure 6.21: Turbulence velocity u' (left) and Ξ_{RT} (right), 420 ms after ignition for a Type C experiment with a half-filled enclosure, back ignition, closed door. Simulation performed with FLACS v10.4-ma-rt.

acting with complex sub-grid geometry (represented by partial porosities) is the main mechanism driving the flame acceleration. Furthermore, the paper underlines that its objective is to analyse the performance of the model in empty enclosures, where a range of subtle interactions between the flow and the combustion rate contribute to the overpressure generation.

Careful validation against experiments is necessary for the development of sub-grid models. In particular, Paper 1 proposes that an alternative burning velocity model for laminar and quasi-laminar flame propagation could improve the general model performance presented for FLACS v9.1r3, as the initial phase affects the timing of important explosion history events. Furthermore, Paper 1 suggests that a sub-grid model for the RT instability should contribute to the simulated flame acceleration. Chapters 4 and 5 of the present thesis discuss the development of several relevant sub-grid models. Results from simulations performed with the development version FLACS v10.4-ma-rt were presented in this section to investigate whether the improvements suggested by Paper 1 would indeed be effective.

It is clear that FLACS v10.4-ma-rt produces more representative initial flame speeds than FLACS 9.1r3 and FLACS v10.4r2. While the failure of the door and the pressure relief panels were more accurately predicted by FLACS v10.4-ma-rt in terms of timing, this did not change the subsequent simulated explosion mechanisms significantly. However, the combustion model developed in Chapter 4 resulted in improved representation of the dominant pressure peak for the Type B experiments with a closed door. As expected, the sub-grid model for the RT instability contributed to the combustion rate when the flame front was accelerated through vent openings. In particular, this contribution was found to be necessary for FLACS v10.4-ma-rt to reproduce the external explosion mechanism in the Type A experiments.

Figure 6.22 (left) shows a scatter plot of the maximum obtained overpressure, p_{max}, for all the simulated tests in Paper 1, for FLACS v10.4r2 and FLACS v10.4-ma-rt. Figure 6.22 (right) shows the corresponding parabola plot of the data set from Figure 6.22 (left). Section 6.1.3 describes the plot types; this information is not repeated here.
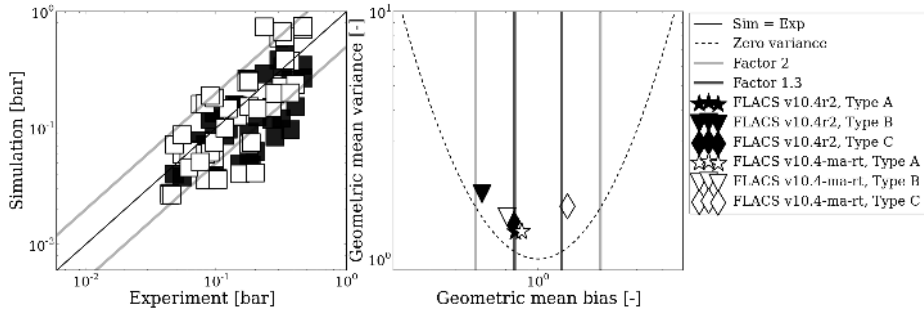
Figure 6.22: Scatter plot (left) and parabola plot (right) of the maximum overpressure, for all simulated tests in Paper 1, FLACS v10.4r2 and FLACS v10.4-ma-rt.

When comparing model performance in terms of p_{max}, FLACS v10.4-ma-rt and FLACS v10.4r2 give similar predictions for the Type A experiments. Meanwhile, FLACS v10.4-ma-rt clearly predicts more representative overpressures for the Type B experiments, compared with those obtained with FLACS v10.4r2. This is consistent with the discussion in Section 6.2.2; the combustion model from Chapter 4 results in higher turbulent combustion rates in the secondary chamber than the model used in standard FLACS releases. For the Type C experiments, FLACS v10.4-ma-rt shows a tendency towards over-prediction of p_2, while FLACS v10.4r2 under-predicts the maximum overpressures. To summarise, the most significant improvement in overpressure predictions from FLACS v10.4-ma-rt, relative to FLACS v10.4r2, is seen for the Type B experiments.

Together with instability effects, turbulence produced by the failure of the interconnecting door and flow through vent openings dominate the overpressure-generation in these experiments. The physical mechanisms promote combustion both internally and externally to the explosion chamber. However, as there are considerable uncertainties associated with the modelling of these processes, it is not straightforward to determine the limitations in either version of the CFD model. By including a wide range of vented explosion scenarios, with different geometric configurations, the relevant sub-grid models can be more extensively tested.

6.3 Large–scale offshore module: repeated tests

In this section, the effect of including the sub-grid models implemented in FLACS for the present doctoral study is investigated for explosion experiments in large–scale complex geometries (referenced in Section 1.3.1). A summary of the results is presented in the following.

The project Blast and Fire Engineering for Topside Structures (BFETS), Phase 3A (sponsored by the Health and Safety Executive) included 45 explosion experiments with natural gas in offshore modules of dimensions 28 m $\times$ 12 m $\times$ 8 m (Al-Hassan and Johnson, 1998; Evans et al., 1999; Foisselon et al., 1998). The investigated parameters included degree of congestion (equipment density), degree of confinement (vent area), ignition location, repeatability, and the effect of various water deluge layouts. The

rigs all had a relatively low degree of confinement. The equivalence ratio of the fuel-air mixture varied between ER=1.0 and ER=1.1. Figure 6.23 shows a representative geometry from this programme.
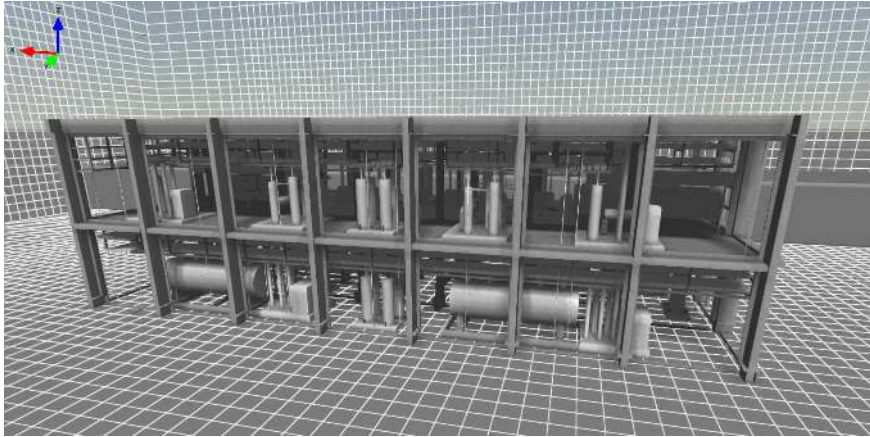

Figure 6.23: Example of experimental rig used in BFETS Phase 3A.

The repeatability of results from large-scale experiments was investigated in the "Alpha-series" (5 repeated experiments) and "Beta-series" (6 repeated experiments) of the BFETS Phase 3A campaign. In general, results from nominally identical experiments may vary due to differences in e.g. fuel concentration and atmospheric conditions that are difficult to control and measure accurately, as well as inherent variability of the physical phenomena, for example resulting from the interaction of shock waves with the flame front (Evans et al., 1999). The "Alpha" and "Beta" experiments are unique; several repetitions of large–scale experiments are rarely performed due to the relatively high costs associated with each test. The two series therefore provide valuable validation cases for consequence models representing gas explosions in realistic geometries.

The "Alpha-series" were performed with the ignition location placed centrally in the offshore module, while in the "Beta-series", the flammable mixture was ignited at the end of the rig. The congestion level in the module was higher overall for the "Alpha-series" (average volume blockage 9.62 %) than for the "Beta-series" (average volume blockage 8.27 %). All tests were performed with near-stoichiometric natural gas-air mixtures with equivalence ratios ϕ ranging between 1.05 and 1.14.

The effect of including the sub-grid models implemented in FLACS for the present doctoral study was investigated for the repeated "Alpha-" and "Beta-series". The realistic offshore modules used in the BFETS Phase 3A campaign differ significantly from the layout of the vented explosions described in sections 6.1 and 6.2; these had a high degree of confinement, and symmetrical, idealised obstacle configurations. Vented explosions are ideal for investigating certain physical phenomena, in particular flame acceleration in the quasi-laminar phase and the effect of the Rayleigh–Taylor instability. In rigs with a low degree of confinement and numerous obstructions of varying size, the effect of turbulence generated downstream obstructions (cf. Section 4.5), together with flame surface area increase due to flame folding around objects (cf. Section 5.1),

is expected to govern the flame acceleration. Additionally, the RT instability may increase flame surface area as the flame is accelerated over obstacles or through the vent openings alongside the rig.

Figures 6.24 and 6.25 compare the maximum overpressures and pressure impulse values predicted by *FLACS v10.4-ma*, *FLACS v10.4-ma-rt* and standard *FLACS v10.4r2* (plotted against the distance from the ignition point) against all tests in the "Alpha-series" and "Beta-series", respectively. These three FLACS versions were also used for the modelling work presented in sections 6.1 and 6.2.
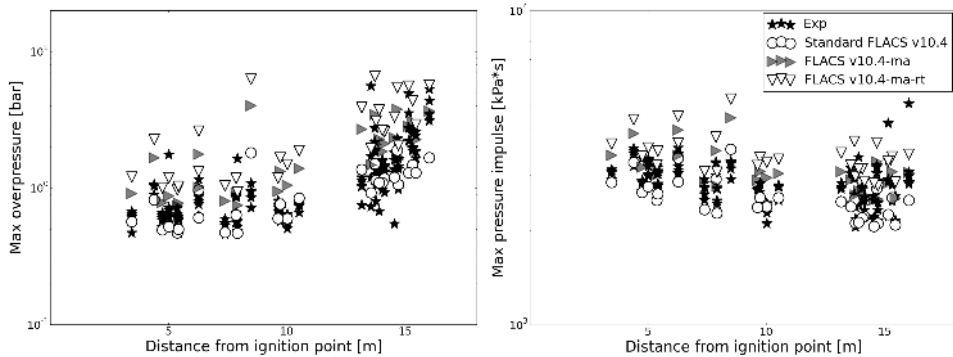
Figure 6.24: Maximum overpressures (left) and maximum pressure impulse (right) vs. distance from ignition point, "Alpha-series".
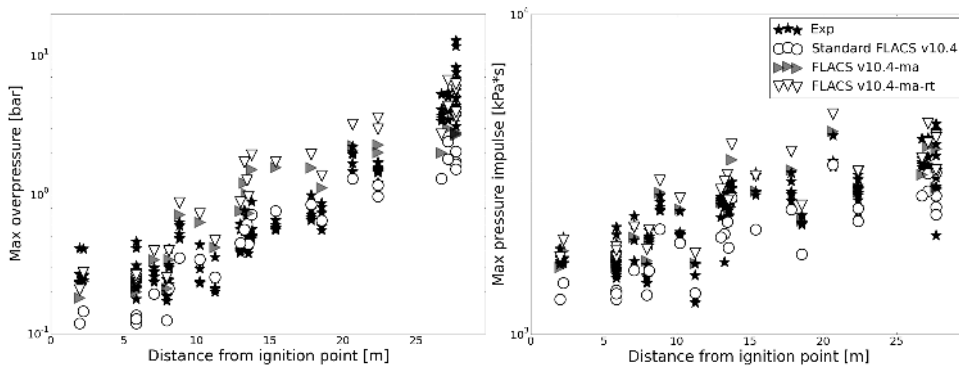

Figure 6.25: Maximum overpressures (left) and maximum pressure impulse (right) vs. distance from ignition point, "Beta-series".

Figures 6.24 and 6.25 show the significant spread in results between repeated experiments for these two configurations (denoted by black stars), which is particularly pronounced at the monitor points positioned the furthest away from the ignition point (maximum variations of ≈ 7 barg for the "Beta-series"). The peak pressure values are extracted from filtered curves, processed with a moving average filter that approximately corresponds to the time-resolution in these specific simulations. For the "Alpha-series", the flammable mixture was ignited centrally in the rig, while for the "Beta-series", the mixture was ignited at the end, so that the flame was allowed to

propagate throughout the length of the rig. Considerable flame acceleration and high overpressures were achieved in the "Beta-series", and deflagration-to-detonation transition (DDT) possibly occurred (or was very close to occurring) as the flame exited the far end of the rig opposite the ignition point. As this phenomenon is highly variable and gives significant overpressures, it would have affected the repeatability of the results. The maximum pressure impulse is less sensitive to narrow spikes occurring in the pressure-time history.

Figures 6.24 and 6.25 show that standard FLACS v10.4r2 predicts maximum overpressure and pressure impulse values in the lower range of the experimental results. For the "Beta-series", the overpressures and pressure impulse are generally under-predicted by FLACS v10.4r2. FLACS v10.4-ma gives consistently higher overpressures than FLACS v10.4r2, likely due to the higher values of the turbulent burning velocity u_t from the Markstein-dependent combustion model (cf. Section 4.6 and Figure 6.13a). Combustion in highly turbulent flow dominates the flame acceleration in these tests. However, FLACS v10.4-ma over-predicts the maximum overpressures and pressure impulse in several monitor points. The over-prediction is most pronounced in the locations where the flame has propagated some distance from the ignition point, and has not yet reached the end of the module. A similar trend can be observed for the FLACS v10. 4r2 predictions of the "Beta-series" (cf. Figure 6.25 (left)) in the intermediate region. As DDT (a phenomenon that is not presently modelled in FLACS) likely generated the highest overpressures observed in the "Beta-series", neither version of the model system will be able to reproduce these values.

The FLACS version that includes the contribution to flame surface area from the RT instability, FLACS v10.4-ma-rt, consistently increases the maximum overpressures for all monitor points when compared with the results from FLACS v10.4-ma. Consequently, FLACS v10.4-ma-rt over-predicts maximum overpressures and pressure impulse values for a range of monitor points, in particular for the "Alpha-series". The local flame acceleration in these tests is such that the increase of flame surface area from the RT instability model (cf. Section 5.4.3) is present throughout the main part of the explosion history. Although the RT instability effect may be necessary for representing the external explosion for vented scenarios, it is not obvious that this instability should have the same relative effect on the flame acceleration for an already highly corrugated flame front in a turbulent flow field. To determine the relative contribution of the RT instability for highly turbulent combustion is not straightforward. Accurate representation of this effect in FLACS will likely require validation and optimisation against a wider range of validation cases, as well as further development of the model system (cf. Chapter 8). To obtain the present results, the same model parameter settings as used for the vented scenarios were applied.

Figure 6.26 shows the pressure-time histories for two locations inside the BFETS Phase 3A rig, measured during the first of the "Beta" tests. The corresponding predictions from FLACS v10.4r2, FLACS v10.4-ma and FLACS v10.4-ma-rt are plotted together with the experimental results. Figure 6.26a shows the pressure-times curves recorded in the ignition end of the rig, in the corner, at ground level, while Figure 6.26b shows the pressure recorded at the centre of the far end of the rig, opposite of the ignition point.

For the monitor point located closest to the ignition point, plotted in Figure 6.26a, FLACS v10.4r2 gives the most accurate time to pressure rise. However, the maximum

overpressure is represented more accurately by FLACS v10.4-ma and FLACS v10.4-ma-rt. The development versions of FLACS predict maximum overpressures within the experimental variations (ranging between 0.2 and 0.4 barg for repeated experiments), while the standard release (giving 0.12 barg) under-predicts the maximum overpressure.

For the monitor point located at the far end of the rig in Figure 6.26b, FLACS v10.4r2 over-predicts the time-of-arrival of the pressure peak, while significantly under-predicting the maximum overpressure. The experimental recordings exhibit a double-peak structure, where the second peak most likely (based on analysis of un-filtered recordings) is due to DDT occurring immediately after the flame front exits the rig. Considering this, the duration of the pressure peak from FLACS v10.4-ma-rt appears to be over-predicted, although the value of the maximum overpressure is within the experimental variations (ranging between 3.4 and 5.1 barg for repeated experiments). FLACS v10.4-ma gives a more representative pressure build-up; however, the model does not predict the narrowest structures of the pressure-time curve (even when compared to a filtered pressure-time curve). As a result, the maximum overpressure is under-predicted by FLACS v10.4-ma. The duration of the pressure peak from FLACS v10.4- ma seems to be somewhat over-predicted, when compared to the first peak of the experimental curve in Figure 6.26b.
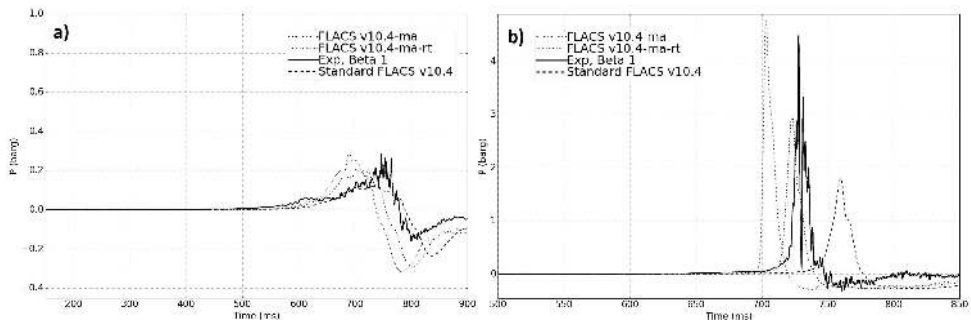

Figure 6.26: Pressure-time curves for two locations in the first test of the Beta-series a) 5.8 m and b) 27 m from the ignition point.

FLACS cannot model DDT directly. However, the CFD tool can output a parameter called *DPDX*, the normalised spatial pressure gradient across the flame front (Middha, 2010). The *DPDX* parameter records when the flame front captures the pressure front, and can therefore indicate whether DDT is likely. Based on validation work, the following ranges have been established: for *DPDX* less than 0.5, DDT is very unlikely, when *DPDX* is in the range 0.5 to 5, DDT is possible, while for *DPDX* exceeding 5, DDT is considered likely (Hansen and Johnson, 2015). However, a sufficiently high *DPDX* value is not sufficient to conclude on the possibility of DDT; the flame front also has to cover a sufficiently large area compared to the detonation cell size of the gas. The detonation front consists of a cell pattern, and the characteristic length scale of the cells determines the minimum geometrical dimensions necessary to support the propagating detonation front. Typically, a minimum area of 13 x 13 detonation cell sizes of gas cloud ahead of the fast flame front is needed for the detonation to sustain in an unconfined situation. For example, assuming that the detonation cell size of a stoichiometric methane-air mixture is around 0.30 m, an area of 4 m $\times$ 4 m is needed for a

detonation to propagate (Gexcon, 2016; Hansen and Johnson, 2015). A mixture of natural gas with air is somewhat more reactive than a pure methane-air mixture, so an area of 4 m × 4 m of *DPDX* exceeding 0.5 should be sufficient for suggesting that DDT is possible.

Figure 6.27 shows the spatial distribution of *DPDX* for a horizontal cut-plane, predicted in a simulation of the "Beta-series" for a) FLACS v10.4r2 and b) FLACS v10.4-ma. Figure 6.27a shows that FLACS v10.4r2 does not predict a sufficiently large region where *DPDX* exceeds 0.5 to suggest that DDT is possible. However, the simulation performed with FLACS v10.4-ma indicates that DDT is possible as the flame front accelerates through the rig, cf. Figure 6.27b. Corresponding results (as for FLACS v10.4-ma) are obtained with FLACS v10.4-ma-rt.
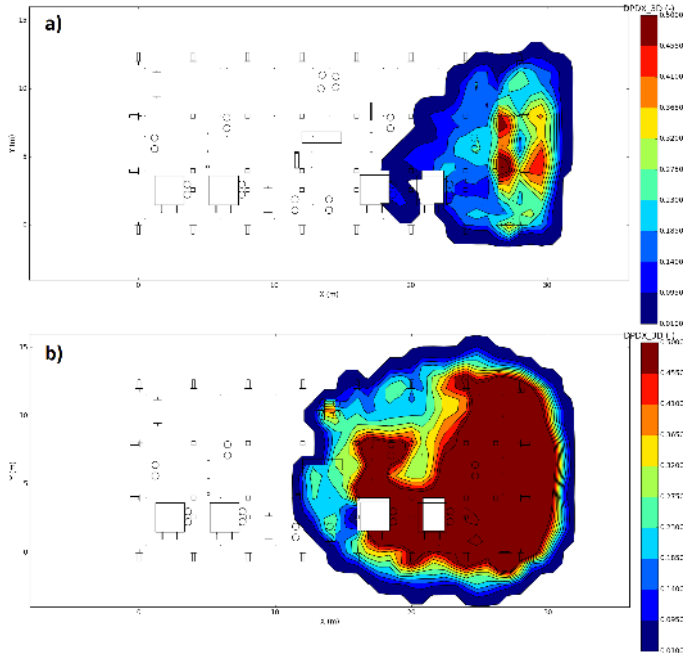

Figure 6.27: The predicted distribution of the normalised spatial pressure gradient *DPDX*, plotted for a) FLACS v10.4r2 and b) FLACS v10.4-ma.

In conclusion, for the "Alpha-" and "Beta-series" of the BFETS Phase 3A campaign, FLACS v10.4-ma appears to give the overall most accurate predictions (disregarding under-prediction of the very high overpressures observed in some "Beta-tests", likely caused by DDT). However, further development of FLACS v10.4-ma-rt may result in improved agreement with experimental results. For example, including effects from shock waves interacting with the flame front, (increasing the flame surface area), may improve the representation of the "Beta-series" in particular. This was not considered feasible for the present doctoral study. As the burning velocity model in FLACS v10.4-ma-rt is based on the recent combustion literature, it provides an appropriate starting point for further model development.

Chapter 7

Concluding remarks and research highlights

The present doctoral study was performed to address the following research question: *"how can the sub-grid representation of flame acceleration mechanisms due to instability effects and flow past obstructed regions be improved in a CFD tool used for consequence assessment of gas explosions?"*. Specifically, the thesis presents and validates new sub-grid models developed for the CFD tool FLACS, focusing on the following flame acceleration mechanisms: (i) the influence of the hydrodynamic and thermal–diffusive instabilities (intrinsic instabilities) on flame acceleration in the initial phase of a gas explosion, (ii) the influence of thermal–diffusive effects on the rate of turbulent combustion for different fuels and mixture concentrations, (iii) the role of the Bénard–von Kármán (BVK) instability downstream of bluff-body obstacles in explosion-induced flow, (iv) how the Rayleigh–Taylor (RT) instability developing on a flame front that is accelerated over an obstacle or a vent opening may enhance the combustion rate, and (v) how flexible obstructions with very small components (in the form of vegetation) induce flame acceleration in gas explosions. There was a lack of available experimental work describing the relative importance of several of the aforementioned effects. Therefore, three experimental campaigns were designed and conducted as part of the doctoral study (cf. papers 2-4 and Appendix B). Experimental findings thus constitute a significant part of the original scientific contribution of the present work; these can be used to develop sub-grid models for any consequence model system. Three additional campaigns, performed by other research groups, were simulated in order to validate the new sub-grid models. The findings of the study are presented and discussed in the four papers associated with the dissertation, and in chapters 4, 5 and 6. This chapter provides overall concluding remarks and summarises the main results from the doctoral work.

7.1 Concluding remarks

This dissertation addresses instability mechanisms that are expected to contribute to the flame acceleration in industrial-scale gas explosions. The selection of mechanisms that is discussed in the present work is based on the presentations by Ciccarelli and Dorofeev (2008) and Oran (2015). *Intrinsic instabilities*, i.e. the Landau–Darrieus and thermal–diffusive instabilities, are important for freely propagating spherical flame fronts. Furthermore, when the flame propagates through areas with confinement and/or obstructions, the Kelvin–Helmholtz, Bénard–von Kármán, Rayleigh–

Taylor, Richtmyer–Meshkov, and acoustic instabilities may increase the flame surface area and the overall combustion rate significantly. These mechanisms are considered to be *geometry-induced*, as the presence of confinement and/or congestion is normally required for these to have an appreciable effect on the flame acceleration.

The dissertation also addresses effects that are relevant for turbulent premixed combustion and flame propagation through congested regions. Key mechanisms relevant for turbulent flame propagation also include the effect of the Markstein number (or length) of the fuel-oxidiser mixture. The mixtures that are most prone to intrinsic instabilities also exhibit enhanced burning rates, relative to their laminar burning velocity, in the flamelet regimes of turbulent premixed combustion. These effects connect the representation of the turbulent burning velocity with the modelling of the cellular phase of flame propagation in consequence models.

Chapter 4 presents theoretical considerations of intrinsic instabilities developing on freely expanding spherical flame fronts. The theory is corroborated by recent experimental findings by Bauwens et al. (2015), Bauwens et al. (2017a) and Bauwens et al. (2017b). These authors expressed the flame speed in the cellular regime in terms of the fractal increase in flame surface area associated with each new generation of cells developing on the surface. The fractal excess was found to vary with the equivalence ratio, and effectively the Markstein number, of the fuel-air mixture. From the simulations presented in Paper 1, Paper 2 and Chapter 6, it is clear that the current model for the quasi-laminar burning velocity (representing the cellular regime of flame propagation) in standard releases of FLACS (Gexcon, 2016) can be improved by including these findings. The theory presented in Chapter 4 is used to formulate sub-grid models for cellular flame propagation. Paper 2 and Chapter 6 demonstrate that the initial phase of flame propagation in experiments generally is better represented in simulations that apply the alternative sub-grid models that were formulated as part of the present doctoral study.

As for the regime of cellular flame propagation, Chapter 4 suggests that the mixture reactivity in the turbulent regime of combustion cannot be represented fully by only considering the laminar burning velocity. In particular, for the regime of turbulent combustion, perturbations in the Markstein number change the relative dependence of the turbulent burning velocity u_t on the laminar burning velocity u_l, the turbulence velocity fluctuation u', the integral length scale ℓ_I and the kinematic viscosity ν. According to Bradley et al. (2005), mixtures characterised by negative Markstein numbers exhibit higher burning rates when exposed to positive stretch rates, are less likely to quench at high stretch rates, and are more prone to develop flame instabilities than mixtures with positive Markstein numbers. The experimental results of Paper 2 support these findings. In this campaign, the effect of varying the fuel concentration in a propane-air mixture, thus effectively changing the physicochemical properties of the mixture in terms of the Markstein number, was explored for different flow regimes. Specifically, for one of the experimental setups, five square cylinders were inserted as obstructions in the explosion rig to induce turbulence in the flow. For this configuration, the maximum pressure peak was produced in the turbulent wake downstream of the obstructions, i.e. prior to the onset of the external explosion. With this particular setup, the maximum explosion overpressure obtained using a stoichiometric propane-air mixture (i.e. with $\phi = 1.0$) was about 0.23 bar. In a corresponding test, involving a fuel-rich mixture with $\phi = 1.4$, the maximum recorded overpressure was 0.18 bar, i.e. approximately 80% of

that obtained for the mixture with $\phi = 1.0$.

However, standard releases of FLACS (at least up to version 10.5 (Gexcon, 2016)) predict the mixture reactivity variations with changes in fuel concentration only as a function of the corresponding changes in the laminar burning velocity. Therefore, the standard FLACS release used in Paper 2 predicted the maximum overpressure for a test with $\phi = 1.4$ to be only 30 % of that predicted for a mixture with $\phi = 1$. Paper 2 and Chapter 6 explore the performance of the Markstein number-dependent burning velocity model that was implemented in a development version of FLACS as part of the present doctoral study. Overall, this combustion model gives significantly improved results compared with the model that is used in standard FLACS releases – in particular for mixtures characterised by negative Markstein numbers.

Accident scenarios involving realistic clouds with e.g. propane or gasoline vapours challenge the domain of applicability of the CFD tool FLACS, as the model has (in the case of hydrocarbon-air explosions) mainly been developed for and validated against near-stoichiometric mixtures – with particular emphasis on natural gas and methane. As discussed in Chapter 1, there is a trend towards increased use of CFD for risk analysis for onshore process facilities. For these applications, the flame front may propagate through extended regions with low degrees of congestion before reaching densely obstructed areas where severe overpressures are produced. Therefore, in order to represent the explosion mechanism, it is important to reproduce variations in flame acceleration with changes in the physicochemical properties of the mixture in the cellular regime of flame propagation. It is obviously also crucial that the turbulent combustion rates in the congested regions accurately reflect the reactivity of the fuel-air mixture. Hence, the combustion model introduced in the present thesis extends the domain of applicability of the CFD tool FLACS.

It is not necessarily straightforward to separate instability-induced flame acceleration from that caused by turbulence. The main flame accelerating mechanism in gas explosions will frequently be a combination of enhancement of flame surface area from large-scale unsteady flow structures, and increased burning rates in the flame brush due to small-scale turbulence produced downstream of obstacles. The review of modelling challenges in Chapter 1 indicated that FLACS may under-predict the flame acceleration in large-scale, elongated geometries with relatively few, large-scale obstructions (Skjold et al., 2013b). To improve model performance, it is therefore relevant to investigate and include the effect of additional flame acceleration mechanisms that can be significant in obstructed regions, such as the Bénard–von Kármán and Rayleigh–Taylor instabilities.

The effect of the Rayleigh–Taylor instability in vented explosions has been studied by several researchers, e.g. Solberg et al. (1981), Cooper et al. (1986), Tsuruda and Hirano (1987), Bauwens et al. (2009a) and Bauwens et al. (2009b). In order to correctly represent the external explosion in simulations of vented scenarios, several researchers have suggested that it is necessary to include this effect, i.e. to only model the effect of turbulence is insufficient (Bauwens et al., 2009b, 2011; Keenan et al., 2014). Pressure relief panels are used for explosion mitigation purposes in a range of applications. For example, accurate predictions of the consequences of vented explosion scenarios are important for designing high-pressure hydrogen systems located in enclosures. Furthermore, performing model validation for vented explosions is highly useful for investigating how a model represents a wide range of physical phenomena –

most of the mechanisms will be active also in other scenarios, for example in unconfined explosions at large-scale process facilities.

A sub-grid model for the production of flame surface area due to the Rayleigh-Taylor instability, based on the linearised theory by Zeldovich et al. (1985) and the approach by Bauwens and Dorofeev (2011), was implemented in a development version of FLACS. The simplified model approach is consistent with the general approach for flame wrinkling in FLACS (Gexcon, 2016). The approach assumes that the effect of acceleration on the burning rate is localised and instant within the current timestep, and that the stabilising effect of the Rayleigh–Taylor mechanism on the flame surface can be neglected. Moreover, the modelling approach assumes that effects that are not explicitly represented can be compensated for by defining appropriate model constants. Chapter 6 explores the effect of including the Rayleigh–Taylor sub-grid model for two experimental campaigns involving vented explosions, including the experimental campaign in Paper 1. The contribution of the Rayleigh–Taylor instability was found to be necessary to reproduce the external explosion in several of the experiments from Paper 1. Further improvement in the modelling of this effect may be obtained by implementing a transport equation for the flame surface area produced by the instability, cf. Chapter 8.

The inclusion of the RT instability effect in the third validation campaign, presented in Section 6.3, lead to over-prediction of the overpressures in a range of monitor points. This campaign involved a series of large–scale explosion experiments performed in a offshore module with a complex geometry layout. Although the RT instability effect may be necessary for representing the external explosion for vented scenarios, it is not obvious that this instability should have the same relative effect on the flame acceleration for an already highly corrugated flame front in a turbulent flow field. To determine the relative contribution of the RT instability for highly turbulent combustion is not straightforward. Accurate representation of this effect will likely require validation and optimisation against a wide range of validation cases, as well as further development of the model system.

In order to develop sub-grid models for the increase in flame surface area due to the Bénard–von Kármán instability, more knowledge about the importance of the mechanism in industrial-scale gas explosions was needed. The experiments of Paper 3 showed that vortex shedding triggered by this instability is significant for the flame acceleration downstream of a circular cylinder in a transient, gas explosion-driven flow. Applying two different passive control methods to the circular cylinder in the experiments of Paper 3 successfully suppressed the instability and reduced the generated explosion overpressures by approximately 32 %. The significant effect of applying control methods developed for suppressing the nominally two-dimensional instability suggests that vortex shedding can be important also in three-dimensional, highly transient flow fields. Overall, based on the findings in Paper 3 and the discussion in Section 5.3.4 of the present thesis, vortex shedding will most likely occur also in gas explosion scenarios with higher Reynolds numbers and more realistic obstacle configurations. Furthermore, since both of the passive control methods used in the experimental campaign of Paper 3 directly affected the global instability in the near-wake (rather than delaying the separation point), they should be effective for a wide range of Reynolds numbers.

However, in order for a control method to be useful for reducing overpressures in a real accident, it must be independent of the flow direction. Consequently, a fixed splitter

plate would be unpractical, while adding a structure to the surface of the obstruction to disrupt the two-dimensional nature of the instability (comparable to adding a helical steel wire as in Paper 3) may be feasible. To confirm whether such an approach could constitute a cost-effective risk-reducing measure in real process facilities would require a series of large-scale experiments, specifically designed to investigate this effect.

In FLACS, the overall effect of vortex shedding downstream of sub-grid obstacles is most likely included in the phenomenological model accounting for localised flame surface area production from unresolved geometry (described in Section 5.1). However, the experiments described in Paper 3 indicate that an important effect of vortex shedding is enhanced turbulence levels further downstream of the bluff-body, caused by dissipation of large-scale, energetic structures. If the effect of unresolved vortex shedding should be accounted for through the enhancement of flame surface area from sub-grid obstructions, the flame wrinkling factor should ideally be a transported quantity. Further modelling work would be required to formulate appropriate production and destruction terms for the flame surface area generated by unresolved geometry. Simulations performed with more fundamentally based CFD models, e.g. LES models that resolve boundary-layers (Gourdain et al., 2009a,b), can provide further knowledge about the increase in flame surface area from obstacles in different flow regimes.

Finally, the present dissertation investigates the effect of flexible obstructions with very small diameter components (in the form of vegetation) on the flame acceleration in gas explosions. The objective of the experimental campaign in Paper 4 was to study the separate effects of flexibility and foliage. Thus, the paper addresses two separate influences on flame propagation in obstructed regions that must be represented sub-grid if modelled by a CFD tool based on the PDR concept. The results suggested that foliage can significantly enhance the overpressures in gas explosions. The presence of needles on spruce branches enhanced peak overpressures by approximately a factor three, relative to tests with bare branches. Furthermore, the effect of flexibility was found to be significant as well; inserting stainless steel models in the channel approximately doubled the maximum overpressures compared to tests with the corresponding flexible branches. Based on the experimental results of Paper 4, the effect of flexibility was included in FLACS simulations by constructing congestion blocks, representing the effective drag area expected to produce turbulence and flame acceleration during the explosion. Branch components smaller than a certain cut-off scale were not included in the effective drag area. This approach is consistent with that applied for the investigation of the Buncefield explosion incident (Bakke, 2010; Pedersen and Brewerton, 2014).

Meanwhile, the degree to which a certain branch will act as a solid object in a gas explosion will depend upon the flow of the specific scenario. For example, for high flame speeds, flexible obstructions will have less time to respond to the explosion-induced flow and act more like a fixed obstacle than for low flame speeds. For modelling potential accident scenarios at onshore process facilities, a conservative approach would be to account for components of all length scales. The influence of foliage was found to be represented most accurately in the simulations in Paper 4 by multiplying the effective drag area from the flexibility analysis with a 'foliage factor'. This factor was based on the approximate average increase in cross-sectional area blockage of the spruce branches with needles relative to the bare branches. For general use in consequence modelling, it would be possible to estimate such foliage factors based on the type of

tree or bush, and a visual interpretation of the density of foliage. Considering the uncertainties associated with the diversity of vegetation, this approach would likely require some conservatism.

In conclusion, the results from the experimental campaigns presented in this thesis have improved the understanding of several important physical effects related to flame acceleration in industrial-scale explosions. The thesis also demonstrates how this knowledge may be used to model gas explosions more accurately. However, for all CFD tools that apply a system of sub-grid models, the combination of the separate pieces results in the observed model performance. Other effects may compensate for inaccuracies in certain sub-grid models, and it can be challenging to improve separate pieces of the code without considering the complete model system. Nonetheless, the model developments discussed in the present thesis are all considered to constitute fundamental improvements with respect to the representation of physical phenomena. The doctoral study thus provides an improved basis for further model development. Chapter 8 outlines future perspectives, building on the present work.

7.2   Research highlights

This section summarises the main findings from the present doctoral study.

- Validation work performed for the present study suggests that the predictive capabilities of the CFD tool FLACS may be improved by introducing updated sub-grid models for the initial phase of flame propagation, where intrinsic instabilities govern the flame acceleration.

- The physicochemical properties of a premixed fuel-air mixture that influence the growth rate of intrinsic instabilities, expressed in terms of the Markstein number of the mixture, also affect the rate of turbulent combustion. The present thesis suggests that variations in the explosion overpressure with a varying equivalence ratio – and effectively a varying Markstein number – are misrepresented by standard FLACS releases (Gexcon, 2016).

- A Markstein number-dependent burning velocity model was implemented in a development version of FLACS as part of the present doctoral study. Overall, this combustion model gives significantly better results compared with the model that is used in standard FLACS releases, in particular for mixtures characterised by negative Markstein numbers.

- Experimental results from the present study suggest that vortex shedding downstream of bluff-bodies, caused by the Bénard–von Kármán instability, can contribute significantly to the overpressure generation in gas explosions. Suppressing the vortex shedding in laboratory-scale experiments with a single obstacle reduced the maximum explosion overpressures by approximately 32 %.

- Based on the findings of the present study, vortex shedding will most likely enhance the flame acceleration also in gas explosion scenarios with higher Reynolds numbers and multiple obstructions. To confirm whether such an approach could constitute a cost-effective risk-reducing measure in real process facilities would

require a series of large-scale experiments, specifically designed to investigate this effect.

- A sub-grid model for the production of flame surface area due to the Rayleigh-Taylor instability was implemented in a development version of FLACS. The contribution of the Rayleigh–Taylor instability was found to be necessary to reproduce the external explosion in several simulations of vented explosions. Further improvement in the modelling of this effect may be obtained by implementing a transport equation for the flame surface area produced by the instability.

- Experimental results from the present study suggest that foliage can significantly enhance the overpressures in gas explosions. The presence of needles on spruce branches enhanced peak overpressures by approximately a factor three, relative to tests with bare branches. Furthermore, the effect of flexibility was found to be significant as well; inserting stainless steel models approximately doubled the maximum overpressures compared to tests performed with the corresponding flexible branches.

- The effect of flexibility of vegetation was included in FLACS simulations by constructing congestion blocks, representing the effective drag area expected to produce turbulence and flame acceleration during the explosion. The influence of foliage was found to be represented most accurately by multiplying the effective drag area from the flexibility analysis with a 'foliage factor'. This factor was based on the approximate average increase in cross-sectional area blockage of the spruce branches with needles, relative to the bare branches.

Chapter 8

Future perspectives

The work presented in this dissertation provides the basis and motivation for several further studies. This chapter outlines selected suggestions for further work.

8.1   Markstein numbers

A Markstein number-dependent model for premixed combustion can in principle account for thermal-diffusive instabilities and pressure effects for any fuel-air mixture. In order to apply the combustion model proposed in the present work to a wider range of fuel types and mixture concentrations, a consistent approach for obtaining the relevant Markstein numbers must be defined. For example, the model for turbulent combustion specifically requires the input of strain rate Markstein numbers. The significance of applying an alternative measure, if necessary, should be evaluated. Some of the required properties can be generated by using detailed chemical kinetics tools. In addition, experimental study of spherical flame propagation in explosion vessels, specifically designed to sustain high pressure levels, can provide results for the mixtures that are challenging to represent by modelling. These values should be used to further validate and improve the simple volume-weighted Markstein number mixing rule that was implemented in FLACS for the present doctoral study.

8.2   Transporting the flame surface area

Replacing the current modelling framework for premixed combustion in FLACS with an approach that solves transport equations for the flame surface area, following the general concept proposed by Weller et al. (1998a), would represent a fundamental model improvement. The burning velocity models developed as part of the present thesis could then provide equilibrium expressions for the transport equations, cf. Section 5.1. A complete model would include equations for flame surface area from turbulence, the Rayleigh–Taylor instability and sub-grid obstacles (Bauwens and Dorofeev, 2011; Puttock et al., 2014). However, solving additional equations requires computational efforts, and the benefit must be weighed against the costs in terms of reduced calculation speed. An appropriate starting point could be to only transport flame surface area due to sub-grid obstacles, and evaluate this development before proceeding. As part of this

work, results from a detailed LES model, such as the AVBP model developed by CER-FACS (Gourdain et al., 2009a,b), would be highly useful for estimating the increase in flame surface area generated by various physical phenomena.

8.3   Adaptive mesh refinement

Adaptive mesh refinement (AMR) (Bell, 2014; Berger and Colella, 1989; Berger and Oliger, 1984) enables the user to apply a fine grid resolution in the areas of the computational domain where steep gradients are located. With AMR, it will therefore be feasible to resolve the flame front and pressure waves with a significantly finer grid than what is presently possible in FLACS. The implementation of an AMR solver will likely reduce grid dependency of the results, and introduce a range of new modelling opportunities. In particular, the representation of the ignition phase and flame propagation through the first control volumes would likely become more accurate and less grid dependent, compared with using a fixed grid in the computational domain. However, to enable the significant re-structuring of the code required to implement AMR, it is crucial to have a robust, well-documented model system with routines for continuous validation to ensure that the overall capabilities of the CFD tool are retained in the process.

8.4   Predicting the consequences of DDT

After several recent incidents at onshore facilities, such as Buncefield in 2005 and Jaipur in 2009, there is growing awareness and concern in the industry about the occurrence of deflagration-to-detonation transition (DDT) (Hansen and Johnson, 2015; Johnson et al., 2015; Oran, 2015; Tam and Johnson, 2016). Accidental explosions typically start with the weak ignition induced e.g. by an electrical spark, or autoignition of the mixture in contact with a very hot surface (Ciccarelli and Dorofeev, 2008). Under certain conditions, the flame can accelerate and undergo DDT. The flame acceleration phenomenon leading up to DDT is strictly a separate process from the actual onset of detonation. The onset of detonation is a local phenomenon that occurs in a very small volume of the unburnt mixture whose thermodynamic state has been conditioned by the flame acceleration processes that take place over significantly larger length and time scales. Once initiated, detonations propagate at super-sonic speeds, generating significantly higher overpressures and more damaging blast waves than deflagrations. Unlike deflagrations, detonations do not depend on diffusion processes and turbulent mixing, but are self-sustained also in regions without congestion. Large-scale tests performed as part of the second Buncefield project showed that detonations could propagate through unconfined propane-air clouds less than 0.2 m deep (SCI, 2014). Significant parts of a flammable cloud can then be expected to sustain a detonation wave.

To address the possibility of such events, Middha et al. (2006), Middha and Hansen (2008) and Middha (2010) presented the development and validation of a new simulation variable in FLACS: a normalised spatial pressure gradient. This variable can give an indication of the likelihood of DDT, if used according to a set of guidelines.

The concept was further developed and validated by Hansen and Johnson (2015). As part of the wider application of FLACS for predicting the likelihood of DDT, it is crucial to correctly represent flame acceleration in the deflagration regime, leading up to a potential transition. According to Ciccarelli and Dorofeev (2008), the study of the flame acceleration process is as important as the actual onset of the detonation event. The possibility of DDT in large-scale vapour cloud explosions therefore constitutes a strong motivation for continued research on how the model represents basic flame acceleration mechanisms in the deflagration regime, i.e. intrinsic and geometry-induced instability effects, as well as flame-turbulence interactions. In particular, the effect of shock waves interacting with the flame front as it accelerates through obstructed regions (through the Richtmyer-Meshkov (RM) instability), may be important for explosions where the flame speeds are approaching the speed of sound in the combustion products. In order to investigate these effects, detailed LES modelling would be highly useful (Jiang et al., 2016).

Hansen and Johnson (2015) propose to use the likelihood predictor for DDT in FLACS to trigger a new regime of flame propagation, where the flame front is induced to propagate with a typical detonation speed. In order to include this capability in the CFD tool, the approach would need to be further tested and validated. In addition, to reproduce representative detonation propagation speeds, adjustments would most likely be required for the numerical flame model.

8.5 Validation and parameter optimisation

In order to ensure the best possible overall model performance for a wide range of scenarios, it is necessary, but not always sufficient, to have formulated physically sound, well-founded sub-grid models. A significant part of the complexity, non-linearity and uncertainty of the physical phenomena that must be included in a consequence model for industrial-scale explosions still need to be represented by empirical constants. There are considerable uncertainties associated with empirical parameters obtained from experiments. Moreover, practical applications of consequence models often involve scaling, and extrapolating results will always entail uncertainty, as other physical phenomena may dominate as time and length scales change (Oran, 2014). For complex CFD models, it is generally not feasible to assess model uncertainty by analysing the validity of its components separately. Instead, comparisons are done between a large number of experimental results and numerical predictions (McGrattan and Toman, 2011). Systematic validation against experiments is therefore crucial for the development of robust and accurate sub-grid models.

Adjustment of individual model parameters may be effective for addressing issues related to model applicability. However, as the same model system is used for a wide range of spatial scales and geometric configurations, and for different purposes, the validation work required to re-qualify the model may be considerable. If adverse effects are observed, a single parameter adjustment may require work on several sub-grid models. It is therefore desirable to adopt more efficient and general methods for parameter optimisation, so that the procedure easily can be repeated with new versions of the model.

Automated optimisation techniques applied for response surfaces, generated from

CFD model results, show promising results for improving model performance relative to key experimental targets (Braatz and Hisken, 2017; Braatz et al., 2016). For example, the sub-grid models that have been formulated as part of the present study will be subject to further validation and optimisation before they are included in a commercial software product. However, it is crucial to combine the use of such methods with an understanding of the underlying physical phenomena.

Appendix A

Numerical methods

This appendix summarises the numerical methods that are used in FLACS to solve the partial differential equations described in sections 2.9 – 2.10.

A.1   The computational grid

Figure A.1 shows the computational grid arrangement in the FLACS PDE solver in a horizontal cut-plane, illustrating the staggered position for velocity components u_1 and u_2 in the x_1- and x_2-directions, respectively, denoted by a cross ($\times$), and the cell-centred position for scalar variables (e.g. density ρ, pressure p and temperature T), denoted by a bullet point ($\bullet$). Figure A.2 shows the three-dimensional control volume, centred around the pressure point p. The corresponding control volumes centred around each velocity point u_i, $i = 1, 2, 3$, are not shown here.
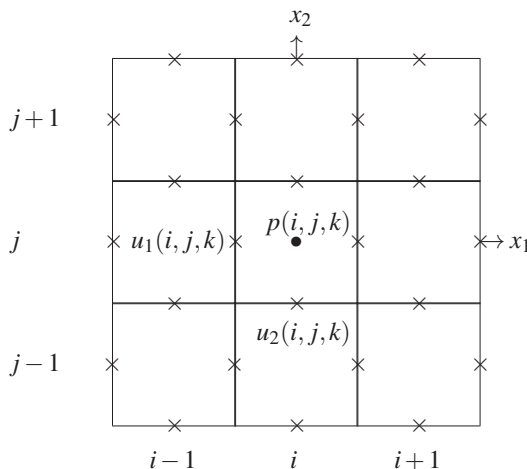
Figure A.1: Staggered Cartesian grid arrangement in FLACS, horizontal view.

According to (Hjertager, 1986), the general conservation equation in FLACS for the variable Φ, assuming the volume and area porosities are all equal to 1, can be written
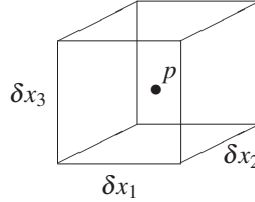
Figure A.2: The three-dimensional control volume (CV), centred around the pressure point p.

on differential form as

$$\frac{\partial}{\partial t}(\rho\Phi) + \frac{\partial}{\partial x_i}(\rho u_i \Phi) - \frac{\partial}{\partial x_i}\left(\Gamma_\Phi \frac{\partial \Phi}{\partial x_i}\right) = S_\Phi \, , \qquad (A.1)$$

where $\Gamma_\Phi = \mu_{\text{eff}}/\sigma_\Phi$ is the effective turbulent diffusion coefficient and S_Φ is the source term for Φ. Sections 2.3 – 2.9 present details on the physical interpretation of each term in Equation (A.1) for each variable Φ.

A.2   The finite volume approach

The PDE solver in FLACS uses the *finite volume approach* (Patankar, 1980; Versteeg and Malalasekera, 2007). Equation (A.1) is integrated over a control volume (CV) with sides of length δx_1, δx_2 and δx_3, a volume of $V_{CV} = \delta x_1 \delta x_2 \delta x_3$ and a surface area $A_{CV} = 2\delta x_1 \delta x_2 + 2\delta x_1 \delta x_3 + 2\delta x_2 \delta x_3$. After using Gauss' divergence theorem, the following equation is obtained:

$$\int_{V_{CV}} \frac{\partial}{\partial t}(\rho\Phi)dV + \int_{A_{CV}} n_i(\rho\Phi u_i)\, dA - \int_{A_{CV}} n_i\left(\Gamma_\Phi \frac{\partial \Phi}{\partial x_i}\right)dA = \int_{V_{CV}} S_\Phi dV \, , \quad (A.2)$$

where n_i is the outward-pointing vector that is everywhere normal to the surface of the control volume.

The gradients in the diffusive fluxes are discretised using 2nd order central differences, and a second order kappa-scheme (a hybrid scheme with weighting between 2nd order upwind and 2nd order central difference, with delimiters for some equations) is used to compute the convective fluxes in Equation (A.2). The convective and diffusive flux of Φ in the x_1-direction, represented by the second and third term on the left hand side of Equation (A.2), respectively, can be expressed in discretised form as

$$a_{i+1,j,k}^\Phi \left(\Phi_{i,j,k} - \Phi_{i+1,j,k}\right) + a_{i-1,j,k}^\Phi \left(\Phi_{i,j,k} - \Phi_{i-1,j,k}\right) \, . \qquad (A.3)$$

The coefficients are given by

$$a^{\Phi}_{i+1,j,k} = \left(\frac{\Gamma_{\Phi,i+\frac{1}{2}}}{\delta x_1} + \langle -\rho_{i+\frac{1}{2}} u_{1,i+1,j,k} \rangle \right) \delta x_2 \delta x_3 \, , \qquad (A.4)$$

$$a^{\Phi}_{i-1,j,k} = \left(\frac{\Gamma_{\Phi,i-\frac{1}{2}}}{\delta x_1} + \langle \rho_{i-\frac{1}{2}} u_{1,i,j,k} \rangle \right) \delta x_2 \delta x_3 \, , \qquad (A.5)$$

where $\langle \rangle$ denotes the differencing according to the kappa-scheme. The source term S_{Φ}, integrated over the control volume in Equation (A.2), is often expressed as a linear function of $\Phi_{i,j,k}$ according to

$$S_{\Phi} = S^0_{\Phi,i,j,k} + S_{\Phi,i,j,k}\Phi_{i,j,k} \, . \qquad (A.6)$$

The first term in Equation (A.2) is discretised according to

$$\int_{CV} \frac{\partial}{\partial t}(\rho\Phi)dV = \rho^0 \left(\Phi_{i,j,k} - \Phi^0_{i,j,k} \right) \frac{\delta x_1 \delta x_2 \delta x_3}{\delta t} = b_{\Phi}\left(\Phi_{i,j,k} - \Phi^0_{i,j,k} \right). \qquad (A.7)$$

After summarizing the fluxes in the x_1, x_2 and x_3-direction, the system of integrated equations corresponding to Equation (A.2) can be expressed as

$$\begin{aligned}
a^{\Phi}_{i,j,k}\Phi_{i,j,k} = &a^{\Phi}_{i+1,j,k}\Phi_{i+1,j,k} + a^{\Phi}_{i-1,j,k}\Phi_{i-1,j,k} + a^{\Phi}_{i,j+1,k}\Phi_{i,j+1,k} + \\
&a^{\Phi}_{i,j-1,k}\Phi_{i,j-1,k} + a^{\Phi}_{i,j,k+1}\Phi_{i,j,k+1} + a^{\Phi}_{i,j,k-1}\Phi_{i,j,k-1} + \\
&S^0_{\Phi,i,j,k} + b_{\Phi}\Phi^0_{i,j,k} \, ,
\end{aligned} \qquad (A.8)$$

where $a_{i,j+1,k}$, $a_{i,j-1,k}$, $a_{i,j,k+1}$ and $a_{i,j,k-1}$ are defined analogously to Equations (A.4) and (A.5), and

$$a^{\Phi}_{i,j,k} = a^{\Phi}_{i+1,j,k} + a^{\Phi}_{i-1,j,k} + a^{\Phi}_{i,j+1,k} + a^{\Phi}_{i,j-1,k} + a^{\Phi}_{i,j,k+1} + a^{\Phi}_{i,j,k-1} + b_{\Phi} - S_{\Phi,i,j,k} \, . \quad (A.9)$$

The velocity components u_i in the momentum equations are integrated over control volumes that are centred in the respective velocity nodes.

The integrated equations are solved using a BI_CGSTAB (bi-conjugate gradient stabilised) solver. The SIMPLE algorithm, which is outlined in the next section, handles the pressure-velocity coupling in the governing equations.

A.3 The SIMPLE algorithm

The SIMPLE algorithm (Patankar and Spalding, 1972) is applied to solve the system of equations described in Section A.2. Hjertager (1982) extended the algorithm to handle compressible flows with additional source terms for the compression work in the enthalpy equation, and additional terms in the pressure correction equation.

The SIMPLE algorithm is initiated by making a guess for the pressure field at t_{n+1}, denoted p^*. The pressure field p^* is then used in the momentum equations to find a corresponding velocity field $\mathbf{u}^*$, and in the equation of state to find a corresponding density field ρ^*. In general, $\mathbf{u}^*$ does not satisfy the continuity equation, therefore iterative corrections are necessary. The pressure correction p' is defined as the difference

between the correct pressure field p and the guessed pressure field p^* (Versteeg and Malalasekera, 2007) according to

$$p = p^* + p' . \tag{A.10}$$

By using the linearised momentum equations, the velocities can be expressed in terms of p' as

$$u_{1,i,j,k} = u_{1,i,j,k}^* + D_{i,j,k}^{u_1} \left(p_{i-1,j,k}' - p_{i,j,k}' \right) , \tag{A.11}$$

$$u_{2,i,j,k} = u_{2,i,j,k}^* + D_{i,j,k}^{u_2} \left(p_{i,j-1,k}' - p_{i,j,k}' \right) , \tag{A.12}$$

$$u_{3,i,j,k} = u_{3,i,j,k}^* + D_{i,j,k}^{u_3} \left(p_{i,j,k-1}' - p_{i,j,k}' \right) , \tag{A.13}$$

where

$$D_{i,j,k}^{u_1} = \frac{\delta x_2 \delta x_3}{a_{i,j,k}^{u_1}} , \quad D_{i,j,k}^{u_2} = \frac{\delta x_1 \delta x_3}{a_{i,j,k}^{u_2}} , \quad D_{i,j,k}^{u_3} = \frac{\delta x_1 \delta x_2}{a_{i,j,k}^{u_3}} .$$

In addition, it is assumed that density variation with pressure is isentropic:

$$\rho = \rho^* + \frac{1}{c_{s,i,j,k}^2} p' , \tag{A.14}$$

where $c_{s,i,j,k}$ is the sound velocity in the point where the scalar variables are defined, with coordinates (i, j, k). When Equations (A.11) to (A.14) are inserted into the discretised continuity equation, an equation for the pressure correction p' is obtained. The source term in the equation for p' represents the mass imbalance resulting from the guessed velocity field $\mathbf{u}^*$, which will in general not satisfy continuity. The equation for p' can be solved to find a value for p', and thus enable the computation of the corrections in equations (A.11)-(A.13). New pressure- and velocity fields are computed using *under-relaxation* to ensure convergence of the solution algorithm:

$$p^{\text{new}} = p^* + \alpha_p p' , \tag{A.15}$$

$$u_1^{\text{new}} = \alpha_{u_1} u_1 + (1 - \alpha_{u_1}) u_1^{n-1} , \tag{A.16}$$

$$u_2^{\text{new}} = \alpha_{u_2} u_2 + (1 - \alpha_{u_2}) u_2^{n-1} , \tag{A.17}$$

$$u_3^{\text{new}} = \alpha_{u_3} u_3 + (1 - \alpha_{u_3}) u_3^{n-1} , \tag{A.18}$$

where the under-relaxation factors $\alpha_p, \alpha_{u_1}, \alpha_{u_2}$ and α_{u_3} take a value between 0 and 1, $\mathbf{u}$ is the corrected velocity field computed without relaxation, and $\mathbf{u}^{n-1}$ is the velocity field obtained in the previous iteration (Hjertager, 1986; Versteeg and Malalasekera, 2007). If convergence has not been obtained, the output from Equations (A.15) to (A.18) is used to perform the corrections in Equations (A.10) to (A.13) again. The procedure is repeated until convergence is obtained. In FLACS, the relaxation factor α_p is set to 0.8. The scalar equations are then solved.

A.4   Resolution in time and space

The time stepping scheme used in the FLACS PDE solver is a *first order backward Euler scheme* (Gexcon, 2016). To ensure stability and sufficient resolution of the governing physical phenomena, guidelines for setting the resolution in time, relative to

the resolution in space, have been established. These rely on CFL (Courant-Friedichs-Lewy) numbers (Courant et al., 1928) based on the speed of sound $c_{s,i}$ and the flow velocity u_i, defined as

$$\text{CFLC} = \frac{c_{s,i}\Delta t}{\Delta x_i} \ , \qquad \text{CFLV} = \frac{u_i\Delta t}{\Delta x_i} \ , \quad i = 1, 2, 3 \ , \tag{A.19}$$

where Δx_i is the grid resolution in the ith direction, and Δt is the time step. For gas explosion simulations, the standard settings in FLACS are CFLC = 5, and CFLV = 0.5.

For each time step and control volume, Δt is computed based on CFLV=0.5, the local flow velocity in each direction u_i, and the local grid size in each direction, Δx_i. Similarly, Δt relative to the local speed of sound, $c_{s,i}$ is computed, using CFLC=5. The strictest criterion found in the computational domain is finally applied (Gexcon, 2016), i.e.

$$\Delta t = \min \left[\frac{\text{CFLC} \ \Delta x_i}{c_{s,i}}, \frac{\text{CFLV} \ \Delta x_i}{u_i} \right] \ . \tag{A.20}$$

Consequently, in the initial phase of a gas explosion, when flow speeds are low, the time step Δt will be restricted by CFLC=5. However, when $u_i > 0.1 \ c_{s,i}$, the criterion CFLV=0.5 will determine the time step length.

Appendix B

Additional information about the experiments

This appendix includes additional details about the experimental campaigns that were performed as part of the doctoral study. Sections B.1-B.4 describe the small-scale experiments from papers 2-4, while Section B.5 describes the medium-scale experiments from Paper 2.

B.1   General description of the small-scale vented channel

A small-scale vented explosion chamber, located in the Gexon research laboratory at Fantoft in Bergen, was used for the experimental campaigns in papers 2-4 of the present thesis. When using small-scale rigs for experimental investigations, it is possible to undertake a higher number of tests than for large-scale experiments, i.e. perform repetitions, explore further parameter variations, etc. Furthermore, the initial conditions, such as the composition of the fuel-air cloud, initial temperature and turbulence levels, are easier to control in a small vessel than in a larger chamber. Therefore, the small-scale channel was considered useful for addressing the research question of the present study.

The rectangular explosion chamber has inner dimensions of 1.5 m × 0.3 m × 0.3 m, with one end wall (of dimensions 0.3 m × 0.3 m) removed, to provide explosion venting to the atmosphere. The vent opening is located opposite of the ignition location. Some minor adjustments were done to the rig for the tests for Paper 3 so that the dimensions of that chamber were 1.5 m × 0.28 m × 0.3 m, cf. Section B.4. Figure B.1 shows the rig geometry.

The inside of the vessel is smooth, except for two 1 1/2" holes for the gas mixing recirculation system, positioned at the top-left and bottom-right of the back-plate. The front wall of the explosion chamber is made from transparent polycarbonate, to enable high-speed video analysis of the flame propagation. The vessel is positioned on a table; therefore, the vent opening is constrained by the table at the bottom. The experiments were performed inside a room of dimensions 18 m × 14 m × 7 m. Due to its size, the effect of the room is considered to be insignificant for the experiments performed in the small-scale rig.

All explosion tests performed in the Gexcon small-scale chamber for the present doctoral study involved an initially quiescent, propane-air cloud. This was achieved by adding a gas composed of 99.9 vol.% propane to the system in Figure B.1, and mixing it with the air in the chamber by recirculation. Specifically, Figure B.1 illustrates the
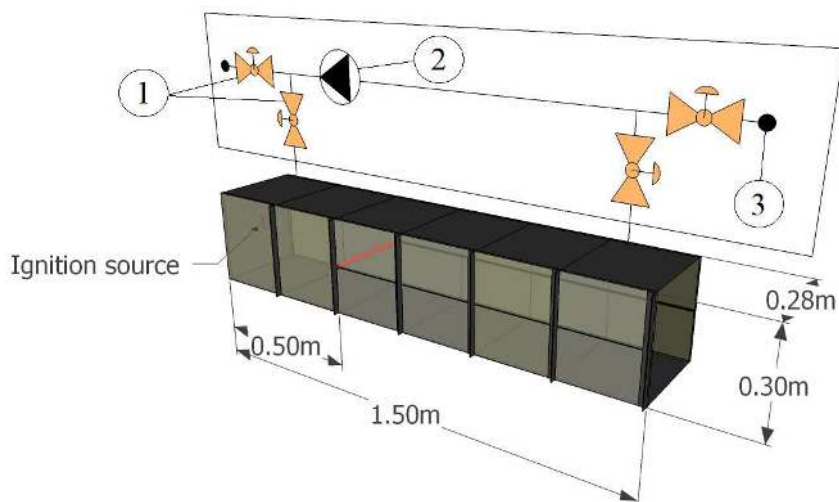
Figure B.1: Recirculation system for the small-scale experiments in papers 2-4.

configuration of the experiments in Paper 3. The same mixing system was used for all experiments performed in this chamber (i.e. also for papers 2 and 4). The symbols in Figure B.1 marked with (1) denote pneumatic actuated ball-valves, (2) denotes a fan, while the black circles (3) mark where the piping connects to the surrounding atmosphere. The gas concentration of the mixtures was monitored using an infrared gas analyser, type Servomex 4200.

In order to contain the gas mixture within the vessel during mixing and filling, the open end was covered with a thin plastic sheet. In the small-scale tests performed for papers 2 and 4, the plastic foil was clamped over the vent opening and was not removed prior to ignition. The opening pressure of this vent panel was observed to be 0.025 ± 0.005 bar (cf. Paper 2). In the tests performed for Paper 3, the plastic foil was held in place by a pneumatic system and released just prior to ignition.

A single spark generator was used as ignition source, positioned at the closed end of the channel (cf. Figure B.1). The energy from the spark was limited by a capacitor, and could reach a maximum energy of 50 mJ. The spark gap was 4 mm, and the ignition source was positioned approximately 15 mm from the wall. Ignition happened at least 1-2 minutes after fan shut-down for each test, in order to allow mixing-induced turbulence to decay.

The overpressure generated within the test vessel during the explosion tests was measured using a maximum of 4 piezo-electric pressure transducers from Kistler (type 701A) connected to Kistler charge amplifiers (type 5011A). The Kistler 701A transducers are specifically chosen for their high frequency response (70 kHz) and ability to capture the transient pressure build up, as well as for their high signal-to-noise ratios.

The signals from the pressure transducers were measured using a purpose-built test control and data acquisition application programmes, based on multi-purpose data acquisition cards (USB-6255) and relay switching cards from National Instruments, together with the LabView programming platform. The data logger was triggered using the relay switching card control system. A 1-2 mm thick insulating silicon layer was

applied to the transducer surface, to reduce signal drift caused by heat from the combustion products. The coordinates of the pressure transducers are given in Table B.1, and the positions of the transducers inside the rig are illustrated in Figure B.2. A varying number of pressure transducers was used for the different campaigns, as described in the following sections. The transducers were calibrated before each test campaign.

Table B.1: Positioning of pressure transducers in the small-scale vented channel. The origin is located in the upper left hand corner of the top view in Figure B.2.

ID	Type	Amplifier	x	y	z
P1	701A	5011A	0 mm	60 mm	240 mm
P2	701A	5011A	130 mm	0 mm	150 mm
P3	701A	5011A	610 mm	0 mm	150 mm
P4	701A	5011A	1100 mm	0 mm	150 mm
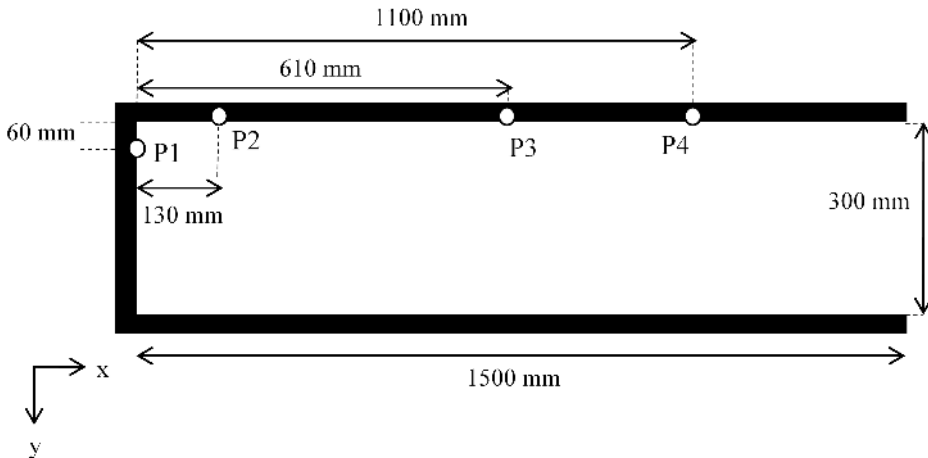
Figure B.2: Position of pressure transducers, top view (the origin is located in the upper left hand corner in this view).

B.2 Investigation of concentration effects in the small-scale vented channel

This section includes additional information about the small-scale explosion experiments performed for Paper 2 of the present thesis. The objective of the experiments was to obtain validation data for a Markstein number dependent burning velocity model, described in Chapter 4, Section 4.6 and Paper 2. Tests were conducted to study the effect on flame speeds and explosion overpressures of varying the fuel concentration in a propane-air mixture, for different flow regimes. Changing the fuel concentration leads to variations in the physicochemical properties of the mixture in terms of the Markstein number and the laminar burning velocity.

In order to study Markstein number effects at low strain rates, as well as for flows with a higher degree of turbulence production, small-scale experiments were performed both in an empty vented channel (termed "Setup 1" in Paper 2) and for the same configuration with 5 rectangular obstructions inserted (termed "Setup 2" in Paper 2). Figure B.3 shows the overall configuration for "Setup 1" and "Setup 2", while Figure B.4 shows the obstacle configuration for "Setup 2" as inserted in the rig.
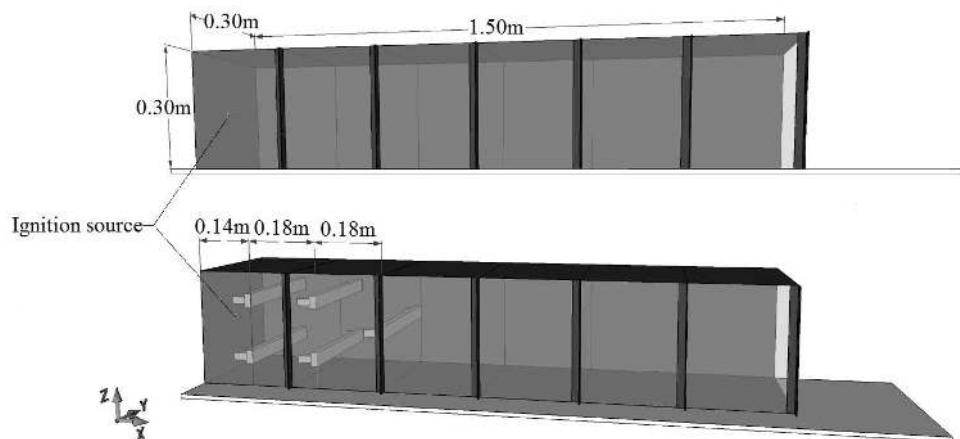

Figure B.3: Layout of small-scale experiments performed for Paper 2, "Setup 1" (top) and "Setup 2" (bottom).
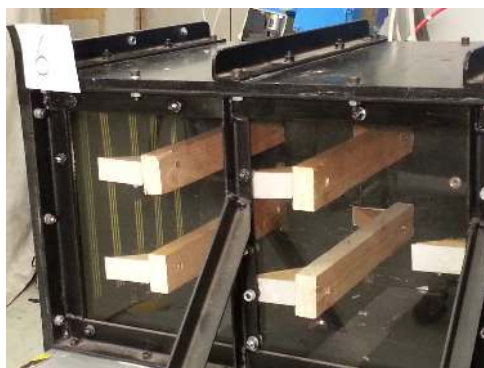
Figure B.4: Obstacle configuration of small-scale experiments performed for Paper 2, with "Setup 2".

Table B.2 presents the full experimental matrix for the experiments in the empty, small-scale channel with "Setup 1". In this phase of the experimental programme, Markstein number effects in fuel-rich mixtures were of primary interest. In order to achieve an appreciable variation in the strain rate Markstein numbers of the mixture, the concentration of propane in air was varied between 4.2 vol % and 7.5 vol % (cf. Section 4.5.2) for the experiments with "Setup 1". For the range of concentrations investigated in the present study (when the equivalence ratio exceeds 1), the Markstein

number decreases with increasing fuel percentage in the flammable mixture (cf. Figure 4.2). All tests (except for the two richest concentrations) were repeated at least twice.

Table B.2: Test matrix, small-scale, "Setup 1" (Paper 2).

	Geometry	vol % propane in air	Comments
Test 1	Setup 1	4.2 vol.%	
Test 2	Setup 1	4.2 vol.%	
Test 3	Setup 1	4.2 vol.%	
Test 4	Setup 1	5.0 vol.%	
Test 5	Setup 1	5.0 vol.%	
Test 6	Setup 1	5.5 vol.%	
Test 7	Setup 1	5.5 vol.%	
Test 8	Setup 1	6.0 vol.%	
Test 9	Setup 1	6.0 vol.%	
Test 10	Setup 1	6.5 vol.%	
Test 11	Setup 1	6.5 vol.%	
Test 12	Setup 1	7.0 vol.%	Pressure recordings lost.
Test 13	Setup 1	7.5 vol.%	

Figures B.5 - B.10 show the unfiltered pressure-time histories recorded for each of the 4 pressure transducers (cf. Table B.1 and Figure B.2), for each test in Table B.2. The pressure recordings from P3 and P4 exhibited signal drift, occurring after the flame has passed, for a majority of the tests. The recordings for Test 12 in Table B.2 are not included in the analysis, as the data files from this test were found to be corrupt.

(a) Test 1   (b) Test 2
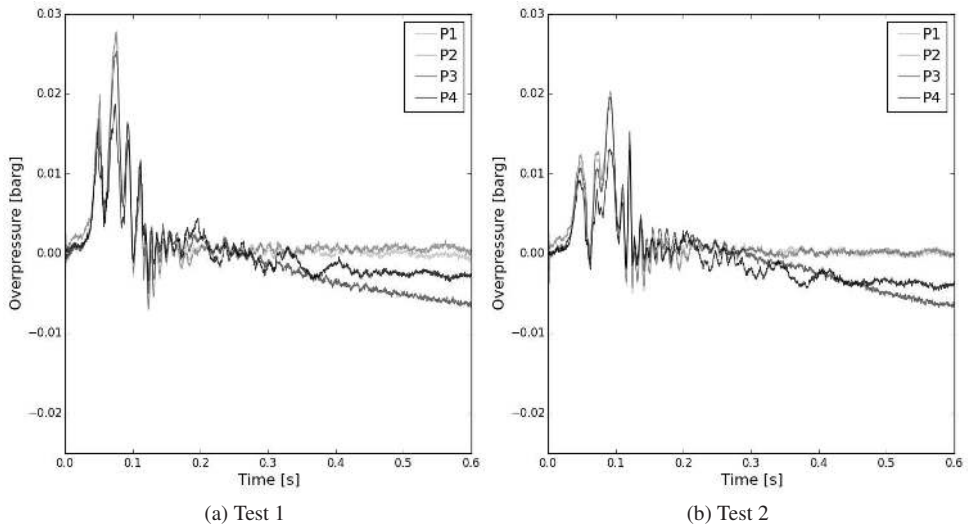
Figure B.5: Pressure-time curves for "Setup 1", Test 1 and Test 2 (Paper 2).

(a) Test 3   (b) Test 4
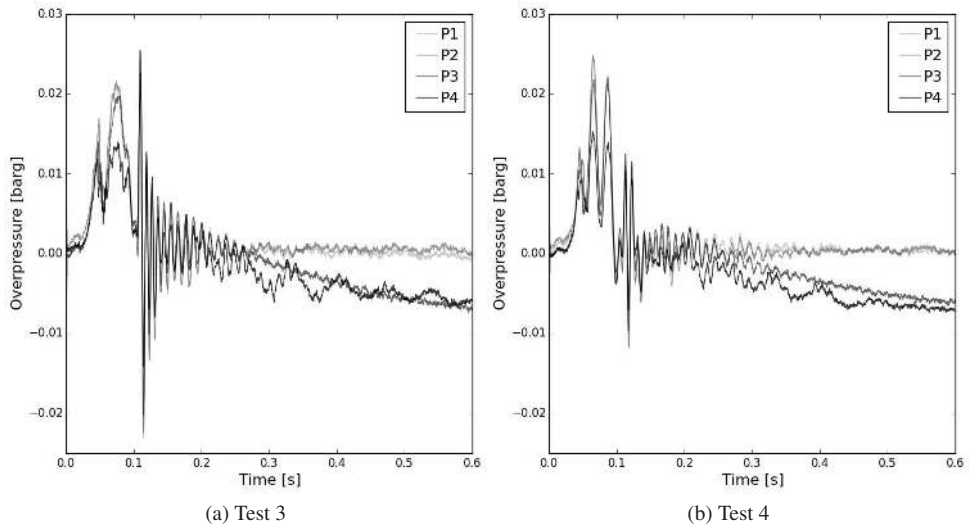
Figure B.6: Pressure-time curves for "Setup 1", Test 3 and Test 4 (Paper 2).

(a) Test 5   (b) Test 6
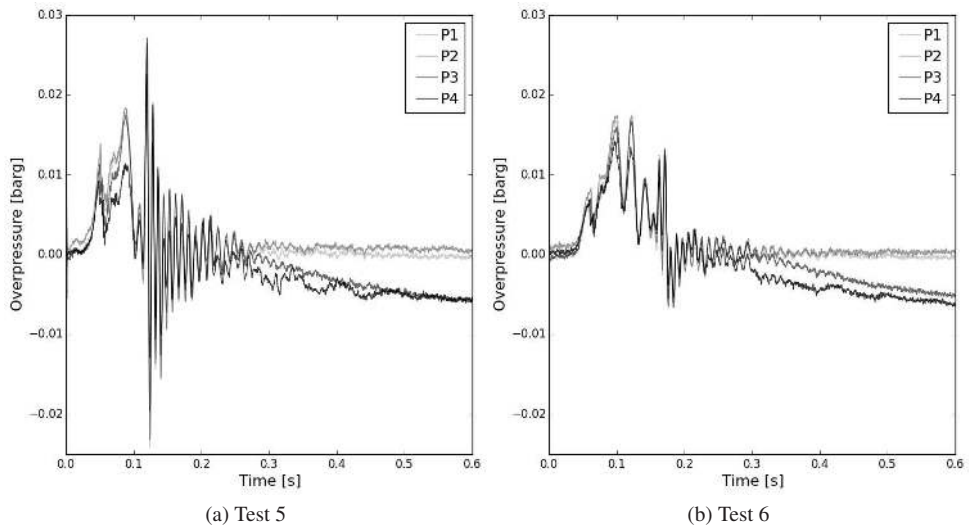
Figure B.7: Pressure-time curves for "Setup 1", Test 5 and Test 6 (Paper 2).

(a) Test 7   (b) Test 8
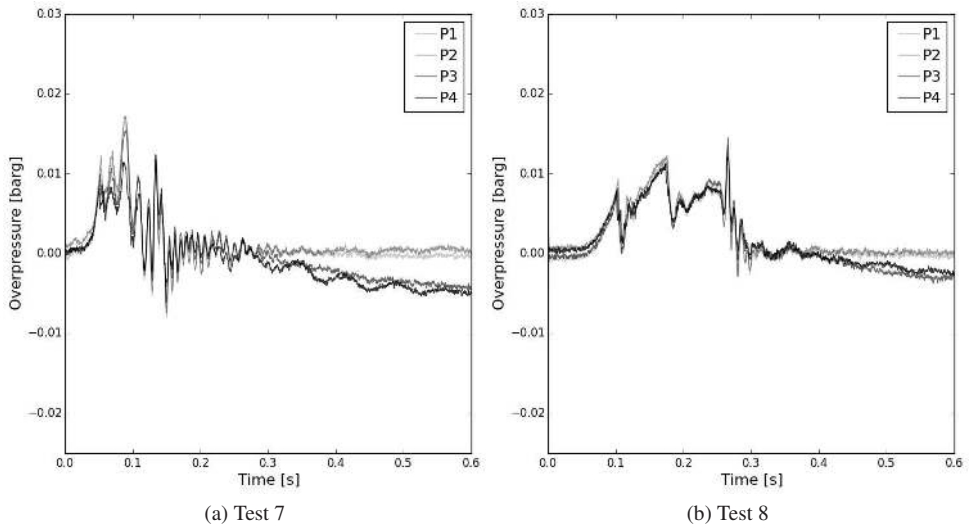
Figure B.8: Pressure-time curves for "Setup 1", Test 7 and Test 8 (Paper 2).

(a) Test 9   (b) Test 10
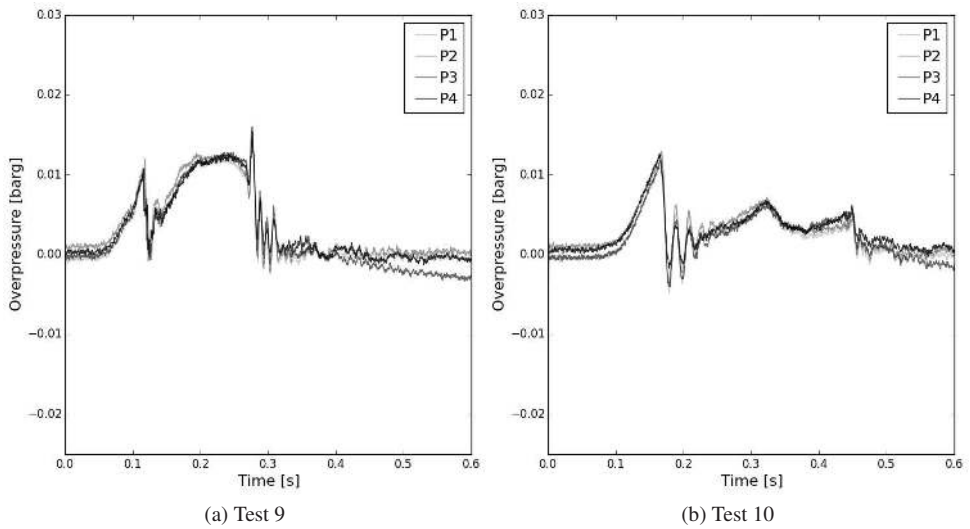
Figure B.9: Pressure-time curves for "Setup 1", Test 9 and Test 10 (Paper 2).

(a) Test 11   (b) Test 13
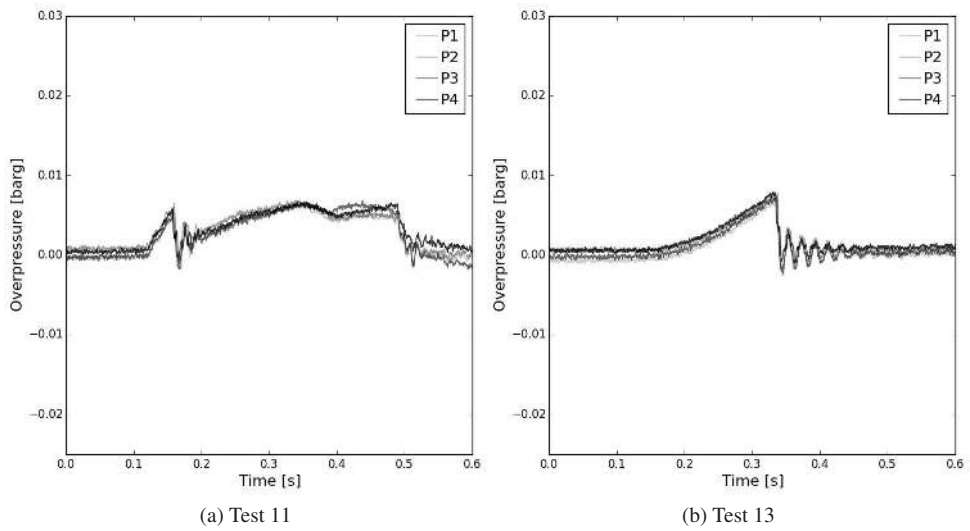
Figure B.10: Pressure-time curves for "Setup 1", Test 11 and Test 13 (Paper 2).

Table B.3 shows the full experimental matrix for the experiments in the small-scale channel with five rectangular obstructions inserted ("Setup 2"). To obtain data for a wider range of Markstein numbers and laminar burning velocities, this series was extended to fuel-lean mixtures. Only P1 and P2 (cf. Table B.1 and Figure B.2) were available for the small-scale tests with "Setup 2". However, as the pressure-time traces are similar for all transducers, the analysis in Paper 2 consistently focuses on the signal from P1.

Table B.3: Test matrix, small-scale, "Setup 2" (Paper 2).

	Geometry	vol % propane in air	Comments
Test 1	Setup 2	3.0 vol.%	
Test 2	Setup 2	3.5 vol.%	Pressure recordings failed.
Test 3	Setup 2	3.6 vol.%	
Test 4	Setup 2	4.0 vol.%	
Test 5	Setup 2	4.3 vol.%	
Test 6	Setup 2	4.5 vol.%	
Test 7	Setup 2	5.0 vol.%	
Test 8	Setup 2	6.0 vol.%	
Test 9	Setup 2	6.0 vol.%	
Test 10	Setup 2	5.5 vol.%	
Test 11	Setup 2	5.6 vol.%	
Test 12	Setup 2	4.9 vol.%	

Figures B.11-B.16 show the unfiltered pressure recordings from the test series with "Setup 2". Due to failure of the LabView logging system, the data for Test 2 with "Setup 2" was lost.
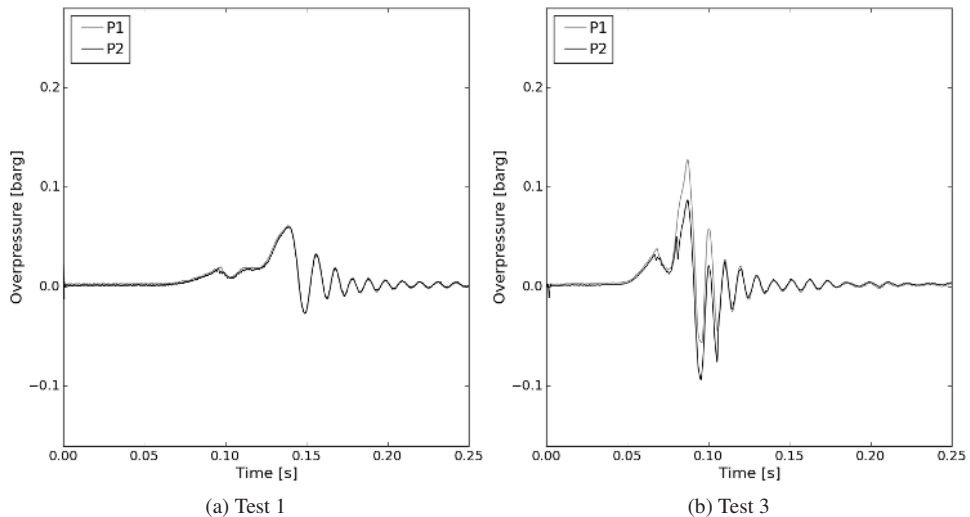
(a) Test 1

(b) Test 3

Figure B.11: Pressure-time curves for "Setup 2", Test 1 and Test 3 (Paper 2).

(a) Test 4   (b) Test 5
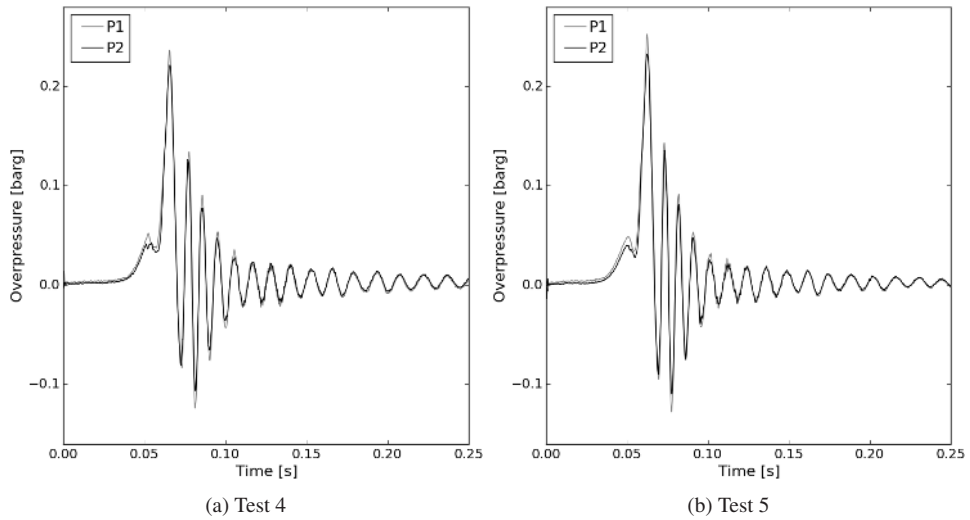
Figure B.12: Pressure-time curves for "Setup 2", Test 4 and Test 5 (Paper 2).

(a) Test 6   (b) Test 7
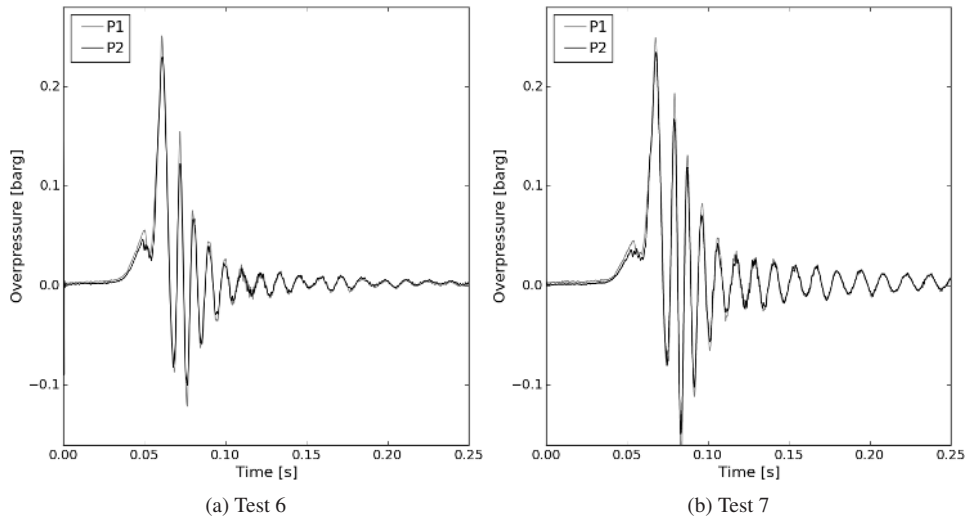
Figure B.13: Pressure-time curves for "Setup 2", Test 6 and Test 7 (Paper 2).

(a) Test 8   (b) Test 9
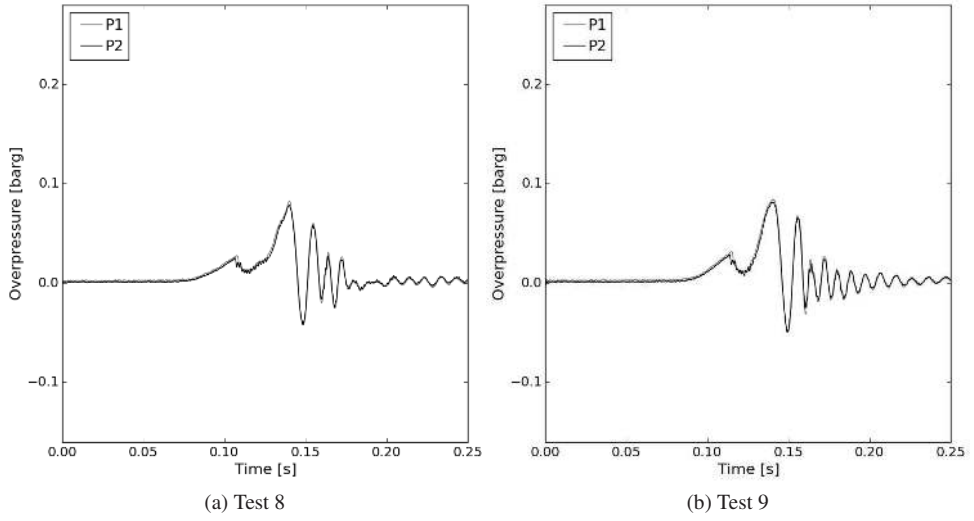
Figure B.14: Pressure-time curves for "Setup 2", Test 8 and Test 9 (Paper 2).

(a) Test 10   (b) Test 11
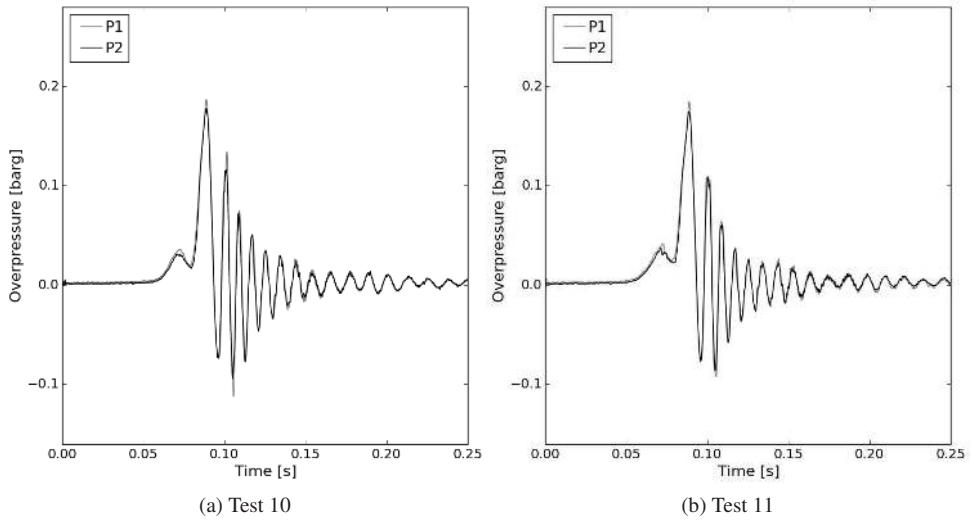
Figure B.15: Pressure-time curves for "Setup 2", Test 10 and Test 11 (Paper 2).
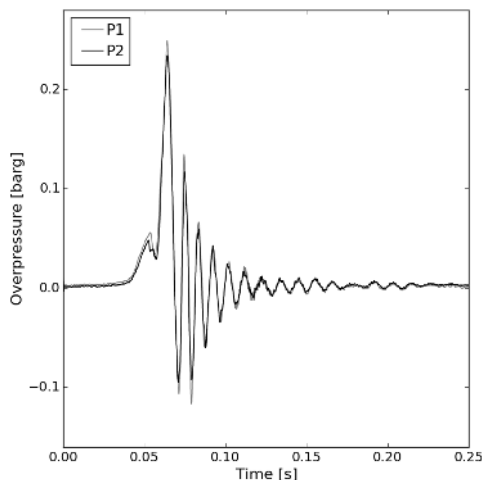
Figure B.16: Pressure-time curves for "Setup 2", Test 12 (Paper 2).

B.3   Investigation of vegetation effects in the small-scale vented channel

The small-scale rig described in Section B.1 was also used for the experiments performed for Paper 4 of the present thesis. The general setup of the experiments in Paper 4 was identical to that described in Section B.1. In this series, all 4 pressure transducers were operative (cf. Table B.1 and Figure B.2).

The experimental study described in Paper 4 was conducted to support the development of a general sub-grid modelling approach to account for vegetation in industrial-scale gas explosions. The need for such an approach was identified in the aftermath of the severe incident that occurred at the fuel storage depot Buncefield, UK, in 2005 (BMIIB, 2008). Specifically, the campaign in Paper 4 involved inserting branches from different types of trees into the small-scale, vented channel during a series of propane-air explosions. Chapter 5 elaborates on the findings of Paper 4.

Table B.4 includes the full experimental matrix of the campaign. Branches from Norway Spruce *(Pies abies)*, Mugo Pine *(Pinus mugo)* and Thuja *(Thuja occidentalis)* were inserted in the channel during a series of near-stoichiometric propane-air explosions. A steel rod was added to the rig to allow for fixing branches in three different positions: 0.35 m, 0.60 m and 0.85 m from the back wall, cf. figures B.17 and B.18. The effect of foliage was investigated by performing tests where all needles were removed from the spruce branches, while the effect of flexibility was studied by replacing the bare spruce branches with stainless steel models with an identical structure. The steel branches provided the same blockage ratio and spatial distribution of obstructions as the real branches, but did not deform when exposed to explosion-generated flow.

Table B.4: Experimental matrix for the small-scale vegetation tests (Paper 4).

Test number	Geometry	Gas	vol % propane in air	Comments
Test 14	1 spruce branch (Branch 1) in middle position	Propane	4.2 %	
Test 15	1 spruce branch (Branch 1) in middle position	Propane	4.2 %	Repeat of Test 14.
Test 16	2 spruce branches, Branch 2 at inner position, Branch 3 at middle position	Propane	4.2 %	
Test 17	3 spruce branches, Branch 2 at inner position, Branch 3 at middle position, Branch 1 at outer position	Propane	4.2 %	
Test 18	3 spruce branches, Branch 2 without needles at inner position, Branch 3 without needles at middle position, Branch 1 without needles at outer position	Propane	4.2 %	
Test 19	3 steel branches, Branch 2 at inner position, Branch 3 at middle position, Branch 1 at outer position	Propane	4.2 %	Video failure. P3 failed.
Test 20	3 steel branches, Branch 2 at inner position, Branch 3 at middle position, Branch 1 at outer position	Propane	4.2 %	Pressure recordings failed. Repeat of Test 19.
Test 21	3 pine branches, Branch 3 at inner position, Branch 2 at middle position, Branch 1 at outer position	Propane	4.2 %	P3 failed.
Test 22	3 thuja branches, Branch 3 at inner position, Branch 2 at middle position, Branch 1 at outer position	Propane	4.2 %	Pressure recordings failed.
Test 23	3 thuja branches, Branch 3 at inner position, Branch 2 at middle position, Branch 1 at outer position	Propane	4.2 %	Repeat of Test 22. P3 failed.
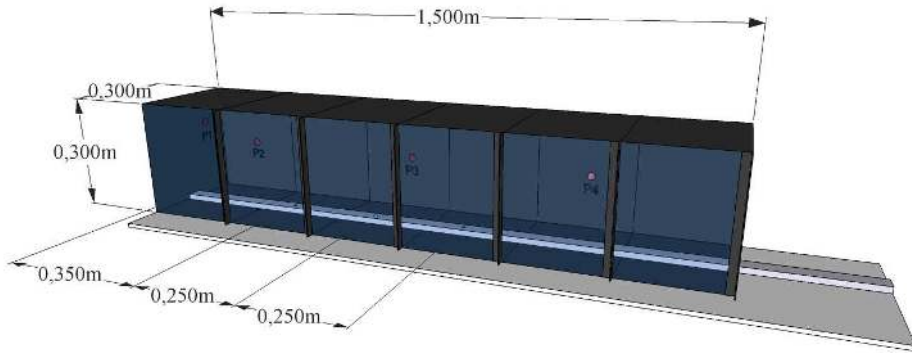
Figure B.17: Rig used for the vegetation tests, indicating the positions of pressure transducers and branches (Paper 4).

Figure B.18: Branch inserted in rig (Paper 4).

Each branch was analysed in detail, and characterised in terms of its projected two-dimensional blockage ratio. This parameter was found from analysis of photographs, by converting colour images of the branches to pure black and white representations, and computing the ratio between the black and white pixels (cf. Figure B.19).

(a) Original photograph of spruce branch 1.   (b) Black/white representation of spruce branch 1.
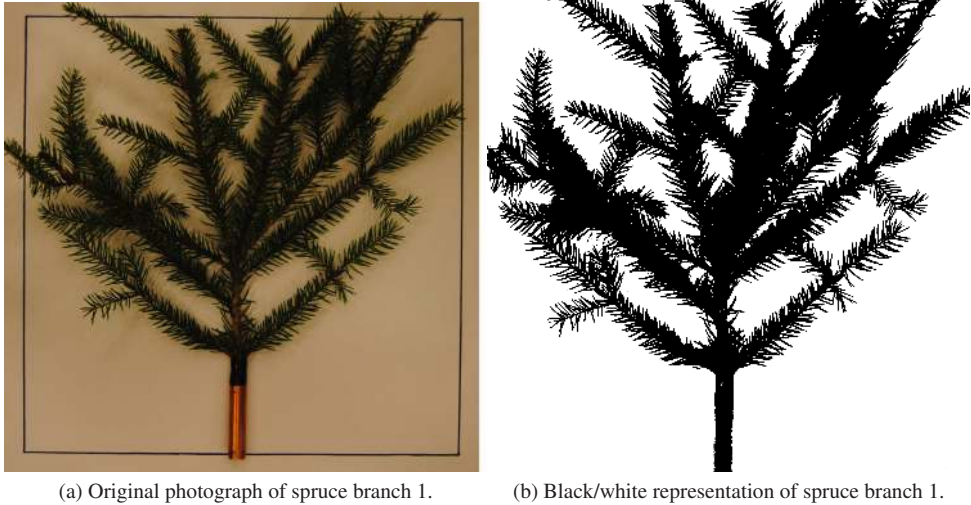
Figure B.19: Photograph analysis of blockage ratio (Paper 4).

In addition, the spruce branches were analysed further: they were weighed to determine their total mass and submerged in water to determine their volume blockage. The latter process is illustrated by Figure B.20. The diameters and lengths of the individual components of the spruce branches were measured. Tables B.5 and B.6 summarise the analysis.

Figure B.20: Volume measurement of spruce branch 3 (Paper 4).

Table B.5: Blockage ratio analysis of all branches (Paper 4).

Branch ID	Blockage ratio
Spruce branch 1	0.36
Spruce branch 1, no needles	0.08
Spruce branch 2	0.37
Spruce branch 2, no needles	0.11
Spruce branch 3	0.32
Spruce branch 3, no needles	0.12
Pine branch 1	0.32
Pine branch 2	0.28
Pine branch 3	0.21
Thuja branch 1	0.62
Thuja branch 2	0.45
Thuja branch 3	0.49
Steel spruce branch 1	0.09
Steel spruce branch 2	0.11
Steel spruce branch 3	0.12

Table B.6: Analysis of the spruce branches (Paper 4).

Branch ID	Total volume	Total length	Mass
Spruce branch 1	19.5 ml	261 cm	21.28 g
Spruce branch 1, no needles	7 ml	261 cm	9.51 g
Spruce branch 2	35 ml	295 cm	37.97 g
Spruce branch 2, no needles	15 ml	295 cm	15.01 g
Spruce branch 3	30 ml	339 cm	32.29 g
Spruce branch 3, no needles	15 ml	339 cm	14.46 g

Figures B.21-B.24 show the recorded, unfiltered pressure-time curves from the experimental campaign performed for Paper 4. For tests 19, 21 and 23, P3 malfunctioned, and did not record the pressure development. For tests 20 and 22, all pressure recordings were lost due to system failure. As in Paper 2, the analysis of test results was performed primarily using recordings from P1. The analysis based on P1 is considered representative for the overall internal pressure development in the different tests.

(a) Test 14.   (b) Test 15.
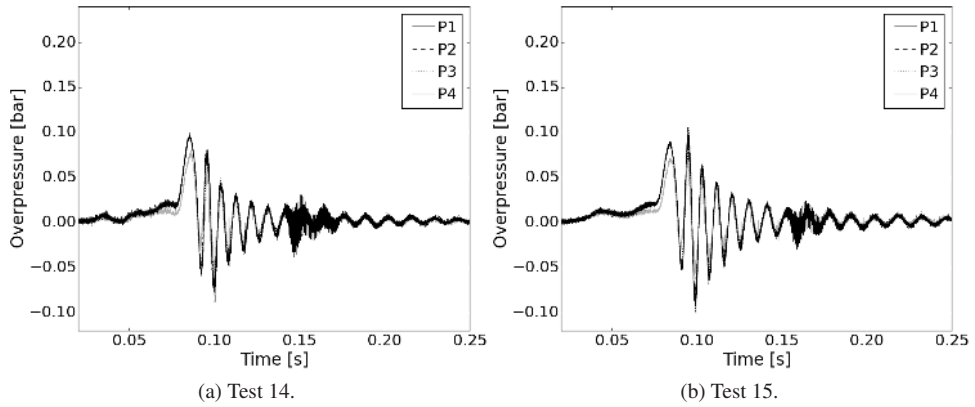
Figure B.21: Tests performed with one spruce branch inserted in the rig (Paper 4).

(a) Test 16.   (b) Test 17.
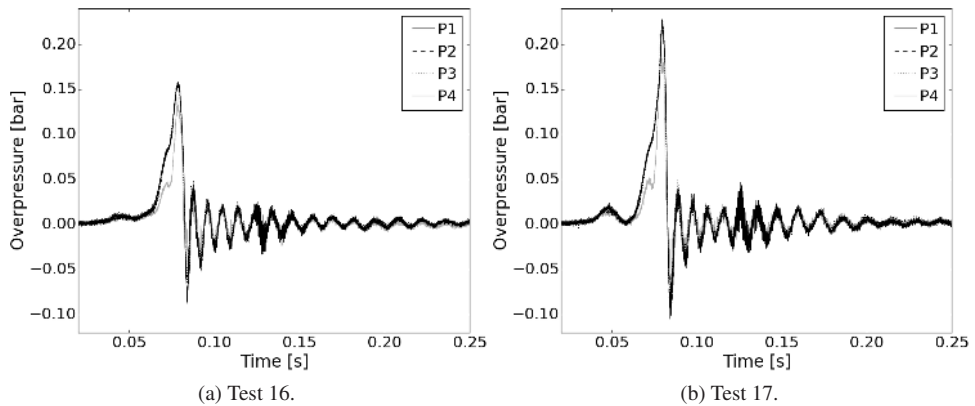
Figure B.22: Tests performed with two spruce branches (left) and three spruce branches (right) inserted in the rig (Paper 4).

(a) Test 18.

(b) Test 19.
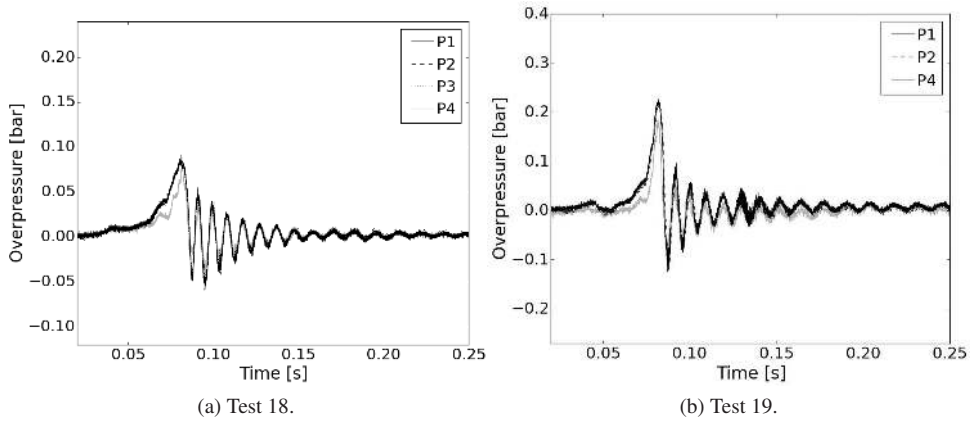
Figure B.23: Tests performed with three spruce branches without needles (left) and three steel branches (right) inserted in the rig (Paper 4).

(a) Test 21.

(b) Test 23.
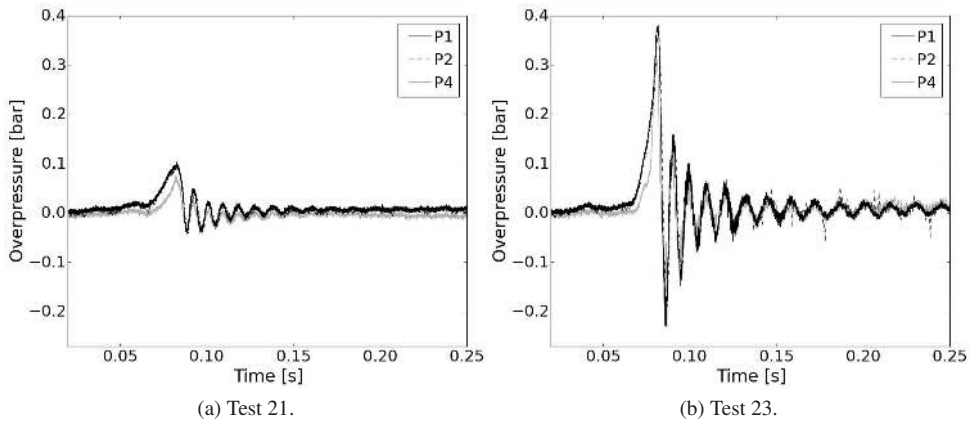
Figure B.24: Tests performed with three pine branches (left) and three thuja branches (right) inserted in the rig (Paper 4).

B.4 Investigation of vortex shedding effects in the small-scale vented channel

For Paper 3, an experimental campaign was performed to investigate the contribution of vortex shedding to the overpressure generation in gas explosions with a single obstacle inserted. The tests for Paper 3 were performed in the small-scale rig described in Section B.1. However, several minor adjustments were done in order to insert the obstructions that were used for this campaign.

A cylinder with a diameter D = 0.0157 m and (effective) length 17.8D was positioned 0.50 m downstream of the ignition point, at the chamber centre-line. The circular cylinder, mounted horizontally, spanned the channel cross-section. In order to mount the cylinder inside the chamber, and at the same time preserve the symmetric and smooth conditions around the wake centre-line all along the length of the rig, two polycarbonate side walls (with dimensions 1.5 m × 0.01 m × 0.30 m) were inserted to cover the back and front walls.

The effect on the explosion overpressure of adding five different splitter plates with a fixed (effective) width of 17.8D, thickness 0.06D and varying length L in the streamwise direction, to the reference case circular cylinder was studied (cf. Figure B.25). For the present study, the polycarbonate walls inside the explosion chamber were modified such that splitter plates could be inserted from the channel's open end through a horizontal slit, see Figure B.26. This unique design enabled ease of operation while maintaining stability and rigidity of both the cylinder and the splitter plates throughout the explosion. Furthermore, tests were performed where two helical steel wires of varying pitch (P) and fixed diameter d = 0.1D were added to the reference case cylinder. Figure B.27 shows the two different helical steel wires mounted on the obstruction. Note that the wire was not completely attached to the cylinder surface and a minimal gap is provided to allow for easy replacement of different wire configurations. Table B.7 gives an overview of all tests in the campaign.
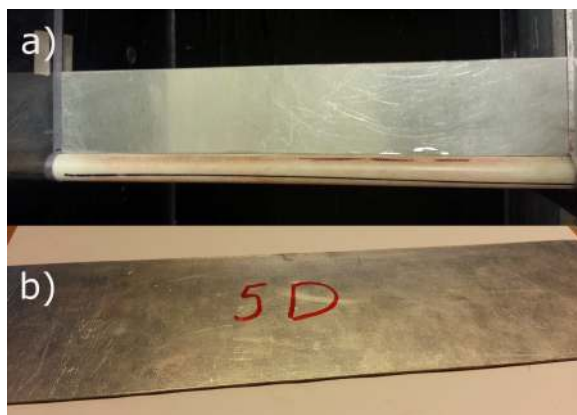

Figure B.25: a) A splitter plate inserted in the experimental rig and b) the splitter plate SP1, with a length of 5.13D.

Figure B.26: Rig used for the vortex shedding tests, with a single circular cylinder inserted (Paper 3).

Figure B.27: Helical steel wire with a pitch of a) 8D and b) 4D, added to the circular cylinder.

Table B.7: Test matrix, experiments for Paper 3.

	Geometry	vol % propane in air	Comments
Test 1	Base case	4.26 vol.%	
Test 2	Base case	4.10 vol.%	
Test 3	SP1, length 5.13D	4.17 vol.%	
Test 4	SP1, length 5.13D	-	Test failed
Test 5	SP1, length 5.13D	4.28 vol.%	
Test 6	SP1, length 5.13D	4.25 vol.%	
Test 7	SP2, length 3.04D	4.23 vol.%	
Test 8	SP2, length 3.04D	4.14 vol.%	
Test 9	SP2, length 3.04D	4.20 vol.%	
Test 10	SP3, length 1.02D	4.19 vol.%	
Test 11	SP3, length 1.02D	4.12 vol.%	
Test 12	SP4, length 0.51D	4.18 vol.%	
Test 13	SP4, length 0.51D	4.17 vol.%	
Test 14	Base case	4.19 vol.%	
Test 15	Base case	4.23 vol.%	
Test 16	SP5, length 0.26D	4.24 vol.%	
Test 17	SP5, length 0.26D	4.29 vol.%	
Test 18	HW1, pitch 4D	4.22 vol.%	
Test 19	HW1, pitch 4D	4.27 vol.%	
Test 20	HW2, pitch 8D	4.24 vol.%	
Test 21	HW2, pitch 8D	4.24 vol.%	

The lightweight plastic sheet was released 0.1 s prior to ignition by a pneumatic system, to allow free flow out of the chamber during the explosion. This was done in order to remove the uncertainty that the variable opening of the plastic panel introduced for the small-scale experiments in papers 2 and 4.

A single transducer of the same type as described in sections B.1, B.2 and B.3 was used to measure the pressure development, in the position of P1 (cf. Table B.1 and Figure B.2). Each test was repeated at least twice, in order to assess the reproducibility of the results. Figures B.28-B.31 show the unfiltered curves for all tests in the experimental campaign.

(a) Base case   (b) SP1
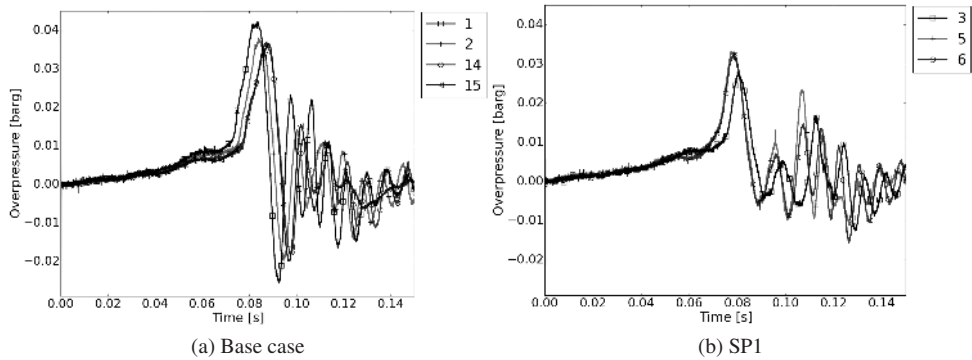
Figure B.28: Tests performed with the base case geometry (a single circular cylinder) (left) and SP1 (right) (Paper 3).

(a) SP2   (b) SP3
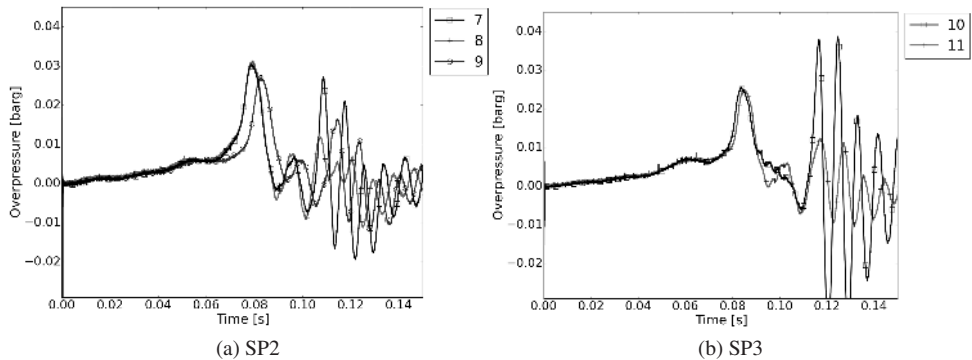
Figure B.29: Tests performed with configuration SP2 (left) and SP3 (right) (Paper 3).

(a) SP4

(b) SP5
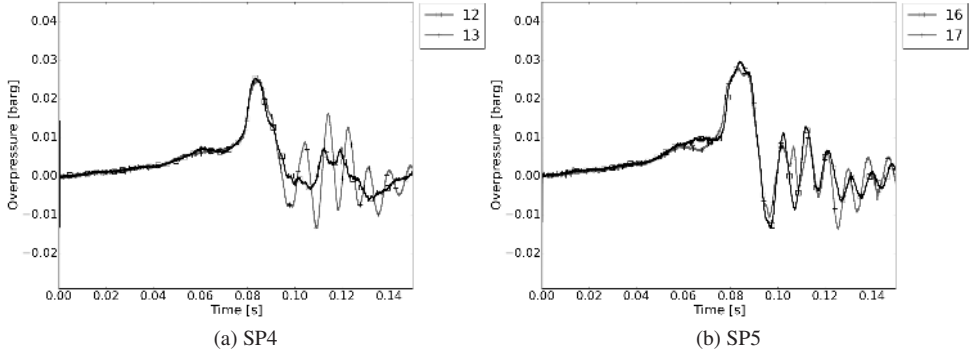
Figure B.30: Tests performed with configuration SP4 (left) and SP5 (right) (Paper 3).

(a) HW4D

(b) HW8D
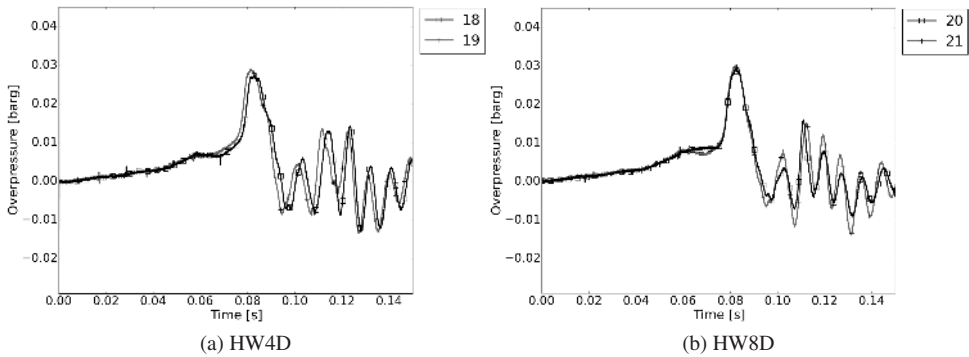
Figure B.31: Tests performed with configuration HW4D (left) and HW8D (right) (Paper 3).

B.5   Investigation of concentration effects in the medium-scale vented channel

To produce additional validation data (at higher strain rates) for the Markstein number-dependent combustion model developed for Paper 2, a series of experiments with varying concentrations of propane in air was performed in a *medium-scale* rig. The medium-scale tests (described in Paper 2) were performed in a 1.21 m $\times$ 1.22 m $\times$ 6.10 mm vessel with a volume of 9.0 m^3. This vessel is a scaled-up version (by a factor 4) of the small-scale rig described in sections B.1-B.4. Corresponding obstacle configurations as for the small-scale experiments ("Setup 1" and "Setup 2") were used for 6 of the experiments in the medium-scale channel (cf. Table B.8). In addition, 11 tests were performed with "Setup 3" (cf. Table B.9). For "Setup 3", 4 arrays of 6 cylindrical obstructions were placed inside the vessel at respectively 2, 3, 4 and 5 meters from the closed end of the vessel. These grids consisted of pipes with a diameter of 20 mm, and the pipes were mounted on 10 mm thick steel brackets. Figure B.32 shows the geometric configurations of the medium-scale experiments. The tests using "Setup 1" and "Setup 2" were performed a year before the experiments with "Setup 3". Therefore, the setup and instrumentation of the tests varied somewhat, as described in the following.
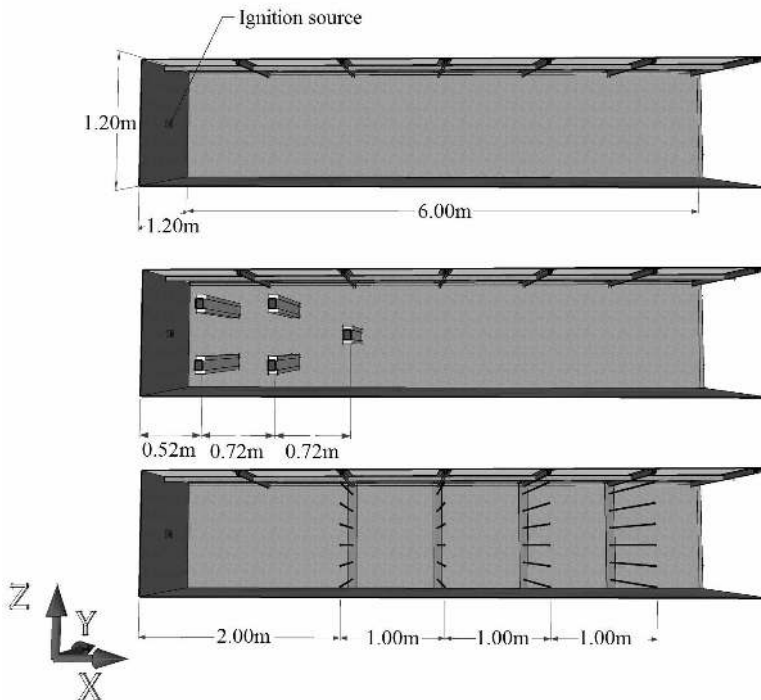
Figure B.32: Layout of medium-scale experiments performed for Paper 2, "Setup 1" (top), "Setup 2" (middle) and "Setup 3" (bottom).

Table B.8: Test matrix, medium-scale, "Setup 1" and "Setup 2". Concentrations in vol % propane in air.

Test ID	Geometry	Target concentration	Measured concentration
Test 70	Setup 1	4.2 vol.%	4.2 vol.%
Test 71	Setup 1	4.2 vol.%	4.2 vol.%
Test 72	Setup 1	5.5 vol.%	5.3 vol.%
Test 73	Setup 2	4.2 vol.%	4.2 vol.%
Test 74	Setup 2	5.5 vol.%	5.5 vol.%
Test 75	Setup 2	6.5 vol.%	6.8 vol.%

Table B.9: Test matrix, medium-scale, "Setup 3". Concentrations in vol % propane in air.

Test ID	Geometry	Measured concentration
Test 17	Setup 3	4.1 vol.%
Test 18	Setup 3	3.8 vol.%
Test 19	Setup 3	5.4 vol.%
Test 20	Setup 3	5.3 vol.%
Test 21	Setup 3	5.0 vol.%
Test 22	Setup 3	4.2 vol.%
Test 23	Setup 3	3.5 vol.%
Test 24	Setup 3	3.6 vol.%
Test 25	Setup 3	6.0 vol.%
Test 26	Setup 3	5.5 vol.%
Test 27	Setup 3	4.9 vol.%

The medium-scale vessel was located outdoors at ground-level (cf. Figure B.33), the vent opening was therefore constrained by the ground outside the vessel. The roof of the vessel was covered with polycarbonate plates to allow filming of the explosion propagation inside the vessel from above. An internal grid made of angle iron was placed under the roof to prevent the polycarbonate plates from breaking during the tests. Figure B.34 shows the roof structure. Figure B.35 shows the obstacles for "Setup 2" inserted in the medium-scale channel.

Figure B.33: Photograph of the medium-scale rig without the roof.
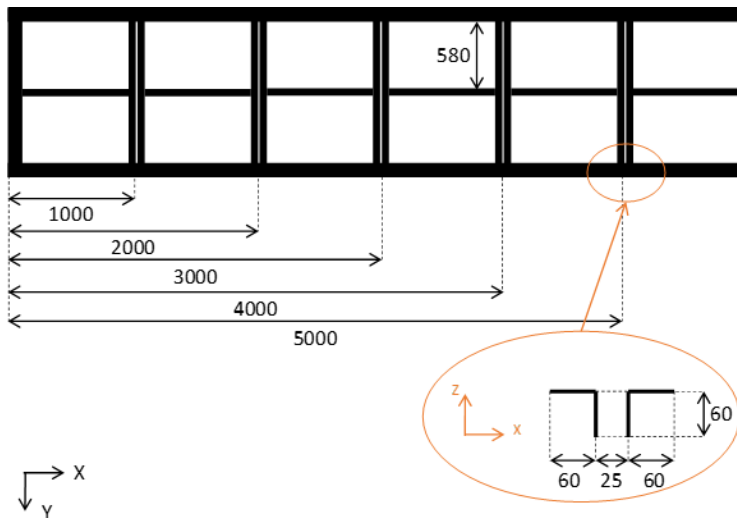
Figure B.34: Steel roof structure on the medium-scale rig.

To allow gas filling, the medium-scale vessel was equipped with a gas recirculation system, consisting of a centrifugal fan and two sets of 4" butterfly valves, all connected with 4" hoses. This enabled the gas mixing system to be isolated from the explosion module prior to ignition. Gas was added to the recirculated flow immediately downstream the fan, and thus gradually mixed with air throughout the vessel. The

Figure B.35: Medium-scale rig with the "Setup 2" obstacle configuration.

gas concentration was continuously monitored throughout the filling procedure using a Servomex 4200 infrared gas analyser.

The oscillating spark used in the medium-scale tests was based on a transformer that transformed the mains to 50 kV, so ignition occurred in an interval up to approximately 20 ms after it was triggered. The spark gap of the ignition source was 4 mm, and the electrodes were located approximately 50 mm from the wall. The open end of the vessel was covered with a thin plastic film in order to keep the gas inside the vessel during gas filling. This plastic film was kept in place during filling using a pneumatic system, and was released 1 second prior to ignition.

The overpressure generated within the test vessel during the explosion tests was measured using up to 8 piezoelectric pressure transducers from Kistler (type 7261) connected to Kistler charge amplifiers (type 5073 or 5011A). The 7261 transducers have a frequency response of 13 kHz. For the tests performed with "Setup 1" and "Setup 2", 4 pressure transducers were used, located in the corresponding positions as for the small-scale tests (cf. Table B.1 and Figure B.2). In the tests performed with "Setup 3", 8 pressure transducers were used to record the pressure-time development inside the experimental rig. The coordinates of the pressure transducers used for "Setup 3" are given in Table B.10.

Table B.10: Positioning of pressure transducers in the medium-scale vented channel for "Setup 3" (Paper 2). The origin is located in the upper left hand corner in the top view in Figure B.34.

ID	Type	Amplifier	x	y	z
P1	7261	5011A	0 mm	330 mm	850 mm
P2	7261	5011A	1050 mm	0 mm	1000 mm
P3	7261	5073	2125 mm	0 mm	200 mm
P4	7261	5073	2200 mm	0 mm	1000 mm
P5	7261	5073	2500 mm	0 mm	200 mm
P6	7261	5073	2750 mm	0 mm	1000 mm
P7	7261	5073	3125 mm	0 mm	200 mm
P8	7261	5073	3200 mm	0 mm	1000 mm

Purpose-built test control and data acquisition application programmes based on two multi-purpose data acquisition cards (USB-6353) and several relay switching cards

from National Instruments, together with the LabView programming platform, were used to perform the experiments. The explosion test control system controlled the timing of all remotely operated equipment. Switching was performed automatically using a general-purpose output unit based on multi-channel electromechanical relay switching cards from National Instruments, controlled by the test control programme.

The medium-scale tests with "Setup 3" were recorded using two high-speed digital SLR cameras (Casio Exilim Ex-F1). The high speed cameras have the ability to record at up to 1200 fps. Flame propagation analysis and flame speed estimates were made from manually extracted flame positions vs. time from the high-speed video recordings. Cameras were only available for the experiments with "Setup 3".

Figures B.36-B.38 show the unfiltered pressure-time curves from the medium-scale tests with "Setup 1" and "Setup 2". Figures B.39-B.44 show the unfiltered pressure-time curves from the medium-scale tests with "Setup 3". P2 malfunctioned throughout the latter series. As for the small-scale tests, the analysis in Paper 2 focused on the recordings from P1.

(a) Test 70, Setup 1.　　　　　　　　(b) Test 71, Setup 1.
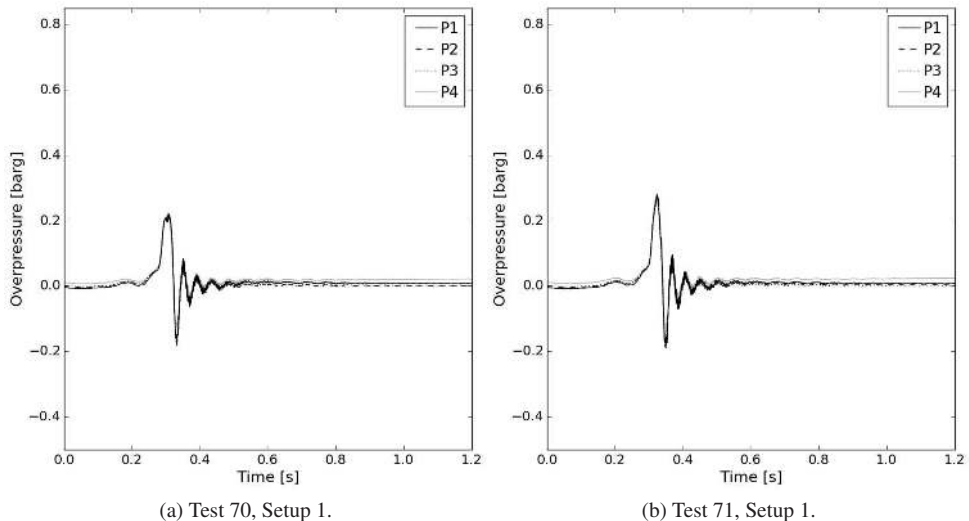
Figure B.36: Pressure-time histories, medium-scale tests, Test 70 and Test 71, "Setup 1" (Paper 2).

(a) Test 72, Setup 1.   (b) Test 73, Setup 2.
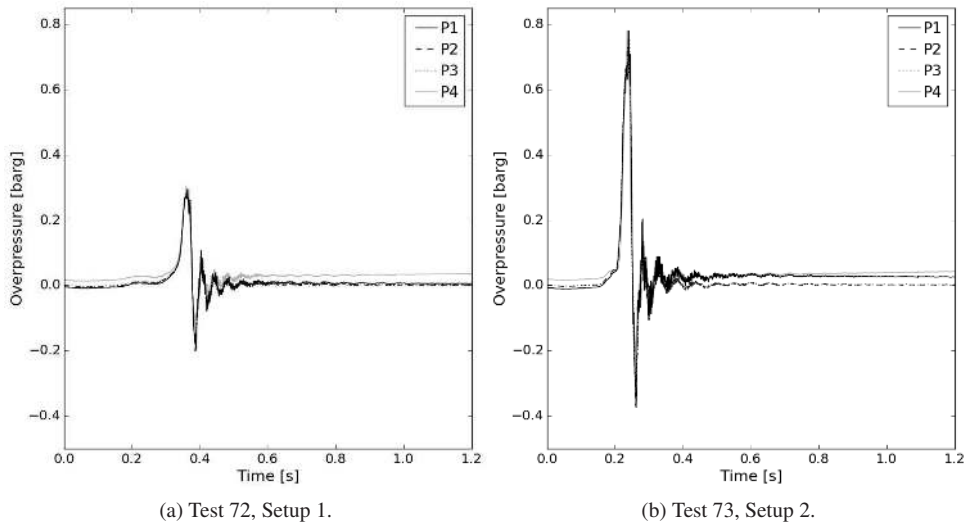
Figure B.37: Pressure-time histories, medium-scale tests, Test 72, "Setup 1", and Test 73, "Setup 2" (Paper 2).

(a) Test 74, Setup 2.   (b) Test 75, Setup 2.
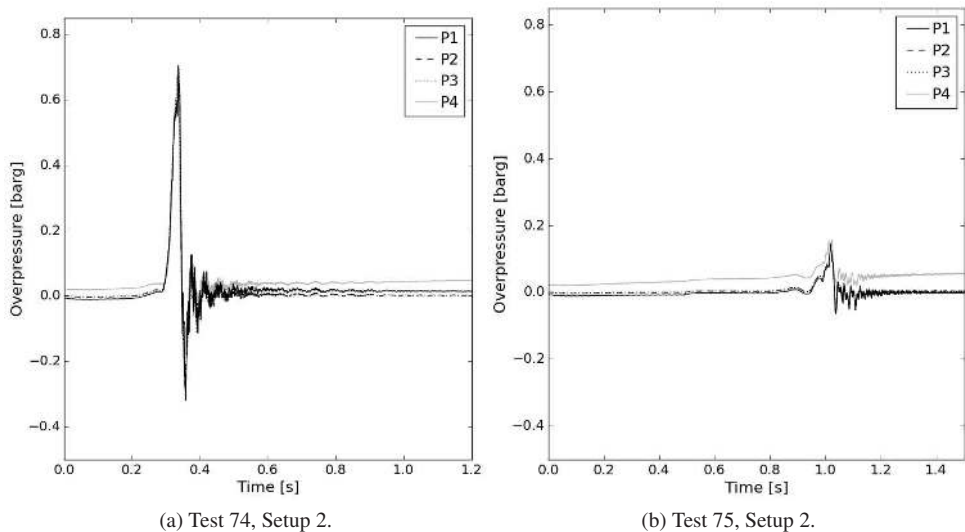
Figure B.38: Pressure-time histories, medium-scale tests, Test 74 and Test 75, "Setup 2" (Paper 2).
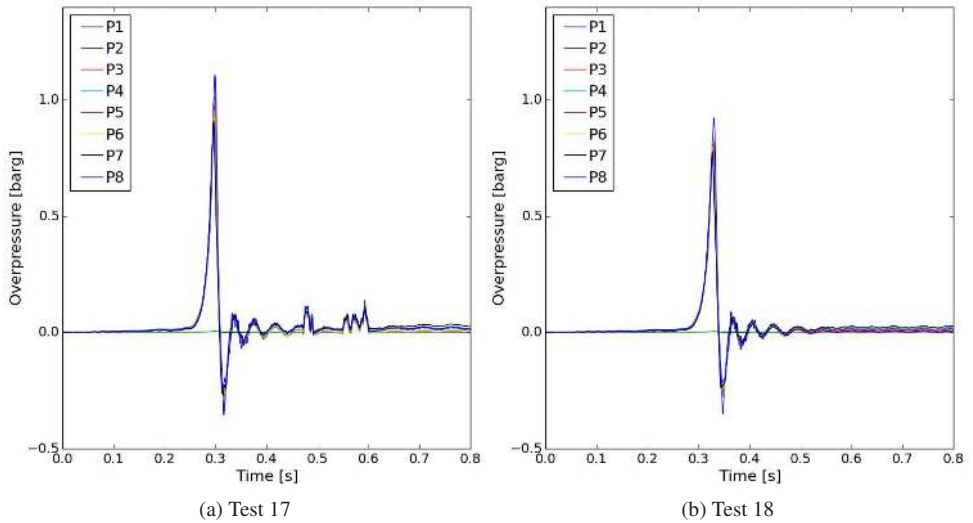
(a) Test 17

(b) Test 18

Figure B.39: Test 17 and Test 18, performed in the medium-scale rig for Paper 2 with "Setup 3".
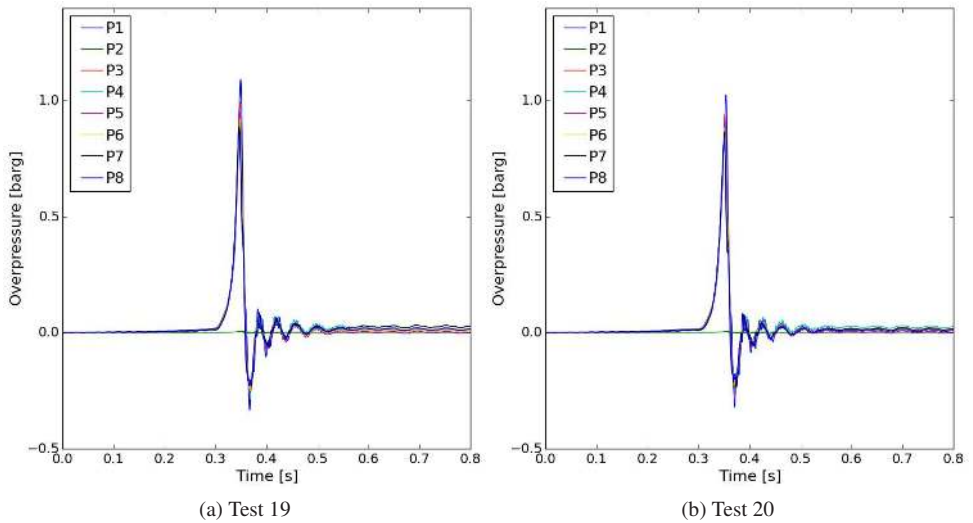
(a) Test 19

(b) Test 20

Figure B.40: Test 19 and Test 20, performed in the medium-scale rig for Paper 2 with "Setup 3".

(a) Test 21   (b) Test 22
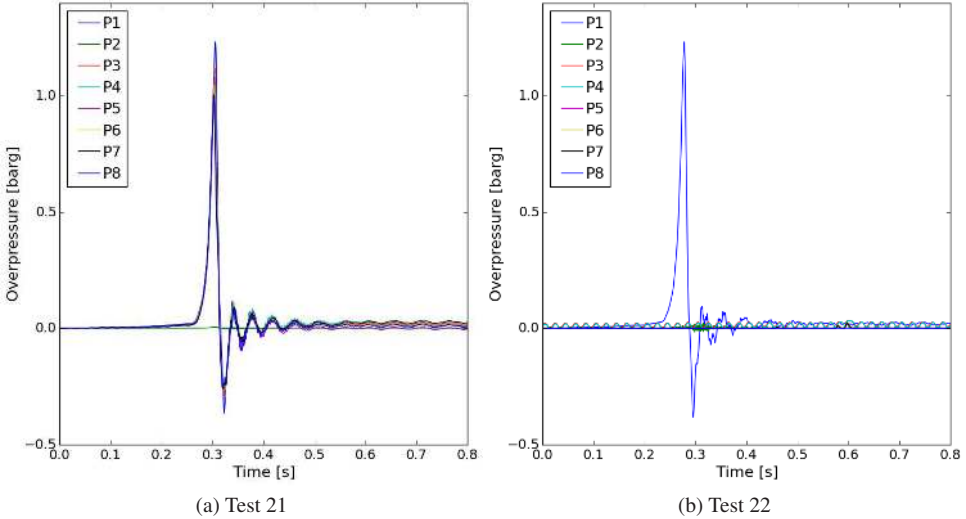
Figure B.41: Test 21 and Test 22, performed in the medium-scale rig for Paper 2 with "Setup 3".

(a) Test 23   (b) Test 24
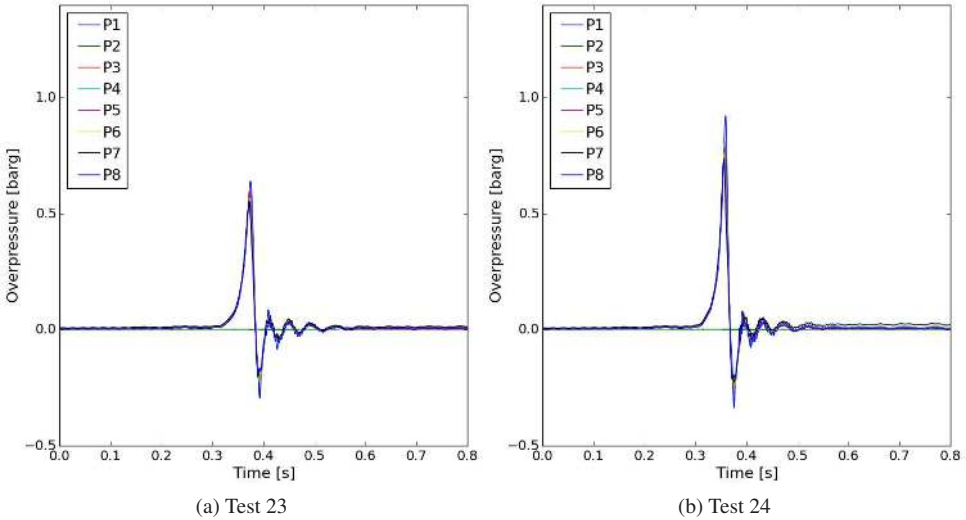
Figure B.42: Test 23 and Test 24, performed in the medium-scale rig for Paper 2 with "Setup 3".

(a) Test 25   (b) Test 26
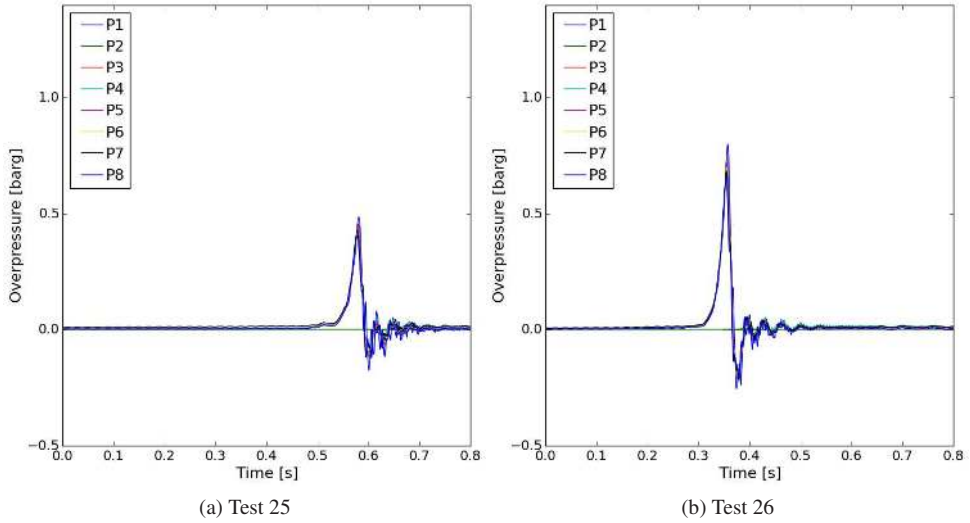
Figure B.43: Test 25 and Test 26, performed in the medium-scale rig for Paper 2 with "Setup 3".
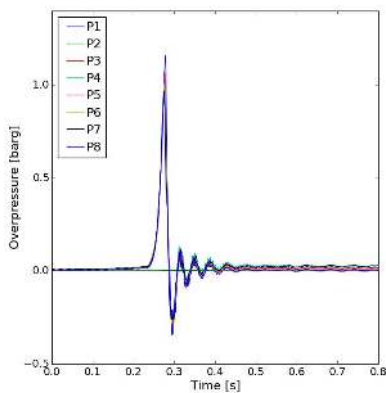
Figure B.44: Test 27, performed in the medium-scale rig with "Setup 3", for Paper 2.

Appendix C

Wall functions

This chapter describes the wall functions that are used as input to the turbulence model and momentum equation in Chapter 2.

Close to a wall boundary, the flow is characterised by large gradients, and a very fine computational grid is generally required to resolve them. In order to avoid this effort, it is common to solve the full system of equations only for the flow away from the wall and apply *wall functions* to model the effects of the wall boundary. The *wall point* is defined as the grid point closest to the wall where the conservation equations are solved.

In addition, a sink term is needed in Equation (2.10), to represent the resistance (drag force per volume) due to walls, e.g.

$$F_{w,i} = -\beta_v \tau_{w,i} \frac{A_w}{V},$$
(C.1)

where the shear stresses caused by the wall, $\tau_{w,i}$, are modelled by

$$\tau_{w,i} = \left\{ \begin{array}{ll} \mu \frac{\widetilde{u}_i}{y} & \text{if } y^+ < E^+ \\ \frac{\overline{\rho} \widetilde{u}_i C_\kappa C_\mu^{1/4} \widetilde{k}^{1/2}}{C_\kappa E^+ + \ln\left(\frac{y^+}{E^+}\right)} & \text{if } y^+ \geq E^+ \end{array} \right\},$$
(C.2)

the dimensionless wall distance is defined by

$$y^+ = \frac{\overline{\rho} C_\mu^{1/4} \widetilde{k}^{1/2} y}{\mu},$$
(C.3)

and A_w is the effective area contributing to the wall resistance. In equations (C.1)–(C.3), y is the distance from the wall point to the wall, C_μ is an empirical constant from the turbulence model (cf. Table 2.2), C_κ is the von Karman constant, and E^+ is the dimensionless boundary of the viscous sub-layer (Gexcon, 2016; Sand and Bakke, 1989).

The production of turbulence kinetic energy G_w in the wall point, cf. Equation (2.28), is modelled by

$$G_w = \left\{ \begin{array}{ll} 0 & \text{if } y^+ < E^+ \\ \frac{2\tau_w^2 \ln\left(\frac{y^+}{E^+}\right)}{y_{cv} \overline{\rho} C_\kappa C_\mu^{1/4} \widetilde{k}^{1/2}} & \text{if } y^+ \geq E^+ \end{array} \right\}.$$
(C.4)

The rate of dissipation of turbulence kinetic energy is given a value at the wall point in the location $y = y_{cv}$ by solving the following integral:

$$\varepsilon_w = \frac{1}{y_{cv}} \int_0^{y_{cv}} \widetilde{\varepsilon} \, dy \, . \tag{C.5}$$

The integral is estimated by

$$\varepsilon_w = \left\{ \begin{array}{l} \frac{1}{y_{cv}} \left(\frac{2\mu\widetilde{k}}{\overline{\rho}y} + \hat{\varepsilon}(y_{cv} - y) \right) \quad \text{if } y^+ < E^+, \quad \text{else if } y^+ \geq E^+ , \text{ then} \\ \frac{1}{y_{cv}} \left(2\mu \left[\frac{\widetilde{k}y^+}{\overline{\rho}yE^+} - \left(\frac{y^+}{E^+} - 1 \right) \left(\frac{\widetilde{k}_{+1} - \widetilde{k}}{\overline{\rho}(y_{+1} - y)} \right) \right] + \frac{C_\mu^{3/4}\widetilde{k}^{3/2}}{C_\kappa} \ln \left(\frac{y^+}{E^+} \right) + \hat{\varepsilon}(y_{cv} - y) \right) \end{array} \right\} ,$$

where $\widetilde{k}_{+1}$ denotes the value of $\widetilde{k}$ and y_{+1} denotes the wall distance in the point beyond the wall point in the opposite direction of the wall. Here, $\hat{\varepsilon}$ denotes the mean value of ε between the cell point and the control volume boundary in the opposite direction of the wall.

Bibliography

Abdel-Gayed, R. G., Bradley, D., and Lawes, M. (1987). Turbulent burning velocities: A general correlation in terms of straining rates. *Proceedings of the Royal Society of London. Series A, Mathematical and Physical Sciences*, 414(1847):389–413. 4.5.2, 4.6.1

Abernathy, F. H. and Kronauer, R. E. (1962). The formation of vortex sheets. *Journal of Fluid Mechanics*, 13(1):1–20. 4.2

Al-Hassan, T. and Johnson, D. M. (1998). Gas explosions in large scale offshore module geometries: Overpressures, mitigation and repeatability. In *Proceedings from OMAE-98, Lisbon, Portugal*. 1.2.1, 1.3.1, 3.2.2, 5.6, 6.3

Anderson, J. D. (1995). *Computational fluid dynamics: The basics with applications*. McGraw-Hill Book Company, New York. 2.4

Arntzen, B. J. (1998). *Modelling of turbulence and combustion for simulation of gas explosions in complex geometries*. PhD thesis, Department of Energy and Process Engineering, Norwegian University of Science and Technology, Norway. 1.2.1, 1.2.2, 1.5, 2.1, 2.9, 3.2.1, 3.2.1, 3.2.2, 4.4.1, 5, 5.1.2, 5.1.2, 5.3, 5.3.3

Astbury, N. F., West, H. W. H., and Hodgkinson, H. R. (1972). Experimental gas explosions: Report of further tests at Potters Marston. Technical Report Special Publication No. 74, British Ceramic Research Association. 6, 6.2

Astbury, N. F., West, H. W. H., Hodgkinson, H. R., Cubbage, P. A., and Clare, R. (1970). Gas explosions in load bearing brick structures. Technical Report Special Publication No. 68, British Ceramic Research Association. 6, 6.2

Aven, T. and Vinnem, J. E. (2007). *Risk management: with applications from the offshore oil and gas industry*. Springer Verlag, New York. 1.1

Bakke, J. R. (1986). *Numerical simulation of gas explosions in two-dimensional geometries*. PhD thesis, University of Bergen and Christian Michelsen Institute, Research and Technology, Norway. 2.2

Bakke, J. R. (2010). A study on the effect of trees on gas explosions. *Journal of Loss Prevention in the Process Industries*, 23(6):878–884. 5.6.1, 7.1

Barenblatt, G. I., Istratov, A. G., and Zeldovich, Y. B. (1962). On the diffusion-thermal stability of a laminar flame. *Journal of Applied Mechanics and Technical Physics*, 4:21–26. (in Russian). 1.1.1, 4.3.1

Batchelor, G. K. (1952). The effect of homogeneous turbulence on material lines and surfaces. *Proceedings of the Royal Society of London. Series A, Mathematical and Physical Sciences*, 213(1114):349–366. 3.1.2

Bauwens, C. R., Bergthorson, J. M., and Dorofeev, S. B. (2015). Experimental study of spherical-flame acceleration mechanisms in large-scale propane–air flames. *Proceedings of the Combustion Institute*, 35(2):2059 – 2066. 4, 4.4, 4.4, 4.4, 4.4.1, 4.6.1, 4.7, 7.1

Bauwens, C. R., Bergthorson, J. M., and Dorofeev, S. B. (2017a). Experimental investigation of spherical-flame acceleration in lean hydrogen-air mixtures. *International Journal of Hydrogen Energy*, 42(11):7691 – 7697. Special issue on The 6th International Conference on Hydrogen Safety (ICHS 2015), 19-21 October 2015, Yokohama, Japan. 4.4.1, 4.6.1, 4.7, 7.1

Bauwens, C. R., Bergthorson, J. M., and Dorofeev, S. B. (2017b). On the interaction of the Darrieus–Landau instability with weak initial turbulence. *Proceedings of the Combustion Institute*, 36(2):2815 – 2822. 4.4.1, 4.7, 7.1

Bauwens, C. R., Chaffee, J., and Dorofeev, S. B. (2009a). Effect of instabilities and acoustics on pressure generated in vented propane-air explosions. In *22nd International Colloquium on the Dynamics of Explosions and Reactive Systems, Minsk, Belarus, 27-31 July 2009*. 1.3.3, 5.4, 5.5, 6.1.1, 7.1

Bauwens, C. R., Chaffee, J., and Dorofeev, S. B. (2009b). Experimental and numerical study of methane-air deflagrations in a vented enclosure. In *Ninth International Symposium on Fire Safety Science*, pages 1043–1054. 1.3.3, 1.5, 5.4, 5.4.2, 6, 7.1

Bauwens, C. R., Chaffee, J., and Dorofeev, S. B. (2010). Effect of ignition location, vent size, and obstacles on vented explosion overpressures in propane-air mixtures. *Combustion Science and Technology*, 182(11-12):1915–1932. 1.3.3, 5.3.4, 5.10, 5.3.4, 5.3.4, 5.4.2, 5.5, 5.7, 6.2

Bauwens, C. R., Chaffee, J., and Dorofeev, S. B. (2011). Vented explosion overpressures from combustion of hydrogen and hydrocarbon mixtures. *International Journal of Hydrogen Energy*, 36(3):2329–2336. 1.5, 4.4, 4.4.1, 5.4, 5.4.2, 5.4.2, 5.4.2, 5.4.3, 5.7, 6, 6.1, 6.1.1, 6.1.2, 6.1.2, 6.1.3, 6.7, 6.8, 6.1.3, 7.1

Bauwens, C. R., Chao, J., and Dorofeev, S. B. (2012). Effect of hydrogen concentration on vented explosion overpressures from lean hydrogen–air deflagrations. *International Journal of Hydrogen Energy*, 37(22):17599–17605. 1.5, 4, 4.4.1, 5.4.2, 5.4.3, 5.7, 6, 6.1, 6.1.1, 6.1.2, 6.1.2, 6.1.3, 6.7, 6.8, 6.1.3

Bauwens, C. R. and Dorofeev, S. B. (2011). Experimental and numerical study on the effect of mixture composition on vented explosions. In Bradley, D. and Molkov, V., editors, *Proceedings of the Sixth International Seminar on Fire & Explosion Hazards*, University of Leeds. 2011 CPD Unit, University of Leeds: Research Publishing. 4.4, 5.1.1, 5.1.1, 5.4.2, 5.4.2, 5.4.2, 5.4.3, 5.4.3, 7.1, 8.2

Bauwens, C. R. and Dorofeev, S. B. (2014). Effect of initial turbulence on vented explosion overpressures from lean hydrogen–air deflagrations. *International Journal of Hydrogen Energy*, 39(35):20509–20515. 4.4.1, 5.4.3, 5.7, 6, 6.1, 6.1.1, 6.1.3, 6.7, 6.8, 6.1.3

Bechtold, J. K. (2001). The dependence of the Markstein length on stoichiometry. *Combustion and Flame*, 127(1-2):1906–1913. 4.4.1

Bechtold, J. K. and Matalon, M. (1987). Hydrodynamic and diffusion effects on the stability of spherically expanding flames. *Combustion and Flame*, 67(1):77–90. 4.3.5, 4.4, 4.7

Beeckmann, J., Hesse, R., Kruse, S., Berens, A., Peters, N., Pitsch, H., and Matalon, M. (2017). Propagation speed and stability of spherically expanding hydrogen/air flames: Experimental study and asymptotics. *Proceedings of the Combustion Institute*, 36(1):1531–1538. 4.3.1, 4.6.2

Bell, J. B. (2014). Center for Computational Sciences and Engineering, Lawrence Berkeley Laboratory. <https://ccse.lbl.gov/index.html>. 8.3

Berger, M. J. and Colella, P. (1989). Local adaptive mesh refinement for shock hydrodynamics. *Journal of Computational Physics*, 82:64–84. 8.3

Berger, M. J. and Oliger, J. (1984). Adaptive mesh refinement for hyperbolic partial differential equations. *Journal of Computational Physics*, 53:484–512. 8.3

Bimson, S. J., Bull, D. C., Cresswell, T. M., Marks, P. R., Masters, A. P., Prothero, A., Puttock, J. S., Rowson, J. J., and Samuels, B. (1993). An experimental study of the physics of gaseous deflagration in a very large vented enclosure. In *Fourteenth International Colloquium on the Dynamics of Explosions and Reactive Systems (ICDERS), 1-6 August 1993, Coimbra, Portugal*. 5.6

Bjerketvedt, D., Bakke, J. R., and van Wingerden, K. (1993). Gas explosion handbook, version 1.2. Technical Report No. CMR-93-A25034, Christian Michelsen Research, Norway. 1.1.1

Bloor, M. S. (1964). The transition to turbulence in the wake of a circular cylinder. *Journal of Fluid Mechanics*, 19:290–304. 5.3.1

BMIIB (2008). The Buncefield incident 11 December 2005, The final report of the Major Incident Investigation Board, vols 1 and 2. Technical report, Buncefield Major Incident Investigation Board. 1.5, 5, B.3

Borghi, R. (1984). *Recent advances in aeronautical science*. Pergamon, London. 3.1.2

Bosschaart, K. J. and de Goey, L. P. H. (2004). The laminar burning velocity of flames propagating in mixtures of hydrocarbons and air measured with the heat flux method. *Combustion and Flame*, 136(3):261–269. 3.1.1

Boussinesq, J. (1877). Essai sur la théorie des eaux courantes. *Mémoires présentés par divers savants à l'Académie des Sciences*, 23(1):1–680. 2.8

Braatz, A.-L. and Hisken, H. (2017). Response surfaces for advanced consequence models: Two approaches. *Journal of Loss Prevention in the Process Industries*, pages –. https://doi.org/10.1016/j.jlp.2017.02.007. 8.5

Braatz, A.-L., Hisken, H., and Rückmann, J.-J. (2016). Surrogate-based optimization of model parameters for the improved modelling of industrial-scale gas explosions. In *5th International Conference on Engineering Optimization (EngOpt), 19-23 June 2016, Iguassu Falls, Brazil*. 8.5

Bradley, D. (1992). How fast can we burn? *Symposium (International) on Combustion*, 24(1):247 – 262. 3.1.2, 4.5.1

Bradley, D. (1999). Instabilities and flame speeds in large-scale premixed gaseous explosions. *Philosophical Transactions: Mathematical, Physical and Engineering Sciences*, 357(1764):3567–3581. 4.3.1, 4.3.2, 4.3.5, 4.3.5, 4.4, 4.4, 4.4, 4.4, 4.4.1, 5.4

Bradley, D., Chamberlain, G. A., and Drysdale, D. D. (2012). Large vapour cloud explosions, with particular reference to that at Buncefield. *Philosophical Transactions of the Royal Society of London A: Mathematical, Physical and Engineering Sciences*, 370(1960):544–566. 5.6.1

Bradley, D., Cresswell, T. M., and Puttock, J. S. (2001). Flame acceleration due to flame-induced instabilities in large-scale explosions. *Combustion and Flame*, 124(4):551–559. 4.4, 4.4, 4.4, 4.4.1

Bradley, D., Gaskell, P. H., and Gu, X. J. (1996). Burning velocities, Markstein lengths, and flame quenching for spherical methane-air flames: A computational study. *Combustion and Flame*, 104(1–2):176 – 198. 4.5.2, 4.5.2, 4.2, 4.6.1, 4.6.2

Bradley, D., Gaskell, P. H., and Gu, X. J. (1998a). The modeling of aerodynamic strain rate and flame curvature effects in premixed turbulent combustion. *Symposium (International) on Combustion*, 27(1):849 – 856. 4.5.2, 4.2, 4.6.2

Bradley, D., Gaskell, P. H., Gu, X. J., and Sedaghat, A. (2005). Premixed flamelet modelling: Factors influencing the turbulent heat release rate source term and the turbulent burning velocity. *Combustion and Flame*, 143(3):227–245. 1.3.1, 4, 4.3.1, 4.5.2, 4.5.2, 4.6, 4.7, 7.1

Bradley, D., Hicks, R. A., Lawes, M., Sheppard, C. G. W., and Woolley, R. (1998b). The measurement of laminar burning velocities and Markstein numbers for iso-octane-air and iso-octane-n-heptane-air mixtures at elevated temperatures and pressures in an explosion bomb. *Combustion and Flame*, 115(1-2):126–144. 4.4, 4.4

Bradley, D., Lau, A. K. C., and Lawes, M. (1992). Flame stretch rate as a determinant of turbulent burning velocity. *Philosophical Transactions: Physical Sciences and Engineering*, 338(1650):359–387. 4.3.3, 4.5.2, 4.6.1

Bradley, D., Lawes, M., Liu, K., and Mansour, M. S. (2013). Measurements and correlations of turbulent burning velocities over wide ranges of fuels and elevated pressures. *Proceedings of the Combustion Institute*, 34(1):1519 – 1526. (document),

1.3.1, 4, 4.3.1, 4.5.2, 4.5.2, 4.6, 4.3, 4.4, 4.6.1, 4.6.1, 4.6, 4.7, 4.6.2, 4.7, 6.2.2, 6.13a, 6.2.2

Bradley, D., Lawes, M., Liu, K., Verhelst, S., and Woolley, R. (2007). Laminar burning velocities of lean hydrogen-air mixtures at pressures up to 1.0 MPa. *Combustion and Flame*, 149(1-2):162–172. 4.4.1, 4.5.2, 4.2, 4.6.1, 4.6.2

Bradley, D., Lawes, M., and Mansour, M. S. (2011a). Correlation of turbulent burning velocities of ethanol-air, measured in a fan-stirred bomb up to 1.2 MPa. *Combustion and Flame*, 158(1):123–138. 1.3.1, 4, 4.3.1

Bradley, D., Lawes, M., and Mansour, M. S. (2011b). Measurement of turbulent burning velocities in implosions at high pressures. *Proceedings of the Combustion Institute*, 33(1):1269–1275. 4.5.2, 4.5.2, 4.7

Bradley, D., Lawes, M., and Mansour, M. S. (2011c). The problems of the turbulent burning velocity. *Flow, Turbulence and Combustion*, 87(2):191–204. 3.1.2, 3.1.2, 4.3.3

Bray, K. N. C. (1990). Studies of the turbulent burning velocity. *Proceedings: Mathematical and Physical Sciences*, 431(1882):315–335. (document), 3.1.1, 3.2.2, 4.5, 4.5.2, 4.5.2, 4.6, 4.3, 4.4, 4.6.1, 4.6.1, 4.6, 4.7, 6.2.2, 6.13a

Brewerton, R. W. (2001). Instructions for use of Natabelle Programme entitled "Simulator for structural response and projectile trajectory". Technical report, Natabelle Ltd. 5.6.1

Butlin, R. N. and Tonkin, P. S. (1974). Pressures produced by gas explosions in a vented compartment. Technical Report Fire Research Note No. 1019, Fire Research Station. 1.3.3, 6.2

Cantwell, B. and Coles, D. (1983). An experimental study of entrainment and transport in the turbulent near wake of a circular cylinder. *Journal of Fluid Mechanics*, 136:321–374. 5.3.2

Catlin, C. A. and Lindstedt, R. P. (1991). Premixed turbulent burning velocities derived from mixing controlled reaction models with cold front quenching. *Combustion and Flame*, 85(3-4):427–439. 3.2.1

Chao, J., Bauwens, C. R., and Dorofeev, S. B. (2011). An analysis of peak overpressures in vented gaseous explosions. *Proceedings of the Combustion Institute*, 33(2):2367–2374. 4.4.1, 5.4.2, 5.4.3, 5.5, 5.7, 6, 6.1, 6.1.1, 6.1.2, 6.1.3, 6.7, 6.8, 6.1.3

Choi, H., Jeon, W.-P., and Kim, J. (2008). Control of flow over a bluff body. *Annual Review of Fluid Mechanics*, 40(1):113–139. 5.3.2, 5.3.4

Ciccarelli, G. and Dorofeev, S. (2008). Flame acceleration and transition to detonation in ducts. *Progress in Energy and Combustion Science*, 34(4):499–550. 1.1.1, 4.1, 4.3.1, 5.4, 5.5, 7.1, 8.4

Clanet, C. and Searby, G. (1998). First experimental study of the Darrieus-Landau instability. *Physical Review Letters*, 80:3867–3870. 4.3.1

Clavin, P. (1985). Dynamic behavior of premixed flame fronts in laminar and turbulent flows. *Progress in Energy and Combustion Science*, 11(1):1–59. 4.3.3, 4.3.3

Clavin, P. and Searby, G. (2016). *Combustion waves and fronts in flows*. Cambridge University Press, Cambridge, UK. 5.5

Clavin, P. and Williams, F. A. (1982). Effects of molecular diffusion and of thermal expansion on the structure and dynamics of premixed flames in turbulent flows of large scale and low intensity. *Journal of Fluid Mechanics*, 116:251–282. 4.3.3

Cooper, M. G., Fairweather, M., and Tite, J. P. (1986). On the mechanisms of pressure generation in vented explosions. *Combustion and Flame*, 65(1):1–14. 1.3.3, 5.4, 5.5, 6.2, 7.1

Courant, R., Friedrichs, K., and Lewy, H. (1928). Über die partiellen Differenzengleichungen der mathematischen Physik. *Mathematische Annalen*. A.4

Cronin, P. and Wickens, M. J. (1986). A large scale experimental study of the conditions required for sustained high speed flame propagation in a flammable vapour cloud. Technical Report No. MRS I 4348, British Gas Corporation, UK. 1.3.1, 5.6

Cronin, P. and Wickens, M. J. (1988). High speed flame propagation in a flammable vapour cloud: Experiments carried out at Spadeadam in 1986/7. Technical Report No. MRS I 4648, British Gas Corporation, UK. 1.3.1, 5.6

CSHIB (2009). Final investigation report: Caribbean petroleum tank terminal explosion and multiple tank fires. Technical Report No. 2010.02.I.PR, U.S. Chemical Safety and Hazard Investigation Board. 5.6.1

Dahoe, A. E., Skjold, T., Roekaerts, D. J. E. M., Pasman, H. J., Eckhoff, R. K., Hanjalic, K., and Donze, M. (2013). On the application of the Levenberg-Marquardt method in conjunction with an explicit Runge-Kutta and an implicit Rosenbrock method to assess burning velocities from confined deflagrations. *Flow, Turbulence and Combustion*, pages 1–37. 4.5, 4.5.2

Damköhler, G. (1940). Der einfluß der turbulenz auf die flammengeschwindigkeit in gasgemischen. *Zeitschrift für Elektrochemie und angewandte physikalische Chemie*, 46:601. 4.5.1

Darrieus, G. (1938). Propagation d'un front de flamme. *Presented at La Technique Moderne (Paris) and in 1945 at Congrès de Méchanique Appliquée (Paris)*. 1.1.1, 4.3.1

Davis, S. G., Engel, D., Groethe, M., and van Wingerden, K. (2016). Large scale deflagration to detonation testing. In *11th International Symposium on Hazard, Prevention and Mitigation of Industrial Explosions (ISHPMIE), 24-29 July 2016, Dalian, China*. 1.3.1

Davis, S. G., Quinard, J., and Searby, G. (2002). Markstein numbers in counterflow, methane- and propane- air flames: a computational study. *Combustion and Flame*, 130(1-2):123–136. 4.3.3, 4.6.2

Duijm, N. J. and Carissimo, B. (2002). *The handbook of hazardous materials spills technology*, chapter "Evaluation methodologies for dense gas dispersion models". McGraw-Hill. 6.1.3

Ertesvåg, I. S. (2000). *Turbulent strøyming og forbrenning: Frå turbulensteori til ingeniørverkty*. TAPIR Forlag, Trondheim, Norway (in Norwegian). 2.8

Evans, J. A., Exon, R., and Johnson, D. M. (1999). The repeatability of large scale explosion experiments. Technical Report OTO 1999 042, Health and Safety Executive. 1.2.1, 1.3.1, 5.6, 6.3, 6.3

Favre, A. (1965). Équations des gaz turbulents compressibles. *Journal Mécanique*, 4:361–421. 2.8

Fey, U., König, M., and Eckelmann, H. (1998). A new Strouhal–Reynolds-number relationship for the circular cylinder in the range 47 < Re < 2 x 10**5. *Physics of Fluids*, 10(7):1547–1549. 5.3.1

Foisselon, P., Hansen, O. R., and van Wingerden, K. (1998). Detailed analysis of FLACS performance in comparison to full-scale experiments. Technical Report CMR-98-F30058, Christian Michelsen Research, Bergen, Norway. 1.2.1, 1.3.1, 3.2.2, 6.3

Frankel, M. L. and Sivashinski, G. I. (1983). On effects due to thermal expansion and Lewis number in spherical flame propagation. *Combustion, Science and Technology*, 31:131–138. 4.3.3

Fureby, C. (2000). A computational study of combustion instabilities due to vortex shedding. *Proceedings of the Combustion Institute*, 28(1):783 – 791. 5.3

Gaster, M., Kit, E., and Wygnanski, I. (1985). Large-scale structures in a forced turbulent mixing layer. *Journal of Fluid Mechanics*, 150:23–39. 5.2.2

Gexcon (2005). FLACS v8.1 User's Manual. Technical report, Gexcon AS, Bergen, Norway. 5.6.1

Gexcon (2011). FLACS v9.1 User's Manual. Technical report, Gexcon AS, Bergen, Norway. 6

Gexcon (2012). FLACS v10.0 User's Manual. Technical report, Gexcon AS, Bergen, Norway. 5.6.3

Gexcon (2015). FLACS v10.4 User's Manual. Technical report, Gexcon AS, Bergen, Norway. 6, 6.1.2

Gexcon (2016). FLACS v10.5 User's Manual. Technical report, Gexcon AS, Bergen, Norway. 1.2.1, 2, 3, 3.2.1, 3.2.2, 3.2.2, 3.2.2, 4.4.1, 4.6.1, 5.1.1, 5.3.3, 5.4.3, 6.3, 7.1, 7.2, A.4, A.4, C

Gostintsev, Y. A., Istranov, A. G., and Shulenin, Y. V. (1988). Self-similar propagation of a free turbulent flame in mixed gas mixtures. *Fizika Goreniya i Vzryva*. 4.3.5, 4.4, 4.4, 4.4, 4.4, 4.4.1

Gostintsev, Y. A., Istranov, A. G., and Shulenin, Y. V. (1999). Autoturbulization of gas flames: Analysis of experimental results. *High Temperature*, 37:282–. 4.4

Gourdain, N., Gicquel, L., Montagnac, M., Vermorel, O., Gazaix, M., Staffelbach, G., Garcia, M., Boussuge, J.-F., and Poinsot, T. (2009a). High performance parallel computing of flows in complex geometries: I. Methods. *Computational Science & Discovery*, 2(1):015003. 5.3.3, 7.1, 8.2

Gourdain, N., Gicquel, L., Staffelbach, G., Vermorel, O., Duchaine, F., Boussuge, J.-F., and Poinsot, T. (2009b). High performance parallel computing of flows in complex geometries: II. Applications. *Computational Science & Discovery*, 2(1):015004. 5.3.3, 7.1, 8.2

Gu, X. J., Haq, M. Z., Lawes, M., and Woolley, R. (2000). Laminar burning velocity and Markstein lengths of methane-air mixtures. *Combustion and Flame*, 121(1-2):41–58. 3.1.1, 4.4, 4.4

Gülder, Ü. L. (1991). Turbulent premixed combustion modelling using fractal geometry. *Symposium (International) on Combustion*, 23(1):835 – 842. 4.5.1

Halter, F., Tahtouh, T., and Mounaim-Rousselle, C. (2010). Nonlinear effects of stretch on the flame front propagation. *Combustion and Flame*, 157(10):1825–1832. 3.1.1

Hanna, S. R., Strimaitis, D. G., and Chang, J. C. (1991a). Hazard response modelling uncertainty (a quantitative method) – Vol. I: User's guide for software for evaluating hazardous gas dispersion models. Technical report, Sigma Research Corporation, Westford, USA. 6.1.3

Hanna, S. R., Strimaitis, D. G., and Chang, J. C. (1991b). Hazard response modelling uncertainty (a quantitative method) – Vol. II: Evaluation of commonly-used hazardous gas dispersion models. Technical report, Sigma Research Corporation, Westford, USA. 6.1.3

Hansen, O. R. and Johnson, D. M. (2015). Improved far-field blast predictions from fast deflagrations, DDTs and detonations of vapour clouds using FLACS CFD. *Journal of Loss Prevention in the Process Industries*, 35:293 – 306. 6.3, 8.4

Harrison, A. J. and Eyre, J. A. (1987). External explosions as a result of explosion venting. *Combustion Science and Technology*, 52(1):91–106. 0010-2202. 1.3.3, 6.2

Hassan, M. I., Aung, K. T., Kwon, O. C., and Faeth, G. M. (1998). Properties of laminar premixed hydrocarbon/air flames at various pressures. *Journal of Propulsion and Power*, 14:479–488. 3.1.1

Hertzberg, J. R., Shepherd, I. G., and Talbot, L. (1991). Vortex shedding behind rod stabilized flames. *Combustion and Flame*, 86(1–2):1–11. 5.3

Hirschfelder, J. O., Curtiss, C. F., and Bird, R. B. (1964). *Molecular theory of gases and liquids*. Wiley, New York. 2.6

Hisken, H., Atanga, G., Skjold, T., Lakshmipathy, S., and Middha, P. (2016). Validating, documenting and qualifying models used for consequence assessment of hydrogen explosion scenarios. In *11th International Symposium on Hazard, Prevention and Mitigation of Industrial Explosions (ISHPMIE), 24-29 July 2016, Dalian, China*. 1.3.2, 6.1.3, 6.1.3

Hjertager, B. H. (1982). Simulation of transient compressible turbulent reactive flows. *Combustion Science and Technology*, 27(5-6):159–170. 1.1.2, A.3

Hjertager, B. H. (1984). Influence of turbulence on gas explosions. *Journal of Hazardous Materials*, 9(3):315 – 346. 1.1.1

Hjertager, B. H. (1986). *Three-dimensional modeling of flow, heat transfer, and combustion. Handbook of heat and mass transfer*, chapter 41, pages 1303–1350. Gulf Publishing, Houston. 1.2, 1.2.2, 2.2, A.1, A.3

Hjertager, B. H., Fuhre, K., and Bjørkhaug, M. (1988). Concentration effects on flame acceleration by obstacles in large-scale methane-air and propane-air vented explosions. *Combustion Science and Technology*, 62(4-6):239–256. 4, 4.5, 5.6

Hoerner, S. F. (1965). *Fluid-dynamic drag*. Hoerner Fluid Dynamics, Bricktown New Jersey. 2.4

Ichard, M. (2012). *Numerical computations of pressurized liquefied gas releases into the atmosphere*. PhD thesis, Department of Physics and Technology, University of Bergen, Norway. 1.2.1

Jiang, H., Dong, G., Chen, X., and Li, B. (2016). A parameterization of the Richtmyer–Meshkov instability on a premixed flame interface induced by the successive passages of shock waves. *Combustion and Flame*, 169(Supplement C):229–241. 8.4

Johnson, D. M. (2009). Characteristics of the vapour cloud explosion incident at the IOC terminal in Jaipur. Technical Report 10181, GL Noble Denton. 5.6.1

Johnson, D. M. (2010). The potential for vapour cloud explosions - Lessons from the Buncefield accident. *Journal of Loss Prevention in the Process Industries*, 23(6):921–927. 5.6.1

Johnson, D. M. (2013). Understanding of gas explosions – the importance of experimental research. *FABIG Newsletter*, 62:4–8. 1.2.1

Johnson, D. M. and Cleaver, R. P. (2002). Gas explosions in offshore modules following realistic releases (Phase 3B): Final summary report. Technical Report R 4853, Advantica Technology. 1.2.1, 4.6.1

Johnson, D. M., Tomlin, G. B., and Walker, D. G. (2015). Detonations and vapor cloud explosions: Why it matters. *Journal of Loss Prevention in the Process Industries*, 36:358–364. 1.3.1, 8.4

Jomaas, G., Zheng, X. L., Zhu, D. L., and Law, C. K. (2005). Experimental determination of counterflow ignition temperatures and laminar flame speeds of C2–C3 hydrocarbons at atmospheric and elevated pressures. *Proceedings of the Combustion Institute*, 30:193–200. 3.1.1

Karlovitz, B., Denniston Jr., D. W., Knapschaefer, D. H., and Wells, F. E. (1953). Studies on turbulent flames: A. Flame propagation across velocity gradients B. Turbulence measurement in flames. *Symposium (International) on Combustion*, 4(1):613–620. 4.5.2

Keenan, J. J., Makarov, D. V., and Molkov, V. V. (2013). Towards the implementation of Rayleigh-Taylor instability into the multi-phenomena deflagration model. In *Seventh International Seminar on Fire & Explosion Hazards (ISFEH7)*, page 932–941. 1.3.3

Keenan, J. J., Makarov, D. V., and Molkov, V. V. (2014). Rayleigh–Taylor instability: Modelling and effect on coherent deflagrations. *International Journal of Hydrogen Energy*, 39(35):20467–20473. 5.4, 7.1

Kelley, A. P. and Law, C. K. (2009). Nonlinear effects in the extraction of laminar flame speeds from expanding spherical flames. *Combustion and Flame*, 156:11844–1851. 3.1.1

Khokhlov, A. M., Oran, E. S., and Wheeler, J. (1996). Scaling in buoyancy-driven turbulent premixed flames. *Combustion and Flame*, 105(1):28–34. 5.4

Kong, D. (1996). *An experimental study of certain aspects of initiation and turbulent propogation of gas explosions*. PhD thesis, University of Bergen, Norway. 1.5, 5, 5.3, 5.3.1, 5.3.4

Kong, D. and Sand, I. Ø. (1996). Experimental investigation of gas explosion driven transient flow in the near wake of bluff bodies - pipe arrays and complex obstacles. Technical Report CMR-96-F20003, Christian Michelsen Research, Bergen, Norway. Confidential. 1.5, 4.5, 5, 5.3, 5.3.1

Kuhl, A. L. (1981). *First specialist meeting (International), The Combustion Institute, Bordeaux*. 1.1.1

Kuo, K. K. and Acharya, R. (2012). *Fundamentals of turbulent and multiphase combustion*. John Wiley & Sons, Inc., Hoboken, New Jersey. 2.1

Landau, L. D. (1944). On the theory of slow combustion. *Acta Physicochim. USSR*. 1.1.1, 4.3.1, 4.3.2, 4.3.2, 4.3.4, 4.7

Launder, B. E. and Spalding, D. B. (1974). The numerical computation of turbulent flows. *Computer Methods in Applied Mechanics and Engineering*, 3(2):269–289. 1.1.2, 1.2.2, 2.8, 2.9, 2.9, 2.10

Law, C. K. (2006). *Combustion physics*, chapter "Aerodynamics of laminar flames, Section 10.9.1: Mechanisms of cellular instabilities", pages 459–460,504. Cambridge University Press. 4.3.3

Lee, T. and Budwig, R. (1991). The onset and development of circular-cylinder vortex wakes in uniformly accelerating flows. *Journal of Fluid Mechanics*, 232. 5.3.1, 5.3.4

Lieuwen, T. C. (2012). *Unsteady combustor physics*. Cambridge University Press. 2.1, 2.4, 4.1, 4.2, 5, 5.2.1, 5.2, 5.2.1, 5.3, 5.5

Lindstedt, R. P. and Sakthitharan, V. (1998). Time resolved velocity and turbulence measurements in turbulent gaseous explosions. *Combustion and Flame*, 114(3-4):469–483. 4.5, 5.3.1

Lipatnikov, A. N. and Chomiak, J. (2002). Turbulent flame speed and thickness: phenomenology, evaluation, and application in multi-dimensional simulations. *Progress in Energy and Combustion Science*, 28(1):1–73. 3.1, 4.5, 4.5.2

Makhviladze, G. (2011). Hydrocarbon releases into the open atmosphere, case studies. Two-phase releases: Ufa catastrophe. Course notes: Explosion Prediction and Mitigation, University of Leeds, UK, 4-8 April 2011. 5.6.1

Mandelbrot, B. B. (1975). On the geometry of homogeneous turbulence, with stress on the fractal dimension of the iso-surfaces of scalars. *Journal of Fluid Mechanics*, 72:401–416. 4.5.1

Markstein, G. H. (1951). Experimental and theoretical studies of flame-front stability. *Journal of Aeronautical Science*, 18:199–209. 4.3.1, 4.3.3

Marsh (2016). The 100 largest losses 1974-2015 – large property damage losses in the hydrocarbon industry. Technical report, Marsh Global Energy Risk Engineering. 1.1

Matalon, M. and Matkowsky, B. J. (1982). Flames as gasdynamic discontinuities. *Journal of Fluid Mechanics*, 124:239–259. 4.3.3

McGrattan, K. and Toman, B. (2011). Quantifying the predictive uncertainty of complex numerical models. *Metrologia*, 48(3):173–180. 8.5

MEGGE (1996). Gas explosion model evaluation protocol - Version 1. Technical report, Model Evaluation Group Gas Explosions (MEGGE). 6.1.3

Mercx, W. P. M. (1994). Modelling and experimental research into gas explosions. Overall Final Report for the MERGE project. Technical report, CEC contract STEP-CT-0111 (SMA). 1.2.1, 5.6

Mercx, W. P. M. (1996). Extended modelling and experimental research into gas explosions. Overall Final Report for the EMERGE project. Technical report, CEC contract EV5V-CT93-0274. 1.2.1, 5.3.1, 5.6

Middha, P. (2010). *Development, use, and validation of the CFD tool FLACS for hydrogen safety studies*. PhD thesis, Department of Physics and Technology, University of Bergen, Norway. 1.3.2, 4.6.1, 6.3, 8.4

Middha, P. and Hansen, O. R. (2008). Predicting deflagration to detonation transition in hydrogen explosions. *Process Safety Progress*, 27(3):192–204. 8.4

Middha, P., Hansen, O. R., and Storvik, I. E. (2006). Prediction of deflagration to detonation transition in hydrogen explosions. *AIChE Spring National Meeting & Fortieth Annual Loss Prevention Symposium, 23-27 April 2006, Orlando, Florida, USA*. 8.4

Moen, I. O., Donato, M., Knystautas, R., and Lee, J. H. (1980). Flame acceleration due to turbulence produced by obstacles. *Combustion and Flame*, 39(1):21–32. 1.1.1, 5.3.1

Moen, I. O., Lee, J. H. S., Hjertager, B. H., Fuhre, K., and Eckhoff, R. K. (1982). Pressure development due to turbulent flame propagation in large-scale methane–air explosions. *Combustion and Flame*, 47:31–52. 1.1.1

Muthusamy, D. and Lilleberg, B. (2012). Validation of FLACS-Fire for jet fires under ventilation-controlled conditions. In *Fifth International Symposium on Fire Investigation Science and Technology (ISFI 2012). University of Maryland, USA, 15-17 October 2012*, pages 485–494. 1.2.1

Narasimhamurthy, V. D. (2015). Transient turbulence. Internal presentation, Gexcon AS. Confidential. 5.3.3

Narasimhamurthy, V. D., Hisken, H., Atanga, G., and Skjold, T. (2015). Porosity/distributed resistance modelling for industrial CFD applications. In Skallerud, B. and Andersson, H., editors, *8th National Conference on Computational Mechanics (MekIT'15)*. 2.9

NTSB (1971). Pipeline accident report. Phillips Pipeline Co., Propane gas explosion. Technical Report NTSB-PAR-72-1, US National Transportation Safety Board. 5.6.1

NTSB (1992). Pipeline accident report. Highly volatile liquids release from underground storage cavern and explosion. MAPCO Natural Gas Liquids, Inc., Brenham, Texas. Technical Report NTSB-PAR-93-01, US National Transportation Safety Board. 5.6.1

Oran, E. S. (2014). Numerical simulations of industrial explosions: discussions of the impossible and the improbable. In *Tenth International Symposium on Hazards, Prevention, and Mitigation of Industrial Explosions Bergen, Norway, 10-14 June 2014*, pages 3–18. 1.1.1, 8.5

Oran, E. S. (2015). Understanding explosions – from catastrophic accidents to creation of the universe. *Proceedings of the Combustion Institute*, 35(1):1 – 35. 1.1.1, 4.1, 5.4, 7.1, 8.4

Pan, K.-L. and Fursenko, R. (2008). Characteristics of cylindrical flame acceleration in outward expansion. *Physics of Fluids*, 20(9):–. http://dx.doi.org/10.1063/1.2981837. 4.4

Park, O., Veloo, P. S., Liu, N., and Egolfopoulos, F. N. (2011). Combustion characteristics of alternative gaseous fuels. *Proceedings of the Combustion Institute*, 33:887–894. 3.1.1

Patankar, S. V. (1980). *Numerical heat transfer and fluid flow*. Hemisphere Publishing Corporation. A.2

Patankar, S. V. and Spalding, D. B. (1972). A calculation procedure for heat, mass and momentum transfer in three-dimensional parabolic flows. *International Journal of Heat and Mass Transfer*, 15(10):1787 – 1806. A.3

Patankar, S. V. and Spalding, D. B. (1974). *Heat Exchangers: Design and Theory Sourcebook*, chapter "A calculation procedure for the transient and steady-state behavior of shell-and-tube heat exchangers", pages 155–176. McGraw-Hill. 1.2.2

Pedersen, H. H. and Brewerton, R. W. (2014). Final report: modelling the experiments of the Buncefield Project, Phase 2, WP3. Technical report GexCon-2014-F46365-RA-1, Gexcon AS, Fantoft, Bergen, Norway. 5.6.1, 5.6.3, 5.6.3, 7.1

Pekalski, A., Puttock, J., and Chynoweth, S. (2014). DDT in a vapour cloud explosion in unconfined and congested space: large scale test. In *Tenth International Symposium on Hazards, Prevention, and Mitigation of Industrial Explosions Bergen, Norway, 10-14 June 2014*, pages 847–857. 5.6

Peters, N. (1988). Laminar flamelet concepts in turbulent combustion. *Symposium (International) on Combustion*, 21(1):1231 – 1250. 3.1.2

Peters, N. (2013). Turbulent combustion: Lecture 5, premixed turbulent combustion - the regime diagram. Lecture at the Combustion Institute Summer School, August 19-23, 2013, Lund, Sweden. 3.1.1, 3.1.2, 4.6.1

Poinsot, T. and Veynante, D. (2011). *Theoretical and numerical combustion*. 3rd edition. 2.1, 2.5, 2.6, 3.1, 4.3.3

Poinsot, T., Veynante, D., and Candel, S. (1991). Diagrams of premixed turbulent combustion based on direct simulation. *Symposium (International) on Combustion*, 23(1):613 – 619. 3.1.2, 4.6.1

Popat, N. R., Catlin, C. A., Arntzen, B. J., Lindstedt, R. P., Hjertager, B. H., Solberg, T., Saeter, O., and Van den Berg, A. C. (1996). Investigation to improve the accuracy of computational fluid dynamic based explosion models. *Journal of Hazardous Materials*, 45:1–25. 1.2.1, 2.9

Prandtl, L. (1945). Über ein neues Formelsystem für die ausgebildete Turbulenz. *Nachrichten Akad. Wiss. Göttingen, Matem.-phys. Klasse 1945.*, pages 6–19. 2.8

Prasad, A. and Williamson, C. H. K. (1997). The instability of the shear layer separating from a bluff body. *Journal of Fluid Mechanics*, 333:375–402. 5.2

Puttock, J., Chakraborty, D., and Farmayan, W. (2014). Gas explosion modelling using PDRFoam. In *Tenth International Symposium on Hazards, Prevention, and Mitigation of Industrial Explosions Bergen, Norway, 10-14 June 2014*. 5.1.1, 5.1.1, 5.1.1, 5.1.2, 5.3.3, 5.4.3, 8.2

Ranzi, E., Frassoldati, A., Grana, R., Cuoci, A., Faravelli, T., Kelley, A. P., and Law, C. K. (2012). Hierarchical and comparative kinetic modeling of laminar flame speeds of hydrocarbon and oxygenated fuels. *Progress in Energy and Combustion Science*, 38(4):468 – 501. 3.1.1, 3.2.2, 6.2.2

Rasbash, D. J., Palmer, K. N., Rogowski, Z. W., and Ames, S. (1970). Gas explosions in multiple compartments. Technical Report Fire Research Note No. 847, Fire Research Station. 6, 6.2

Reynolds, O. (1895). On the dynamical theory of incompressible viscous fluids and the determination of the criterion. *Philosophical Transactions of the Royal Society*, 186:123–164. 2.8

Rodríguez, I., Lehmkuhl, O., Chiva, J., Borrell, R., and Oliva, A. (2015). On the flow past a circular cylinder from critical to super-critical Reynolds numbers: Wake topology and vortex shedding. *International Journal of Heat and Fluid Flow*, 55:91 – 103. Special Issue devoted to the 10th Int. Symposium on Engineering Turbulence Modelling and Measurements (ETMM10) held in Marbella, Spain on September 17-19, 2014. 5.3.1, 5.3.4

Roshko, A. (1961). Experiments on the flow past a circular cylinder at very high Reynolds numbers. *Journal of Fluid Mechanics*, 10:345–. 5.3.1, 5.3.4

Roshko, A. (1993). Perspectives on bluff body aerodynamics. *Journal of Wind Engineering and Industrial Aerodynamics*, 49:79–100. 5.3, 5.3.1, 5.3.2

Rozenchan, G., Zhu, D. L., Law, C. K., and Tse, S. D. (2002). Outward propagation, burning velocities, and chemical effects of methane flames up to 60 atm. *Proceedings of the Combustion Institute*, 29:1461–1469. 3.1.1

Sand, I. Ø. and Bakke, J. R. (1989). Wall-function boundary conditions in the solution of the Navier-Stokes and the energy equations. Technical Report CMI-25110-3, Christian Michelsen Institute, Bergen, Norway. Confidential. C

Schadow, K. C. and Gutmark, E. (1992). Combustion instability related to vortex shedding in dump combustors and their passive control. *Progress in Energy and Combustion Science*, 18(2):117–132. 5.3.2

Schelkin, K. I. (1940). Influence of tube roughness on the formation and detonation propagation in gas. *Zhurnal Eksperimentalnoi i Teoreticheskoi Fiziki*, 10:823–827. 1.1.1

Schiller, L. and Linke, W. (1933). Druck und reibungswiderstand des zylinders bei reynoldsaachen zahlen 5000 bis 40000. *Z. Flugtech. Motorluft.*, 24:193–. 5.3.1

SCI (2009). Buncefield explosion mechanism phase 1, volume 1 and 2. Technical report, Steel Construction Institute. Crown copyright. 1.3.1, 1.5, 5, 5.6.1

SCI (2014). Dispersion & explosion characteristics of large vapour clouds, Volume I and II. Technical Report ED024, Steel Construction Institute. 1.3.1, 1.5, 5, 5.6, 5.6.1, 8.4

Searby, G. and Quinard, J. (1990). Direct and indirect measurements of Markstein numbers of premixed flames. *Combustion and Flame*, 82(3):298–311. 4.3.1

Selby, C. and Burgan, B. (1998). Blast and Fire Engineering for Topside Structures, Phase 2. Final summary report. Technical Report 253, Steel Construction Institute. 1.2.1, 3.2.2, 5.6

Sha, W. T. and Launder, B. E. (1979). A model for turbulent momentum and heat transport in large rod bundles. Technical Report Report ANL-77-73, Illinois: Argonne National Laboratory. 2.9

Sha, W. T., Yang, C. I., Kao, T. T., and Cho, S. M. (1982). Multidimensional numerical modeling of heat exchangers. *Journal of Heat Transfer*, 104(3):417–425. 1.2.2

Sivashinsky, G. I. (1977). Diffusional-thermal theory of cellular flames. *Combustion Science and Technology*, 15(3-4):137–145. 1.1.1, 4.3.1

Skippon, S. M. (1985). Large scale confined explosions in a twin compartment vessel. Technical report, Midlands Research Station. 6.2.1

Skjold, T. (2014). *Flame propagation in dust clouds: Numerical simulation and experimental investigation*. PhD thesis, Department of Physics and Technology, University of Bergen, Norway. 1.1, 1.2.1

Skjold, T., Castellanos, D., Olsen, K. L., and Eckhoff, R. K. (2014a). Experimental and numerical investigation of constant volume dust and gas explosions in a 3.6-m flame acceleration tube. *Journal of Loss Prevention in the Process Industries*, 30:164–176. 1.3.1, 4

Skjold, T., Hisken, H., Atanga, G., Narasimhamurthy, V. D., Lakshmipathy, S., Storvik, I. E., and Pesch, L. (2017a). Modelling Escalating Accident Scenarios and the Use of Risk-reducing technology for Explosion safety (MEASURE), final report. Confidential. Technical report, Gexcon AS, Bergen, Norway. 3.2.2, 4.5.1, 5.3.3

Skjold, T., Pedersen, H. H., Bernard, L., Middha, P., Narasimhamurthy, V. D., Landvik, T., Lea, T., and Pesch, L. (2013a). A matter of life and death: Validating, qualifying, and documenting models for simulating flow-related accident scenarios in the process industry. *Chemical Engineering Transactions*, 31:6 pp. 4.5.2, 6.1.3

Skjold, T., Pedersen, H. H., Narasimhamurthy, V. D., Lakshmipathy, S., Pesch, L., Atanga, G. F., Folusiak, M., Bernard, L., Siccama, D., and Storvik, I. E. (2014b). Pragmatic modelling of industrial explosions in complex geometries: review of the state-of-the-art and prospects for the future. In Borisov, A. A. and Frolov, S. M., editors, *Zel'dovich Memorial: Accomplishments in the Combustion Science in the last decade*, volume 1, pages 70–74. Torus Press. 1.1.1

Skjold, T., Siccama, D., Hisken, H., Brambilla, A., Middha, P., Groth, K. M., and LaFleur, A. C. (2017b). 3D risk management for hydrogen installations. *International Journal of Hydrogen Energy*, 42(11):7721 – 7730. Special issue on The 6th International Conference on Hydrogen Safety (ICHS 2015), 19-21 October 2015, Yokohama, Japan. 1.3.2

Skjold, T., van Wingerden, K., Storvik, I. E., Pesch, L., Melheim, J. A., Ichard, M., Narasimhamurthy, V. D., Middha, P., Pedersen, H. H., Bernard, L., Hansen, O. R., Lilleberg, B., and Khalil, M. (2013b). Final report 'JIP FLACS 2011 and beyond'. Technical Report GexCon-13-F46240-C-1, Gexcon AS, Bergen, Norway. Confidential. 1.3.1, 3.2.1, 5.2.2, 7.1

Solberg, D. M., Pappas, J. A., and Skramstad, E. (1981). Observations of flame instabilities in large scale vented gas explosions. *Symposium (International) on Combustion*, 18(1):1607–1614. 1.3.3, 5.4, 6.2, 7.1

Sommersel, O. K., Vaagsaether, K., and Bjerketvedt, D. (2017). Hydrogen explosions in 20' ISO container. *International Journal of Hydrogen Energy*, 42(11):7740–7748. Special issue on The 6th International Conference on Hydrogen Safety (ICHS 2015), 19-21 October 2015, Yokohama, Japan. 1.3.2

Soulopoulos, N., Kerl, J., Sponfeldner, T., Beyrau, F., Hardalupas, Y., Taylor, A. M. K. P., and Vassilicos, J. C. (2013). Turbulent premixed flames on fractal-grid-generated turbulence. *Fluid Dynamics Research*, 45, 061404:1–18. 5.6.2

Sponfeldner, T., Soulopoulos, N., Beyrau, F., Hardalupas, Y., Taylor, A. M. K. P., and Vassilicos, J. C. (2015). The structure of turbulent flames in fractal- and regular-grid-generated turbulence. *Combustion and Flame*, 162(9):3379–3393. 5.6.2

Sreenivasan, K. R., Ramshankar, R., and Meneveau, C. (1989). Mixing, entrainment and fractal dimensions of surfaces in turbulent flows. *Proceedings of the Royal Society of London. Series A, Mathematical and Physical Sciences*, 421(1860):79–108. 4.4, 4.5.1

SUSANA (2016). The state-of-the-art in physical and mathematical modelling of safety phenomena relevant to fuel cells and hydrogen technologies. Technical report, SUpport to SAfety ANalysis of Hydrogen and Fuel Cell Technologies. 5.4.3

Tam, V. H. Y. and Johnson, M. (2016). Detonation: why it should be included in risk and hazard assessment. *Loss Prevention Bulletin*, 252. 1.3.1, 8.4

Tam, V. H. Y. and Lee, R. (1998). Gas explosion modelling of FPSO. *Journal of Loss Prevention in the Process Industries*, 11(1):67 – 73. 1.1.2, 6.1.3

Taylor, S. C. (1991). *Burning velocity and the influence of flame stretch*. PhD thesis, University of Leeds, UK. 4.5.2, 4.2, 4.6.1, 4.5

Thomann, H. (1959). Measurements of the recovery temperature in the wake of a cylinder and of a wedge at Mach numbers between 0.5 and 3. Technical Report 84, Aeronautical Research Institute of Sweden (FFA). 5.3.1, 5.3.4

Tomlin, G. B. (2015). *Gas Explosions in Dwellings: The Effects of Interconnected Rooms and Obstacles, and the Interpretation of Thermal Damage*. PhD thesis, Energy Research Institute, School of Chemical and Process Engineering, University of Leeds, UK. 1.1, 1.3.3

Tomlin, G. B., Johnson, D. M., Cronin, P., Phylaktou, H. N., and Andrews, G. E. (2015). The effect of vent size and congestion in large-scale vented natural gas/air explosions. *Journal of Loss Prevention in the Process Industries*, 35:169–181. 1.3.3, 5.6

Truffaut, J.-M. and Searby, G. (1999). Experimental study of the Darrieus-Landau instability on an inverted-'V' flame, and measurement of the Markstein number. *Combustion Science and Technology*, 149(1-6):35–52. 4.3.1

Tseng, L. K., Ismail, M. A., and Faeth, G. M. (1993). Laminar burning velocities and Markstein numbers of hydrocarbons-air flames. *Combustion and Flame*, 95:410–426. 4.6.1

Tsuruda, T. and Hirano, T. (1987). Growth of flame front turbulence during flame propagation across an obstacle. *Combustion Science and Technology*, 51(4-6):323–328. 1.3.3, 5.4, 7.1

Vagelopoulos, C. M. and Egolfopoulos, F. N. (1998). Direct experimental determination of laminar flame speeds. *Symposium (International) on Combustion*, 27(1):513–519. 3.1.1

van Wingerden, C. J. M. (1989). On the venting of large-scale methane-air explosions. In *Sixth international symposium on loss prevention and safety promotion in the process industries, 19-22 June 1989, Oslo, Norway*. 1.3.3, 6.2

van Wingerden, C. J. M. and Zeeuwen, J. P. (1983a). On the role of acoustically driven flame instabilities in vented gas explosions and their elimination. *Combustion and Flame*, 51:109–111. 1.1.1, 1.3.3, 4, 5.5, 6.2

van Wingerden, C. J. M. and Zeeuwen, J. P. (1983b). Venting of gas explosions in large rooms. In *Fourth international symposium on loss prevention and safety promotion in the process industries, 12-16 September 1983, Harrogate, England*. 1.3.3, 6.2

van Wingerden, K. (2013). Advances in explosion modelling. *FABIG Newsletter*, 62:9–20. 1.1.2, 1.2.1

van Wingerden, M. and Wilkins, B. (2011). Buncefield Explosion Mechanism Phase 2, WP 3.1, Medium-scale tests to investigate the influence of vegetation on flame propagation within semi-confined enclosures. Technical Report Gexcon-11-F44140-RA-1, Gexcon AS, Norway. 5.6.1

Versteeg, V. and Malalasekera, W. (2007). *An introduction to computational fluid dynamics: The finite volume method*. Pearson Education Limited, 2nd edition. 2.8, A.2, A.3, A.3

Vik, K.-A. (2014). Comparison of burning velocity differences in a numerical explosion simulator. Master's thesis, Department of Physics and Technology, University of Bergen, Norway. 3.2.1

Vinnem, J. E. (2014). *Offshore risk assessment: Principles, modelling, and applications of QRA studies*, volume I and II. Springer, 3rd edition. 1.1, 1.1.2, 1.2.2

Vyazmina, E. and Jallais, S. (2016). Validation and recommendations for FLACS CFD and engineering approaches to model hydrogen vented explosions: Effects of concentration, obstruction vent area and ignition position. *International Journal of Hydrogen Energy*, 41(33):15101–15109. 1.3.2, 1.3.3

Wang, Y. L., Holley, A. T., Ji, C., Egolfopoulos, F. N., Tsotsis, T. T., and Curran, H. J. (2009). Propagation and extinction of premixed dimethyl-ether/air flames. *Proceedings of the Combustion Institute*, 32:1035–1042. 3.1.1

Warnatz, J., Maas, U., and Dibble, R. W. (2006). *Combustion: Physical and chemical fundamentals, modeling and simulation, experiments, pollutant formation*. Springer-Verlag, 4th edition. 2.1, 2.4, 3.1.3

Weller, H. G., Tabor, G., Gosman, A. D., and Fureby, C. (1998a). Application of a flame-wrinkling les combustion model to a turbulent mixing layer. *Symposium (International) on Combustion*, 27(1):899–907. 4.4, 5.1.1, 5.1.1, 5.1.1, 5.3.3, 5.4.2, 5.4.3, 5.7, 8.2

Weller, H. G., Tabor, G., Jasak, H., and Fureby, C. (1998b). A tensorial approach to computational continuum mechanics using object-oriented techniques. *Computers in Physics*, 12(6):620–631. 4.4

Wilkins, B. A., van Wingerden, K., and Pedersen, G. H. (1999). Gas explosions in congested open geometries. Technical Report no. CMR-99-F30087, Christian Michelsen Research, Bergen, Norway. 5.6

Williams, F. A. (1976). Criteria for existence of wrinkled laminar flame structure of turbulent premixed flames. *Combustion and Flame*, 26(0):269 – 270. 3.1.2

Williams, F. A. (1985). *Combustion theory: the fundamental theory of chemically reacting flow systems*. Perseus Books Group. 1.1.1, 4.3.1, 4.3.3

Williamson, C. H. K. (1996). Vortex dynamics in the cylinder wake. *Annual Review of Fluid Mechanics*, 28(1):477–539. 5.3, 5.3.1, 5.4, 5.3.4

Wu, C. K. and Law, C. K. (1985). On the determination of laminar flame speeds from stretched flames. *Symposium (International) on Combustion*, 20:1941–1949. 3.1.1

Yu, M.-H. and Monkewitz, P. A. (1990). The effect of nonuniform density on the absolute instability of two-dimensional inertial jets and wakes. *Physics of Fluids A Fluid Dynamic*, 2(7):1175–1181. (document), 5.3.1, 5.5, 5.3.1

Zalosh, R. G. (1979). Gas explosion tests in room-size vented enclosures. In *Proceedings of the 13th Loss Prevention Symposium, Houston, USA*, pages 98–108. 5.5

Zdravkovich, M. (1997). *Flow around circular cylinders: Volume 1: Fundamentals*. New York: Oxford University Press. 5.3, 5.3.1

Zdravkovich, M. (2003). *Flow around circular cylinders: Volume 2: Applications*. New York: Oxford University Press. 5.3, 5.3.1, 5.3.2

Zeldovich, Y. B., Barenblatt, G. I., Librovich, V. B., and Makhviladze, G. M. (1985). *The mathematical theory of combustion and explosions*. Consultants Bureau, New York. 4.3.2, 4.3.2, 4.3.4, 4.3.5, 4.3.5, 4.7, 5.4.1, 5.4.3, 7.1

Zhou, Y., Nagata, K., Sakai, Y., Suzuki, H., Ito, Y., Terashima, O., and Hayase, T. (2014). Relevance of turbulence behind the single square grid to turbulence generated by regular- and multiscale-grids. *Physics of Fluids*, 26(7):1–22. 5.6.2

Papers

This chapter contains the four papers associated with the dissertation.

Paper 1

Modelling large-scale vented gas explosions in a twin compartment enclosure

Pedersen, H.H., Tomlin, G., Middha, P., Phylaktou, H.N. & Andrews, G.E.

CrossMark

Modelling large-scale vented gas explosions in a twin-compartment enclosure

H.H. Pedersen [a,b,*], G. Tomlin [c,d], P. Middha [b], H.N. Phylaktou [c], G.E. Andrews [c]

[a] Department of Physics and Technology, University of Bergen, Allégaten 55, 5007 Bergen, Norway
[b] GexCon AS, Research and Development, Fantoftveien 38, P.O. Box 6015, Postterminalen, 5892 Bergen, Norway
[c] School of Process, Environmental and Materials Engineering, University of Leeds, Leeds LS2 9JT, UK
[d] GL Noble Denton, Holywell Park, Ashby Road, Loughborough LE11 3GR, UK

ARTICLE INFO

ABSTRACT

Natural gas and LPG are common fuels that have been used relatively safely in the home for many decades. However, when there is a release of gas within a dwelling, or gas from a leaking external pipeline migrates into a building, an explosion may occur. Most of the experimental research into vented gas explosions has been conducted in single enclosure, cuboid or spherical geometries which are not representative of accidental explosions in dwellings or process industries. This paper discusses the findings of a comprehensive large-scale experimental programme undertaken by British Gas Research and Development and also compares FLACS CFD (Computational Fluid Dynamics) simulations against a number of these experiments. The results suggest that the software is useful in gaining a greater understanding of the dynamics of explosion development in dwellings. The paper highlights areas of good performance of the software as well as areas of shortcomings where further understanding and modelling effort is needed.

© 2013 Elsevier Ltd. All rights reserved.

1. Introduction

Accidental gas explosions represent an ever-present hazard for process industries handling flammable gases and liquids. The hazard is also present in many homes. In the UK, there are on average thirty accidental gas explosions per year, causing 2 fatalities, over 30 non-fatal injuries and costing the UK economy millions of pounds (Health and Safety Executive (HSE, 2011)).

In industrial and process enclosures, installing pressure relief panels (commonly termed explosion relief) can provide effective mitigation against the consequences of a gas explosion. However, for cost and aesthetic reasons, it is usually not practical to install explosion relief in buildings used as offices or for accommodation. When accidental explosions occur in such buildings, the structure is often fortuitously vented, as weak components fail (e.g. windows), allowing hot expanding combustion gases to escape through the openings, relieving the pressure and limiting the damage to the building. The effectiveness of the fortuitous opening or purpose provided explosion relief will depend on several parameters; including, the fundamental properties of the fuel, the size of the relief opening (vent), the vent opening pressure, the ignition position and the presence of obstacles.

Whilst there are empirically based correlations for the prediction of overpressure and for vent sizing (e.g. EN 14994, 2007; NFPA 68, 2007 etc.), these are limited in application to simple, compact enclosures with no obstacles. A typical building has interconnected spaces and contents which would act as congestion to the propagating flame, and potentially increase the flame acceleration considerably. Therefore, the simple guidelines and correlations, referred to above cannot be applied with any confidence to these situations for either design or post-incident investigation purposes.

Experimental research undertaken in empty, single compartment enclosures demonstrated that the pressure—time history of a vented explosion will in general have a number of peaks, with different physical phenomena contributing to each peak (Bauwens, Chaffee, & Dorofeev, 2010; Butlin & Tonkin, 1974; Cooper, Fairweather, & Tite, 1986; Harrison & Eyre, 1987; Solberg, Pappas, & Skramstad, 1979, 1980; van Wingerden, 1989; van Wingerden & Zeeuwen, 1983). Most buildings consist of several rooms or compartments connected by doorways, making the situation even more complex. When a gas explosion propagates from one chamber into

another, explosion overpressures may be significantly higher than for an explosion in a single chamber of similar total volume and vent size (Astbury, West, & Hodgkinson, 1972; Astbury, West, Hodgkinson, Cubbage, & Clare, 1970; Rasbash, Palmer, Rogowski, & Ames, 1970).

In the early 1980s, a comprehensive large-scale experimental programme was undertaken in order to gain a more detailed understanding of the mechanism of gas explosions in large and multiple compartment enclosures, representative of a typical UK home (Skippon, 1985). Some of the results of this experimental programme are presented here with a comparison with numerical simulations.

2. The experimental programme

In total, eighty-five experiments were carried out using natural gas/air mixtures of varying concentration and distribution, in an explosion chamber that consisted of two 22 m³ enclosures connected by a door. The dimensions of each enclosure were 2.4 m × 3.6 m × 2.4 m, with each enclosure having a vent opening of variable size, fitted to the upper half of its front face (Fig. 1).

For the experiments presented in this study, the vent panel consisted of 12.5 mm fibreboard clamped around the edge of the vent opening and the connecting door was of a 'lightweight' type, typical of that used in UK housing at that time. The effects of varying the following experimental variables were investigated: the vent dimensions and configuration, the position of the interconnecting door, the ignition position, and the depth of the gas layer (i.e. half-filled/full compartment).

The vent openings were either 2.48 m², 1.49 m² or 0.74 m². Correspondingly, the vent coefficients (K), defined as the area of the front face divided by the area of the vent opening, were approximately 2.4, 4 or 8. The K = 4 and K = 8 reliefs could be fitted either to the left or the right side of the vent opening. The doorway between the enclosures measured 1.98 m × 0.76 m, with the door being either in the closed or fully open position. The natural gas/air mixture was ignited by an electric spark positioned in the left enclosure. The ignition position was either the centre of the rear enclosure wall or the geometric centre of the enclosure. The required natural gas/air mixtures were pre-mixed prior to admission into the explosion chamber and were introduced into each enclosure through a large diffuser located in the enclosure ceiling. This procedure allowed the formation of natural gas/air layers extending downwards from the ceiling. Experiments involving layers of natural gas/air mixtures were conducted with layers equal to half the height of the enclosure. The fuel concentration was measured by withdrawing samples of the natural gas/air mixture at
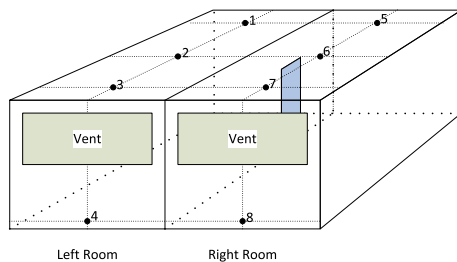
various heights in the enclosure through remote monitored sampling probes. The sampling probes were withdrawn from the enclosures prior to ignition.

The pressures generated in the explosions were measured by eight piezoelectric pressure transducers located in the ceiling and front of the enclosures. The positions of the pressure transducers are marked in Fig. 1.

3. The numerical model

The Computational Fluid Dynamics (CFD) tool FLACS is frequently used by the oil and gas industry for explosion risk assessment in offshore and onshore installations. The CFD model solves the 3D Reynolds-averaged Navier–Stokes equations on a Cartesian grid. The conservation equations for mass, momentum, enthalpy and chemical species are solved using a finite-volume method. Turbulence is modelled using the two-equation $k-\varepsilon$ model (Launder & Spalding, 1974). The interaction between the reactive fluid flow and the surrounding geometry is taken into consideration through a distributed porosity concept. The $k-\varepsilon$ model is modified to capture the effect of turbulence production from subgrid geometry. The numerical flame is thickened, typically 3–5 control volumes. See Arntzen (1998) and GexCon AS (2010) for a more detailed description of the numerical model.

Since the typical grid resolution in FLACS is significantly larger (0.1–1 m) than the scales where the small scale turbulence and the chemical heat release interact (0.0001–0.01 m), several phenomenological subgrid models are included. In order to be successful, the development of such models must therefore be based on an extensive amount of validation against various experiments. In particular, the results from high-quality, large-scale experiments are essential.

4. Model setup

FLACS, version 9.1, release 3 (GexCon AS, 2010) was used to simulate a selection of the large-scale vented explosion tests described in Section 2. The model's ability to capture the effect of vent size and configuration and the influence of the flow interactions between the two enclosures on the flame propagation (and consequently its prediction of overpressure) is of main interest. Concentration effects are not considered here.

The pressure relief panels are modelled in FLACS as planes with porosities varying in time from an initial porosity of 0 (i.e. completely closed) to a given end porosity. The end porosities of the


Fig. 1. Location of the pressure transducers within the explosion chamber.
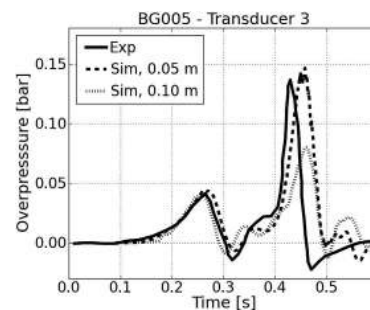
Fig. 2. An example of the grid sensitivity.

vent panels on the face of the enclosure were given to be 0.8 (to represent the breaking process), while the interconnecting door (when present) was given an end porosity of 1. In the simulations, both the door and the front vent panels were assigned a mass that ensured a representative opening time of 25 ms.

A grid resolution of both 0.10 m and 0.05 m was tested for a range of setups to investigate the grid sensitivity. A grid resolution of 0.05 m appears to be necessary to resolve the involved mechanisms satisfactorily (Fig. 2). It is not always possible to refine the mesh until a grid independent solution is found, due to the coupling between the propagating reaction zone and the flow equations in the model. For resolutions close to or below 1 cm, the thickened flame may cause severe grid dependency. Thus, a grid resolution of 0.05 m was found to be appropriate, and is used throughout the study.

5. Results and discussion

5.1. General remarks

In almost all of the experiments, the explosion overpressure–time profiles displayed two distinct pressure peaks. The first pressure peak was always associated with the removal of one or both of the explosion relief vent panels (in either of the two enclosures) and its magnitude was equal to or slightly greater than the failure pressure of the vent panel. Initially, combustion is taking place in a totally confined enclosure and the expansion of the hot products of combustion generates a pressure rise. As soon as the explosion relief vent panel opens, unburnt fuel/air mixture is allowed to escape causing the pressure to fall and giving rise to the first pressure peak (P_1). The second pressure peak was found to be more complex in origin and significantly more variable in its magnitude. Although in some instances, the mechanism of generation of this second pressure peak was found to be similar to that of an explosion in a single compartment, it was also found to arise from the complex interaction of the combustion in each of the two compartments. This mechanism is discussed in more detail in Sections 5.2–5.4.

During analysis of the experimental results, it was found that the mechanism of overpressure generation was largely dependent upon the vent configuration. Consequently, it is convenient to categorise the experiments as follows:

- Type A: Both enclosures were fitted with vent panels of identical size, and consequently, nearly identical failure pressures.
- Type B: The left enclosure was fitted with a large vent panel of relatively low failure pressure, whilst the right enclosure was fitted with a smaller vent panel of higher failure pressure.
- Type C: The left enclosure was fitted with a small vent panel of relatively high failure pressure, whilst the right enclosure was fitted with a larger vent panel of lower failure pressure.

For the sake of brevity, selected cases will be presented for each configuration. Overview plots are provided in Section 5.5.

5.2. Experiments of Type A

The simulated Type A tests are summarised in Table 1.

In the Type A experiments, the pressure–time profile (see Fig. 4) was very similar to that which would be generated in an explosion in a single enclosure of the same total volume. The first pressure peak was associated with the almost simultaneous failing of both the right and left enclosure pressure relief panels. Analysis of the video records showed that the second pressure peak (P_2) occurred as a result of the combustion outside of the explosion chamber, of the cloud of turbulent unburnt natural gas/air mixture expelled through the vent openings. The origin of the P_2 pressure peak was confirmed by the fact that the magnitude of the second peak was significantly greater for rear than central ignition. This occurs because, in the case of rear ignition, a greater volume of unburnt gas/air mixture is expelled through the vents before the turbulent cloud ignites.

In the Type A tests, the position of the door (either open or closed) appeared to have no effect on the maximum pressure generated. However, the magnitude of the pressure generated was always higher in the right enclosure than the left (ignition enclosure). This is the result of turbulence enhanced combustion in the right enclosure induced by flow through the doorway.

The effects on the overpressure–time profiles for both model and experimental results from the degree of filling, and of inserting a closed, lightweight interconnecting door, are illustrated for rear ignition in Figs. 3 and 4. The dark grey solid and dashed lines represent the failure of the pressure relief panels and the arrival time of the flame at the vent opening in the FLACS simulations, respectively. These lines are only drawn for the enclosure (left or right) whose pressure–time development is plotted. Correspondingly, the light grey solid and dashed lines represent the beginning of the vent breaking process and time of arrival of the flame at the opening in the experiments. This information is not always available, due to occasional video failure. Where only one plot is shown, the events in both chambers were simultaneous.

The occurrences of the simulated pressure peaks appear to correspond to the same events as observed in the experiments, and the agreement is well within the experimental uncertainties for all configurations. However, the pressure peaks were predicted to occur earlier in the explosion, as the ignition and very initial laminar propagation of the flame is more violent in the model for numerical reasons. The simulated flame propagation for experimental test BG014, indicated by the burnt product gases and the velocity vectors, is shown Fig. 5.

The simulated flame propagation mechanism is similar to that observed during the experiment. There is some turbulence generation as the high velocity flow is drawn towards the large vent opening in the right chamber, driven by the pressure differential, through the porosities representing the door. The turbulence that is created when the door is opened is represented through a source term for flow through partially porous regions. Consequently, the turbulence generated may be somewhat dissimilar to that generated by the opening of the real door in the experiments. Contrary to the experiments, the left vent panel generally opens before combustion has started in the right chamber, indicating that the rate of combustion in the early phase of the explosion is somewhat different from that observed in the experiments. The central ignition experiments (not shown here) exhibited lower overpressure amplitudes than rear ignition — otherwise, the observations for the rear ignition model results also apply to central ignition.

Table 1
The simulated Type A experiments.

Test no.	Vent coefficients (K)		Initial door position	Ignition position	Layer/Full
	Left	Right			
BG003	2.4	2.4	Open	Rear	Layer
BG005	2.4	2.4	Open	Rear	Full
BG010	2.4	2.4	Open	Central	Layer
BG014	2.4	2.4	Closed	Rear	Layer
BG017	2.4	2.4	Closed	Rear	Full
BG021	2.4	2.4	Open	Central	Full
BG022	2.4	2.4	Closed	Central	Layer
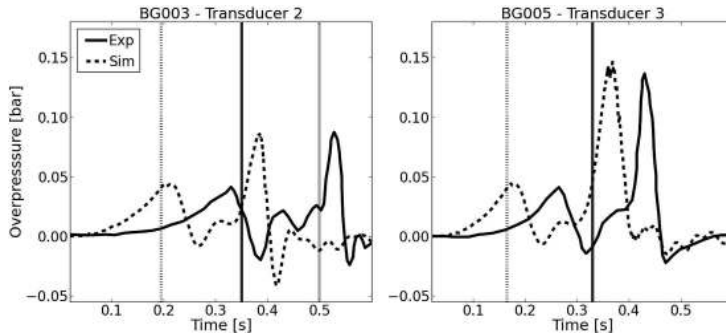
Fig. 3. Overpressure–time for half-layer (left) and filled gas conditions (right), rear ignition, open door.

5.3. Experiments of Type B

The experimental specifications of the simulated Type B experiments are summarised in Table 2.

In the Type B experiments, the enclosure in which ignition was initiated had a vent panel of $K = 2.4$, whilst the right enclosure had a smaller panel of $K = 4$ or 8. It was observed that the important factor was not the difference in vent area, but the difference in vent failure pressure.

The influence of the door was found to have a significant effect on the explosion process. Comparison of video records against the pressure–time profile of Type B experiments (with the door in the closed position) has allowed the most likely explanation for the explosion process to be postulated. Fig. 6 shows the probable flame–time profile for the two enclosures in test BG026.

One hundred (100) ms after ignition, the pressure started to rise in the left enclosure and because the interconnecting door was closed, a pressure difference existed between the two enclosures. 150 ms after ignition, the door opened (as this had a lower opening pressure than the vent panel) and the pressure began to equalise in the two enclosures. The flow through the doorway distorted the flame and when the flame front reached the door opening, combustion began in the right enclosure (shown at C in Fig. 6). At D, the pressure had risen sufficiently for the vent panel in the left enclosure to fail and the pressure in this enclosure began to fall giving

rise to a P_1 peak (in this enclosure) at 265 ms. At this point, there was rapid combustion of the turbulent mixture in the right enclosure resulting in a pressure difference between the two enclosures. Consequently, there was a flow from the right enclosure through the doorway into the left enclosure causing the pressure to drop in the right enclosure and giving rise to a P_1 peak (in the right enclosure) at 285 ms. The sudden relief of the right enclosure into the left caused the pressure to drop below ambient in the right enclosure and, as the pressure was now lower than that in the left enclosure, the flame front 'jetted' back into the right enclosure possibly assisted by the pressure produced from the external combustion. This caused rapid, turbulent combustion, resulting in a rapid pressure rise and the failure of the vent panel in the right enclosure. The rate of pressure rise in this enclosure was greater than it can be relieved through the vent opening resulting in a higher maximum pressure being attained. Thus, it is proposed that it is the ignition of a turbulent mixture in the right enclosure by a jetted flame that produced the high overpressures observed (over 400 mbar in some experiments). Moreover, it was observed, that when the interconnecting door was open, the lower degree of turbulence resulted in an explosion mechanism that was similar to Type A experiments.

It was also found that central ignition generally resulted in lower overpressures. This appeared to occur because the flame front reached the vent opening of the left enclosure at an earlier
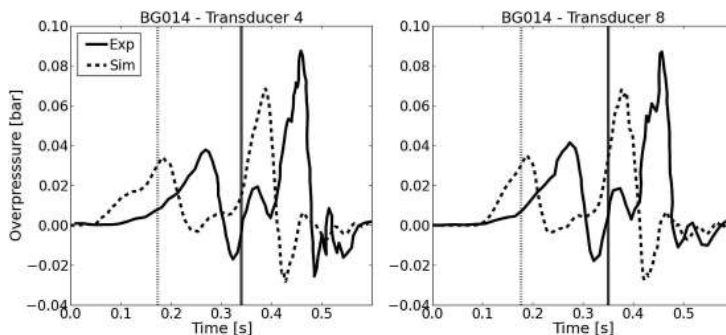
Fig. 4. Overpressure–time curves for left chamber (left) and right chamber (right), half-layer, rear ignition, closed door.
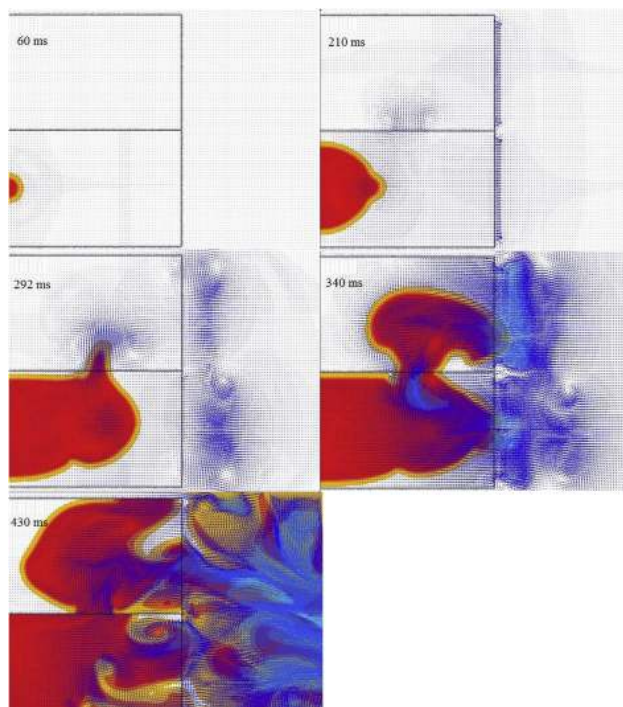
Fig. 5. Flame propagation in time for BG014.

stage of the explosion and consequently the initial turbulence generated in the right enclosure was less than in the case of rear ignition. Furthermore, the outside combustion was of smaller magnitude (because less unburnt mixture was expelled) resulting in a lower jet velocity into the right enclosure and consequently less turbulence was generated.

Figs. 7 and 8 show the model results for the Type B experiments BG026 (discussed in the proposed explosion mechanism above) and BG024. The vertical lines mark the same events as in the

Table 2
The simulated Type B experiments.

Test no.	Vent coefficients (K)		Initial door position	Ignition position	Layer/Full
	Left	Right			
BG024	2.4	4(*l*)[a]	Open	Rear	Layer
BG026	2.4	4(*l*)	Closed	Rear	Layer
BG027	2.4	4(*l*)	Closed	Central	Layer
BG034	2.4	8	Open	Central	Layer
BG035	2.4	8	Closed	Central	Layer
BG036	2.4	8	Closed	Rear	Layer
BG037	2.4	4(*r*)	Open	Central	Layer
BG038	2.4	4(*r*)	Open	Central	Full
BG040	2.4	4(*r*)	Closed	Rear	Full

[a] The terms (*l*) and (*r*) indicate whether the vent relief panel was positioned to the left or the right side of the vent opening.

previous plots. It can be seen that the presence of a closed door is significant, with overpressures enhanced by a factor of three compared to the open door tests. The pressure peaks and events in the experiments and simulations seem to correspond.

Fig. 9 shows the modelled flame propagation for a rear ignition experiment with a closed interconnecting door. In the simulations, the door is generally forced open after 60 ms for back ignition and somewhat earlier for centre ignition.

The pressure is equalised by flow of unburnt mixture into the right chamber, however, the flow reverses when the venting of the left room increases, pushing the flame front away from the door opening. At the onset of the external explosion outside of the left vent opening, the flame propagates into the right compartment, generating the high, second pressure peak. The early breaking of the left pressure panel with respect to the onset of combustion in the right chamber leads to a history of events that somewhat differs from that in the experiments. Due to the importance of door effects in the Type B experiments, this has a more significant effect on the pressure–time curves than for the Type A experiments.

Later in the explosion history, the turbulence generation from the opening of the door does not appear to compensate sufficiently to reproduce the overpressures in Type B experiments, where the right vent opening is smaller, and yields at a later point in time. The flow reversals seen in the experiments resulted in increased flame surface areas, and consequently enhanced combustion rates, due to

Fig. 6. Proposed explosion mechanism for Type B experiments (rear ignition, door closed).
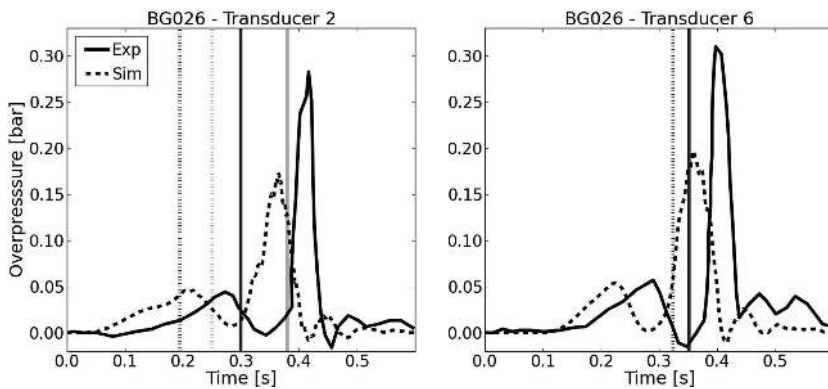
Fig. 7. Rear ignition, half-layer, closed door, overpressure–time for left and right chamber.
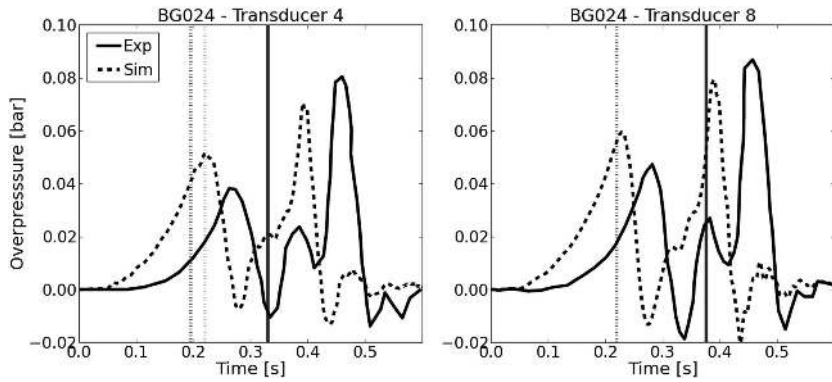
Fig. 8. Type B experiments with an open door, rear ignition and a half-layer of gas.
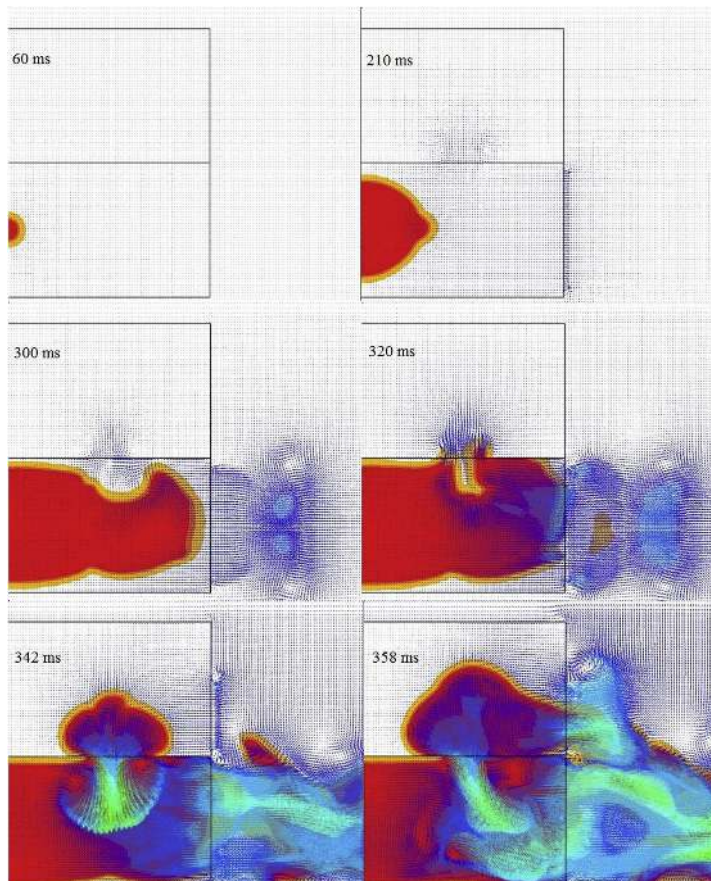

**Fig. 9.** Flame propagation for a Type B experiment with rear ignition.
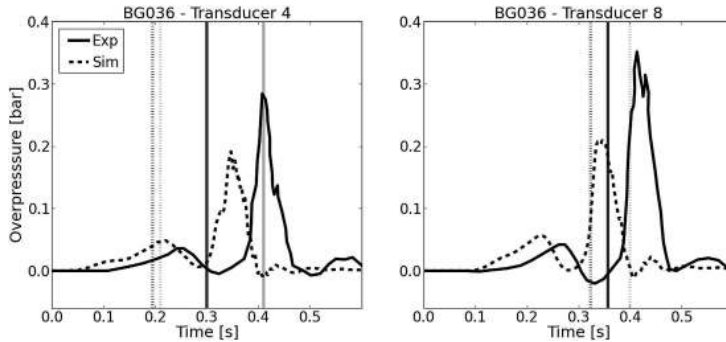
Fig. 10. Rear ignition, half-layer, closed door, overpressure–time for left and right enclosure, right vent with $K = 8$.

Rayleigh–Taylor instabilities. The pressure wave–flame interactions induced by the bursting of the vents and of the closed door also have an enhancing effect on the combustion rate.

Inserting a smaller vent panel ($K = 8$) in the right chamber has a modest effect on the experimental and simulated results, see Fig. 10. This is most probably because venting can take place from the right enclosure through the doorway into the left enclosure, and the doorway is approximately the same size as $K = 4$. The model results for the central ignition experiments showed the same tendencies as the modelled rear ignition experiments; except that they exhibited lower overpressures, see Fig. 11.

5.4. Experiments of Type C

The experimental variables of the Type C tests used for FLACS simulation are summarised in Table 3.

In the Type C experiments, the right enclosure had a vent panel of $K = 2.4$, whilst the left enclosure (in which ignition was initiated) had a smaller panel of $K = 4$ or 8. Similarly to Type B tests, it was observed that the important factor was the difference in vent failure pressure and not the difference in vent area. Fig. 12 shows the proposed mechanism for Type C experiments, derived from video analysis and pressure–time profiles (Skippon, 1985).

In the early stages of the explosion (A and B of Fig. 12) the mechanism was found to be similar to that of the Type B experiments. Following ignition in the left enclosure, an initial pressure differential built up between the enclosures causing the door to swing open into the right enclosure. The subsequent flow from the left enclosure into the right caused the flame to distort towards the door (stage C), and at this point, the pressure had risen in the right enclosure such that its explosion relief failed, giving rise to P_1 (in the right enclosure). As the pressure in the left enclosure was able to relieve through the door, the P_1 peak in the left enclosure showed shortly after. This venting, through the doorway, caused the flame front to 'jet' into the right enclosure towards the vent opening, creating turbulence and enhancing the combustion rate considerably within the right enclosure. This increased combustion rate caused the pressure to rise in the right enclosure creating a pressure difference between the two enclosures. The pressure difference results in a reversing of flow back into the left enclosure causing the flame front to 'jet' back into the left enclosure igniting a large volume of unburnt gas/air mixture. The resulting rapid combustion throughout the enclosure produced a high rate of pressure rise and generating a P_2 peak.

It was observed that of all the test types, this Type C explosion mechanism produced the P_2 peaks of greatest magnitude. Moreover, large P_2 pressures were produced even when the door was initially

Fig. 11. Central ignition, half-layer, closed door, right vent with $K = 4$.

219

Table 3
The simulated Type C experiments.

Test no.	Vent coefficients (K)		Initial door position	Ignition position	Layer/Full
	Left	Right			
BG044	4(r)	2.4	Closed	Rear	Layer
BG046	4(r)	2.4	Closed	Central	Layer
BG047	4(r)	2.4	Open	Central	Layer
BG051	8	2.4	Open	Rear	Layer
BG054	8	2.4	Closed	Rear	Layer
BG056	8	2.4	Closed	Central	Layer

open. Fig. 13 shows the pressure–time profile of a FLACS simulation of test BG 44 (half-layer of gas, a closed door, and rear ignition). The vertical lines mark the same events as in the previous plots.

During the early stage of the explosion, FLACS predicted that a pressure differential developed between the enclosures, causing the door to fail. As before, the large vent opening (now in the right chamber) failed before combustion had commenced in the right chamber, producing the first pressure peak in this enclosure. As the flame propagated into the right enclosure, the right, small vent panel broke, leading to some flow reversal through the doorway.

Fig. 14 shows the simulated flame propagation mechanism for a Type C experiment with rear ignition, an open door and a half-filled layer with gas/air mixture.

Fig. 15 shows the effect of decreasing the vent coefficient in the left enclosure. In the experiments, the overpressures were somewhat enhanced when the vent coefficient of the left enclosure was increased from $K = 4$ to $K = 8$ (i.e. the vent size decreased). The same effect can be seen in the FLACS simulated results. For the Type C experiments, the flame propagation mechanism and the overpressures were well reproduced by FLACS — the high overpressures achieved even without an interconnecting door were also reproduced.

5.5. Overview of results

The maximum overpressure is often used to evaluate the results from a study, and to determine the severity of an explosion. In Figs. 16 and 17, the ratio of the predicted to experimental results is compared in the manner suggested by the *Gas Explosion Model Evaluation Protocol* (Model Evaluation Group Gas Explosions (MEGGE, 1996), p. 32). Fig. 16 compares the experimental to the simulated results in a scatter plot, marking the limits for 50%

A — 100 ms — Initial pressure rise

B — 150 ms — Door opens, flow into right enclosure

C — 225 ms — Flame enters right enclosure

D — 265 ms — Vent opens in right enclosure, pressure drops

E — 300 ms — Flame dragged towards vent opening

F — 360 ms — External turbulent combustion, rapid pressure rise in right enclosure

G — 375 ms — High pressure in the right enclosure causes flow reveral into the left enclosure resulting in rapid combustion in both enclosures. Vent fails in left enclosure

Fig. 12. Proposed mechanism for Type C experiments (rear ignition, door closed).

Fig. 13. Half-layer of gas, closed door, rear ignition, left vent panel $K = 4$.

discrepancy. Fig. 17 shows the geometric mean and variance of the dataset (the ratio of predicted to observed values), which respectively represents systematic bias towards over or underprediction and the variance measures the probability of getting an agreement within certain bounds (Tam, 1998). All model results from the study are consistently predicted to be within a factor of 2 of the observed values. The observations described in the previous sections for each type of experiment is reflected in these overview plots, for example, note the tendency towards underprediction for the closed door configurations vs. the open door cases in Fig. 17.
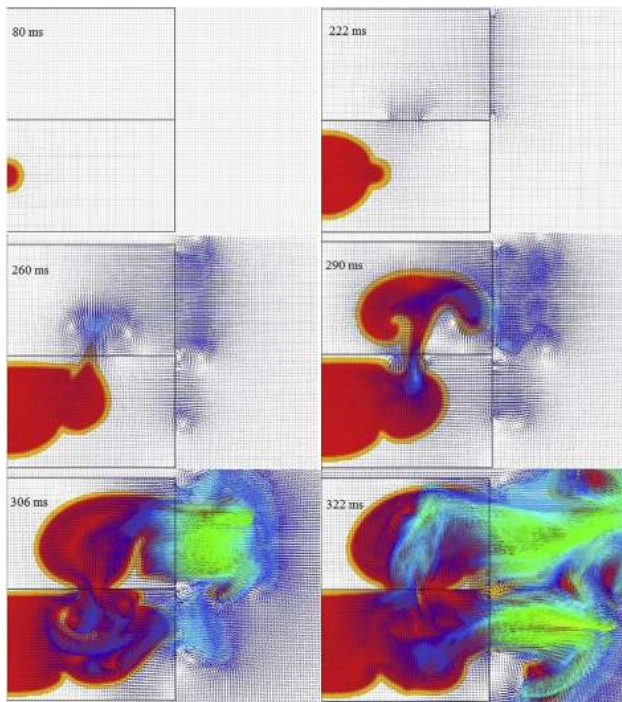
Fig. 14. Simulated flame propagation for a Type C experiment.
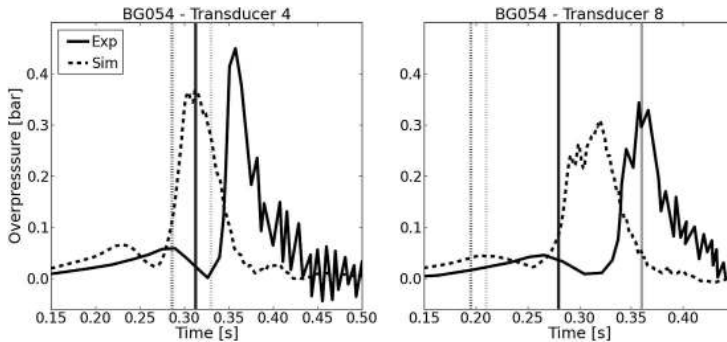
Fig. 15. Half-layer of gas, closed door, rear ignition, left vent panel $K = 8$.
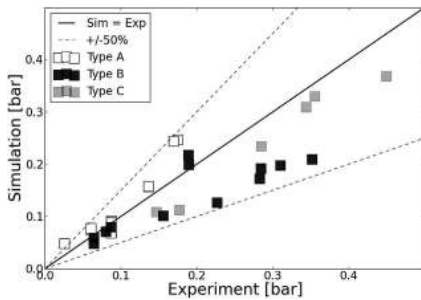
Fig. 16. Maximum overpressure, experiment vs. simulations.
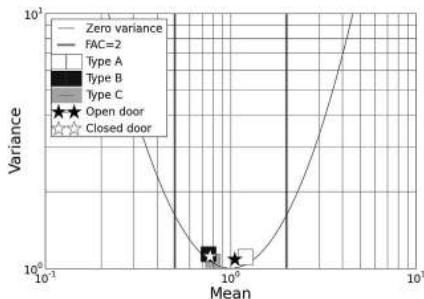
Fig. 17. Geometric mean and variance of ratio of predicted to observed values.

6. Concluding remarks

Some of the results of a series of large-scale experiments carried out in a vented twin-compartment explosion chamber, have been presented along with the results of simulations using the CFD tool FLACS.

Generally, the pressure–time history displayed two pressure peaks. The first pressure peak was always associated with the removal of one or both of the explosion relief vent panels. The second pressure peak was found to be more complex in origin – its magnitude varying with the vent configuration, degree of filling, and sometimes significantly enhanced by the presence of an interconnecting door.

FLACS has mainly been developed for predicting the effects of explosions in congested areas, where the flow's interactions with complex subgrid geometries (represented by porosities) represent the main flame accelerating mechanism. It was a valuable exercise to analyse the performance of the tool in empty enclosures, with complex and subtle interactions between flow and combustion. Validation against experiments is necessary for the further development of subgrid models.

The model persistently overpredicted the rate of explosion development at the very early stages of the explosion, i.e. during the period when the actual flame propagation was mainly in the laminar propagation mode, and this fed through to the earlier timing of subsequent events. The pressure relief panel model used in the FLACS simulations that attempts to model the opening and closing of the interconnecting door is a simplified approach, and will therefore not always give an exact representation when the results are sensitive to the door effects, as was the case for the Type B experiments.

Despite the issues discussed, the numerical code predicts maximum overpressure results within a factor of two over the complete range of experimental configurations, and produces a representative overpressure–time profile for a wide range of configurations, which is acceptable when considering the experimental uncertainties. When evaluated by methods recommended by the *Gas Explosion Model Evaluation Protocol* (MEGGE, 1996) the results show low bias and variance. The results thus suggest that the software can be useful for gaining a greater understanding of the dynamics of explosion development in dwellings.

Acknowledgements

References

Arntzen, B. J. (1998). *Modelling of turbulence and combustion for simulation of gas explosions in complex geometries*. Dr. Ing. Thesis. Trondheim: NTNU.

Astbury, N. F., West, H. W. H., & Hodgkinson, H. R. (1972). *Experimental gas explosions: Report of further tests at Potters Marston.* Special Publication No. 74. The British Ceramic Research Association.

Astbury, N. F., West, H. W. H., Hodgkinson, H. R., Cubbage, P. A., & Clare, R. (1970). *Gas explosions in load bearing brick structures.* Special Publication No. 68. The British Ceramic Research Association.

Bauwens, C. R., Chaffee, J., & Dorofeev, S. (2010). Effect of ignition location, vent size, and obstacles on vented explosion overpressures in propane-air mixtures. *Combustion Science and Technology, 182*(11), 1915–1932.

Butlin, R. N., & Tonkin, P. S. (1974). *Pressures produced by gas explosions in a vented compartment.* Fire Research Note No. 1019. Fire Research Station.

Cooper, M. G., Fairweather, M., & Tite, J. P. (1986). On the mechanisms of pressure generation in vented explosions. *Combustion and Flame, 65*, 1–14.

EN 14994. (June 2007). *Gas explosion venting protective systems.* Brussels: European Standard, CEN.

GexCon AS. (2010). *FLACS v9.1 user's manual.* GexCon AS.

Harrison, A. J., & Eyre, J. A. (1987). External explosions as a result of explosion venting. *Combustion Science and Technology, 52*(1), 91–106.

Health and Safety Executive (HSE). (2011). *Incidents relating to the supply and use of flammable gas* [online]. 2006/07–2010/11. Retrieved from: http://www.hse.gov.uk/statistics/tables/index.htm#gas.

Launder, B. E., & Spalding, D. P. (1974). The numerical computation of turbulent flows. *Computer Methods in Applied Mechanics and Engineering, 3*(2), 269–289.

Model Evaluation Group Gas Explosions (MEGGE). (1996). *Gas explosion model evaluation protocol — Version 1.* Model Evaluation Group Gas Explosions (MEGGE).

NFPA 68. (2007). *Standard on explosion protection by deflagration venting* (2007 Ed.). USA: National Fire Protection Association.

Rasbash, D. J., Palmer, K. N., Rogowski, Z. W., & Ames, S. (1970). *Gas explosions in multiple compartments.* Fire Research Note No. 847. Fire Research Station.

Skippon, S. M. (1985). *Large scale confined explosions in a twin compartment vessel.* Unpublished research. British Gas Research and Development.

Solberg, D. M., Pappas, J. A., & Skramstad, E. (1979). *Gas explosions in confined or partly confined spaces.* Norwegian Maritime Research. No. 4.

Solberg, D. M., Pappas, J. A., & Skramstad, E. (1980). Experimental investigations on flame acceleration and pressure rise phenomena in large scale vented gas explosions. In *Third international symposium on loss prevention and safety promotion in the process industries, 15–19th September 1980, Basel, Switzerland.*

Tam, V. (1998). *Explosion model evaluation.* Fire and Blast Information Group. Article R320, Newsletter Issue No 22.

van Wingerden, C. J. M. (1989). On the venting of large-scale methane–air explosions. In *Sixth international symposium on loss prevention and safety promotion in the process industries, 19th–22nd June 1989, Oslo, Norway.*

van Wingerden, C. J. M., & Zeeuwen, J. P. (1983). Venting of gas explosions in large rooms. In *Fourth international symposium on loss prevention and safety promotion in the process industries, 12–16th September 1983, Harrogate, England.*

Paper 2

Investigation of concentration effects on the flame acceleration in vented channels

Hisken, H., Enstad, G.A., Middha, P. & van Wingerden, K.

CrossMark

Investigation of concentration effects on the flame acceleration in vented channels

H. Hisken [a, b, *], G.A. Enstad [b], P. Middha [c], K. van Wingerden [b]

[a] Department of Physics and Technology, University of Bergen, Allégaten 55, 5007 Bergen, Norway
[b] GexCon AS, Fantoftveien 38, 5072 Bergen, Norway
[c] GexCon UK, Suite 218 BE Business Centre Wembley, 1 Olympic Way, Wembley, HA9 0NP, United Kingdom

ARTICLE INFO

ABSTRACT

Propane—air gas explosion experiments were performed in two vented channels of dimensions 1.5 m × 0.3 m × 0.3 m (lab-scale) and 6 m × 1.2 m × 1.2 m (medium-scale). The pressure—time development and flame speed were recorded. Tests were performed with several obstacle configurations. The equivalence ratio ϕ was varied between 0.7 and 1.7, to study the corresponding effects on the flame acceleration and maximum explosion overpressure. The experimental results were compared to numerical simulations performed with the computational fluid dynamics (CFD) tool FLACS, employing two different burning velocity models: (i) the standard burning velocity model in FLACS, (ii) an alternative burning velocity model that incorporates Markstein number effects. Both models gave acceptable predictions of the experimental maximum overpressures for $\phi < 1.4$. For fuel-rich mixtures, $\phi > 1.4$, the standard burning velocity model in FLACS generally under-predicted the maximum overpressures. The Markstein number-dependent burning velocity model gave improved results, consistently predicting overpressures within $\pm 10\%$ of the experimental values.

© 2015 Elsevier Ltd. All rights reserved.

1. Introduction

In order to predict the consequences of accidental gas explosions in realistic geometries, it is necessary to consider the small-scale interactions between the flame zone and the flow, and how they feed back to the larger scales. The use of computational fluid dynamics (CFD) for explosion consequence analysis in the process industries therefore increases. CFD software computes approximate solutions to a set of partial differential equations describing fluid flow in time and three-dimensional space. However, in order to carry out efficient gas explosion simulations for real process facilities, a range of sub-grid models must be invoked to allow for grid cell sizes of 1—2 m. These cell sizes are generally larger than the flame thickness, and are often larger than important geometry details and the turbulence length scales generated during the explosion. Extensive model validation is necessary to ensure that sub-grid models are appropriate for the applications where they are

used (Skjold et al., 2013).

The majority of large-scale gas explosion experiments found in the literature have been performed using near-stoichiometric fuel—air mixtures, as these often have the highest laminar burning velocity and are assumed to lead to the most severe consequences. These experiments form the validation basis for the sub-grid models in CFD tools. To improve the validity of sub-grid models for more general scenarios, it is crucial to further extend the matrix of gas explosion experiments involving off-stoichiometric mixtures, complementing earlier studies (Wingerden and Zeeuwen, 1983; Hjertager et al., 1988; Skjold et al., 2014; Bauwens et al., 2015).

Bradley et al. (2013) recently proposed a correlation for the turbulent burning velocity in terms of the strain rate Markstein number Ma_{sr}, to account for the response of laminar flamelets to stretch rates in a turbulent flow. Markstein number effects are important also at low turbulence levels, e.g. for spherical flame propagation in the initial phase of gas explosions under initially quiescent conditions (Bradley, 1999; Bradley et al., 2001; Jomaas et al., 2007).

This paper presents results from 42 propane—air gas explosion experiments where the equivalence ratio ϕ of the homogeneous fuel—air mixture was varied between 0.7 and 1.7. The experiments

---

* Corresponding author. GexCon AS, Fantoftveien 38, 5072 Bergen, Norway.
E-mail addresses: helene.hisken@gexcon.com (H. Hisken), gisle.enstad@gexcon.com (G.A. Enstad), prankul@gexcon.com (P. Middha), kees@gexcon.com (K. van Wingerden).

were done primarily to produce additional validation data for numerical models, and to investigate whether a burning velocity model that incorporates Markstein number effects would be beneficial for predicting the consequences of gas explosions in lab-scale and medium-scale rigs with varying obstacle configurations. Overpressures and flame speeds were compared to numerical simulations performed with the CFD tool FLACS (GexCon AS, 2015).

2. The numerical model

The CFD tool FLACS solves the three-dimensional Favre-averaged conservation equations for the densities of mass ρ, momentum ρu_i, enthalpy ρh, turbulent kinetic energy ρk, rate of dissipation of turbulent kinetic energy $\rho \varepsilon$, mass-fraction of fuel ρY_f and mixture-fraction $\rho \xi$ on a structured Cartesian grid. The equations are closed by invoking the ideal gas equation of state and the standard $k-\varepsilon$ model for turbulence (Launder and Spalding, 1974). Boundary layers are not resolved in FLACS, instead wall-functions are used to compute turbulence production and drag forces for objects that are on-grid, i.e. larger than the size of a computational cell (GexCon AS, 2015).

Geometry is represented on the computational grid using the porosity/distributed resistance (PDR) concept (Hjertager, 1986; Bakke, 1986). A volume porosity β_v, denoting the ratio of open volume to the total volume of each computational cell, is computed prior to the simulation and defined at the respective grid cell centre. Similarly, area porosities β_j represents the ratio of the projected open area between two neighbouring cell centres to the total area of the respective control volume face. The general variable Φ (representing either ρ, ρu_i, ρh, ρk, $\rho \varepsilon$, ρY_f or $\rho \xi$) is thus integrated over the porous part of the control volume, and the flux terms in the conservation equation for Φ are weighted with the area porosity β_j:

$$\frac{\partial}{\partial t}\left(\beta_v \rho \Phi\right) + \frac{\partial}{\partial x_j}\left(\beta_j \rho u_i \Phi\right) - \frac{\partial}{\partial x_j}\left(\beta_j \rho \Gamma_\Phi \frac{\partial}{\partial x_j}\Phi\right) = \beta_v(S_\Phi - R_\Phi),$$
(1)

where Γ_Φ is the effective turbulent exchange coefficient; S_Φ is the source term for Φ; and R_Φ represents additional resistance, additional mixing, and/or additional heat transfer caused by solid obstructions in the flow. The $k-\varepsilon$ model is extended to have a source term for the turbulence generation due to sub-grid obstructions.

To model premixed combustion, FLACS applies the flamelet concept with one-step reaction kinetics. Empirical burning velocity expressions that depend on the local mixture reactivity, pressure, temperature and flow conditions are used to model the reaction rate. The reaction rate is coupled with the source term in the equation for ρY_f using a modified version of the eddy dissipation model of Magnussen and Hjertager (Magnussen and Hjertager, 1977; Arntzen, 1998). The flame zone, defined by the gradient of Y_f, is numerically thickened to cover approximately three control volumes.

2.1. Burning velocity correlations in standard FLACS

The laminar burning velocity u_ℓ used in FLACS is based on literature values. An empirical model for the quasi-laminar burning velocity $u_{q\ell}$ controls the phase of cellular flame propagation, accounting for flame acceleration due to hydrodynamic instabilities (Darrieus, 1945; Landau, 1944) and thermo-diffusive effects (Barenblatt et al., 1962; Sivashinsky, 1977):

$$u_{q\ell} = u_\ell\left(1 + C_{q\ell}\sqrt{R_f}\right),$$

where $C_{q\ell}$ is an empirical constant defined for each fuel and R_f is the flame radius. The turbulent burning velocity u_t is based on the expression by Bray (1990), correlating the 1650 experiments presented by Abdel-Gayed et al. (1987) according to

$$u_t = 0.875 u' K^{-0.392},$$
(2)

with the Karlovitz stretch factor $K = 0.157(u'/u_\ell)^2 R_l^{-0.5}$. Here, R_l is the turbulent Reynolds number based on the integral length scale l, and u' is the root mean square (rms) turbulence velocity. The correlation for u_t is valid for mixtures with Lewis numbers $Le \leq 1.3$ (Bray, 1990). Equation (2) in the form used in FLACS takes mixture reactivity into account only through u_ℓ.

2.2. A Markstein number-dependent burning velocity model

The Markstein number Ma quantifies the effect of flame stretch on the localized burning velocity (Markstein, 1951), and generally depends on the mixture composition, pressure and temperature (Bradley et al., 1998a; Bechtold and Matalon, 2001). The stretched laminar burning velocity u_n can be expressed in terms of the unstretched laminar burning velocity u_ℓ, the laminar Karlovitz stretch factor accounting for flow strain $K_{\ell s}$ and flame curvature $K_{\ell c}$, together with the corresponding Markstein numbers Ma_{sr} and Ma_c (Clavin, 1985; Bradley et al., 1996) as

$$\frac{u_\ell - u_n}{u_\ell} = K_{\ell s} Ma_{sr} + K_{\ell c} Ma_c.$$
(3)

It follows from Equation (3) that mixtures with low Ma have an increased effective laminar burning velocity when exposed to positive stretch rates, compared to mixtures with higher Ma. Davis et al. (2002) computed Markstein numbers relative to the burnt gases in counterflow propane–air flames ranging from 3.56 for $\phi = 0.63$ to −0.46 for $\phi = 1.50$.

The cellular pattern and corresponding flame acceleration appearing at a critical flame radius R_0 in a spherically expanding gas explosion will depend on the value of Ma (Bradley, 1999; Bradley et al., 2001). Assuming that the cellular flame surface follows a fractal pattern, the flame radius R_F for a freely propagating spherical flame as a function of time can be expressed as

$$R_F = R_0 + At^b,$$

where A is a mixture specific constant and the time exponent b is related to the fractal dimension D of the flame surface by $D = (3b - 1)/b$ (Gostintsev et al., 1988; Bauwens et al., 2015). Bauwens et al. (2015) combined new experimental findings with fractal considerations, and expressed the increase in flame velocity due to cell formation on the flame surface as

$$\frac{u_{q\ell}}{u_\ell} = \left(\frac{R_F}{R_0}\right)^\zeta.$$
(4)

The value for ζ in Equation (4) is derived from experimental observations.

Furthermore, the Markstein number affects how the burning rate of flamelets in turbulent premixed combustion responds to the flame stretch rate. In particular, the flamelets in mixtures with negative Ma appear to have significantly higher burning rates compared to mixtures with positive Ma, and are less likely to quench at high strain rates (Bradley et al., 2005). Bradley et al. (2013) expressed the turbulent burning velocity u_t in terms of an

effective rms turbulence velocity u'_k and the Karlovitz stretch factor $K = 0.25(u'/u_\ell)^2 R_\ell^{-0.5}$:

$$\frac{u_t}{u'_k} = \alpha K^\beta, \text{ for } K > 0.05. \tag{5}$$

Equation (5) contains the empirical parameters α and β which are explicitly expressed in terms of the strain rate Markstein number Ma_{sr}. u'_k accounts for effects at the early stages of flame propagation, and tends towards the initially measured u' as the flame propagates (Bradley et al., 2011). The form of Equation (2) is similar to that of Equation (5), identifying u' and the strain rate as governing parameters for turbulent premixed combustion. However, correlations in terms of Ma_{sr} have been found to give improved agreement with computed values and experimental measurements of u_t for a range of mixtures (Bradley et al., 2005). An important consequence of using Equation (5) rather than Equation (2) to predict u_t is that the dependency of the turbulent burning velocity on the turbulence variables u' and l changes with different values of Ma_{sr}.

As part of this study, an alternative burning velocity model based on Equation (4) and Equation (5) were implemented in FLACS. Updated values for Ma_{sr} (Bradley et al., 1998b) and laminar burning velocities u_ℓ (Law et al., 1988) were used.

3. Experimental setup

The experimental setup comprised a homogeneous, initially quiescent propane—air mixture contained within a square channel of dimensions 1.5 m × 0.3 m × 0.3 m (lab-scale) and 6 m × 1.2 m × 1.2 m (medium-scale). Table 1 gives an overview of the investigated configurations. All lab-scale tests were repeated twice, while only a selection of medium-scale tests were repeated.

The mixture was ignited by a low-energy electric spark at the centre of the closed end of the channel. The open end was covered by a light plastic sheet to contain the flammable mixture. Obstructions were included primarily to produce additional turbulence, so that explosion overpressures and flame speeds at various turbulence levels could be studied. Pressure transducers (2, 4 or 8 depending on the test) were mounted internally and recorded the overpressure—time development with a sampling rate of 40 kHz, while high-speed cameras recorded the flame propagation.

Fig. 1 shows the two configurations used in the lab-scale experiments: an empty channel (Setup 1) and five rectangular obstructions of size 0.023 m × 0.30 m × 0.042 m inserted (Setup 2). The lab-scale rig was fitted with a 1 m long and 0.4 m wide plate outside the vent opening, to reproduce ground effects. One side wall of the rig was transparent to allow for video recordings of the flame propagation. A Phantom v210 high-speed camera recording 5000 frames per second (fps) was used to record the lab-scale tests. The plastic sheet burst at a low pressure and was subsequently

removed by the explosion.

Fig. 2 gives an overview of the medium-scale setup. The medium-scale tests included corresponding geometrical configurations to those in the lab-scale tests, scaled up by a factor of 4. In addition to Setup 1 and 2, a third configuration with circular cylindrical obstructions with diameters of 20 mm, arranged in 4 grids of 6 obstructions per grid was used (Setup 3). The medium scale-rig was situated at ground level, and the roof had transparent sections to allow for video recordings of the flame propagation. A Casio Exilim Pro EX-F1, recording 600 fps, was used. For the medium-scale tests, the plastic sheet was released automatically at ignition.

4. Experimental results

The pressure—time curves were filtered using a Savitzky—Golay filter (Savitzky and Golay, 1964), neglecting oscillations with frequencies higher than 1 kHz. As all the internal transducers recorded similar pressure—time histories, only one representative curve is presented for each experiment. The representative pressure—time trace was recorded at the closed end of the channel, since there was a transducer present there in all tests.

In the following, the flame speed is presented as a function of the distance from the ignition point to the flame front. The flame speed was determined from video analysis, whenever a recording was available. The development of the flame front position in time in the lab-scale tests was analysed with a LabVIEW script (National Instruments, 2013).

Due to limited optical access to the rig, a detailed video analysis was not feasible for the medium-scale tests. To get an indication of the flame speed, data points were obtained by manually noting the flame position in each video frame.

4.1. Lab-scale tests

Fig. 3 shows representative pressure—time traces and corresponding flame speed curves from two repeated lab-scale experiments with Setup 2, $\phi = 1.40$.

The first pressure peak (P1) in Fig. 3 is associated with the plastic sheet yielding. For Setup 2, the sheet consistently broke at 0.025 ± 0.005 bar. The subsequent removal process of the sheet varied somewhat, and most likely influenced the turbulence level close to the vent opening. This was later confirmed by additional tests performed with and without an automatic release system. Without automatic release of the plastic sheet at ignition, the magnitude of the oscillations were enhanced by a factor of 2 in average.

The second pressure peak (P2) consistently resulted in the highest overpressure for all lab-scale tests with Setup 2, and was always due to flame acceleration in the shear layers and wakes downstream of the obstacles. The second pressure peak and the flame speed up to 1 m from ignition were reproduced within ±5% in repeated tests. The flame speed displayed a higher variability (±25%) in the final 0.5 m of the channel, most likely due to the remaining fragments of the plastic sheet creating various degrees of additional turbulence and blockage to the outflow. This variability was also reflected in the third pressure peak (P3) in Fig. 3, due to the external explosion, and the subsequent Helmholtz oscillations.

Fig. 4 shows selected video frames from a test with $\phi = 1.40$, corresponding to the pressure—time and flame speed curves in Fig. 3. A cellular structure has developed on the flame surface before the flame folds around the first set of obstructions. The plastic sheet yields at 72 ms, as the flame reaches the second set of obstructions. Turbulent shear layers and unsteady wakes are generated as unreacted mixture is accelerated past the obstacles. Upon flame arrival, the turbulence structures and unsteadiness of

Table 1
Test conditions.

| Geometry	Description	Equivalence ratio ϕ	
		Lab-scale	Medium-scale
Setup 1	Empty	1.05, 1.26, 1.39, 1.52, 1.66	1.0, 1.1, 1.3
Setup 2	5 rectangular obstructions	0.74, 0.87, 0.89, 1.00, 1.07, 1.12, 1.23, 1.26, 1.40, 1.52	1.1, 1.3, 1.7
Setup 3	4 × 6 cylindrical obstructions		0.8, 0.9, 1.0, 1.1, 1.2, 1.3, 1.4, 1.5
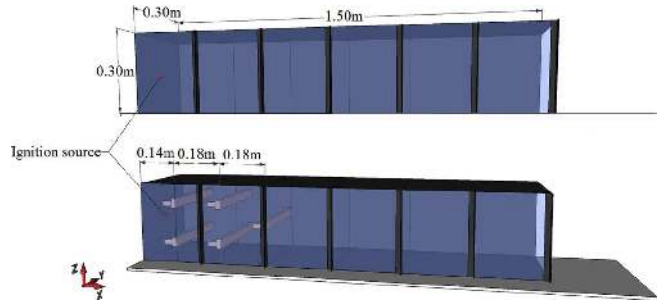
**Fig. 1.** Lab-scale Setup 1 (top) and Setup 2 (bottom).
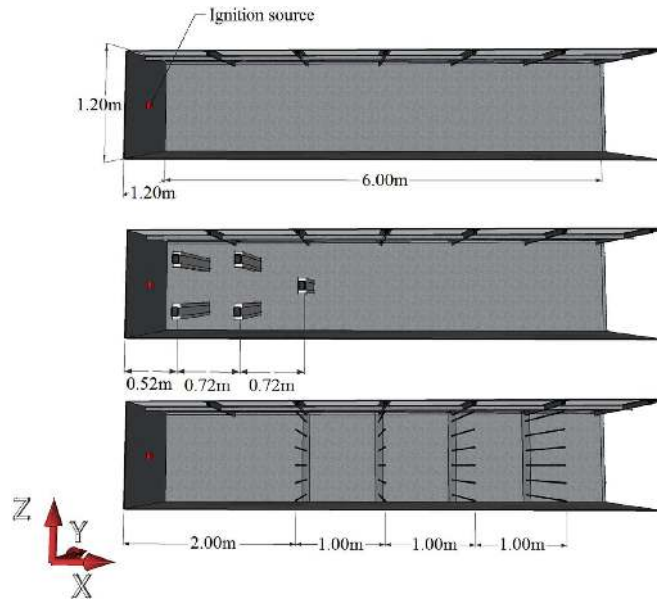
Fig. 2. Medium-scale Setup 1 (top), Setup 2 (middle) and Setup 3 (bottom).
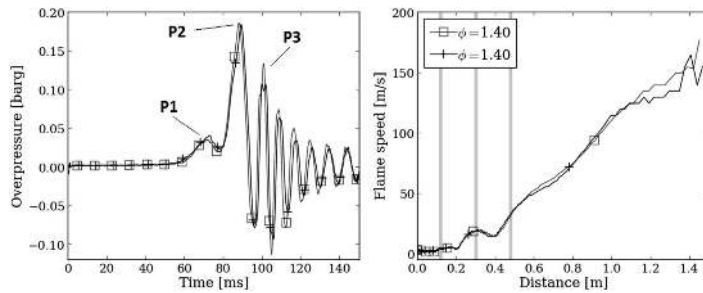

Fig. 3. Pressure–time (left) and flame speed (right) curves from lab-scale tests with Setup 2. Grey vertical lines signify obstacle locations.
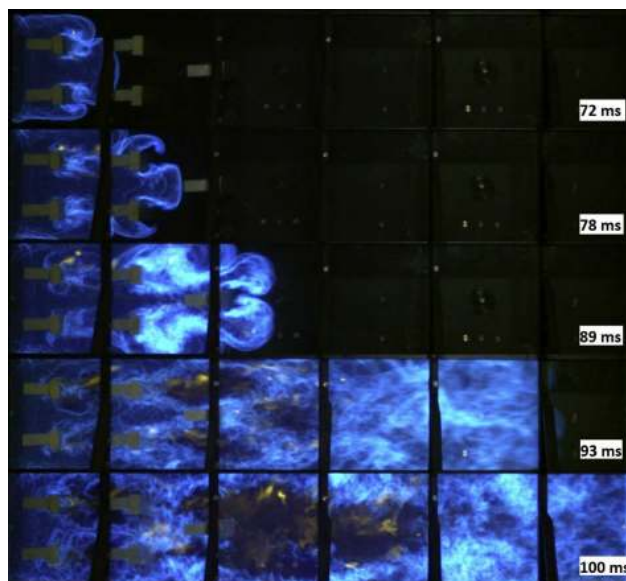
Fig. 4. Explosion test in the lab scale rig, $\phi = 1.40$, Setup 2.

the flow enhance the flame area and the burning rate. Luminosity is higher in the regions where intense flame wrinkling and burning take place. The flame accelerates some distance downstream of each of the three positions where obstructions are located (marked with grey vertical lines in Fig. 3) producing the second pressure peak at 89 ms. When the flame front has propagated approximately 1.1 m from ignition, dark patches appear in the areas downstream of the obstacles where intense combustion previously was observed, indicating that the flame has reached the channel walls in those regions. Combustion in the middle section of the channel is therefore partly finished when the flame front reaches the vent opening at 96 ms. A series of Helmholtz oscillations with a frequency of 120 Hz is initiated, and the channel alternates between an under-vented and over-vented state. Reactants will have been pushed out of the vent opening during the internal explosion, forming a turbulent combustible cloud outside the rig.

The external explosion generates P3 in Fig. 3 at 100 ms, and appears to be in phase with the Helmholtz oscillations. The luminosity of the cellular-like flame wrinkles in the innermost part of the channel increase at the time of arrival of the pressure peaks. The Helmholtz oscillations might be further enhanced by the Rayleigh–Taylor instability increasing the flame area by producing additional wrinkles when the burnt products pushes towards the denser reactants (Solberg et al., 1981; Cooper et al., 1986; Bauwens et al., 2008, 2010). However, due to the high aspect ratio of the rig and the ignition position at the closed end, a significant part of the reactants inside the channel are burnt before the exit of the flame. Flame acceleration through the wakes downstream of the obstructions is the dominant pressure-generating mechanism for Setup 2.

Fig. 5 shows the pressure–time and flame speed curves for selected lab-scale tests with $\phi = 1.00$, $\phi = 1.23$ and $\phi = 1.52$ for Setup 2. The same pressure-generating mechanisms as for $\phi = 1.40$ produce the pressure peaks P1, P2, P3 and subsequent Helmholtz oscillations. However, for $\phi = 1.52$, the flame decelerates significantly before exiting the channel, leading to under-pressure even before the venting of combustion products starts. For the slow burning velocities in fuel-rich mixtures, heat loss to the walls might play a more significant role than for the leaner mixtures with a higher reactivity (Skjold et al., 2014). The flame accelerates again as it propagates through the turbulent flow at the vent opening.

For the empty rig tests (Setup 1), pressures of 0.010–0.030 bar and flame speeds of 10–50 m/s were obtained. For the Setup 1 test series, the plastic sheet consistently yielded at 0.010 ± 0.005 bar. At the low turbulence levels in the empty rig, the breaking process of the vent panel becomes important for the pressure–time behaviour, leading to a higher variability of $\pm 30\%$ in maximum overpressures and average flame speeds between repeated tests. The most significant variations in flame speeds were seen as oscillations in the last 0.5 m of the channel. Fig. 6 shows pressure–time and flame speed curves for selected equivalence ratios.

For $\phi = 1.05$ and $\phi = 1.39$, the first two pressure peaks in Fig. 6 are associated with the vent panel yielding, first partly, then fully. The third pressure peak is a result of flame acceleration due to the development of a cellular flame, generation of vorticity in the boundary layers along the walls, and the corresponding increase in flame surface area. The external explosion generates a pressure peak at 120 ms for $\phi = 1.05$ and at 135 ms for $\phi = 1.39$. There is less combustion inside of the channel after the flame has reached the vent opening than for Setup 2, as the slower flame speed and more homogeneous flow conditions allow the flame to propagate out to the walls before external combustion commences. For $\phi = 1.39$, the
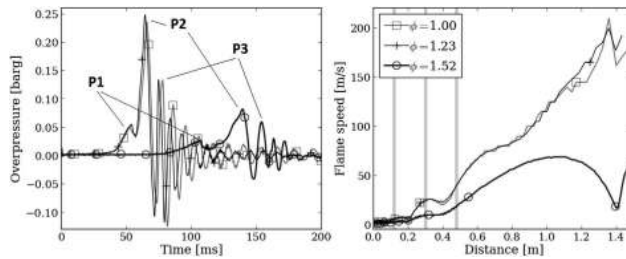
Fig. 5. Pressure–time curves (left) and flame speeds (right) from the lab-scale test programme, Setup 2, with increasing ϕ. Grey vertical lines signify obstacle locations.
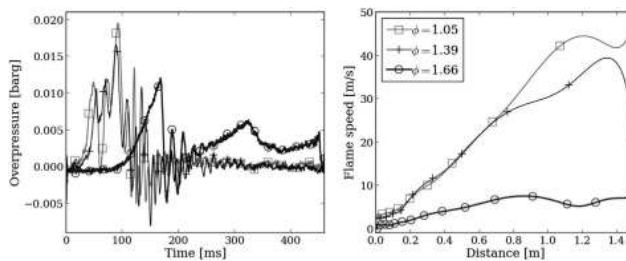

Fig. 6. Pressure–time curves (left) and flame speeds (right) from the lab-scale test programme, Setup 1.

flame surface visibly transitions to the cellular regime at approximately 0.2 m; this is associated with the flame front accelerating from 0.15 m to 0.3 m. The cellular structures appears later for $\phi = 1.05$, at approximately 0.5 m from ignition.

For the test with $\phi = 1.66$, flame propagation is slow throughout the explosion. Combustion closer to the roof is promoted due to buoyancy effects, producing an asymmetrical flame profile. The pressure peak at 170 ms is associated with the initial breaking of the plastic sheet, and subsequent pressure oscillations are insignificant in comparison. The flame reaches the vent opening at 450 ms.

4.2. Medium-scale tests

Fig. 7 shows the pressure–time curves from two medium-scale configurations, empty channel (Setup 1) and with five rectangular obstructions inserted (Setup 2). The maximum overpressures in the medium-scale experiments were reproduced within ±10% in repeated tests. As the medium-scale rig included an automatic system that released the plastic sheet at ignition, the yielding of the panel did not produce a pressure peak. Video recordings and consequently flame speed measurements were not available for Setup 1 and 2. Fig. 7 shows that the maximum overpressure generated in the fuel-rich tests ($\phi = 1.3$) were of comparable magnitude to that observed for the near-stoichiometric mixtures ($\phi = 1.1$). The pressure oscillations following the main pressure
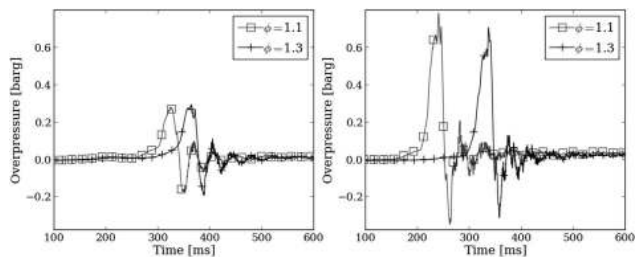
Fig. 7. Selected pressure–time curves, Setup 1 (left) and Setup 2 (right), medium-scale.
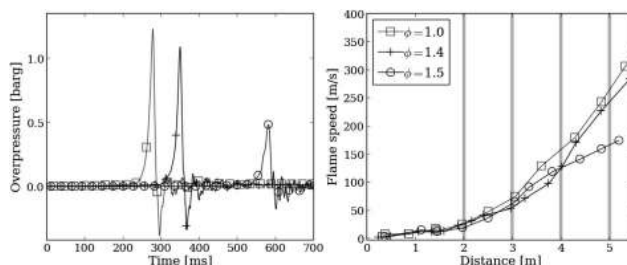
Fig. 8. Representative pressure−time curves (left) and flame speeds (right) from the medium-scale tests with Setup 3. Grey lines signify obstacle locations.

peak appears to have been insensitive to the mixture concentration.

Fig. 8 shows the pressure−time traces and corresponding flame speeds of representative tests using Setup 3 with $\phi = 1.0$, $\phi = 1.4$ and $\phi = 1.5$. The grey vertical lines in Fig. 8 (right) mark the position of the obstacle grids relative to the ignition point. The dominating pressure peak in all the tests shown in Fig. 8 are associated with the flame acceleration through the last 3 m of the channel combined with the external explosion. The obstacles in Setup 3 were located towards the open end of the channel, promoting continuous rapid flame acceleration starting from 2 m from ignition, and creating a highly turbulent gas cloud outside the vent opening.

The average amplitude of the Helmholtz oscillations in the medium-scale tests were consistently smaller relative to the dominating pressure peak than in the lab-scale experiments. As the plastic sheet was released at ignition, it played a less significant role. The presence of a larger ground area outside the vent opening in the medium scale configuration may have contributed to a more effective dampening of the Helmholtz oscillations.

Although less information is available for the medium-scale experiments compared to the lab-scale experiments, the relatively large scale and the reproducibility of the maximum overpressures make the tests highly relevant for model validation.

5. Numerical results

All experiments in Table 1 were simulated with a development version of FLACS v10.3r2. Two different combustion models were investigated: (i) the standard FLACS burning velocity model, denoted SBV in the following and (ii) a Markstein number-dependent burning velocity model, denoted MBV.

5.1. Lab-scale tests

The lab-scale tests were simulated using a uniform computational grid size of 0.05, 0.03 and 0.015 m, to investigate how the results depend on the grid resolution. A vent panel was specified at the open end of the channel with an opening pressure of 0.010 bar and 0.025 bar for Setup 1 and 2, respectively. A submodel accounting for heat loss to the channel walls was activated (Skjold et al., 2014; GexCon AS, 2015). Applying a grid size of less than 0.02 m is not recommended in standard FLACS due to the particular settings in the sub-grid models for turbulence and combustion (GexCon AS, 2015). In the Markstein number-dependent burning velocity model (MBV), a correction was implemented in the flame model, enhancing the thickness of the flame numerically, so that a grid size of 0.015 m could be used. Overall, the maximum overpressure varied with less than 30% with each mesh refinement. Fig. 9 shows representative results for FLACS using MBV.

The 0.05 m grid consistently gave the highest overpressures and flame speeds for both SBV and MBV. Some grid dependency of results is expected, as the resolution of flow structures and the flame surface changes with the grid resolution. Moreover, the sub-grid models for turbulence and combustion are optimized to represent a certain range of grid cell sizes and spatial scales that are typically larger (0.1−1 m) than those used in the lab-scale simulations. In particular, flame propagation in the initial phase depends on the grid, due to the ignition model for the numerically thickened flame. This grid dependency can be seen as a difference in the time of arrival of the first pressure peak in Fig. 9. However, it should be noted that the arrival time is not considered to be the most important model validation variable for FLACS, as it is the peak height and dynamics that determines any structural response to the
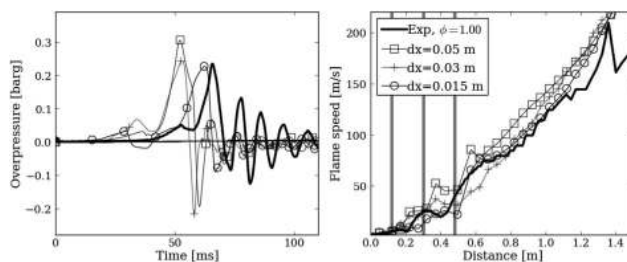

Fig. 9. Simulated pressure−time curves (left) and flame speeds (right) for a lab-scale test with Setup 2, using FLACS with MBV.

explosion.

Numerical and experimental pressure–time curves and flame speeds are plotted in Figs. 10 and 11 for Setup 1 and 2, respectively, using a grid cell size of 0.03 m. Black curves are the experimental results, grey curves are simulated with the standard combustion model SBV, dashed curves with the new combustion model MBV. The simulated first pressure peak for all tests with both Setup 1 and 2 is produced by the vent panel yielding, as in the experiments. However, Figs. 10 and 11 show that the ignition model over-predicts the flame speed in the initial phase for both combustion models, so that the panel consistently yields earlier in the simulations compared to the experiments.

For $\phi = 1.05$ with Setup 1, the burning velocity is over-predicted with SBV throughout the channel. The burning velocity predicted by MBV is more representative, but over-predicts in the initial phase and after the flame has propagated 1.0 m from ignition.

Results obtained for empty, small-scale enclosures, are particularly sensitive to the settings of the wall functions that model the turbulence production in the boundary layers along the channel walls. Fig. 10 shows that the numerical flame speeds for both SBV and MBV decrease around 0.6 m from ignition before the flame front accelerates again. This is likely caused by the modelled turbulence production along the walls starting to grow at this point. For both SBV and MBV the simulated pressure peak giving the maximum overpressure for $\phi = 1.05$ is due to the continuous flame acceleration through the last 0.75 m of the channel. This is also true for MBV when $\phi = 1.39$. The breaking of the vent panel gives a slightly higher pressure peak when using SBV for $\phi = 1.39$. For $\phi = 1.66$, the yielding of the vent panel gives the maximum overpressures for both combustion models. FLACS using MBV reproduces the experimental pressure peak at 300 ms, however, it is associated with flame acceleration through the last 0.75 m of the channel where the
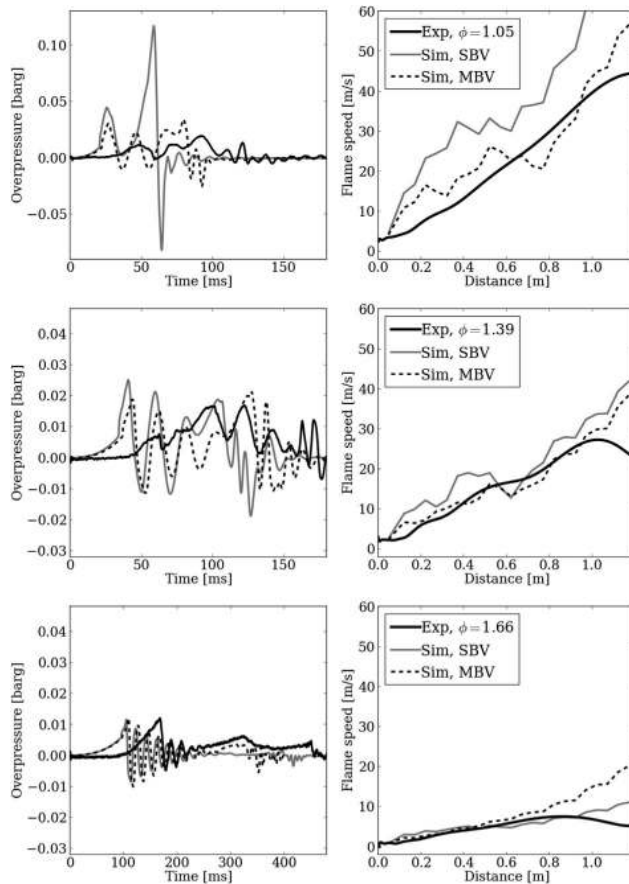

Fig. 10. Selected experimental and numerical pressure–time curves (left) and flame speeds (right), Setup 1, lab-scale.
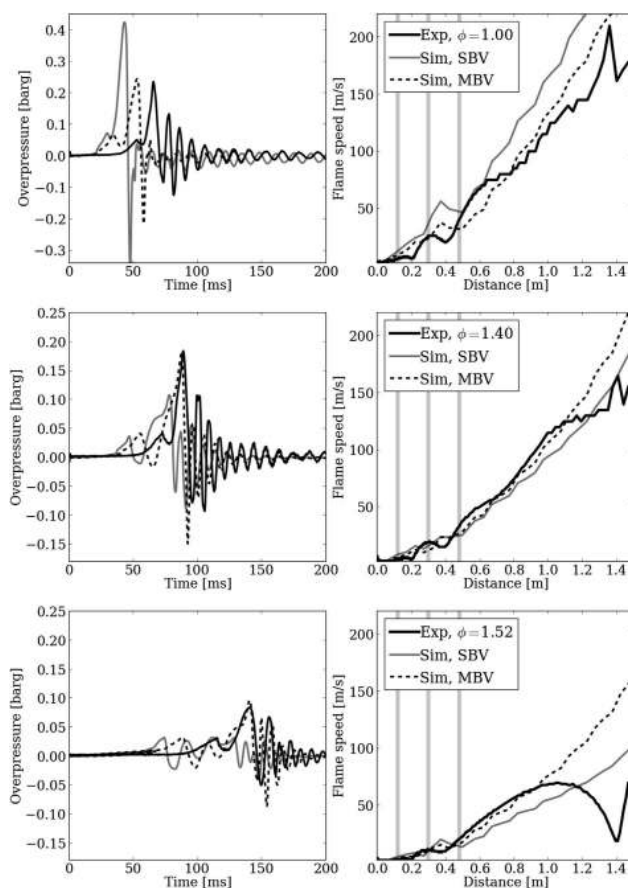
Fig. 11. Selected experimental and numerical pressure—time curves (left) and flame speeds (right), Setup 2, lab-scale. Grey vertical lines signify obstacle locations.

flame speed is over-predicted.

The flame speeds close to the vent opening seems to be consistently higher in the simulations than in the experiments. The combined effect of heat loss, boundary layer effects and the breaking of the plastic sheet is challenging to model exactly. However, except from SBV with $\phi = 1.05$, both models produce pressures peaks within the experimental uncertainty.

The pressure peaks resulting in the maximum overpressure for all the tests presented in Fig. 11 occur as the flame propagates through the wakes and turbulent shear layers downstream of the obstructions, as in the experiments. After the external explosion is initiated in the simulations, pressure builds up within the channel again, producing a second pressure peak of approximately 0.050 bar. The pressure oscillations following the second pressure peak are generally less distinct than in the experiments. This may

be partly explained by the effects of the plastic sheet breaking in a non-uniform manner in the experiments; as this process cannot be represented exactly in the simulations. It is possible that the oscillations observed in the experiments are further enhanced by the continuous combustion inside the explosion chamber. Due to the limited resolution of the flame surface and flow structures, combustion is more effectively distributed in the simulations. Internal combustion of reactants is therefore more or less completed at the onset of the external explosion.

For the tests with Setup 2 and $\phi = 1.40$ and $\phi = 1.52$, Fig. 11 shows that the simulated overpressures are under-predicted by FLACS using SBV. This is consistent with the earlier observations by Skjold et al. (2014). The burning velocity predicted by MBV has a higher dependency on the rms turbulence velocity u' for the negative Ma_{sr} of fuel-rich propane—air mixtures, relative to the

near-stoichiometric mixtures with positive Ma_{sr}. This changes the timing of events and produces more representative overpressures for the fuel-rich explosions than with standard FLACS, in particular for $\phi > 1.4$. Furthermore, the ϕ-dependent formulation of the quasi-laminar burning velocity u_{ql} in MBV introduces Markstein number effects on the regime of cellular flame propagation in the absence of significant turbulence production.

5.2. Medium-scale tests

The medium-scale tests were simulated using three different grid resolutions: 0.20, 0.12 and 0.06 m. Overall, the maximum overpressure varied with less than 30% with each refinement. The highest overpressures and flame speeds were consistently obtained using a grid resolution of 0.20 m.

Fig. 12 shows numerical and experimental pressure–time curves and flame speeds for Setup 1, using a uniform grid cell size of 0.12 m. The simulated maximum overpressures for Setup 1 are produced by continuous flame acceleration through the channel; the peak occurs as the venting of hot combustion products starts. Simulations with Setup 2 are shown in Fig. 13. The same pressure generating mechanism as in the corresponding simulated lab-scale tests, i.e. flame propagation through the turbulent wakes due to the obstructions, produces the main pressure peak. The time of arrival of the pressure peaks for both Setup 1 and 2 is

under-predicted by both models, however, FLACS using MBV gives improved results.

Fig. 14 shows the results for Setup 3. The simulated dominating pressure peaks predicted by FLACS using both SBV and MBV are generated by the continuous flame acceleration due to the presence of obstructions, in combination with the external explosion, as observed in the experiments. The flame acceleration due to obstructions can clearly be seen as a rapid increase in flame speed after each of the grey lines in Fig. 14. It is not possible to conclude whether a correspondingly rapid acceleration occurred in the experiments, due to the limited number of flame speed measurements. For both combustion models, the simulated flow reverses after the main pressure peak, and creates a second pressure peak and subsequent oscillations that are very similar to those observed in the experiments. The time of arrival of the pressure peak is consistently under-predicted by FLACS using SBV. FLACS using MBV under-predicts the time of arrival somewhat for $\phi = 1.0$ and $\phi = 1.4$, and over-predicts somewhat for $\phi = 1.5$. The differences in timing of events between SBV and MBV are most likely explained by the varying dependency of MBV on the modelled turbulence variables for different ϕ. The explosion events predicted by FLACS using MBV generally are more closely linked to the particular build-up of the rms turbulence velocity u' than for FLACS using SBV.

Overall, the modelled flame speed and overpressures using both combustion models match the experimental values well. However,
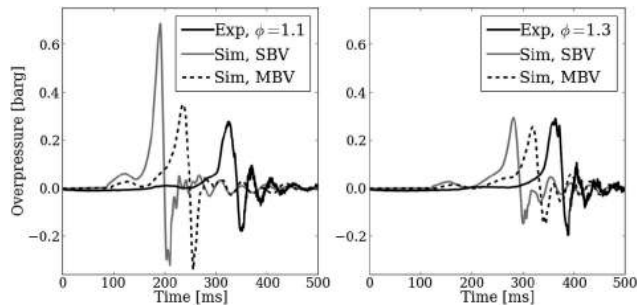

**Fig. 12.** Selected experimental and numerical pressure–time curves, Setup 1, medium-scale.
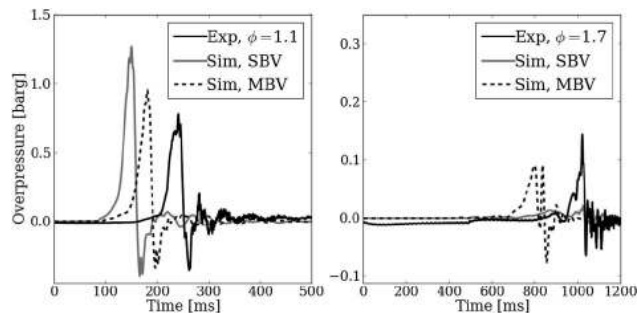
Fig. 13. Selected experimental and numerical pressure–time curves, Setup 2, medium-scale.
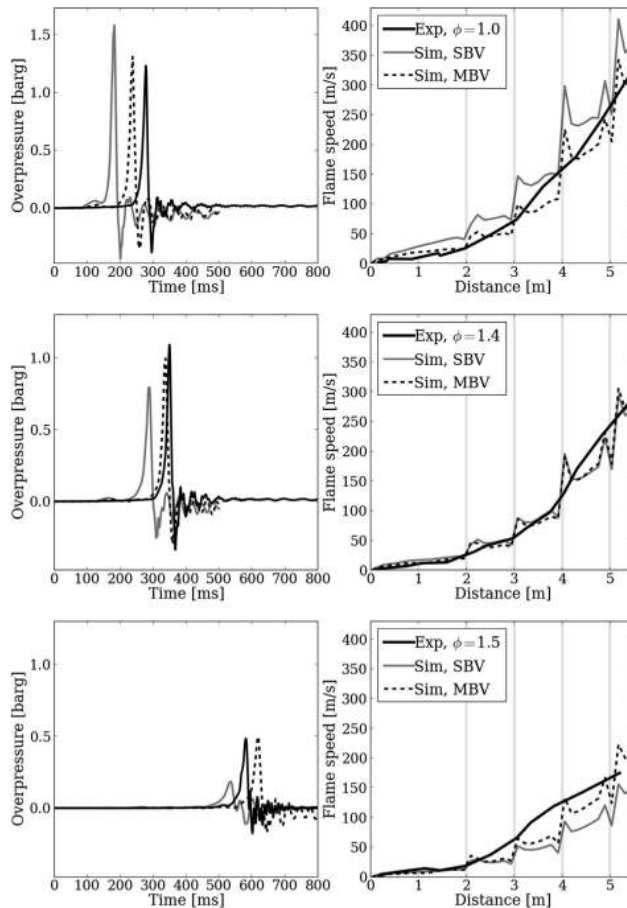
Fig. 14. Selected experimental and numerical pressure–time curves (left) and flame speeds (right), Setup 3, medium-scale. Grey vertical lines signify obstacle locations.

the pressure peaks for the fuel-rich mixtures, $\phi = 1.4$ and $\phi = 1.5$, are under-predicted compared to that of $\phi = 1.0$. Results for fuel-rich mixtures improve when a burning velocity model that incorporates Markstein number effects is applied.

5.3. Summary of model performance

The model evaluation protocol by Model Evaluation Group Gas Explosions (MEGGE, 1996) suggests using parameters such as the geometric mean bias (MG), quantifying systematic bias, and the corresponding geometric mean variance (VG) defined as

$$\text{MG} = \exp\left[\frac{1}{n}\sum_{i=1}^{n}\ln\left(\frac{x_p}{x_o}\right)\right], \quad \text{VG} = \exp\left[\frac{1}{n}\sum_{i=1}^{n}\ln\left(\frac{x_p}{x_o}\right)^2\right] \quad (6)$$

to measure model performance. Here, x_p is the predicted (simulated) variable and x_o is the observed (experimental) variable. Fig. 15 shows MG and VG for the maximum overpressures obtained in all the tests of the present study, together with a scatter plot of the same data. Experimental results are compared with simulation results using the intermediate grid resolution of 0.03 m (lab-scale) and 0.12 m (medium-scale), for FLACS using both SBV and MBV.

The maximum overpressures for $\phi < 1.4$ are somewhat conservative for FLACS using SBV, with a mean bias with respect to the
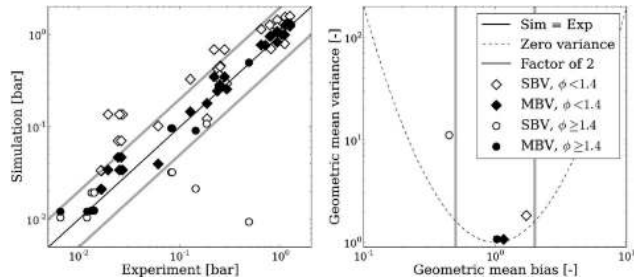
Fig. 15. Scatter plot (right) and parabola plot (left) of the maximum overpressure obtained in all tests of the programme.

experimental values of 1.7 ± 0.1, while the results for FLACS using MBV are very accurate, producing a mean bias of 1.2 ± 0.1. Maximum overpressures for mixtures with negative Ma_{sr} (corresponding to $\phi > 1.4$) obtained with standard FLACS are underpredicted, with a mean bias of 0.4 ± 0.1, while a model that incorporates Markstein number effects gives improved agreement with a geometric mean bias of 1.0 ± 0.1.

6. Conclusions

A series of lab-scale and medium-scale gas explosion experiments involving propane–air mixtures with equivalence ratios ϕ ranging between 0.7 and 1.7 performed in two vented channels have been presented. Three obstruction layouts were used to produce different turbulent flow regimes. Numerical simulations using two different sub-grid models for premixed combustion in the CFD tool FLACS were compared to the experimental results: (i) the burning velocity model used in standard FLACS (SBV), (ii) an alternative burning velocity model that incorporates Markstein number effects (MBV) based on recent findings (Bauwens et al., 2015; Bradley et al., 2013).

It was found that the experimental maximum overpressures for $\phi < 1.4$ were reproduced well by both models, with somewhat conservative results for standard FLACS. For fuel-rich propane–air mixtures with $\phi > 1.4$, standard FLACS under-predicted the maximum overpressures by more than a factor of 2. The findings were consistent with earlier studies (Skjold et al., 2014). Meanwhile, the Markstein number-dependent model reproduced the experimental overpressures with a geometric mean bias of 1.0 ± 0.1. The results show that a sub-grid model taking into account Markstein number effects improves the CFD simulation results for fuel-rich propane–air explosions. However, further validation including a wider range of scenarios is needed before concluding on the modelling of propane–air mixtures with $\phi < 1.4$.

Acknowledgements

References

Abdel-Gayed, R., Bradley, D., Lawes, M., 1987. Turbulent burning velocities: a general correlation in terms of straining rates, proceedings of the Royal Society of London. Ser. A Math. Phys. Sci. 414 (1847), 389–413.

Arntzen, B., 1998. Modelling of Turbulence and Combustion for Simulation of Gas Explosions in Complex Geometries (Ph.D. thesis). Department of Energy and Process Engineering, Norwegian University of Science and Technology, Norway.

Bakke, J.R., 1986. Numerical Simulation of Gas Explosions in Two-dimensional Geometries (Ph.D. thesis). University of Bergen and Christian Michelsen Institute, Research and Technology, Norway.

Barenblatt, G.I., Zel'dovich, Ya. B., Istratov, A.G., 1962. On the diffusive-thermal stability of a laminar flame. J. Appl. Mech. Tech. Phys. 4, 21–26.

Bauwens, C., Chaffee, J., Dorofeev, S., 2008. Experimental and numerical study of methane-air deflagrations in a vented enclosure. In: Fire Safety Science - Proceedings of the Ninth International Symposium, pp. 1043–1054.

Bauwens, C., Chaffee, J., Dorofeev, S., 2010. Effect of ignition location, vent size, and obstacles on vented explosion overpressures in propane-air mixtures. Combust. Sci. Technol. 182 (11–12), 1915–1932.

Bauwens, C.R., Bergthorson, J.M., Dorofeev, S.B., 2015. Experimental study of spherical-flame acceleration mechanisms in large-scale propane-air flames. Proc. Combust. Inst. 35 (2), 2059–2066.

Bechtold, J.K., Matalon, M., 2001. The dependence of the Markstein length on stoichiometry. Combust. Flame 127 (1–2), 1906–1913.

Bradley, D., 1999. Instabilities and flame speeds in large-scale premixed gaseous explosions. Philos. Trans. Math. Phys. Eng. Sci. 357 (1764), 3567–3581.

Bradley, D., Gaskell, P.H., Gu, X.J., 1996. Burning velocities, Markstein lengths, and flame quenching for spherical methane-air flames: a computational study. Combust. Flame 104 (1–2), 176–198.

Bradley, D., Hicks, R., Lawes, M., Sheppard, C., Woolley, R., 1998. The measurement of laminar burning velocities and markstein numbers for iso-octane-air and iso-octane-n-heptane-air mixtures at elevated temperatures and pressures in an explosion bomb. Combust. Flame 115 (1–2), 126–144.

Bradley, D., Gaskell, P., Gu, X., 1998. The modeling of aerodynamic strain rate and flame curvature effects in premixed turbulent combustion. Symp. Int. Combust. 27 (1), 849–856.

Bradley, D., Cresswell, T.M., Puttock, J.S., 2001. Flame acceleration due to flame-induced instabilities in large-scale explosions. Combust. Flame 124 (4), 551–559.

Bradley, D., Gaskell, P., Gu, X., Sedaghat, A., 2005. Premixed flamelet modelling: factors influencing the turbulent heat release rate source term and the turbulent burning velocity. Combust. Flame 143 (3), 227–245.

Bradley, D., Lawes, M., Mansour, M., 2011. The problems of the turbulent burning velocity. Flow Turbul. Combust. 87 (2), 191–204.

Bradley, D., Lawes, M., Liu, K., Mansour, M., 2013. Measurements and correlations of turbulent burning velocities over wide ranges of fuels and elevated pressures. Proc. Combust. Inst. 34, 1519–1526.

Bray, K.N.C., 1990. Studies of the turbulent burning velocity. Proc. Math. Phys. Sci. 431 (1882), 315–335.

Clavin, P., 1985. Dynamic behavior of premixed flame fronts in laminar and turbulent flows. Prog. Energy Combust. Sci. 11 (1), 1–59.

Cooper, M., Fairweather, M., Tite, J., 1986. On the mechanisms of pressure generation in vented explosions. Combust. Flame 65 (1), 1–14.

Darrieus, G., Propagation d'un front de flamme, Presented at La Technique Moderne (Paris) and in 1945 at Congrès de Méchanique Appliquée (Paris).

Davis, S., Quinard, J., Searby, G., 2002. Markstein numbers in counterflow, methane-and propane- air flames: a computational study. Combust. Flame 130 (1–2), 123–136.

GexCon AS, 2015. FLACS v10.3r2 Users Manual, Tech. Rep., GexCon AS. Norway, Bergen.

Gostintsev, Yu. A., Istranov, A.G., Shulenin, Yu. V., 1988. Self-similar propagation of a free turbulent flame in mixed gas mixtures. Combust. Explos. Shock Waves 24, 563–569.

Hjertager, B., 1986. Three-dimensional Modeling of Flow, Heat Transfer, and Combustion. In: Handbook of Heat and Mass Transfer. Gulf Publishing, Houston,

pp. 1303–1350. Ch. 41.

Hjertager, B., Fuhre, K., Bjørkhaug, M., 1988. Concentration effects on flame acceleration by obstacles in large-scale methane-air and propane-air vented explosions. Combust. Sci. Technol. 62, 239–256.

Jomaas, G., Law, C.K., Bechtold, J.K., 2007. On transition to cellularity in expanding spherical flames. J. Fluid Mech. 583, 1–26.

Landau, L.D., 1944. On the theory of slow combustion. Zh. Eksp. i Theor. Fiz. 14, 240.

Launder, B.E., Spalding, D.B., 1974. The numerical computation of turbulent flows. Comput. Methods Appl. Mech. Eng. 3 (2), 269–289.

Law, C., Zhu, D., Yu, G., 1988. Propagation and extinction of stretched premixed flames. Symp. Int. Combust. 21 (1), 1419–1426.

Magnussen, B., Hjertager, B., 1977. On mathematical modeling of turbulent combustion with special emphasis on soot formation and combustion. Symp. Int. Combust. 16 (1), 719–729.

Markstein, G.H., 1951. Experimental and theoretical studies of flame-front stability. J. Aeronaut. Sci. 18, 199–209.

Model Evaluation Group Gas Explosions (MEGGE), 1996. Gas Explosion Model Evaluation Protocol – Version 1, Tech. Rep.

National Instruments, 2013. LabVIEW System Design Software. http://sine.ni.com/np/app/main/p/docid/nav-104/lang/no/fmid/1762/ (accessed 10.01.14).

Savitzky, A., Golay, M., 1964. Smoothing and differentiation of data by simplified least squares procedures. Anal. Chem. 36 (8), 1627–1639.

Sivashinsky, G., 1977. Diffusional-thermal theory of cellular flames. Combust. Sci. Technol. 15 (3–4), 137–145.

Skjold, T., Pedersen, H., Bernard, L., Middha, P., Narasimhamurthy, V., Landvik, T., Lea, T., Pesch, L., 2013. A matter of life and death: validating, qualifying, and documenting models for simulating flow-related accident scenarios in the process industry. Chem. Eng. Trans. 31, 6.

Skjold, T., Castellanos, D., Olsen, K.L., Eckhoff, R.K., 2014. Experimental and numerical investigation of constant volume dust and gas explosions in a 3.6-mflame acceleration tube. J. Loss Prev. Process Ind. 30, 164–176.

Solberg, D., Pappas, J., Skramstad, E., 1981. Observations of flame instabilities in large scale vented gas explosions. Symp. Int. Combust. 18 (1), 1607–1614.

Wingerden, C.V., Zeeuwen, J., 1983. On the role of acoustically driven flame instabilities in vented gas explosions and their elimination. Combust. Flame 51, 109–111.

Paper 3

Vortex shedding in gas explosions and its mitigation: an experimental study

Hisken, H., Enstad, G.A., & Narasimhamurthy, V.D.

CrossMark

Suppression of vortex shedding and its mitigation effect in gas explosions: an experimental study

H. Hisken [a, b, *], G.A. Enstad [b], V.D. Narasimhamurthy [b, c]

[a] Department of Physics and Technology, University of Bergen, Allégaten 55, 5007, Bergen, Norway
[b] Gexcon AS, Research and Development, P.O. Box 6015, NO-5892, Bergen, Norway
[c] Department of Applied Mechanics, Indian Institute of Technology Madras, Chennai, 600036, India

ABSTRACT

This paper reports occurrence of vortex shedding behind bluff-bodies in gas explosions, methods to suppress them using passive flow control techniques, and their overall impact on explosion over-pressures. The pressure-time histories from a series of explosion tests, using an initially quiescent propane-air mixture in a vented channel of dimensions 1.5 m × 0.28 m × 0.3 m, are presented. Selected high-speed video frames visualizing the flame propagation are also presented. Three different bluff-obstruction scenarios are considered: 1) a reference case with a single smooth circular cylinder of diameter D = 0.0157 m, 2) a single cylinder identical to that in the reference case, mounted with a splitter plate of varying length from 5.13D to 0.26D, width 17.8D and thickness 0.06D, and 3) a single helically wired cylinder with wire diameter 0.1D and pitch 4D or 8D. All circular cylinders had a length of 17.8D and were mounted normal to the direction of the flow, spanning the channel cross-section 0.5 m downstream of the ignition point. The obstructions were inserted in the rig using a unique experimental setup. The peak overpressure generated by the explosion is of main interest. Both vortex shedding suppression techniques 2) and 3) yielded significant reduction in maximum overpressures when compared to the reference cylinder case 1). While all splitter plate configurations successfully reduced the maximum explosion overpressure, the splitter plates with length 1.02D and 0.51D were the most efficient, with an average reduction in overpressure of 32 ± 3%. The helical steel wire configurations also had a significant effect, with 25 ± 3% and 20 ± 3% reduction in the maximum overpressure for pitch 4D and 8D, respectively. The high-speed video visualization further buttressed the quantitative findings in the pressure measurements and clearly showed vortex shedding suppression. The current observations imply that the contribution from vortex shedding, i.e. apart from turbulence effects, to the overpressure generation in gas explosions is significant. The modelling community must consider this while preparing their simulators.

© 2016 Published by Elsevier Ltd.

1. Introduction

The industries associated with energy extraction and conversion often involve the handling and storage of large quantities of flammable gases or liquids. Gas or vapour cloud explosions following an accidental release of a flammable gas or liquid may cause fatalities and severe material and environmental damage — examples are Piper Alpha (July 6, 1988), Buncefield (December 11, 2005),

Deepwater Horizon (April 20, 2010), and Fukushima Daiichi (March 11, 2011) (Marsh, 2014; Skjold et al., 2014). Industrial-scale gas explosions generally involve premixed combustion embedded in unsteady, turbulent flows in complex geometries. The interplay between turbulence and premixed combustion depends on the characteristic time and length scales of turbulence relative to those of the chemical reactions. Vortices of sufficient strength increase the overall flame surface area, promote mixing and heat transfer, leading to higher mass burning rates in the propagating flame brush, see e.g. (Damköhler, 1940; Spalding, 1971; Libby et al., 1979; Peters, 1988). The primary mechanism for flame acceleration in congested geometries is the positive feedback between the expansion of combustion products, turbulence generated in the

unreacted mixture downstream of the propagating flame front, especially in shear- and boundary-layers from flow past obstacles and walls, and enhanced combustion rates (Wheeler, 1919; Shchelkin, 1940; Moen et al., 1980, 1982). Rapid flame acceleration creates pressure waves that can potentially damage structures; therefore, the severity of an explosion is usually given in terms of the generated overpressure, its spatial distribution, and the associated pressure impulse.

The process industries invest considerable resources in reducing the probability and consequences of a potential accident; the latter can be addressed by applying appropriate mitigation measures (Eckhoff, 2005). In order to reduce the gas explosion hazard, it is crucial to have detailed knowledge of the physical phenomena leading to flame acceleration. This is particularly important when developing engineering software for consequence prediction of industrial scale explosions. For computational fluid dynamics (CFD) software used to simulate large-scale gas explosions in complex geometries, phenomenological or empirical sub-grid models are implemented to represent processes that are not resolved on the computational grid. For example, such CFD models must account for turbulence production by sub-grid scale obstructions (Skjold et al., 2014). Other than turbulence, a range of fluid flow instabilities, either intrinsic in nature or induced by the surrounding geometry, may also promote flame acceleration in gas explosions (Ciccarelli and Dorofeev, 2008). For a certain range of Reynolds numbers, the Bénard–von Kármán (BVK) instability, resulting in the phenomenon called *vortex shedding*, occurs in non-reacting bluff-body wake flows (Zdravkovich, 1997). The BVK instability introduces a strong periodicity in the velocity and pressure measurements just downstream of the bluff-body, and is associated with a significant increase in the form drag, enhanced mixing, as well as possible structural vibrations and noise. Therefore, a range of engineering techniques to suppress or control vortex shedding has been developed (Choi et al., 2008; Zdravkovich, 1997).

The BVK instability and its effects have been extensively studied for non-reacting flow (Roshko, 1993; Williamson, 1996), and in reacting flow for flame holder configurations in various combustor applications (Hertzberg et al., 1991; Fureby, 2000; Lieuwen, 2013). Some investigators (Kong, 1996; Kong and Sand, 1996) measured and discussed vortex shedding in transient, explosion driven flow past various bluff-bodies. However, to the present authors' knowledge, no information is available on the effect of applying control methods to bluff-bodies in gas explosions. This experimental study investigates the occurrence of vortex shedding behind a single circular cylinder embedded in a premixed fuel-air cloud during a gas explosion, ways to control the shedding, and finally its overall impact on the overpressure generation.

2. Theory and background

2.1. Flow around a circular cylinder

The circular cylinder is a canonical object in practical applications and has been widely studied in the field of fluid mechanics (Roshko, 1993; Zdravkovich, 1997, 2003). For flow across a circular cylinder, the Reynolds number is defined as $Re = UD/\nu$, where U is the upstream flow speed, D is the diameter of the cylinder, and ν is the kinematic viscosity of the fluid. The two-dimensional flow around a circular cylinder can be represented by a thin viscous boundary-layer, surrounded by an external potential flow. Upstream of the highest point of the curved body, where the streamlines converge, the pressure gradient is *favourable*, i.e. it points in the opposite direction of the flow. However, downstream of the highest point of the curved body the streamlines diverge, giving rise to a positive pressure gradient with respect to the flow

direction, i.e. an *adverse* pressure gradient. The boundary-layer experiences the same pressure as the external flow. If the adverse pressure gradient is sufficiently strong, the flow near the wall will decelerate faster than the external flow, and eventually reverses its direction leading to boundary-layer separation.

Following flow separation, shear layers emanate from each side of the bluff-body. At Re from ~4 to 47, the separated shear-layers roll up to form two counter-rotating steady laminar vortices behind the circular cylinder. When Re exceeds ~47, the two-dimensional wake becomes globally unstable and unsteady. The BVK instability is initially observed as a periodic oscillation of the laminar wake, producing two staggered rows of counter-rotating vortices in an anti-symmetric pattern. Regions of concentrated vorticity are then *shed* periodically from alternate sides of the cylinder and convected downstream, forming a *von Kármán vortex street*. The vortex shedding is nominally two-dimensional in nature for $Re < 190$. At $Re \approx 190$, three-dimensional effects due to intrinsic secondary instabilities becomes appreciable (Williamson, 1996). The periodic oscillations persist, albeit with less coherence, as Re increases, and the three-dimensional structures become increasingly disordered. At $Re > 1200$, vortices generated by the convective Kelvin–Helmholtz instability in the separated shear layers start to appear (Bloor, 1964). The turbulence transition point in the shear layers move upstream towards the cylinder with increasing Re (Schiller and Linke, 1933). The boundary-layer around the circular cylinder itself undergoes transition to turbulence at $Re \approx 200,000$. The more energetic turbulent boundary-layer can resist the adverse pressure gradient and hence separation for a longer time than the laminar boundary-layer. Consequently, the boundary-layer transition leads to less pressure deficiency across the cylinder, i.e. less *form drag*, and a narrower wake (Roshko, 1993). However, for $Re > 200,000$, coherent vortex shedding can still be discerned (e.g. Thomann, 1959; Roshko, 1961; Williamson, 1996; Rodríguez et al., 2015).

2.2. Flow control methods

The flow oscillations due to two-dimensional vortex shedding can be characterized by the Strouhal number $St = fD/U$, where f is the shedding frequency. For a circular cylinder, St can be expressed as a piecewise linear function of $1/\sqrt{Re}$ in the flow regimes from $47 < Re < 2 \times 10^5$ (Fey et al., 1998). Based on these relations, St varies between 0.18 and 0.21 for $1000 < Re < 2 \times 10^5$. As vortices shed alternately from each side of the cylinder in a counter-rotating fashion, they produce a lateral force on the cylinder. For flow past real structures, this may cause damaging vortex-induced vibrations (VIV) if the shedding has some critical frequency close to the natural frequency of the structure (i.e. the so-called *lock-in* phenomenon). Overall, the onset of vortex shedding is associated with a significant increase in the form drag, enhanced mixing, as well as possible structural vibrations and noise. Therefore, several engineering techniques to eliminate or suppress vortex shedding have been developed, and are applied for structures such as oil-rigs and suspension bridges.

Flow control methods for bluff-body wakes can be either *passive* or *active* (Choi et al., 2008). The present study focuses on passive control methods, as they do not require any power input or feedback sensor, and therefore are straightforward to implement. In particular, the methods for controlling bluff-body wake flows considered here entail direct modification of either (i) the near-wake or (ii) the boundary-layer. A classical type (i) method is to introduce a thin splitter plate along the wake centre-line at the base region downstream of the cylinder, as illustrated in Fig. 1. A splitter plate prevents the two separated shear layers from interacting, and thus stabilizes the near-wake (Roshko, 1993).
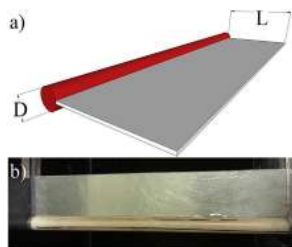
Fig. 1. A circular cylinder with a splitter plate, a) illustration and b) photograph, as inserted in the experimental rig.

Boundary-layer separation in a straight line along the spanwise length of the circular cylinder seems to be necessary for coherent vortex shedding (Buresti, 2000). Fig. 2 illustrates a common control method of type (ii) i.e. adding "edges" to the bluff-body surface, for example using helical wires. The added edges force the boundary-layer to separate in-homogeneously along the cylinder span, and thus disrupt the two-dimensional nature of the instability. According to Zdravkovich (2003), a spiral with a pitch P around 8D would effectively suppress the shedding in non-reacting flows. Both of the passive control methods described here directly affect the global instability in the near-wake, rather than delaying the separation point, and should therefore be effective for a wide range of Re (Choi et al., 2008).

2.3. Vortex shedding mechanisms in gas explosions

The theory described in Sections 2.1 and Section 2.2 concerns vortex shedding in non-reacting, quasi-steady, uniform density flows. For bluff-bodies located inside a fuel-air cloud during a gas explosion, additional factors make the situation more complex. Combusting flows generally involve significant density gradients, which directly affect the stability of the bluff-body wake. Yu and Monkewitz (1990) presented a local stability analysis for the two-dimensional wake behind a bluff-body with non-uniform density gradients. The analysis shows that the wake can be further de-stabilized if the fluid in the wake has a higher density than the approach flow. Similarly, the presence of a heated, low-density wake stabilizes the BVK instability.

Furthermore, flow induced by flame propagation in a gas explosion will generally be transient. Lee and Budwig (1991)
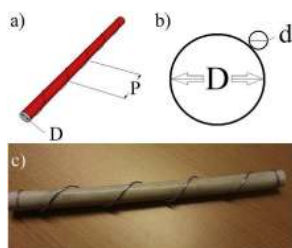
Fig. 2. A circular cylinder with a helical steel wire, a) illustration, b) diameter of wire vs. diameter of cylinder and c) photograph.

investigated vortex shedding in uniformly accelerating flow at $20 < Re < 330$, and found that the critical Re for the onset of the BVK instability increased with increasing flow acceleration. Flow deceleration had the opposite (de-stabilizing) effect. However, the overall time to onset of the BVK instability decreased with increasing flow acceleration, and the temporal growth rate of the instability was approximately proportional to the applied flow acceleration. As part of the Gas Safety Programme (1993–1996), and the EMERGE (Extended Modelling and Experimental Research into Gas Explosions) project, Chr. Michelsen Research (CMR) evaluated drag, loading and turbulence velocities in the near-wake of circular and square cylinders (Kong, 1996; Kong and Sand, 1996; Mercx, 1996). Velocities were measured in both steady flow with Re varying between 1.4×10^4 and 7×10^4, and in transient, explosion driven flow with maximum upstream flow speeds comparable to those of the steady flows. In the transient experiments, the bluff-bodies were not inserted inside the premixed fuel-air cloud due to sensitivity of the LDA (Laser-Doppler anemometry) system to temperature changes, but in a test section downstream of the explosion. The investigators observed significant effects from vortex shedding on the measured velocities in the near-wake of a single circular cylinder in both steady and transient flow. Furthermore, they found significant turbulence fluctuations also in the spanwise direction, indicating that three-dimensional effects in the near wake were non-negligible. The measured time-varying mean velocity due to vortex shedding in the transient flow was irregular, in contrast to the quasi-periodic variation in the steady flow conditions. In the transient case, the overall turbulence production was measured to be lower in the near-wake (2D and 4D downstream of the circular cylinder) compared to the corresponding steady configurations. However, the contributions from large-scale vortices were significant in this region, so Kong and Sand (1996) suggested that the larger-scale structures located there had not yet merged and dissipated to smaller-scale turbulence. From the velocity measurements, they estimated St to 0.22 to 0.25 in the near-wake, and suggested that a similar relation between St and Re as in steady flow exists also for transient flow.

In the present study, explosions in a confined enclosure with a vent opening are considered. As the ignition point is located at the closed end of the chamber, unburned fuel-air mixture is pushed towards the vent opening, through the cross-section where the bluff-body is situated. The gas expansion behind the flame front accelerates the flow upstream of the obstruction. The bluff-body wake initially consists of high-density reactants, however, as the flame propagates into the wake and folds around the obstruction, reactants burn, and the near-wake is filled with low-density combustion products. Due to the higher kinematic viscosity of the combustion products relative to the un-burned fuel-air mixture, Re at the circular cylinder will likely be somewhat lower after the flame has passed. Turbulence and unsteady flow structures that have formed in the reactant flow just prior to flame arrival will lead to flame acceleration in the bluff-body wake (Moen et al., 1980; Lindstedt and Sakthitharan, 1998).

The characteristic length scales of the vortices determine how the flame zone and the turbulent flow field interact. Large-scale flow structures distort and increase the overall flame surface area, leading to an overall higher fuel consumption rate; small-scale turbulence structures promote mixing in the flame brush and enhance the combustion rate locally. Most theoretical and experimental studies on turbulent premixed combustion relate the turbulent burning velocity u_t to the turbulence velocity fluctuations in the ith direction, u_i', and express u_t as increasing with u_i' before quenching effects become important (Lipatnikov and Chomiak, 2002). For flow past a bluff-body in non-reacting flow, where a splitter plate suppresses the vortex shedding, the highest values of

the Reynolds stresses $\overline{u_i'u_j'}$ are found in the separated shear layers. In a bluff-body wake without a splitter plate, where vortex shedding dominates, the Reynolds stresses are higher and more evenly distributed compared to the splitter plate case (Cantwell and Coles, 1983; Roshko, 1993). Large-scale coherent structures eventually break down into smaller-scale turbulence (Schadow and Gutmark, 1992). Coherent vortex shedding may therefore promote combustion further downstream of the bluff-body more efficiently than the separated shear layers.

In summary, the presence of vortex shedding behind bluff-bodies is expected to significantly influence the flame acceleration in gas explosions. However, the combined effect of the relevant physical phenomena is not straightforward to estimate. In order to quantify these effects, a series of lab-scale propane-air gas explosion experiments were performed, employing the two passive flow control methods described in Section 2.2.

3. Experimental setup

The experiments were conducted in an explosion chamber of internal dimensions 1.5 m × 0.28 m × 0.30 m, with one end wall (of dimensions 0.28 m × 0.30 m) removed, to provide explosion venting to the atmosphere. Fig. 3 shows the layout of the experimental rig, together with a schematic diagram of the recirculation system. The front wall of the explosion chamber shown in Fig. 3 is made from transparent polycarbonate, to enable high-speed video analysis of the flame propagation. One piezo-electric pressure transducer (P1) of type Kistler 701a mounted internally at the closed end recorded the overpressure-time development with a sampling rate of 50 kHz. Previous experiments showed that the pressure-time history in the rig could be sufficiently described by a single transducer (Hisken et al., 2015). A Phantom v210 high-speed camera recorded the flame propagation at a rate of 4000 frames per second.

A cylinder with a diameter D = 0.0157 m and (effective) length 17.8D was positioned 0.50 m downstream of the ignition point, at the chamber centre-line. The circular cylinder, mounted horizontally, spanned the channel cross-section. The experimental setup was such that symmetric and smooth conditions prevailed on either side of the wake centre-line all along the length of the rig. To achieve this, additional polycarbonate plates (measuring 1.5 m × 0.01 m × 0.30 m) had been inserted to cover the back and front walls.

Prior to each test, the channel was filled with a mixture of 4.2 (±0.1) volume% propane in air. This was achieved by adding a gas
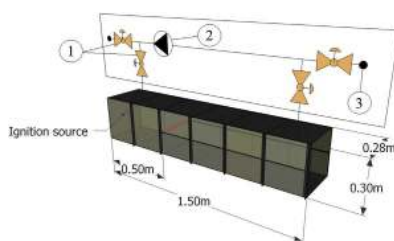

Fig. 3. The experimental rig, with a schematic diagram of the recirculation system. The vent opening is located at the far right of the rig in the figure, opposite of the ignition location. The symbols marked with (1) denote pneumatic actuated ball-valves, (2) denotes a fan, while the black circles (3) mark where the piping connects to the surrounding atmosphere.

composed of 99.9 vol% propane to the system presented in Fig. 3, and mixing it with the air in the chamber by recirculation. During the fuel-air mixing stage, a lightweight plastic sheet covered the open end of the channel in order to contain the flammable mixture. After the desired fuel concentration was obtained, the fuel-air mixture was allowed to rest for 1–2 min for mixing-induced turbulence to decay. A spark-plug generated low-energy electric spark at the centre of the channel's closed end ignited the mixture. The lightweight plastic sheet was released 0.1 s prior to ignition by a pneumatic system, to allow free flow out of the chamber.

The effect on the explosion overpressure of adding five different splitter plates with a fixed (effective) width of 17.8D, thickness 0.06D and varying length L in the streamwise direction, (cf. Fig. 1 and Table 1) to the reference case circular cylinder was studied. Furthermore, tests were performed where two helical steel wires of varying pitch (P) and fixed diameter d = 0.1D (cf. Fig. 2 and Table 2) were added to the reference case cylinder. Note that the helical wire was not completely attached to the cylinder surface and a minimal gap is provided to allow for easy replacement of different wire configurations. For the present study, the polycarbonate walls inside the explosion chamber were modified such that splitter plates could be inserted from the channel's open end through a horizontal slit. This unique design enabled ease of operation while maintaining stability and rigidity of both the cylinder and the splitter plates throughout the explosion. Fig. 4 illustrates the configuration of different obstruction types in the rig. Each test was repeated at least twice, in order to assess the reproducibility of the results. All pressure-time curves were filtered by the technique proposed by Savitzky and Golay (1964), using a window size of 25 points. The flame velocity curves were post-processed using a moving average filter with 10 side points.

4. Results and discussion

4.1. Reference case

High-speed videos were used to analyse the flame propagation inside the explosion chamber. Fig. 5 presents selected high-speed video frames from a test with the reference case geometry (cf. Fig. 4a). Fig. 6a and b show the overpressure-time history and the flame speed vs. distance from ignition (determined by video analysis of the leading flame front), respectively, for the reference case in Fig. 5. The dominant pressure peak was reproduced within ±0.0008 bar (or approximately ±3%) for similar initial conditions, while the maximum pressure impulse, integrated over the main pressure peak, varied by approximately ±0.0007 kPa s (or ±2%).

In Fig. 5, the flame appears to propagate from the ignition point in the shape of a half-ellipsoid. Some large-scale structures on the flame surface are present from ignition; however, the smaller, more uniformly distributed cellular pattern associated with hydrodynamic and thermo-diffusive instabilities (Bradley et al., 2001) cannot be discerned here. The expanding combustion products push the flame front and the downstream reactant mixture towards the vent opening, located at the right hand side of Fig. 5. As the flame accelerates from the ignition point, the volume expansion starts to exceed the venting rate, leading to a pressure rise of approximately 0.0065 bar from ignition at $t = 0.000$ s to the flame front reaches the channel walls at $t = 0.060$ s. The overpressure in the chamber is approximately constant between $t = 0.060$ s and $t = 0.070$ s, possibly due to cooling effects from the wall. No further (significant) pressure rise is measured until the flame front reaches the circular cylinder at $t = 0.075$ s.

As the flame propagates past the cylinder, a pocket of reactants persists in the near-wake. At $t = 0.077$ s, the flame fronts on each side of the pocket curve downwards around the reactants

Table 1
Splitter plate specification, reduction in overpressure and pressure impulse. All plates had the same thickness 0.06D and width 17.8D.

Splitter plate	Length (L)	Average reduction in maximum overpressure	Average reduction in maximum pressure impulse
SP1	5.13D	25%	21%
SP2	3.04D	26%	25%
SP3	1.02D	32%	25%
SP4	0.51D	31%	21%
SP5	0.26D	20%	4%

Table 2
Helical steel wire specification and reduction in overpressure. Both wires had the same diameter d = 0.1D.

Helical steel wire	Pitch (P)	Average reduction in maximum overpressure	Average reduction in maximum pressure impulse
HW1	4D	25%	16%
HW2	8D	20%	13%
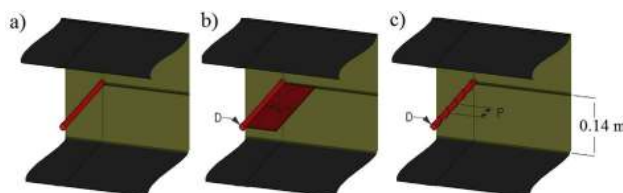
Fig. 4. Obstructions as inserted in test rig: a) reference case, b) splitter plate and c) helical steel wire.

remaining in the near-wake. The flame fronts propagate into the near-wake from each side, and an antisymmetric, 'sinusoidal' pattern of increased luminosity can be observed downstream of the obstruction from $t = 0.079$ s. Inside of the antisymmetric, large-scale structures, the combustion rate is clearly enhanced, and the shape of the leading flame front is seen to have changed accordingly at $t = 0.081$ s. These large-scale structures are qualitatively similar to the von Kármán vortex street observed in the wake of bluff-bodies in a range of non-reacting and combusting flows (see e.g. Thomann, 1959; Williamson, 1996; Lieuwen, 2013). This suggests that the BVK instability leading to vortex shedding, as described in Section 2, indeed has occurred behind the circular cylinder.

After $t = 0.086$ s, the flow speed past the cylinder is likely lower than prior to flame arrival, and the combusting region in the near-wake has become symmetric with respect to the circular cylinder centre-line. At the time of the peak overpressure (at $t = 0.088$ s), the symmetric near-wake in Fig. 5 consists of a central region where combustion appears to be completed, and two shear layers on either side of the cylinder where combusting vortices are still visible. Turbulent combustion further downstream is still anti-symmetric, and an extensive region of intense burning is observed there. As the flame propagates further downstream of the bluff-body, the antisymmetric luminous structures are further distributed across the channel cross-section, and the regions of enhanced burning appear more disorganized. The flame front reaches the vent opening at $t = 0.096$ s, and venting of combustion products and external combustion commences. Fig. 6a shows that the increased venting rate of low-density combustion products at first leads to under-pressure in the chamber, thereafter Helmholtz oscillations over the vent opening are triggered. Compared to the dominant pressure peak, the amplitude of the subsequent pressure oscillations is not significant.

4.2. Effect of splitter plates

To investigate the effect of applying flow control methods on the explosion overpressure, splitter plates of varying length (cf. Table 1), were inserted in the rig. Fig. 6a presents the overpressure-time history after adding a splitter plate (SP3) with L = 1.02D to the cylinder, together with the reference case. For both configurations, the main pressure peak was generated by flame acceleration in the circular cylinder wake. However, the splitter plate with L = 1.02D reduced the magnitude of the main pressure peak by 32% compared to the reference case, and the maximum pressure impulse was reduced by approximately 25%. Fig. 6b shows the corresponding flame speeds as a function of distance from the ignition point. The flame speeds are similar before the flame front passes the cylinder. In the reference case, the most significant flame acceleration occurs at approximately 0.7 m downstream of the ignition point, producing the pressure peak at 0.088 s. The flame front continues to accelerate until it reaches the vent opening. There is significantly less flame acceleration in the corresponding region for the splitter plate test, resulting in a lower maximum overpressure. For this configuration, the leading flame front propagates with an approximately constant speed from a distance of 1 m from the ignition point.

Table 1 presents the reduction in overpressure and the corresponding pressure impulse relative to the reference case for each splitter plate configuration, computed as the average over all repeated tests. The reduction varied with less than ±3% between repeated tests.

The high-speed video frames in Fig. 7 visualize the effect of the splitter plate with a length of 5.13D on the flame propagation through the cylinder wake. Prior to flame arrival at the obstruction, the flame propagation seems to be very similar to the reference case in Fig. 5. As the flame propagates past the cylinder at $t = 0.073$ s, the flame fronts surrounding the reactants just
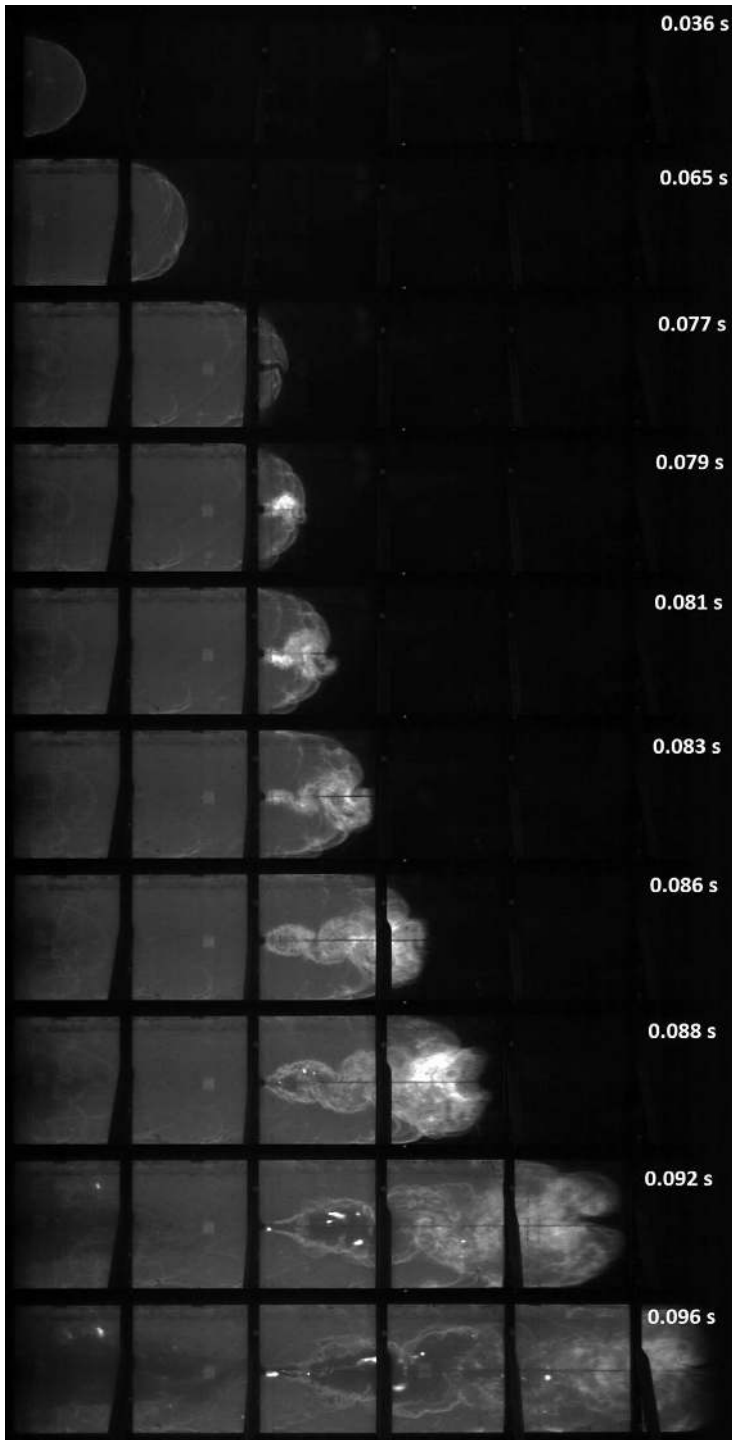
Fig. 5. Selected high-speed video frames, reference case.
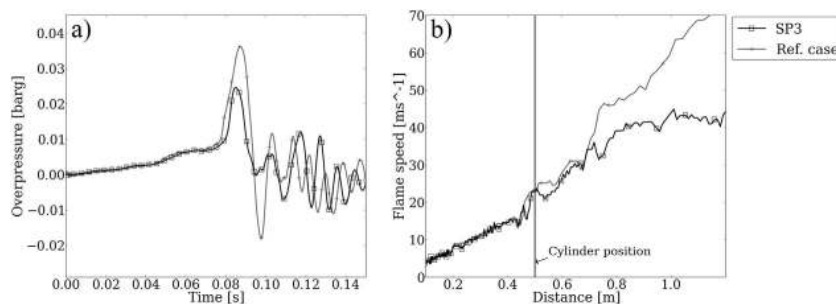
Fig. 6. a) Overpressure-time history and b) flame speed vs. distance curves for the reference case (+), and with a splitter plate inserted, L = 1.02D (□).

downstream of the cylinder appear to be symmetric with respect to the cylinder centre-line (in contrast to the reference case at $t = 0.077$ s in Fig. 5). The enhanced rate of combustion due to increased mixing in the turbulent shear layers is clearly visualized from $t = 0.074$ s in Fig. 7. The burning shear layers curve symmetrically on each side of the splitter plate, in a convex shape with respect to the combustion products, and meet at the end of the splitter plate at $t = 0.077$ s.

In the high-speed video frames at $t = 0.077$ and 0.078 s (in Fig. 7), it is clear from the increased luminosity that combustion is also promoted in the boundary-layers along both sides of the splitter plate. These mechanisms generate the main pressure peak at $t = 0.078$ s. At $t = 0.085$ s, the wake still appears to be symmetric, and combustion seems to be completed in the regions around the splitter plate. The luminous structures further downstream stay narrow and symmetric around the channel centre-line until the flame front reaches the vent opening at $t = 0.096$ s.

Table 1 indicates that all splitter plates SP1-SP5 to some extent prevented the shear layers in the near-wake from interacting and thereby stabilized the near-wake, as the maximum overpressures were all significantly reduced. Furthermore, high-speed video analysis suggests that the longest splitter plates, SP1 and SP2, are able to suppress the vortex shedding completely. However, apart from stabilizing the near-wake, splitter plates introduce additional boundary-layers to the flow, resulting in increased skin-friction drag. The maximum overpressures for the longer splitter plates SP1 and SP2 in Table 1 suggest that the fine-scale turbulence produced in this region promotes flame acceleration somewhat compared to the shorter splitter plates SP3 and SP4.

Splitter plates SP3 and SP4 were nearly equally efficient with a reduction in maximum overpressure of approximately 32%, and 25% reduction in maximum pressure impulse. Fig. 8a–e shows high-speed video frames at the time of occurrence of the maximum pressure peak for five different geometries. For configurations SP1-SP4, coherent vortex shedding is not observed in the high-speed videos. While the wake, as visualized by enhanced burning rates, appears to be symmetric for SP1 and SP2 (cf. Figs. 7 and 8b for SP1), the video frames for SP3 and SP4 show a slightly antisymmetric pattern emerging as the flame passes the splitter plate (cf. Fig. 8c for SP3).

The shortest splitter plate, SP5, had a mitigation effect comparable to that of SP1 and SP2 for the maximum overpressure, however, the pressure impulse was not significantly reduced (cf. Table 1). For SP5, an antisymmetric pattern reminiscent of that observed in the reference case could be discerned downstream of

the splitter plate in the cylinder wake (cf. Fig. 8d). Fig. 9a confirms that the pressure peak is wider when SP5 is applied, and Fig. 9b shows that the corresponding flame acceleration is significantly higher towards the vent opening, compared to SP3 in Fig. 6b. In summary, a splitter plate with L = 0.26D does not appear to completely suppress vortex shedding in the present test setup. However, the circular cylinder wakes with added splitter plates, as visualized by increased burning rates in Figs. 7 and 8b–d, all appear narrower and less energetic than for the reference case in Figs. 5 and 8a.

4.3. Effect of helical wires

Fig. 10a shows the effect on the overpressure-time history of adding a helical steel wire with P = 4D (HW1) or P = 8D (HW2) to the circular cylinder surface, while Fig. 10b shows the corresponding flame speeds. Compared to the reference case, the maximum overpressure is reduced also in this configuration, by an average of 25% and 20% for P = 4D and P = 8D, respectively. The reduction in pressure impulse is somewhat less, approximately 16% and 13% for P = 4D and P = 8D, respectively. Fig. 10b compares the flame speeds for the helical steel wire configurations to that obtained for the reference case. The flame speeds are initially similar. However, in contrast to the reference case, the flame front for the helical wire configurations decelerates after propagating 0.8 m from the ignition point. These observations are confirmed by the high-speed videos frames in Fig. 11, visualizing the flame propagation for the configuration HW1 (helical wire with P = 4D). Combustion seems to be most intense in the near-wake, generating the main pressure peak at $t = 0.081$ s. Coherent vortex shedding is not observed in the bluff-body wake; the flow structures in the wake appear to be more "three-dimensional" and disorganized than in the previous configurations. As the flame propagates towards the vent opening, combustion appears markedly less intense compared to the reference case. Table 2 presents the average reduction in maximum overpressure and pressure impulse, relative to the reference case for the cylinders with a helical steel wire.

4.4. General discussion

Fig. 8 shows high-speed video frames at the time of the maximum overpressure for five different configurations. The reference case in Fig. 8a clearly stands out when compared to Fig. 8b–e, as the flame front has progressed significantly further from the cylinder at the time of the maximum overpressure. When
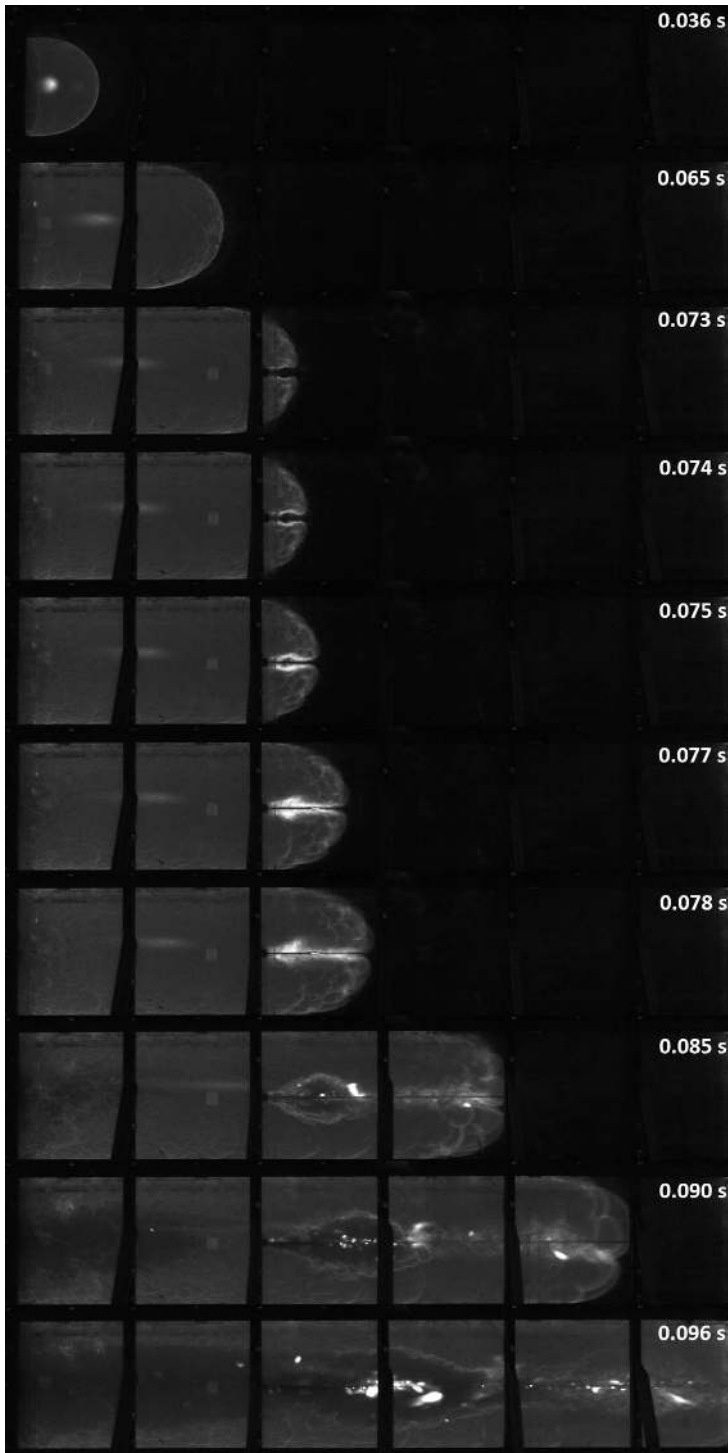
**Fig. 7.** Selected high-speed video frames, cylinder with a splitter plate of length 5.13D (SP1).
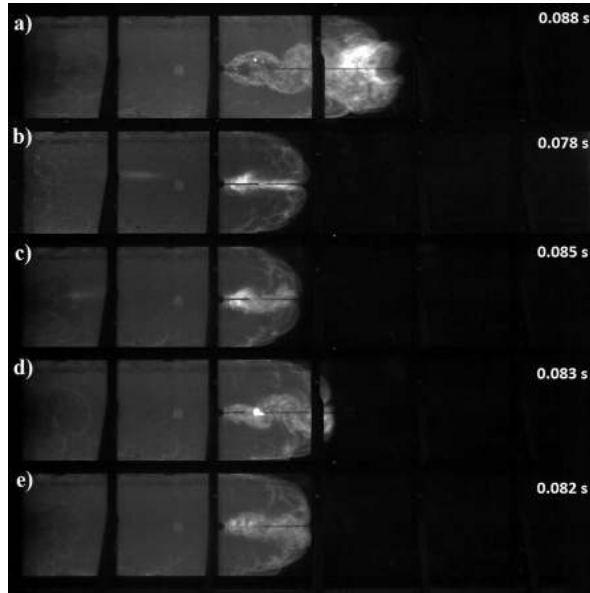
Fig. 8. High-speed video frame at time of peak overpressure, a) reference case, b) SP1, c) SP3, d) SP5, e) HW1.
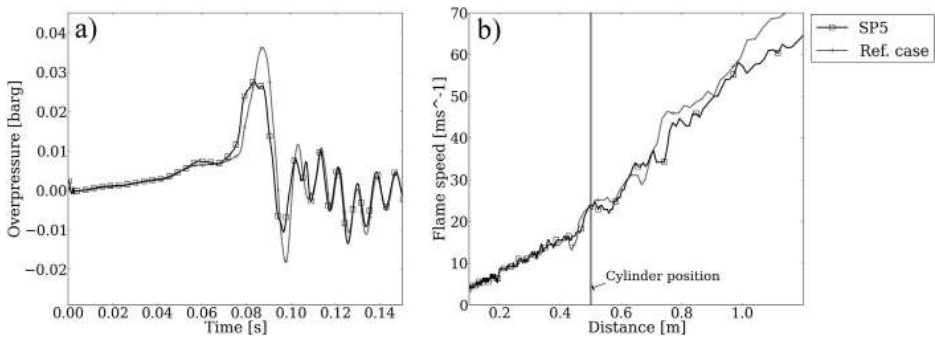

Fig. 9. a) Overpressure-time history and b) flame speed vs. distance curves for the reference case (+) and with a splitter plate inserted, L = 0.26D (□).

vortex shedding is allowed to develop freely, relatively large regions with intense burning rates seem to be produced in the far-wake. Presumably, the large-scale coherent structures promote macroscopic flame folding, and breaks down in the far-wake to scales at which combustion is efficiently promoted. The small-scale turbulence generated in the near-wake of the cylinder, for example in the boundary-layers along splitter plates, promotes combustion in the regions closer to the obstruction. The maximum overpressure (the average over all repeated tests) is plotted against

splitter plate length in Fig. 12a, and against the pitch of the steel wire helix in Fig. 12b.

With the current experimental setup, the wake of the obstruction prior to flame arrival cannot be visualized. However, the high-speed video recordings can be used together with a simple method for analysing vented explosions to derive an order-of-magnitude estimate of Re around the circular cylinder, prior to flame arrival. For example, the method presented by Hernandez et al. (2015) uses the ideal gas law for the combustion reactants and products
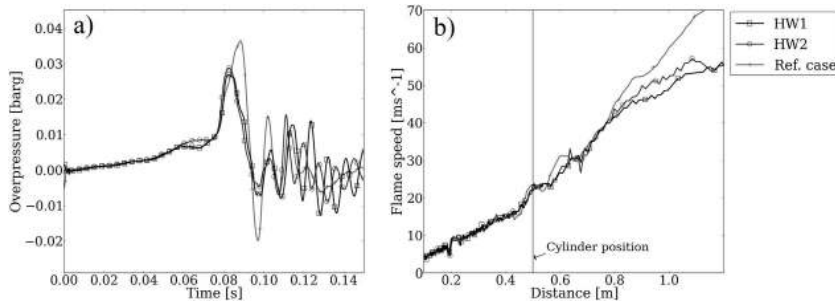
Fig. 10. a) Overpressure-time history and b) flame speed vs. distance for a single cylinder (+) and the same configuration with a helical steel wire, P = 4D (□) and P = 8D (○).

together with the basic conservation principle for mass in the explosion chamber. It is similar to approaches presented by e.g. Bradley and Mitcheson (1976) and Molkov and Nekrasov (1981).

The temperature and molar mass is assumed to be constant for each of the two gas components (reactants and products), and the pressure is assumed to be uniformly distributed within the enclosure. The rate of change of reactant mass with time inside the chamber, dm_r/dt, can be expressed as

$$\frac{dm_r}{dt} = -\frac{dV_{reacting}}{dt}\rho_r - \frac{dm_r}{dt}\Big|_{vented}, \tag{1.1}$$

where $dV_{reacting}/dt$ is the volumetric burning rate, ρ_r and m_r are the density and the mass of the reactants, respectively. The second term on the right hand side of Equation (1.1) denotes the rate of outflow of reactants through the vent opening. Similarly, the rate of change of combustion product mass with respect to time inside the chamber, dm_p/dt, can be expressed as

$$\frac{dm_p}{dt} = \frac{dV_{reacting}}{dt}\rho_r - \frac{dm_p}{dt}\Big|_{vented}. \tag{1.2}$$

Prior to venting of combustion products, the second term on the right hand side of Equation (1.2) can be set to zero. In the following, V_p and V_r are the volume of the products and reactants inside the chamber, respectively. The rate of volume of reactants that are converted to combustion products, $dV_{reacting}/dt$, can be expressed in terms of V_p by inserting the following relation (derived from the ideal gas law) into Equation (1.2)

$$\frac{dm_p}{dt} = \frac{M_p}{RT_p}V_p\frac{dP}{dt} + \frac{M_p}{RT_p}P\frac{dV_p}{dt}, \tag{1.3}$$

where P is the (uniformly distributed) time-dependent pressure inside the chamber, M_p and T_p are the molar mass and the temperature of the combustion products, respectively, and R is the ideal gas constant. The resulting expression,

$$\frac{dV_{reacting}}{dt}\frac{\rho_r}{\rho_p} = \frac{dV_p}{dt} + \frac{dP}{dt}\frac{V_p}{P}, \tag{1.4}$$

where ρ_p is the density of the combustion products, holds prior to venting of combustion products.

The volume of combustion products, V_p, and the rate of change of combustion product volume with respect to time inside the chamber, dV_p/dt, in Equation (1.4) can be estimated from analysis of

the leading flame front in the high-speed video recordings. The combustion products are initially assumed to be shaped like a half-ellipsoid, with dimensions estimated from the high-speed video frames. After the flame has reached the walls, the combustion products are assumed to have the shape of a half-ellipsoid followed by a square cylinder with a cross-section equal to that of the chamber. Any irregularities of the flame surface are neglected. These assumptions are considered reasonable before the flame front reaches the circular cylinder. The corresponding expression to Equation (1.3) for dm_r/dt can be applied together with the relation

$$V_r + V_p = V_{chamber}, \tag{1.5}$$

where $V_{chamber}$ is the (constant) volume of the vented channel, to determine $dm_r/dt|_{vented}$ from Equation (1.1). If the flow of reactants is assumed to be approximately uniform along the length of the channel prior to flame arrival at the cylinder, an average speed U of the reactants through the cross-section just upstream of the circular cylinder can be estimated from the outflow rate of reactants through the vent opening.

Fig. 13 shows $Re = UD/\nu$ as a function of time for a representative test, where U is the estimated flow of reactants just upstream of the circular cylinder, $D = 0.0157$ m is the cylinder diameter, and $\nu = 1.78 \times 10^{-5}$ m²/s is the kinematic viscosity of the reactant mixture. Prior to flame arrival at the cylinder, the flow speed was found to be similar (<5% variation) for all configurations. Due to the presumably larger uncertainties in the flow speed computations, the estimation of Re in Fig. 13 is assumed representative for all tests. According to Fig. 13, Re in the cylinder wake increases rapidly from $O(10^2)$ to $O(10^4)$ in a time interval of approximately 50 ms. Previous investigations in non-reacting flows for the indicated range of Re (Section 2) suggest that vortex shedding will occur in the turbulent cylinder wake prior to flame arrival. In particular, Kong and Sand (1996) reported significant vortex shedding effects on velocity measurements in the near-wake of a circular cylinder for transient, explosion-driven flow with similar overpressures and build-up times as in the present study. Furthermore, Kong & Sand (1996) observed that broadband fluctuations due to turbulence were less developed in the near-wake compared to tests with a steady upstream flow. Fig. 13 indicates that the boundary-layer transition, which appears at $Re \approx 2 \times 10^5$, has not yet occurred at flame arrival at the circular cylinder in the present study. These observations further corroborate the proposition that the coherent structures observed in Fig. 5 are indeed due to vortex shedding in the cylinder wake.

As noted in Section 2, the BVK instability is essentially two-
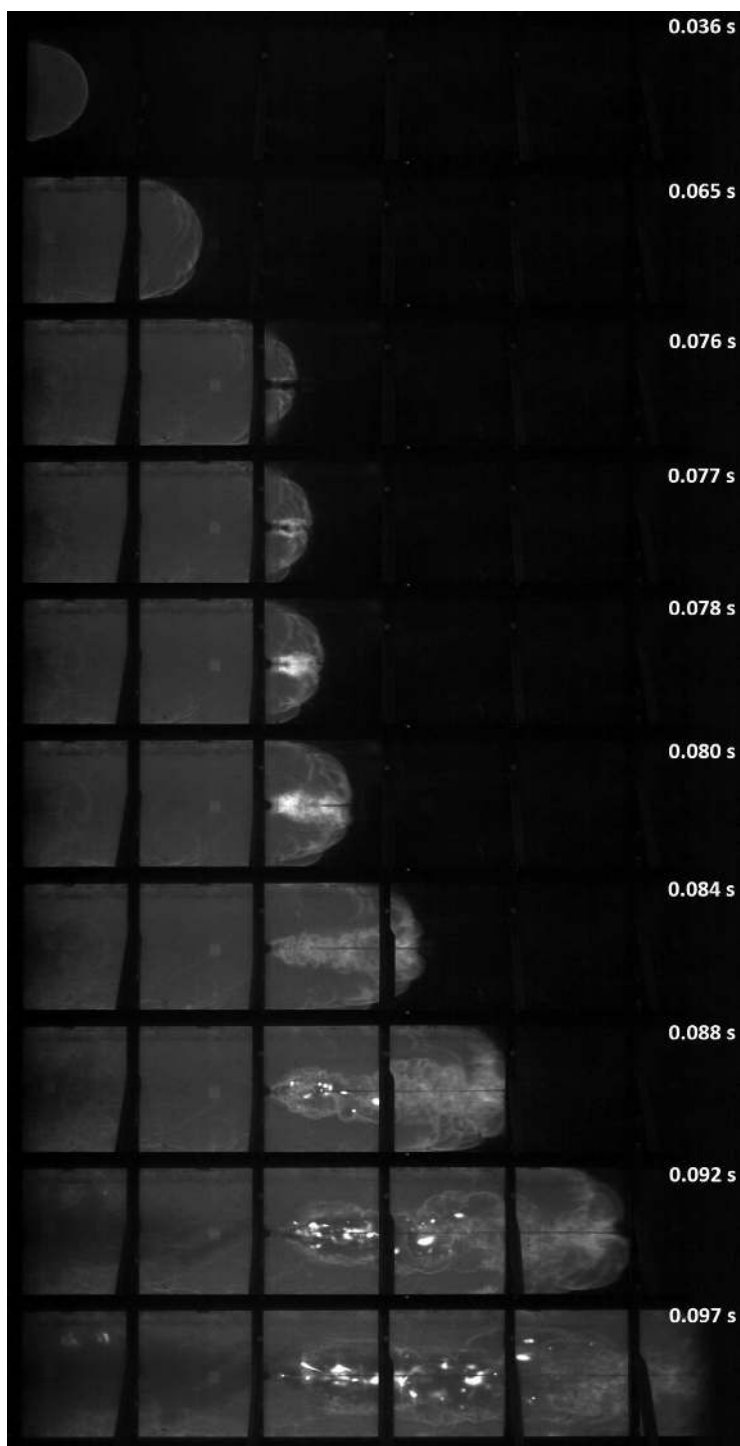
Fig. 11. Selected high-speed video frames, cylinder with a helical steel wire, P = 4D (HW1).
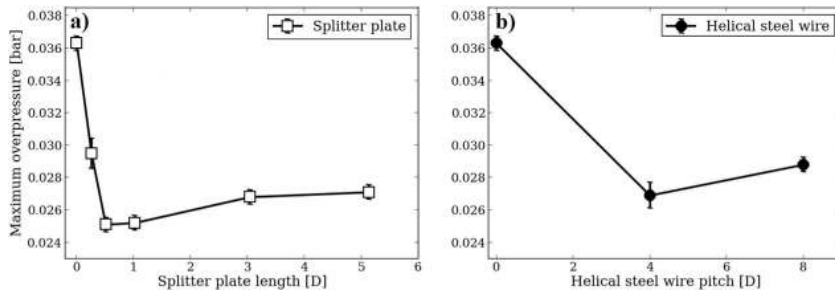
Fig. 12. Parametric study for a) splitter plates of varying length, and b) helical steel wires of varying pitch vs. maximum overpressure (with error bars).
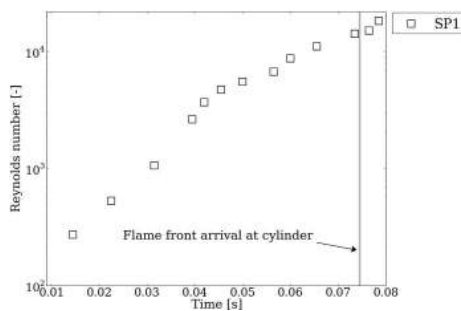

Fig. 13. Reynolds number vs. time (□), vertical grey line marks the arrival of the flame at the cylinder.

dimensional in nature. In the experiments discussed here, the flame front approaching the cylinder originates from a point ignition. The flame front initially has the shape of a half-ellipsoid, and therefore creates a three-dimensional flow field upstream of the cylinder in the initial phase. In addition, boundary-layers are created as the flow is pushed along the channel walls, and the flow past the circular cylinder will likely be affected by end effects and various three-dimensional instabilities (Kong, 1996). For a circular cylinder with an aspect ratio of 17.8 in an accelerating flow, confining walls may delay somewhat the onset of BVK instability (Lee and Budwig, 1991). For the present experimental setup, three-dimensional effects cannot be further analysed. However, the significant effects of applying control methods developed for suppressing the nominally two-dimensional instability suggest that the effects of the instability can be important also in three-dimensional, transient flow fields. Furthermore, the efficiency of the present control methods at relatively high Re implies that the prime instability mode associated with the von Kármán vortex street dominates a wide range of flows (Choi et al., 2008).

5. Conclusions

The experimental results presented in this paper imply that vortex shedding due to the Bénard–von Kármán (BVK) instability in the wake of a bluff-body may have a significant effect on the overpressure generation in gas explosions. Furthermore, the results

show that applying passive control methods to the bluff-body can significantly reduce the maximum explosion overpressure. In the present study, two different passive bluff-body control methods were applied to a circular cylinder, inserted in a series of propane-air explosions. For method i) a splitter plate of varying length L was inserted just downstream of the cylinder, and for method ii) a helical steel wire of varying pitch P was added to the cylinder surface. The most effective splitter plate lengths for method i) were 1.02D and 0.51D, while for method ii), a pitch of 4D gave the most significant reduction in overpressure. For these configurations, the maximum overpressures were reduced by approximately 32% and 25% for method i) and ii), respectively, while the corresponding reductions in maximum pressure impulse were 25% and 16%, respectively. High-speed video recordings visualized the flame propagation in each test. Regions of enhanced burning rates in the circular cylinder wake, in large coherent structures resembling the von Kármán vortex street, could be observed when no control method was applied. When the control methods were successful, coherent shedding could not be discerned in the high-speed videos, and the circular cylinder wakes appeared less energetic.

The results from the present study can be used as input to empirical sub-grid models in gas explosion simulators, as resolving vortex shedding for small-scale obstructions in typical CFD tools may require considerable computational resources. In these situations, the effects of vortex shedding must be accounted for by appropriate sub-grid models. To extend the study further, bluff-body control methods should be applied in corresponding large-scale gas explosion tests, to investigate the effect of vortex shedding on flame propagation at higher Reynolds numbers. Experiments should also be performed with several bluff-bodies inserted in various configurations, to study the effects of vortex shedding suppression on wake interactions in more realistic geometries. Depending on the results of further investigations, practically applicable flow control techniques (such as fairings, helical wires or straking) may even be considered as potential explosion mitigation methods.

References

Bradley, D., Mitcheson, A., 1976. Mathematical solutions for explosions in spherical vessels. Combust. Flame 26, 201–217.

Bradley, D., Cresswell, T.M., Puttock, J.S., 2001. Flame acceleration due to flame-induced instabilities in large-scale explosions. Combust. Flame 124 (4), 551–559.

Bloor, M.S., 1964. The transition to turbulence in the wake of a circular cylinder. J. Fluid Mech. 19, 290–304.

Buresti, G., 2000. Bluff-body aerodynamics. In: Solari, G. (Ed.), Proceedings of the International School on Wind-exited and Aeroelastic Vibrations of Structures, Genoa, Italy, June 12–16. Department of Aerospace Engineering, University of Pisa, Italy, pp. 1–31.

Cantwell, B., Coles, D., 1983. An experimental study of entrainment and transport in the turbulent near wake of a circular cylinder. J. Fluid Mech. 136, 321–374.

Choi, H., Jeon, W.-P., Kim, J., 2008. Control of flow over a bluff body. Annu. Rev. Fluid Mech. 40, 113–139.

Ciccarelli, G., Dorofeev, S., 2008. Flame acceleration and transition to detonation in ducts. Prog. Energy Combust. Sci. 34 (4), 499–550.

Damköhler, G., 1940. Der Einfluss der Turbulenz auf die Flammengeschwindigkeit in Gasgemischen. Z. für Elektrochem. 46, 601–652. English translation: NASA Tech. Mem. 1112, 1947.

Eckhoff, R.K., 2005. Explosion Hazards in the Process Industries. Gulf Publishing Company, Houston, Texas.

Fey, U., König, M., Eckelmann, H., 1998. A new Strouhal–Reynolds-number relationship for the circular cylinder in the range $47 < Re < 2 \times 10^5$. Phys. Fluids 10 (7), 1547–1549.

Fureby, C., 2000. A computational study of combustion instabilities due to vortex shedding. Proc. Combust. Inst. 28 (1), 783–791.

Hernandez, F., Abdel-jawad, M., Hao, H., 2015. Simplified multiple equations' inverse problem of vented vessels subjected to internal gas explosions. J. Loss Prev. Process Ind. 35, 65–79.

Hertzberg, J.R., Shepherd, I.G., Talbot, L., 1991. Vortex shedding behind rod stabilized flames. Combust. Flame 86, 1–11.

Hisken, H., Enstad, G.A., Middha, P., van Wingerden, K., 2015. Investigation of concentration effects on the flame acceleration in vented channels. J. Loss Prev. Process Ind. 36, 447–459.

Kong, D., 1996. An Experimental Study of Certain Aspects of Initiation and Turbulent Propagation of Gas Explosions. PhD thesis. Department of Physics and Technology, University of Bergen.

Kong, D., Sand, I.Ø., 1996. Experimental Investigation of Gas Explosion-driven Transient Flow in the Near Wake of Bluff Bodies. Technical report, CMR-96–F20003. Chr. Michelsen Research, Bergen, Norway.

Lee, T., Budwig, R., 1991. The onset and development of circular-cylinder vortex wakes in uniformly accelerating flows. J. Fluid Mech. 232, 611–627.

Libby, P.A., Bray, K.N.C., Moss, J.B., 1979. Effects of finite reaction rate and molecular transport in premixed turbulent combustion. Combust. Flame 34, 285–301.

Lieuwen, T., 2013. Unsteady Combustor Physics. Cambridge University Press, New York, USA.

Lindstedt, R.P., Sakthitharan, V., 1998. Time resolved velocity and turbulence measurements in turbulent gaseous explosions. Combust. Flame 114 (3–4), 469–483.

Lipatnikov, A., Chomiak, J., 2002. Turbulent flame speed and thickness: phenomenology, evaluation, and application in multi-dimensional simulations. Prog. Energy Combust. Sci. 28 (1), 1–73.

Marsh, 2014. The 100 Largest Losses 1974-2013 – Large Property Damage Losses in the Hydrocarbon Industry. Technical report. Marsh Global Energy Risk Engineering, London.

Mercx, W.P.M., 1996. Extended Modelling and Experimental Research into Gas Explosions. Overall final report for the EMERGE project. Technical report, CEC contract EV5V-CT93–0274.

Moen, I.O., Donato, M., Knystautas, R., Lee, J.H., 1980. Flame acceleration due to turbulence produced by obstacles. Combust. Flame 39 (1), 21–32.

Moen, I.O., Lee, J.H.S., Hjertager, B.H., Fuhre, K., Eckhoff, R.K., 1982. Pressure development due to turbulent flame propagation in large-scale methane-air explosions. Combust. Flame 47, 31–52.

Molkov, V., Nekrasov, V., 1981. Dynamics of gas combustion in a constant volume in the presence of exhaust. Combust. Explos. Shock Waves 17 (4), 363–369.

Peters, N., 1988. Laminar flamelet concepts in turbulent combustion. Symp. Int. Combust. 21 (1), 1231–1250.

Rodríguez, I., Lehmkuhl, O., Chiva, J., Borrell, R., Oliva, A., 2015. On the flow past a circular cylinder from critical to super-critical Reynolds numbers: wake topology and vortex shedding. Int. J. Heat Fluid Flow 55, 91–103.

Roshko, A., 1961. Experiments on the flow past a circular cylinder at very high Reynolds numbers. J. Fluid Mech. 10, 345.

Roshko, A., 1993. Perspectives on bluff body aerodynamics. J. Wind Eng. Ind. Aerodyn. 49, 79–100.

Savitzky, A., Golay, M., 1964. Smoothing and differentiation of data by simplified least squares procedures. Anal. Chem. 36 (8), 1627–1639.

Schadow, K.C., Gutmark, E., 1992. Combustion instability related to vortex shedding in dump combustors and their passive control. Prog. Energy Combust. Sci. 18 (2), 117–132.

Shchelkin, K., 1940. Influence of tube roughness on the formation and detonation propagation in gas. J. Exp. Theor. Phys. 10, 823–827.

Schiller, L., Linke, W., 1933. Druck und Reibungswiderstand des Zylinders bei Reynoldsaachen Zahlen 5000 bis 40000. Z. Flugtech. Motorluft, vol. 24, p. 193.

Skjold, T., Pedersen, H., Narasimhamurthy, V., Lakshmipathy, S., Pesch, L., Atanga, G., Folusiak, M., Bernard, L., Siccama, D., Storvik, I., 2014. Pragmatic modelling of industrial explosions in complex geometries: review of the state-of-the-art and prospects for the future. In: Borisov, A., Frolov, S. (Eds.), Zel'dovich Memorial: Accomplishments in the Combustion Science in the Last Decade, vol. 1. Torus Press, pp. 70–74.

Spalding, D., 1971. Mixing and chemical reaction in steady confined turbulent flames. Symp. Int. Combust. 13 (1), 649–657.

Thomann, H., 1959. Measurements of the Recovery Temperature in the Wake of a Cylinder and of a Wedge at Mach Numbers between 0.5 and 3. Aeronautical Research Institute of Sweden (FFA), report number 84.

Wheeler, R., 1919. The inflammation of mixtures of ethane and air in a closed vessel: the effects of turbulence. J. Chem. Soc. – Trans. Br. CXV Part I (VIII), 81–94.

Williamson, C.H.K., 1996. Vortex dynamics in the cylinder wake. Annu. Rev. Fluid Mech. 28, 477–539.

Yu, M.-H., Monkewitz, P.A., 1990. The effect of nonuniform density on the absolute instability of two-dimensional inertial jets and wakes. Phys. Fluids 2, 1175–1181.

Zdravkovich, M.M., 1997. Flow Around Circular Cylinders: Volume 1: Fundamentals. Oxford University Press, New York.

Zdravkovich, M.M., 2003. Flow Around Circular Cylinders: Volume 2: Applications. Oxford University Press, New York.

Paper 4

The effect of vegetation with various degrees of foliage on gas explosions in a 1.5 m channel

Pedersen, H.H., Enstad, G.A., Skjold, T. & Brewerton, R.W.

uib.no